Experimental Development and Performance Investigation of a Self-Consuming, Hybrid Autophage Rocket Propulsion System

Krzysztof W. Bzdyk

James Watt School of Engineering
College of Science and Engineering
University of Glasgow

Submitted in fulfilment of the requirements of the Degree of
Doctor of Philosophy

November 2024

I would like to dedicate this thesis to my loving wife, friends and family.

Abstract

The hybrid autophage engine concept, or self-eating rocket, is an emerging rocket engine technology which aims to greatly reduce launch vehicle dry mass over conventional propulsion systems and allow for the miniaturization of launch vehicles for small satellite payloads. This is achieved by replacing the fuselage of a conventional bi-propellant launch vehicle with a polymer material. By using the heat from the combustion chamber, the fuselage may be vaporized and combined with liquid fuel and oxidiser drawn from the diminishing propellant tanks such that the structural mass of the rocket decreases throughout the launch and contributes toward the total propellant mass flow rate. This greatly increases the efficiency of the rocket allowing for smaller launch vehicles to deliver a payload to low earth orbit.

This study was an investigation in the design and test of a novel hybrid autophage engine system to evaluate the feasibility of the concept, identify key parameters that influence autophage engine performance, and form a performance baseline to anchor computational models for future development. The project consisted of three engines (Ouroboros-1, 2, 3) which were iteratively designed and tested in various configurations.

Ouroboros-1 and Ouroboros-2 were operated as bi-propellant engines which served as prototyping platforms and performance baselines for the Ouroboros-3 autophage engine. All bi-propellant tests were conducted in a steady state operating mode; while autophage tests were conducted in both steady state and pulsed operating modes. Additionally, both the bi-propellant and autophage tests were operated across a range of mixture ratios and engine inlet conditions to characterise engine performance over a wide operating box.

A performance analysis was conducted on the resulting experimental data to compare to theoretical performance of a chemical equilibrium model. Further analysis of the engines evaluated the influence of combustion chamber temperature, throttle setting and mixture ratio on the autophage contribution to both total fuel mass flow rate and total propellant mass flow rate. Additionally, frequency analyses investigated the influence of the autophage engine design on the formation of combustion instabilities.

When compared to bi-propellant operation, the fuselage was recorded as contributing between 5.1% to 15.7% of the total propellant mass during steady state operation and 0% to 18.6% when operating in pulsed mode. These results envelope typical values for the structural mass fraction of conventional launch vehicles and support the feasibility of autophage engines for larger scale development.

Table of contents

List of figures

List of tables

Nomenclature

Greek Symbols

α	Autophage Acceleration Ratio
ρ	Density
μ	Dynamic Viscosity
ε	Structural Coefficient
Γ	Autophage Mass Ratio
γ	Ratio of Specific Heats
σ_θ	Hoop Stress
λ	Payload Ratio
θ	Spray Angle
σ	Surface Tension
δ	Thickness
ζ	Propellant Mass Fraction

Subscripts

c	Combustion Chamber
p	Payload
e	Exhaust/Exit
f	Final
F	Feed
0	Freestream
$fuel$	Fuel
i	Initial

k	Kinetic Friction
m	mean
ox	Oxidiser
p	Propellant
s	Structural
T	Thrust

Other Symbols

A	Area
a	Speed of sound
t_b	Burn Time
C_D	Drag Coefficient
C_d	Discharge Coefficient
D	Diameter
t_d	Combustion Chamber Pressure Decay Time
E	Young's Modulus
F	Force
$C_{f(\dot{m})}$	Fuel Mass Flow Rate Correction Factor
g_0	Gravity Constant
I_{sp}	Specific Impulse
k	liquid residence time
l	Length
m	Mass
$\dot{m}$	Mass Flow Rate
M	Mach Number
M_R	Launch Vehicle Mass Ratio
Oh	Ohnesorge Number
P	Pressure
R	Gas Constant

Re	Reynolds Number
t_r	Combustion Chamber Pressure Rise Time
V	Volume
v	Velocity
We	Weber Number

Acronyms / Abbreviations

AN	Ammonium Nitrate
AP	Ammonium Perchlorate
$BSPP$	British Standard Parallel Pipe
CAD	Computer Aided Design
LEO	Control Volume
$DACS$	Data Acquisition and Control System
DC	Duty Cycle
$FORP$	Fuel-Oxidiser Reaction Products
LEO	Low-Earth Orbit
LH	Liquid Hydrogen
LOX	Liquid Oxygen
NPT	National Pipe Taper
TMR	Total Momentum Ratio
TRL	Technology Readiness Level

Acknowledgements

I would like to acknowledge all the support from my loving wife Jackie and our dog Arya throughout the duration of my research. Additionally, I thank Jack and Patrick for all their help throughout the test campaigns and making these tests a reality.

Thank you to the personnel at DSUK and Machrihanish Airbase for so eagerly allowing us to use their facility to conduct our engine tests and Dr. Adam Baker for facilitating. I would also like to acknowledge the University of Stirling Marine Environmental Research Laboratory for their kindness and generosity in providing critical equipment during the test campaigns.

To the unsung heroes, the support staff at the University of Glasgow, thank you to those working in the procurement office, logistics team, technical services and all others who helped in some way. The research we do would not have been possible without you.

The development of the Ouroboros-3 engine was funded through the Defense and Security Accelerator (DASA) operated by the Defense Science and Technology Laboratory (DSTL) of the UK Ministry of Defense; thank you Jonathan White, Leon Plouviez and James Monk for your support on the programme. Additional hot-fire test campaigns were also funded by the Impact Acceleration Account of the Science and Technology Facilities Council (STFC); thank you Steffan Gwyn and Keith Dingwall for their support.

Finally, I would like to acknowledge the groundbreaking work of Professor Yemets, without which the field of autophagic propulsion would not be active today.

Declaration

I hereby declare that except where specific reference is made to the work of others, the contents of this dissertation are original and have not been submitted in whole or in part for consideration for any other degree or qualification at the University of Glasgow or any other institution.

Krzysztof W. Bzdyk
November 2024

Chapter 1

Introduction

1.1 Overview

Over the last decade there has been a significant increase in the number of small satellites, nanosatellites, and CubeSats launched to low earth orbit. Furthermore, these small satellite systems have become a common platform for much of the aerospace industry due to their relative low-cost and high return on investment and it is predicted that the use of small satellite systems will continue to increase over the next decade [1]. However, current launch methods are unlikely to adequately satisfy the demand for delivering these satellites to low-earth orbit.

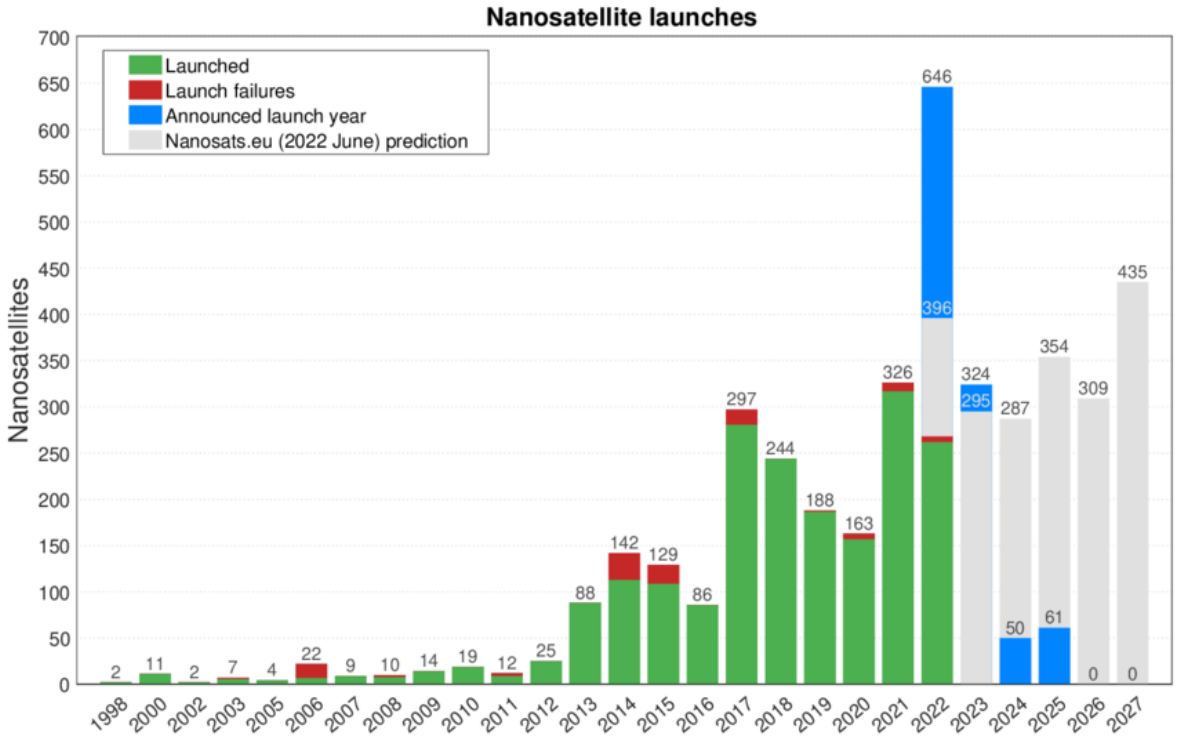

Fig. 1.1 Predicted forecast of nanosat launches made by the Nanosat Database in 2022 [1].

Ideal launch opportunities for these small satellites are already difficult to find and often the only way for small satellites to get to orbit is on a ride-share with a larger payload or with multiple other small satellites. While providing a cost-effective solution, ride-shares are not ideal for some small satellites which may be looking for a particular orbit insertion, rapid

development, or for satellites that may be carrying hardware such as propulsion systems that may not be approved to fly on larger manifests. Thus, there is a business need for miniaturized launch systems capable of launching a payload of up to a few kilograms into low earth orbit.

However, the cost per kilogram to launch a payload into LEO tends to increase as the size of the launcher decreases, as illustrated in Fig. 1.2. One of the smallest operational small launch vehicles is the OneSpace: OS-M capable of launching 100kg to LEO at a price of over $40,000/kg [2] compared to the SpaceX Falcon 9 capability to deliver 22,800 kg to orbit at $2,720/kg [3]. In many cases, the operational advantages of launching a small satellite on a dedicated single payload platform are insufficient to justify the cost when ride-share options at a much lower cost are available, despite the immediacy loss.

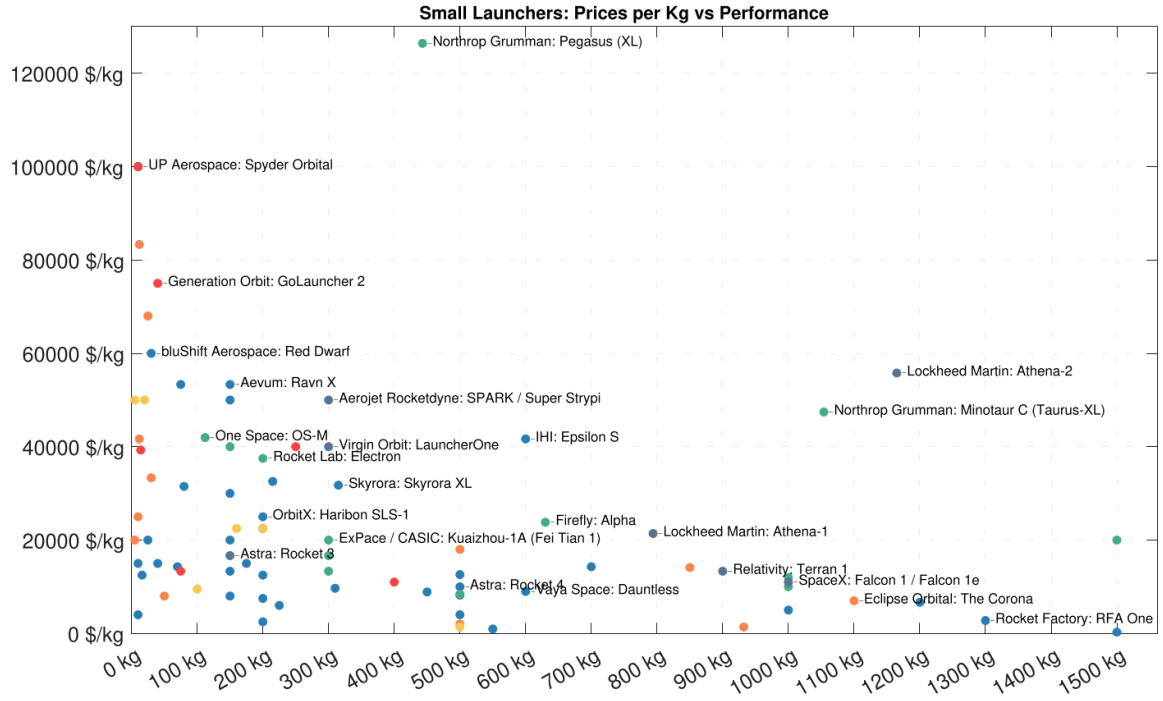

Fig. 1.2 Cost per Kilogram for LEO launch versus payload capability of small launchers [2].

Reducing the cost per kilogram to LEO is vital in achieving viability of small launchers for commercial operation. However, the market opportunity and business needs of small launch vehicles are the result of a larger technological challenge in rocket design. Currently, it is not feasible to miniaturize conventional rockets to an affordable price point for individual small satellite launches due to the scalability of the structural mass fraction. As the launch vehicle becomes smaller, the structural mass fraction becomes larger which in turn reduces the available payload mass and increases the cost per kg of a payload reaching orbit; this is a result of the interaction between the square-cube law [4] and the Tsiolkovsky rocket equation [5].

1.1.1 Effect of the Square-Cube Law on Launch Vehicle Sizing

The square-cube law states that as a three dimensional shape grows in size, its volume grows faster than its surface area. This is represented mathematically by Eq. (1.1) and Eq. (1.2).

$$A_2 = A_1 \left(\frac{l_2}{l_1} \right)^2 \tag{1.1}$$

$$V_2 = V_1 \left(\frac{l_2}{l_1} \right)^3 \tag{1.2}$$

The result of the square-cube law has significant implications when a physical object is scaled up but maintains the same density. Its volume and mass are increased by the cube of the multiplier while its surface area increases only by the square of the same multiplier. In terms of launch vehicles the available propellant is a function of its internal volume and the structural mass is a function of the surface area. As the design of a launch vehicle decreases in size, the available propellant decreases at a higher rate than the structural mass, this shifts the ratio of structural mass and propellant mass.

Moreover, the square-cube law method of scaling makes the assumption that the entirety of the structural mass is capable of being scaled. This is a best-case assumption for conventional launch vehicles and in actuality a portion of the structural mass is referred to as inert mass and is not capable of being scaled. The inert mass of a launch vehicle includes a range of components such as guidance systems, computers, turbomachinery, attitude control, and propulsion systems; which may have static masses or minimum sizes that do not follow the square-cube law scaling in the same way that the launch vehicle fuselage and propellant tanks do [6]. This effectively means that the structural mass of launch vehicles decreases at an even lower rate than the best-case, square-cube law scaling.

1.1.2 Review of Launch Vehicle Mass Ratios

Mass ratios rather than absolute mass values are typically used when discussing the various contributions to the total mass of a launch vehicle. These include the propellant mass fraction, structural coefficient, and payload ratio.

$$m_i = m_p + m_s + m_d \tag{1.3}$$

$$\zeta = \frac{m_p}{m_i} \tag{1.4}$$

$$\varepsilon = \frac{m_s}{m_s + m_p} = \frac{m_s}{m_i - m_d} \tag{1.5}$$

$$\lambda = \frac{m_d}{m_s + m_p} = \frac{m_d}{m_i - m_d} \tag{1.6}$$

The ratio of initial to final mass is typically referred to as the launch vehicle mass ratio, M_R.

$$M_R = \frac{m_i}{m_e} = \frac{1 + \lambda}{\varepsilon + \lambda} = \frac{1}{1 - \zeta} \tag{1.7}$$

When the square-cubed law is applied to the mass fractions, we find that the propellant mass fraction decreases as a result of the propellant mass decreasing at a faster rate than the structural mass. Consequently the structural coefficient increases and, if the payload ratio remains constant (this assumes the payload mass scales linearly with vehicle mass), the launch vehicle mass ratio also decreases. This has a significant impact in the achievable change in velocity of a launch vehicle per the Tsiolkovsky equation.

1.1.3 Review of the Tsiolkovsky Idealized Rocket Equation

The Tsiolkovsky rocket equation is an idealised mathematical equation that governs the basic principles of rocket flight due to the conservation of momentum. It states that the maximum change of velocity of a launch vehicle is a function of its effective exhaust/exit velocity and mass ratio.

$$\Delta v = v_e \, ln\,(M_R) \tag{1.8}$$

Where the exhaust velocity can be written in terms of gravity constant and specific impulse.

$$v_e = g\, I_{sp} \tag{1.9}$$

Thus, a decrease in launch vehicle mass ratio will significantly decrease the maximum change in velocity of a launch vehicle. This directly impacts the feasibility of launch vehicle miniaturisation by limiting what parameters can be changed to maintain the minimum Δv required for orbit insertion without even considering losses due to gravity, air resistance, thrust vectoring and off-nominal nozzle expansion [7].

1.1.4 Methods for Scaling Conventional Launch Vehicles

When considering the Tsiolkovsky rocket equation, there are only four variables that are able to change the total Δv of a launch vehicle: v_e, ε, λ, and number of stages[1]. The exhaust velocity is a function of propulsion system design and the molecular weight of propellants. Practically, there is a limit to the maximum achievable exhaust velocity of all propulsion systems. In chemical propulsion systems, this maximum is due to both the available chemical energy of the propellants, combustion inefficiencies, and material constraints. Propulsion systems operating on liquid oxygen and liquid hydrogen (LOX/LH) have some of the highest theoretical exhaust velocities of up to 4,500 m/s [8]. Thus, changing the exhaust velocity of a scaled launch vehicle is not feasible when using chemical propulsion systems. The structural coefficient, ε is also unable to be changed in conventional launch vehicles because it is a result of the scaling.

Historically, when launch vehicles have been scaled to smaller designs the payload ratio, λ, and the number of stages are typically what is changed in order to achieve the required Δv to reach orbit. As λ is reduced, the launch vehicle mass ratio will increase; however, the

[1]There are some other launch methods that influence Δv of a launch vehicle such as horizontal launch capabilities; however, these are not considered since they change the required Δv rather than the actual capabilities of the launch vehicle design

increase in Δv does not scale linearly with a decrease in λ as shown when combining Eq. (1.7) and Eq. (1.8). When taking into account that the total mass of the launcher must stay constant (due to the scaling), a reduction in λ also corresponds to a decrease in total propellant mass, m_d.

This is the fundamental reason why the cost per kilogram to reach LEO is significantly higher for small launchers than for larger launchers. In order to achieve their desired Δv, small launchers will typically be designed with a lower payload ratio which will also significantly reduce their maximum payload capacity. Additionally, there is a physical limit to how much a conventional system is able to be scaled using this method because a reduction in payload mass to zero can still result in miniaturised designs having insufficient Δv.

The alternative method to increasing the total Δv of a scaled conventional launch vehicle is by adding launcher stages [9]. This is done by a summation of the Δv contribution of each stage per Eq. (1.10) whereby the payload mass of each stage equals the total mass of each subsequent stage per Eq. (1.11).

$$\Delta v_f = \sum_{1}^{n} \Delta v = \Delta v_1 + \Delta v_2 + \Delta v_3 + \dots \tag{1.10}$$

$$m_{d1} = m_{i2} = m_{p2} + m_{s2} + m_{d2} \tag{1.11}$$

While there have been many feasibility studies and proposed designs for single-stage-to-orbit vehicles (SSO); at this time, there has never been a launch vehicle developed capable of reaching orbit on a single stage [10, 11]. This is due to material limitations in reducing the structural coefficient to a favorable mass ratio capable of reaching orbit [12]. Therefore, it is almost guaranteed that conventional launch vehicles will have at minimum 2 stages.

Fundamentally, staging operates by discarding empty tankage or "dead mass" during launch vehicle ascent as the propellant is burned. This can be accomplished through the use of boosters and parallel staging or through serial (tandem) staging. Each additional stage further increases the total Δv; however, it also adds complexity, potential failure modes,and inert mass in the form of couplers, separation systems and propulsion systems. Therefore, the majority of multi-stage launch vehicles operate between 2-4 stages [13].

1.1.5 Consideration of an Infinitely Staged Launch Vehicle

Nevertheless, if we consider the idealized staging solution the result is an infinitely staged launch vehicle. For every discrete unit of propellant burned, a corresponding unit of structural mass would also be ejected. This would be a system that continuously eliminates the non-inert component of the structural mass thereby never carrying empty tankage or structural components that are not actively contributing to the launch.

Thus, the non-inert structural mass of an infinitely staged vehicle can be treated as a propellant mass with zero exhaust velocity. This resolves the minimum size limitations of conventional launch vehicle scaling by only needing to consider the inert mass when calculating the structural coefficient and total mass ratio. In this way, the idealized infinite staged

rocket solution resolves into a single-stage-to-orbit with a minimised structural coefficient and a maximised mass ratio [14].

The Tsiolkovksy equation can be applied to the infinitely staged rocket concept to compute the ideal Δv by deriving the rocket equation from the basic momentum equation.

$$m_i \frac{dv}{dt} = \frac{dm}{dt} v_e \tag{1.12}$$

Where the change in total vehicle mass is given by:

$$\frac{dm}{dt} = \frac{dm_i}{dt} - \frac{dm_s}{dt} \tag{1.13}$$

Introducing a new parameter, K which equals the ratio of inert structural mass to propellant mass for an infinitely staged vehicle

$$K = \frac{m_s}{m_p} \tag{1.14}$$

and substituting for $\frac{dm}{dt}$ and v_e the equation becomes:

$$dv = -g I_{sp} \frac{dm_p}{m_d + (1+K)m_p} \tag{1.15}$$

Equation (1.15) can then be integrated across the initial and final limits which results in Eq. (1.8) for single-stage vehicles, as expected, and Eq. (1.16) for infinitely staged vehicles [15].

$$\Delta v = \frac{g I_{sp}}{1+K} ln \frac{1}{1-(1+K)\zeta} \tag{1.16}$$

This is the basic operating principle behind the autophage engine concept which seeks to maximise the launch vehicle mass ratio by using sections of the fuselage as a source of fuel. Overall, an autophage system would allow for further miniaturisation of launch vehicles beyond current capabilities. This is advantageous for maintaining a competitive cost per kilogram for small satellite payloads to LEO but also in delivering constrained mass payloads on smaller launch platforms with applications in the missile and missile defense sector.

1.2 Propulsion Theory

This section presents the fundamentals of propulsion including the conservation of momentum, supersonic flow, principles of a nozzle, and the derivation of the engine thrust equation. It further introduces characteristic velocity, thrust coefficient, and specific impulse which are key concepts in describing rocket engine performance. These concepts are then applied to an autophage vehicle architecture to demonstrate its theoretical feasibility.

1.2.1 Thrust

There are two components to the thrust equation: the momentum contribution and the pressure contribution. The momentum contribution is a function of the propellant mass flow rate

and the exit velocity; and provides the largest contribution by far in chemical propulsion systems. The pressure contribution is a function of nozzle exit area and the difference between the nozzle exit pressure and the ambient atmospheric pressure. The combination of these two contributions to the thrust equation results in a force which propels the rocket forward. Fundamentally, this is what allows rockets to operate in a vacuum with the nozzle conducting work on the exhaust gases to facilitate a transfer of momentum.

The thrust equation is derived by taking the integral of all pressures with a projection onto the thrust axis as shown in Fig. 1.3. Any decomposed forces acting radially do not contribute towards the thrust due to symmetry of the combustion chamber and nozzle.

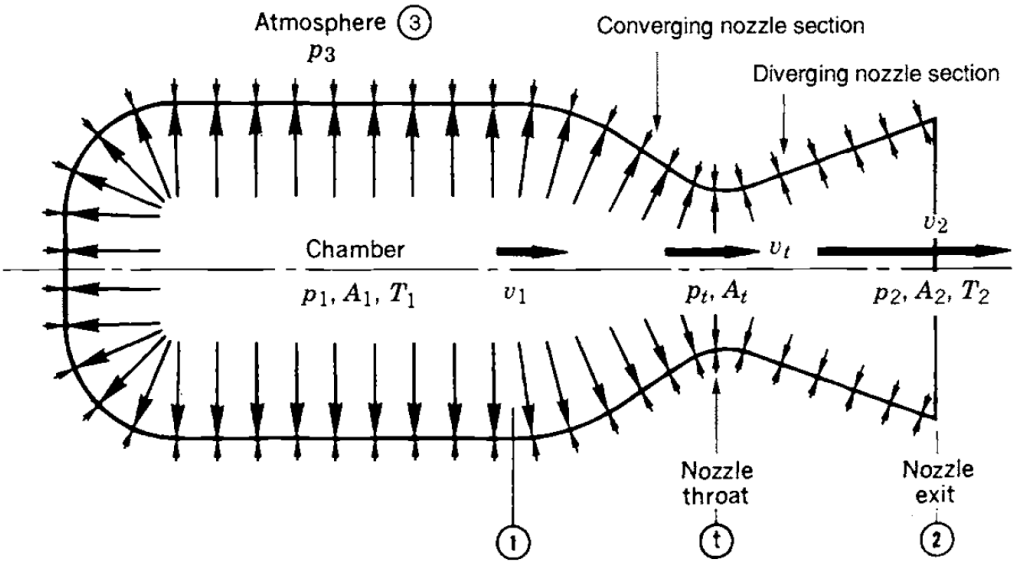

Fig. 1.3 Forces acting on a classical rocket engine combustion chamber and nozzle [13].

Integrating the pressures acting on the rocket nozzle results in Eq. (1.17).

$$F_T = \int P\,dA = \dot{m}\,v_e + (P_e - P_0)\,A_e \tag{1.17}$$

Thus the engine thrust is a function of the propellant mass flow rate, $\dot{m}$, multiplied by the exhaust velocity, v_e, plus the pressure contribution. The pressure contribution is defined as the difference between the nozzle exit pressure, P_e, and the ambient pressure, P_0, multiplied by the exit area, A_e.

1.2.2 Specific Impulse

The specific impulse, I_{sp}, represents the thrust generated per unit of propellant mass. It is a key component in evaluating propulsion systems since a higher specific impulse is indicative of better performance. If the total propellant mass flow rate is given as $\dot{m}$ and the gravitational constant as g_0, the I_{sp} can be written as:

$$I_{sp} = \frac{\int_0^t F_T\,dt}{g_0 \int_0^t \dot{m}\,dt} \tag{1.18}$$

For a constant propellant mass flow rate and constant thrust Eq. (1.18) can be re-written as Eq. (1.19).

$$I_{sp} = \frac{F_T}{g_0 \dot{m}} \tag{1.19}$$

The resulting I_{sp} is given in units of "seconds" and is a time-averaged value.

1.2.3 Characteristic Velocity

The characteristic velocity, $c*$, of a rocket engine is a useful term for comparing the relative performance of different chemical rocket propulsion system designs and propellants. It is independant of nozzle characteristics and can be determined directly from measurements of propellant mass flow rate, combustion chamber pressure, and throat area as given by Eq. (1.20).

$$c* = \frac{P_c A_t}{\dot{m}} \tag{1.20}$$

1.2.4 Supersonic Flow and Fundamentals of a de Laval (Converging-Diverging) Nozzle

In order to generate the high exhaust velocities necessary for effective rocket propulsion systems, exhaust gases are accelerated to supersonic velocities. This is often done through the use of a de Laval (converging-diverging) nozzle. In a converging-diverging nozzle the hot gases from the combustion chamber are converged down to a minimum area, or nozzle throat. As the gases travel through the throat they are accelerated to the sonic velocity where the flow is choked by the nozzle throat, restricting the mass flow rate. Downstream of the throat, the flow is isentropically expanded to a supersonic Mach number which decreases the static pressure and temperature. The exit temperature determines the exit speed of sound and thus the exit velocity. To understand how the converging-diverging nozzle is able to accelerate flows to supersonic velocities we start with the conservation of mass equation:

$$\dot{m} = \rho v A = constant \tag{1.21}$$

Differentiating yields Eq. (1.22).

$$\frac{d\rho}{\rho} + \frac{dv}{v} + \frac{dA}{A} = 0 \tag{1.22}$$

Consider the conservation of momentum,

$$\rho v dv = -dp \tag{1.23}$$

isentropic flow relation, where γ is the ratio of specific heats,

$$dp = \frac{\gamma p}{\rho d\rho} \tag{1.24}$$

and equation of state, where R is the gas constant and T is the temperature.

$$\frac{p}{\rho} = RT \tag{1.25}$$

Combining equations (1.24) and (1.25) yields

$$dp = \gamma RT\,\rho \tag{1.26}$$

This can be simplified by applying the equation for the speed of sound given by (1.27):

$$a = \sqrt{\gamma RT} \tag{1.27}$$

$$dp = a^2\,d\rho \tag{1.28}$$

Combining this result with the change in pressure within Eq. (1.23) yields the following:

$$\rho\, v\, dv = -(a^2)\,d\rho \tag{1.29}$$

$$\frac{v}{a^2}dv = -\frac{d\rho}{\rho} \tag{1.30}$$

$$\frac{-(\frac{v}{a})^2\,dv}{v} = \frac{d\rho}{\rho} \tag{1.31}$$

Using the definition of Mach number given by

$$M = \frac{v}{a} \tag{1.32}$$

and combining the result with the conservation of mass flow equation, Eq. (1.22) results in:

$$\frac{(1-M^2)}{v}dv = -\frac{dA}{A} \tag{1.33}$$

This result is critical to understanding supersonic flow since it describes how the velocity of the flow changes when area changes. This is dependent on the Mach number of the flow. When Mach number is less than 1 (subsonic), constricting the the flow results in an increase in velocity. However, when the Mach number is greater than 1 (supersonic) expanding the area increases the flow velocity. Thus, a converging-diverging nozzle is able to accelerate subsonic flows by constricting the area up to the nozzle throat such that the flow is choked and reaches $M = 1.0$. The flow is then expanded and accelerated to generate the high exhaust velocities necessary for rocket propulsion systems.

1.2.5 Application to an Autophage Engine

In a solid-propellant autophage rocket proposed by many early patents [16, 17], the combustion chamber pressure, and by approximation the momentum contribution of the thrust, acts mostly on the fuselage rather than the injector face of the combustion chamber. This architecture will effectively eject the fuselage out of the engine. To illustrate this, consider Fig. 1.4 which is a

simplification of early proposed autophage rockets. This figure assumes a cross-section of a rectangular autophage engine, in a vacuum, and subsonic/incompressible flow through an orifice at the nozzle.

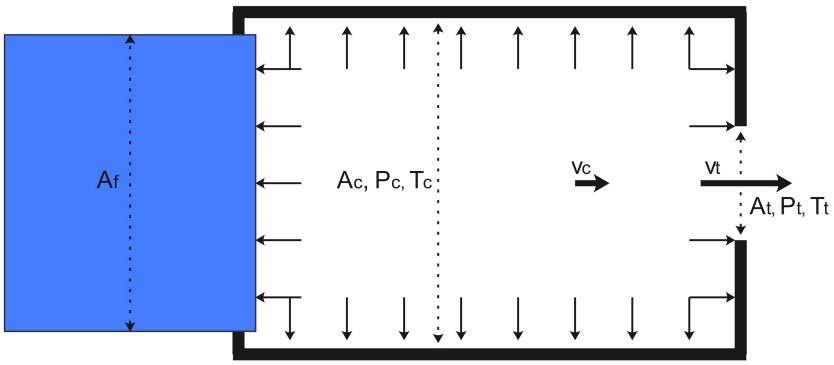

Fig. 1.4 Simplified solid-propellant autophage engine with direct fuselage insertion into the combustion chamber.

As in a conventional system, the pressures within the combustion chamber act uniformly and perpendicular to the combustion chamber surfaces. However, at the front of the combustion chamber, there are two surfaces which the pressures act on: the combustion chamber area, A_c, and the fuselage area A_f. The integration of all the pressures yields a simplified net thrust equivalent to (1.34).

$$F_T = P_c A_t \tag{1.34}$$

The net thrust is distributed uniformly across surfaces A_f and A_c and can be decomposed into two forces, F_c and F_f which act on the combustion chamber and fuselage respectively.

$$F_c = F_T \frac{A_c}{A_f + A_c} \tag{1.35}$$

$$F_f = F_T \frac{A_f}{A_f + A_c} \tag{1.36}$$

From the Fig. 1.4, when A_f is greater than A_t, the force F_c will act in the opposite direction of F_f and thus push the combustion chamber and fuselage apart. However, consider an autophage engine design where A_f is significantly smaller than A_t (Fig. 1.5) and the mass of the fuselage is significantly greater than the mass of the combustion chamber.

In this case, a small F_f acts on a large-mass fuselage, while a greater F_c acts on the small-mass combustion chamber in the same direction. The forces and masses can be used to calculate the acceleration of each component. The relationship between the fuselage and combustion chamber accelerations can then be written as an autophage acceleration ratio, α.

$$\alpha = \frac{\frac{F_c}{M_c}}{\frac{F_f}{M_f}} \tag{1.37}$$

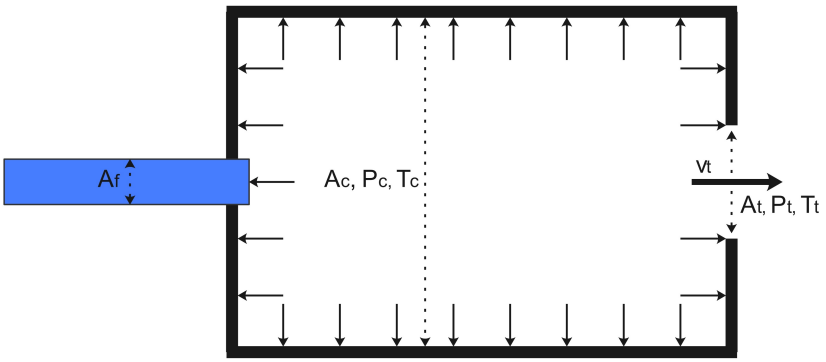

Fig. 1.5 Simplified solid-propellant autophage engine with a small fuselage area.

Substituting in (1.34), (1.35), and (1.36) yields

$$\alpha = \frac{A_c M_f}{A_f M_c} \tag{1.38}$$

Under this simplified calculation (which does not include the effects of friction), when α is greater than 1.0, the pressure within the combustion chamber will impart an acceleration onto the engine that is greater than the acceleration of the fuselage. This difference in relative acceleration will cause the fuselage to be inserted into the engine. However, this autophage rocket design is impractical since the diameter of the engine far exceeds the diameter of the fuselage. Additionally, as the fuselage is consumed as propellant during the flight trajectory, α will continuously decrease as the total mass of the fuselage decreases. These are major issues that affect the feasibility of a self-sustaining autophage rocket since the proposed advantage of this architecture is to use the rocket structure as a source of propellant to reduce the overall total mass of a launch vehicle.

One solution is to use a tubular solid propellant with space on the inside of the fuselage for a mechanical system that can exert the required force and drive the fuselage into the combustion chamber (Fig. 1.6).

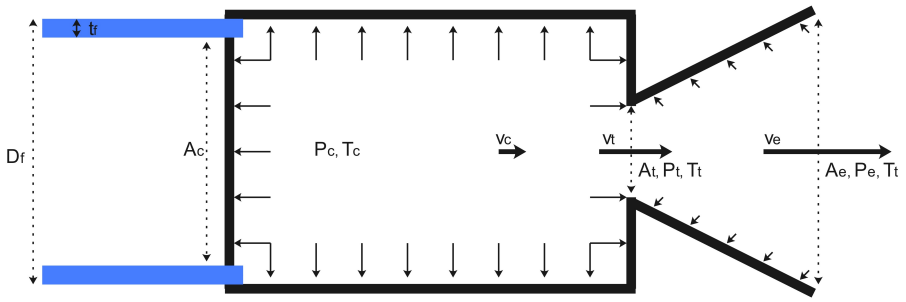

Fig. 1.6 Simplified solid-propellant autophage engine with a small, tubular fuselage area.

1.3 Historical Review On Autophage Propulsion Systems

The concept of an autophage (self-eating) rocket has existed effectively as long as the infinite staged rocket architecture and by extension launch vehicle staging itself. Autophage systems operate specifically as infinite staged rockets by consuming unproductive structural mass continuously throughout the launch. For a solid rocket, this unproductive structural mass consists of the spent motor casing and for a liquid rocket it can consist of both the fuselage and empty tankage.

Various patents and design concepts for autophage system can be dated to the 1930s with sporadic development through to the 1980s. While autophage concepts had been theorized for almost a century, the technology had never been physically designed and tested until an autophage end-burning solid-propellant prototype engine was tested by Dnipro University in 2015 [18].

1.3.1 Early Development and Patents

The first recorded autophage concept dates back to a patent in 1938 for a self-propelling projectile [16]. This concept was designed to operate as an end-burning solid rocket motor whereby the motor casing was burned alongside the propellant resulting in the length of the projectile decreasing over the course of the burn.

A subsequent patent in 1966 expanded on the autophage end-burning solid rocket design by introducing a thrust chamber that would travel across the length of the motor [17]. As propellant is burned inside the thrust chamber, the fuselage is continuously fed into the chamber at a constant rate.

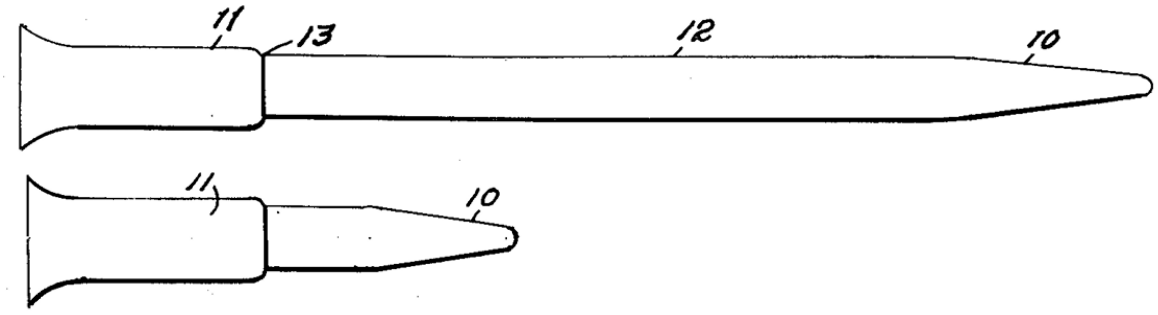

Fig. 1.7 Drawing of an early autophage end-burning solid-propellant rocket concept[17] with the rocket body being fed into the thrust chamber.

The patent also calculates that the inertia of the launch vehicle and engine thrust contribute towards a net force that will feed the fuselage into the combustion chamber. However, this calculation is incomplete, makes an incorrect assumption regarding how the combustion chamber pressure acts on the cross-sectional area of the fuselage, and it does not account for the momentum contribution of the thrust equation.

This concept of a tubular propellant can also be extended out to hybrid and liquid propulsion systems. This architecture first appeared in a patent from 1987 which proposed bi-

propellant tanks to be made from a kevlar-epoxy material which could be burned on ascent alongside liquid propellants [19].

Overall, the theoretical performance benefits of an infinitely staged autophage launch vehicle over conventional multi-stage systems have been well understood since before even the world's first multistage rocket (the WAC Corporal) was launched in 1948. Interest in the infinitely staged rocket has continued, with the US Air Force Rocket Propulsion Laboratory identifying it as an advanced propulsion concept in 1972 while the Apollo program was still landing men on the Moon. However, in their words:

> "Infinite staging is an illusive concept that has not been accomplished by any technique that really delivers a significant payoff in flight performance. There are various schemes for eliminating system inerts, but in general they are not true infinite staging concepts." [15]

This addresses the crux of the difficulties in the development of a functional autophage rocket; which is that the proposed concepts and designs in practice did not exceed the performance of conventional systems used to deliver very large payloads to orbit. Since that evaluation however, technology has advanced and the average small satellite mass has significantly decreased over the past 50 years. Improvements to electronics, propulsion system design, and materials science have progressed to a point that it is feasible to once again consider how current technology can be applied to an infinitely-staged, autophage rocket.

1.3.2 Development and Test of an Autophage Proof-of-Concept

While autophage concepts had been theorized and proposed for almost a century, the technology had never been rigorously studied nor physically designed and tested to verify the actual performance until a proof-of-concept demonstration in 2015 by Yemets, et al. at Dnipro National University [18]. Additionally, early development had been made by the team into the theoretical flight trajectory of an autophage launch vehicle to reach LEO which eventually led to multiple laboratory tests of a proof-of-concept autophage engine.

The work by the Dnipro team was the first to seriously consider the flight trajectory of an autophage rocket beyond the simplified lens of the Tsiolkovsky equation. The researchers considered a solid-propellant autophage platform which, much like previous designs, fed the rocket fuselage into a thrust chamber where the propellants would react. The goal of the trajectory analysis was to determine the feasibility of using a polymer as the fuselage material which would provide the structural support of the launch vehicle. The key parameters considered were the temperature of the contracting rocket airframe surface during ascent and the resulting G-loading on the airframe.

As any projectile travels through the atmosphere it experiences a range of atmospheric flow conditions that are dependant on both projectile velocity, altitude, and Mach number. In particular, high velocity flight at low altitudes is an area where launch vehicles can have significant losses due to excessive drag. Though, the Dnipro researchers found that autophage engines have an additional challenge of airframe skin temperature during those flight conditions. This is because proposed autophage designs typically use a polymer as the

fuselage material with most having a maximum melting temperature at approximately 200°C [20].

Using an axisymmetric Navier-Stokes solver to calculate the thermal loads, the Dnipro team found that the airframe skin temperature of their proposed autophage launcher reached peak temperatures of up to 1400K at 14 seconds into the burn. This far exceeds the melting point of the launch vehicle structure and thus, necessitates either using a protective shell or coating on the fuselage skin, altering the flight trajectory in a way to lower the maximum skin temperature, or a combination thereof. One of the potential solutions for changing the flight trajectory involved introducing a pause in engine operation via an engine shutdown and restart midflight.

When evaluating the G-loading for such a trajectory, it was determined that the fuselage would have sufficient structural strength for a majority of the ascent. However, the maximum G-load would be exceeded in some instances requiring a capability to throttle the engine in addition to the aforementioned shutdown and restart capabilities. This however is not feasible with typical solid-propellant systems and necessitates the development of a throttleable solid-propellant engine. This resulted in the design, development and test of the first proof-of-concept autophage engine at Dnipro National University to meet the requirements of autophage flight.

The design featured a "gasification chamber" at the fuselage and thrust chamber interface. There the heat from the combustion chamber would cause the solid-propellants to sublimate and the resulting gases would be injected into the thrust chamber to perpetuate the combustion process. As the rocket burns, the fuselage is inserted into the combustion chamber and the launch vehicle length decreases throughout the duration of the trajectory.

The propellant used was a mixture of powdered ammonium perchlorate (AP) and ammonium nitrate (AN) as the oxidiser; encased by the fuel which was polypropylene based. Two of the major challenges in this design were engine ignition and maintaining steady state heat transfer to the propellants. In order to address the first challenge, the design used a pilot gas to start the engine and to heat the chamber to a high enough temperature such that vaporization of the propellants could begin. This was sufficient to achieve ignition and demonstrate the first in the world test of a proof-of-concept autophage engine. The results showed a maximum feed rate of 3.0 mm/s of the fuselage into the thrust chamber and data on the feed force and chamber pressure. However, the test rig was not configured in a way that made measuring thrust possible.

While the design had a successful test it also had a recurring problem of detonations inside the engine causing destruction of the test rig. This was due to sensitivity to priming the engine and the solid-propellant igniting inside the gasification chamber instead of the thrust chamber (Fig. 1.8). Overall though, the research was very successful at overcoming the nontrivial challenge of actually building and testing an autophage engine concept after almost a century of only being theorized. Additionally, the conclusions of that first test campaign would shape the development of autophage engines to the present day and of the research contained herein by identifying key areas for development. These were: development of a

throttleable autophage engine, maximisation of fuselage feed rate, and an investigation into the effect of pulsed mode operation on feed rate.

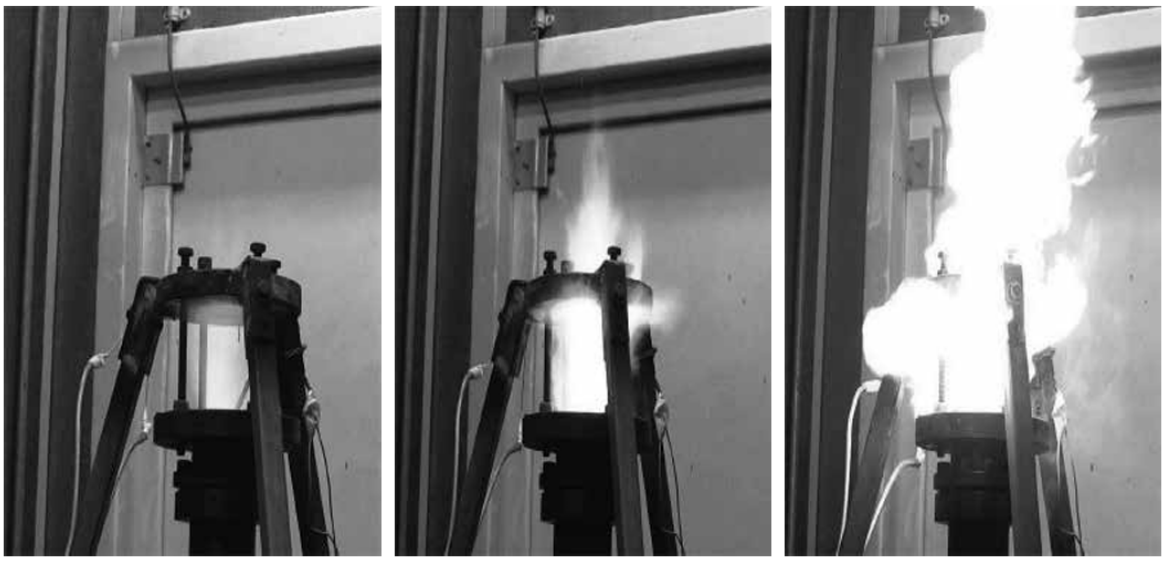

Fig. 1.8 First known proof-of-concept autophage engine tests [18]. The final image shows an engine failure caused by pre-ignition in the gasification chamber.

Continued development of this system led to design improvements by the Dnipro team and a new set of hot-fire tests in 2018 [21]. A depiction of the improved Dnipro solid-propellant autophage concept is shown in Fig. 1.9. The major change over the previous design was in the gasification chamber which was now covered by a heat transfer surface in an effort to improve the feed rate.

The results of the second test campaign were also an improvement and yielded an extended firing duration of 60 seconds in steady state, autophage operation. However, much like the previous test firings, the test rig was unable to measure engine thrust and the engine failed due to a detonation in the chamber. It was hypothesized that the detonations could be due to combustion instabilities; however, the sampling rate of the combustion chamber pressures was only 5 Hz which is insufficient to measure low frequency instabilities such as chug (100-300 Hz) let alone high frequency combustion instabilities such as screech (2-5 kHz). Therefore, while these proof-of-concept tests have demonstrated the feasibility of building and testing an autophage engine they lack comprehensive data acquisition to accurately characterise the engine performance and operating conditions.

1.4 Motivation of Current Studies

With the rise in small satellite development over the past decade, dedicated nanolauncher platforms capable of delivering payloads of up to 100 kg to LEO have become increasingly desirable. An affordable nanolauncher would give small satellite teams an opportunity for rapid-deployment, targeted orbit insertion, as well as launch location and payload flexibility that are not achievable through most ride share programs. However, miniaturisation of conventional launch system designs is difficult due to the square-cube law which increases the structural coefficient and by extension the cost per kilogram to reach LEO.

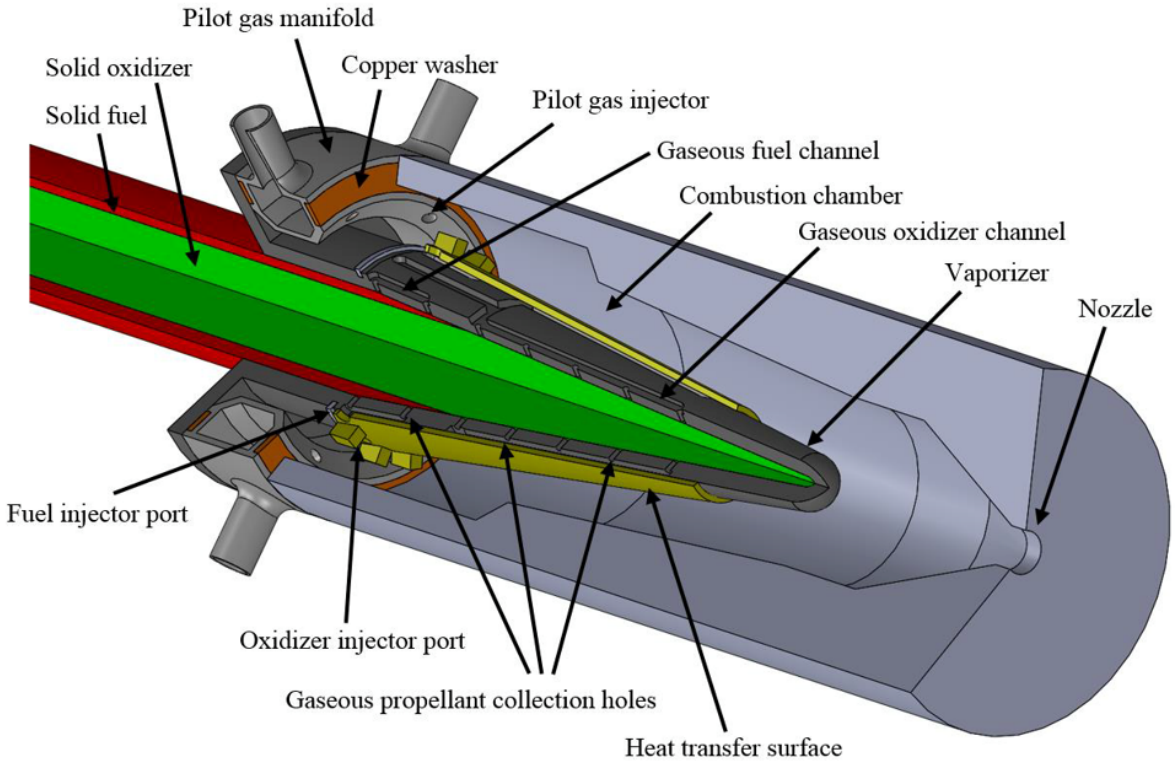

Fig. 1.9 Testbed of the Dnipro autophage solid-propellant engine concept [21].

Current examples of dedicated small launch vehicles reach a very high cost per kilogram to LEO and are not affordable for most payloads. Fundamentally, the only ways to increase the capabilities of nanolaunchers and reduce the cost per launch is either in a breakthrough in the performance of propulsion systems or in the minimisation of the structural coefficient. Research in propulsion system breakthroughs include the use of aerospikes, rotating detonation engines, and high energy density propellants; all of which may be able to provide small increases in engine performance but often at the expense of higher structural mass which can offset any theoretical gains in engine performance.

On the other hand, reducing the structural coefficient addresses the root cause behind the launch vehicle scaling problem and could even be used in conjunction with breakthroughs in propulsion system designs to act as a force multiplier of launch vehicle capabilities. Recent advances in carbon fibre composites and additive manufacturing have been able to slightly reduce the structural coefficient of launch vehicles but not enough to significantly lower the cost per kilogram of small satellite payloads to reach LEO. However, the concept behind an infinitely staged rocket could provide the breakthrough needed to make the use case of small launch vehicle platforms feasible.

The infinitely staged launch vehicle has been theorised since the 1930s in the form of various patents, designs, and studies. It operates by leveraging the concept of continuously jettisoning all vehicle mass that is not actively functioning; for a solid-propellant system this means eliminating the motor casing as it is used while for a liquid-propellant system it is both eliminating the fuselage and empty tankage during ascent. If the system uses the "dead mass" as propellant it is known as an autophage, or self-eating rocket.

Even though an infinitely-staged, autophage rocket could provide a significant increase to launch vehicle capabilities, the concept is still an emerging technology and until recently it had never been physically built and tested. And while the first solid-propellant autophage engines developed by Dnipro National University demonstrated the system as a proof-of-concept and elevated the technology readiness level to 2, the operating conditions and the resulting performance data of those tests were limited in scope. Thus, research in this field required a more robust experimental campaign that would test a wider operating box, engine throttleability and pulsed mode operation to further advance the technology readiness level of autophage propulsion systems.

1.5 Research Objectives

The research contained herein was conducted with the purpose of expanding the knowledge of autophage and infinitely staged launch vehicles through the development and experimental test of a novel hybrid autophage propulsion system. The experimental results form a comprehensive dataset that can be used in the development of autophage launch vehicle trajectory simulations, engine performance models, and in the refining and scaling of autophage engine designs. The following sections detail the specific objectives of the research in order to elevate the TRL of autophage systems from 2 to 4.

1.5.1 Liquid Bi-Propellant Architecture as an Autophage System

One of the key changes in the current studies versus those conducted at Dnipro was to switch the architecture from a solid-propellant to a liquid bi-propellant autophage engine. This was decided in-part based on a study done by the University of Glasgow regarding the sizing of autophage engines for cubesat-scale nanolaunchers [22]. Based on the Dnipro test data, the analysis found that even when scaled to larger engine sizes the solid-propellant platform would still likely need an external feed force to drive the fuselage into the thrust chamber and may not be self-sustaining under its own thrust. However, liquid bi-propellant could be a more successful architecture for a multitude of reasons.

First, it is able to be operated in both a bi-propellant configuration and an autophage configuration. This allows verification of the engine design as a bi-propellant system which can isolate problems and failure modes during engine development. The capability to operate as either a bi-propellant engine or an autophage engine also allows us to identify the impact that autophage operation has on engine performance. Additionally, the engine no longer needs to be primed to operating temperature using a pilot gas since it can reach steady state operation immediately under its bi-propellants.

The second reason a bi-propellant architecture is advantageous is due to having direct control over the engine inlet conditions. By using a combination of valves and pressure regulators, the mass flow rate and inlet pressures can be regulated such that both the mixture ratio and throttle setting of the engine can be fine-tuned to adjust the feed rate and engine performance. This functionality allows for a wider margin in developing a suitable flight trajectory for a launch vehicle due to the precise throttling that liquid bi-propellant systems

provide. Additionally, precise valve control can also operate the engine in a pulsed mode which adds an additional variable for operators to control engine performance.

Finally, a bi-propellant architecture will require a lower feed force to drive the fuselage into the thrust chamber. This is due to the lower cross-sectional area of the fuselage when compared to a solid-propellant system. A lower A_c will result in a lower required feed force; making the design of a launch vehicle capable of reaching the required feed force under its own thrust more feasible. Overall, a hybrid autophage rocket propulsion system that is able to operate as both a liquid bi-propellant and also burn a polymer as a supplementary fuel provides many operational advantages over the previously tested solid-propellant concepts. It also expands the breadth of research in infinitely staged launch vehicles and advances the technology readiness level as a whole.

1.5.2 Iteratively Designed Systems

In order to maximise the output of these studies, three different engines were iteratively designed with the intent to reach a final, functioning hybrid autophage engine design. Each of the engines would be designed to operate with the same standard inlet conditions. However, the first two engines, Ouroboros-1 and 2, would be designed to be operated and tested as bi-propellant systems in order to verify nominal engine operation before including an autophage component. Thus, they would be used as the control when evaluating the autophage performance of Ouroboros-3.

1.5.3 Performance Characterisation of the Autophage Operating Box

A key motivation of this research is an expansion of the operating box and resulting performance of autophage propulsion systems. Of particular interest is the effect that mixture ratio and throttle setting have on the autophage feed rate. Having an understanding of how the inlet conditions affect the feed rate is critical in the dynamic modeling of an autophage launch vehicle flight trajectory in which both the vehicle mass and geometry are changing. Furthermore, having experimental performance data allows for the anchoring of such models to provide more precise simulations used in the development of launch vehicles.

1.5.4 Comprehensive Data Acquisition

Additionally, a more robust data acquisition system is needed to collect data on the performance of autophage engines; specifically, a method of measuring engine thrust. This requires a unique test stand that is able to both administer and measure a feed force as well as resulting engine thrust. Additional parameters that will be measured include:

- Thrust
- Feed Force
- Combustion Chamber Pressure

- Combustion Chamber Temperature
- Fuel Inlet Pressure
- Oxidizer Inlet Pressure
- Fuel Mass Flow Rate
- Oxidizer Mass Flow Rate
- Fuselage Feed Rate

Furthermore, existing autophage engine performance data has been collected at sampling frequencies far below the threshold needed to detect combustion instabilities. Both low (100-300Hz) and high (2-5kHz) frequency combustion instabilities can impact performance and lead to catastrophic engine failures. By sampling at higher frequencies, instabilities can be detected for specific designs and operating conditions which can then be used to drive future autophage engine designs.

1.5.5 Investigation of Autophage Throttleability

As identified by the Dnipro team [18], throttleability of an autophage launch vehicle is critical in order to stay below both the thermal limit of the airframe skin as well as the G-load limit of the structure. Thus, a method of accurately controlling the throttle setting of an autophage engine is necessary. A hybrid autophage engine that uses liquid bi-propellants is an ideal candidate to experimentally verify its throttleability since conventional bi-propellant systems are well known to have throttle capabilities. Therefore, the dedicated hot-fire test campaigns of the Ouroboros engines would operate across a range of throttle settings in order to verify throttle capabilities.

1.5.6 Study of Pulsed Operating Modes on Autophage Performance

The final research objective was a study of the effect of pulsed operating modes on autophage performance, specifically on the feed force and feed rate. Pulsed operating modes could theoretically lower the required feed force by reducing P_c to equal P_0 during off-times. This could be advantageous for low altitude flight where air density is high and the resulting face drag of the launch vehicle could in turn be sufficient to drive the fuselage into the thrust chamber during pulsed mode off-times.

1.6 Contributions to the Research Field

1.6.1 Conference Publications

Investigation of the Operating Parameters and Performance of an Autophage, Hybrid Rocket Propulsion System [23]

This paper was the first public release of images and data from the successful testing of a hybrid autophage engine and was presented at the 2024 AIAA SciTech Forum in Orlando, Florida. The paper not only demonstrated the first evidence of long duration testing of an autophage engine in both steady state and pulsed mode but it proved a correlation between engine throttle, propellant mixture ratio, and pulsed mode duty cycle on the autophage propellant contribution. This work was recognized by Scottish Parliament via motion S6M-11911.

Development and Roadmap of the Ouroboros Programme Hybrid Autophage Propulsion System for Rapid Low-Earth Orbit Access [24]

This paper was written and presented at the 9th Annual Space Propulsion Conference in Glasgow, UK. It presented the current state-of-the-art of autophage propulsion systems and identified key technologies that are required to further advance the technology readiness level of autophage launch vehicles. The current key challenges are in thrust scaling, heat transfer optimisation, and the flight dynamics modeling of an autophage rocket. Future challenges that should also be considered are autophage fuselage feed mechanisms, collapsible propellant tanks, inertial loading on the fuselage, fuselage thermal management, and materials.

Introduction of Topology Optimisation in Regenerative Cooling Channel Design within Liquid Rocket Engines [25]

This paper was written for and presented at the 9th Annual Space Propulsion Conference in Glasgow, UK. It covered the use of topology optimisation algorithms to determine optimal geometries for regenerative cooling channels in liquid rocket engines to minimise pressure losses while maintaining favorable heat transfer characteristics in the nozzle and combustion chamber. Optimising regenerative cooling channel designs and heat transfer characteristics is a vital component of increasing the viability of autophage rocket systems.

Autophage Engines for cubesat-scale nanolaunchers [22]

This paper was written for and presented at the 7th Annual Reinventing Space Conference in Belfast, UK. It presented a summary of the current known advancements in autophage propulsion systems and proposed the use of a hybrid rocket architecture rather than a solid propellant architecture for an autophage rocket. The hybrid autophage architecture could greatly reduce the required feed force to drive the fuselage into a combustion chamber and increase the feasibility of autophage launchers.

1.6.2 Journal Publications

Steady State and Pulsed Performance Results of a Tri-Propellant Autophage Engine Architecture

This journal paper has been submitted to the AIAA Journal of Propulsion and Power and is currently in review. It presents the performance results of the Ouroboros-3 tri-propellant autophage engine for both steady state and pulsed operating modes. The paper evaluates the effect of mixture ratio, chamber pressure, and pulsed mode duty cycle on their effect of the autophage fuel contribution to the total propellant mass flow rate.

1.6.3 Other Contributions

MachLab Propulsion Test Facility

The MachLab Propulsion Test Facility was a collaboration that facilitated between the University of Glasgow and Machrihanish Airbase Community Company that was funded by the UK Space Agency. After initial successful testing of the Ouroboros autophage engines at the test site, a substantial grant was awarded through the LaunchUK funding scheme to design and build a cryogenic propellant feed system and test stand for rocket engine testing up to 10 kN of thrust. The facility also included a host of operating procedures for hot-fire testing, leak testing and pressure testing. MachLab is scheduled to be completed and fully operational by 2025 and will be the first propulsion test facility in Scotland and an asset to the UK space sector.

1.7 Summary of Remaining Chapters

1.7.1 Chapter 2: Theoretical Performance and Impact of an Autophage Rocket Architecture

An evaluation of the performance of three conventional rocket architectures (missile system, sounding rocket, and small satellite launch vehicle) is performed. A literature review is conducted to determine an approximate mass distribution for three characteristic systems to determine the available fuselage mass that could be used as fuel for an autophage rocket of the same architecture. An analysis is then performed to determine the impact an autophage system would have on system performance. Other sources for increasing performance are then considered to determine a maximum achievable performance increase for an autophage launch vehicle to determine the overall viability of an autophage architecture.

1.7.2 Chapter 3: Hybrid Autophage Engine Design Methodology

The design of the Ouroboros-1, 2 and 3 autophage engines and key design considerations are presented. Two main designs are considered: the depolymerisation chamber architecture and the direct fuselage insertion architecture. The depolymerisation chamber architecture utilises

regenerative cooling to extract thermal energy to melt the autophage fuel before injecting it into the combustion chamber. The direct fuselage insertion architecture deploys the autophage fuel directly into the combustion chamber where it is combusted, similar to a hybrid rocket motor.

1.7.3 Chapter 4: Test Apparatus and Experimental Setup

A test apparatus was designed and built to support the empirical testing of the Ouroboros autophage engines. The experimental setup covers the: test location, test stand, propellant feed system, instrumentation, data acquisition, and control systems. Also presented is the hot-fire test plan which contains the operating conditions for the Ouroboros engine tests.

1.7.4 Chapter 5: Depolymerisation Chamber Architecture, Bi-Propellant Test Results

The results of the first test campaigns conducted on Ouroboros-1 are presented. Ouroboros-1 was designed using the depolymerisation chamber architecture. The first test was conducted with the engine in a bi-propellant configuration without using an autophage fuel. This was done to set a performance baseline. The engine operated in steady state mode for approximately 52 seconds, during that time the engine experienced a burn-through of the combustion chamber and no further tests were conducted on this architecture.

1.7.5 Chapter 6: Direct Fuselage Insertion Architecture, Bi-Propellant Test Results

The direct fuselage insertion architecture performance using the Ouroboros-2 autophage engine is evaluated. As done previously, the Ouroboros-2 engine was tested solely in a bi-propellant configuration to set a performance baseline. Multiple successful tests were conducted, providing a range of throttled and standard inlet condition results. A frequency analysis was conducted on the engine pressures to evaluate the presence of any combustion instabilities. Combustion instabilities were detected, improvements to the Ouroboros-2 injector design were considered to be implemented for Ouroboros-3 which would use the direct fuselage insertion architecture in a full, autophage configuration.

1.7.6 Chapter 7: Direct Fuselage Insertion Architecture, Autophage Test Results

The results of the Ouroboros-3, tri-propellant autophage engine are presented. A total of 5 tests were successfully conducted on the Ouroboros-3 engine in the autophage configuration. The autophage fuel was successfully inserted into the engine combustion chamber and burned as a secondary source of fuel. The engine was operated across a range of inlet conditions and the performance was compared to the Ouroboros-2 baseline. The Ouroboros-3 engine was also operated in steady state and pulsed mode. The parameters of throttling, mixture ratio,

and pulsed mode were evaluated to determine their effect on the autophage fuel mass flow rate contribution. A frequency analysis was conducted on the engine pressures to evaluate the presence of any combustion instabilities.

1.7.7 Chapter 8: Conclusions

The conclusions of the autophage engine tests are presented. It was found that the autophage fuel contributed between 5.1%-15.7% of the total propellant mass flow rate and was influenced significantly by engine throttling and pulsed mode duty cycles, while mixture ratio had a moderate correlation to the autophage contribution. Overall, the research successfully operated an autophage engine design for durations of over 60 seconds and established parameters that can be used to control the autophage contribution.

Chapter 2

Theoretical Performance and Impact of an Autophage Rocket Architecture

As discussed in Section 1.1.5 an idealised infinitely staged vehicle will provide an overall performance increase to the rocket. However, a physical autophage rocket design must consider the additional mass of the engine and mechanisms that may be required for autophage flight. The reduction in structural mass (fuselage consumed as fuel) must then be evaluated against the increase in engine mass to determine under what conditions does the autophage architecture provide a net increase to the total ΔV of the rocket. Since no autophage rockets have ever been flight tested, the total mass of a hypothetical autophage engine must be estimated. The following sections compare three conventional launch vehicle architectures of various sizes to a hypothetical autophage rocket, of similar capabilities, to determine the inflection point at which an autophage architecture may be advantageous over a conventional rocket.

2.1 Conventional Launch Vehicle Performance

A modern conventional launch vehicle which has had success in delivering small satellites to orbit is the Rocket Lab Electron. The Electron is a two-stage small-lift launch vehicle capable of delivering a payload of up to 200 kg to low-Earth orbit using a cluster of 9 Rutherford engines on the core stage [26]. While Rocket Lab does not publish the propellant mass fraction of the Electron core stage (CS) it can be estimated. First, consider the payload mass, upper stage fuel mass, and an estimated propellant mass fraction of 0.9. The estimated propellant mass fraction aligns with other upper stages operating with LOX/RP-1 bi-propellant engines [27]. Using EQ. (1.4), the total Electron second stage mass was calculated at 2,542 kg (This includes the payload, fairing, and kick stages masses). Considering an estimated structural coefficient of 0.10 for the core stage, the reported lift-off mass, and the calculated total second stage mass; the dry mass of the core stage was estimated to be 1046 kg. The Δv of the launcher was then calculated from the specific impulse and mass values of the rocket using EQs. (1.7), (1.8), and (1.9).

This process was repeated based on data gathered from two other launch systems. The second architecture considered is the single-stage configuration of the Black Brant VC sounding rocket [28]. The third architecture is an air-to-air missile system using publicly available data on the AIM-54 Phoenix with an Aerojet Mk 60 motor [29–33]. The payload mass of the AIM-54 constitutes the warhead mass. The resulting baseline vehicle characteristics of all three architectures were calculated and shown in Table 2.1.

Table 2.1 Calculated mass and performance characteristics of conventional rockets.

	Mass, kg				Mass Ratio				
Vehicle	m_i	m_p	m_s	m_d	ζ	ε	λ	I_{sp}, s	Δv, m/s
Electron CS	13,000	9,412	1,046	2,542	0.72	0.10	0.24	311	3,884
Black Brant VC	1,544	1,017	301	226	0.66	0.23	0.17	223	2,349
AIM-54 Phoenix	464	163	240	61	0.35	0.60	0.15	262	1,107

The structural mass of these launch systems can be further decomposed into constituent parts such as engine/motor mass, fuselage structure, propellant tanks, cryogenic insulation, power and electronics, and thrust vectoring/control surfaces; with the specific mass breakdown dependant on the vehicle platform. For both the Black Brant VC and AIM-54 Phoenix, the motor insulation is included as part of the motor mass. A structural mass breakdown of the previously introduced vehicle platforms is shown in Table 2.2. Where possible, the structural mass constituent categories were pulled from publicly available data. However, only the engine mass was available for both the Electron and Black Brant VC rockets. All the data for the AIM-54 Phoenix missile was publicly available.

To estimate the mass of each category, the relative percentage of each category versus the total structural mass was calculated using data from a proposed single task orbit transfer vehicle [34, 35]. For Electron, the mass of the propellant storage tanks was further reduced by 40% to align with their claims of mass savings due to composite construction [26]. Additionally, the cryogenic insulation was sized according to a relative percentage based on the earth departure stage of the Ares V rocket which has data specifically on cryogenic tank insulation [27]. The fuselage mass was then the final variable which was adjusted such that the sum of the components equaled the total structural mass of each launch platform.

Table 2.2 Calculated structural mass distribution across subsystems in conventional rockets.

Mass Category, kg	Electron Core Stage	Black Brant VC	AIM-54 Phoenix
m_s	1,046	301	240
Engine/Motor Casing	315	118	44
Fuselage	456	135	55
Propellant Storage	90	0	0
Cryogenic Insulation	20	0	0
Avionics and Electrical	115	33	136
Control Systems	50	15	5

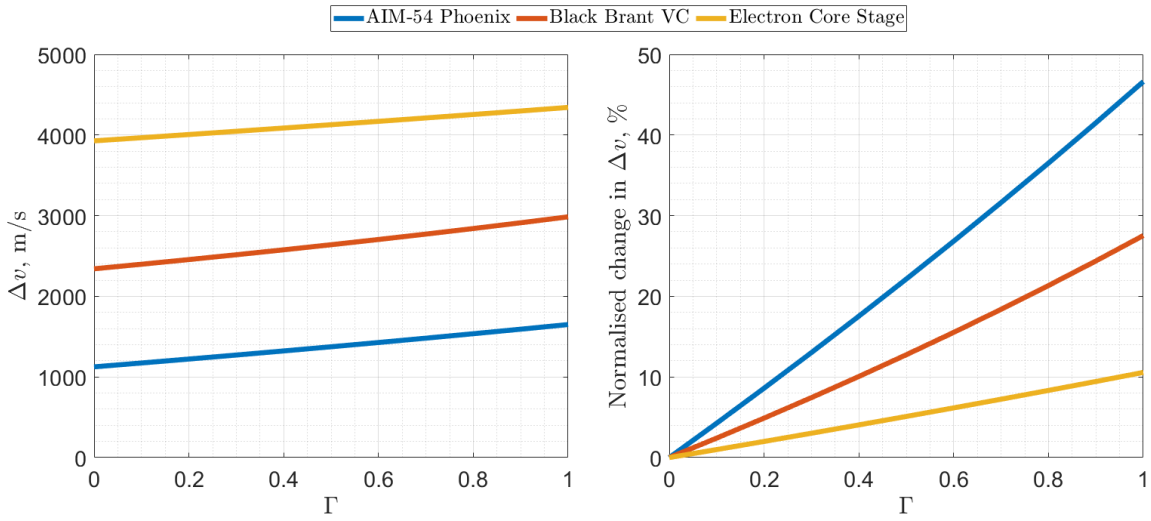

Fig. 2.1 Autophage architecture impact on Δv using nominal engine mass.

2.2 Autophage Launch Vehicle Performance

To evaluate the feasibility of autophage launch vehicles, the data from Tables 2.1 and 2.2 was used as a performance baseline for a hypothetical autophage replacement sized for each of the three architectures. The objective of this analysis was to determine the change in Δv as a function of percentage of fuselage mass used as propellant. The total rocket mass and payload mass were held constant according to each architecture. With the exception of the fuselage mass, all other structural mass categories were also held constant. This analysis considered that the engine mass of each autophage architecture remained unchanged from the corresponding conventional engine masses as a best-case scenario. The resulting Δv, as well as a normalised Δv, were plotted in Fig. 2.1. The term Γ is used to describe the ratio of fuselage mass used as propellant over the initial fuselage mass, this is the autophage mass ratio.

At a Γ of 100%, the average increase in Δv across all three architectures was calculated as 528 m/s. This increase in Δv is of the same magnitude as the contribution from the Earth's rotation when launching from an equatorial launch site, 465 m/s [9]; and when using air-assisted launch, 400-800 m/s [36].

However, the normalised change in Δv shows a significant difference between the three architectures. When compared to the AIM-54 Phoenix, an autophage missile of the same size could contribute up to a 46% increase in velocity. This translates to significantly longer range and the higher velocity correlates with a lower likelihood of interception by missile defense systems. An autophage rocket with the same total mass as the Black Brant VC may contribute up to a 27% increase in Δv. When sized for the Electron launch vehicle, an autophage system may increase the Δv by up to 10%. As the total launch vehicle mass increases, an autophage architecture has less of an effect on the normalised increase in Δv. This is expected due to the effects of the square-cubed law described in Section 1.1.1.

This analysis assumed a scenario where the engine mass and I_{sp} remain at the same values as that of each conventional architecture. However, an autophage engine is likely to have a higher mass than conventional systems due to the complexity and additional mechanisms used

to control the feed rate. An additional analysis was conducted to evaluate how an increase in engine mass would effect the Δv and normalised change in Δv for each architecture. As in the previous analysis, the total launch vehicle mass, payload mass, and engine I_{sp} were held constant. The effect on Δv, due to the increase in engine mass, was charted for autophage systems with a Γ of 30%, 60%, and 90% (Fig. 2.2). All other structural mass categories were held constant.

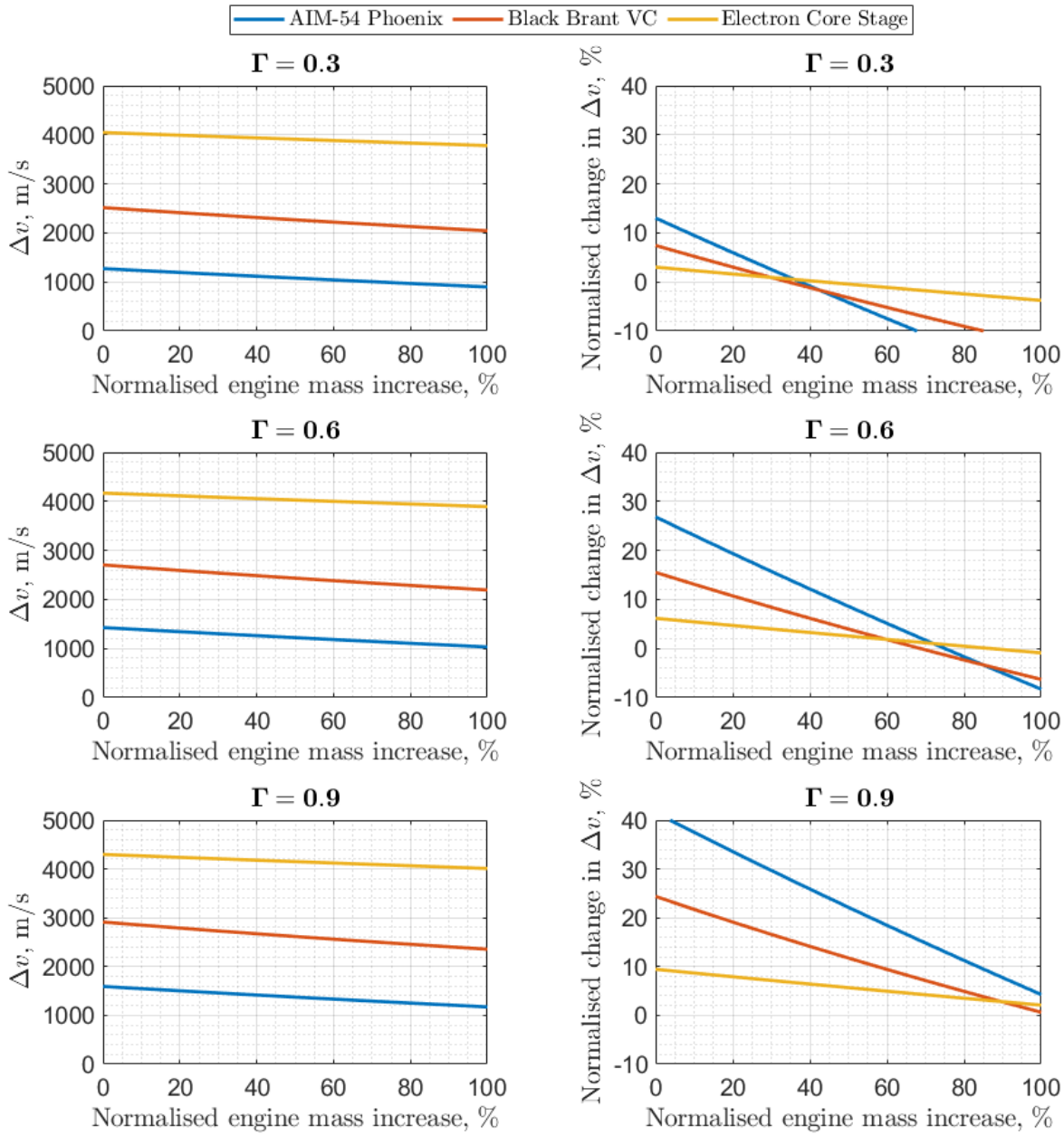

Fig. 2.2 Effect of engine mass increase on autophage performance at various Γ.

When considering an autophage system with a Γ of 0.3, a normalised increase in engine mass of over 40% resulted in a net decrease of Δv across all three architectures. This is undesirable as the complexity of the system is increased with no benefits to performance. However, as Γ is increased to 0.6, the autophage architecture yields a net performance increase to Δv even when accounting for an increase in engine mass. At an engine mass increase of 40%, the autophage AIM-54 Phoenix yielded an increase in Δv of 12%. Further, when Γ is

set to 0.9, the normalised change in Δv of the same system is increased up to 23% compared to the conventional architecture.

While the lower mass of the AIM-54 Phoenix architecture receives the largest potential increase in performance, it is noted that an increase in engine mass reduces the normalised change in Δv at a higher rate. This is a result of the autophage architecture having a greater effect on ζ of lower mass vehicles. Based on this analysis, autophage architectures will provide the largest performance benefit to missiles and sounding rockets, with marginal increases to the performance of launch vehicles with a gross lift-off mass greater than 13,000 kg. However, using synergistic existing and emerging technologies in conjunction with an autophage architecture may result in a net performance multiplier that could extend the viability of autophage rockets.

2.3 External Sources of Autophage Performance Increase

The autophage rocket architecture is most viable when the total mass of the launch vehicle is relatively low. The largest performance increases correlate with missile and sounding rocket architectures; however, the application of other technologies that are synergistic with an autophage rocket may result in a net performance multiplier that extends the viability to small satellite launch vehicle platforms. The following sections identify key technologies and their potential impact on the theoretical autophage launch vehicle performance discussed in Section 2.2.

2.3.1 Altitude Adaptive Nozzles

As discussed in Section 1.2.4, converging-diverging nozzles are used to accelerate exhaust gases to supersonic conditions to maximise the momentum transfer and thrust of a rocket engine. The most widely used is the parabolic bell-shaped nozzle due to its simplicity and improved performance versus a conical nozzle. For nozzles with a throat Reynolds number range of 2×10^4 to 4×10^4, depending on the atmospheric pressure, the bell-shaped nozzle can improve the specific impulse of a rocket by 5% at 500 kPa, 6% at 370 kPa, and 12% at 225 kPa when compared to a conical nozzle [37].

However, both conical and bell-shaped nozzles are optimised to operate at a set altitude and corresponding atmospheric pressure. Operating outside of the design altitude will result in overexpanded exhaust gases at lower altitudes, which will reduce specific impulse and can cause flow separation and significant forces on the nozzle sidewall [38]. Conversely, underexpanded exhaust gases at higher altitudes also reduce performance and can cause plume impingement on critical structures [39]. Figure 2.3 presents data on how significantly the specific impulse of an engine can vary depending on its operating altitude.

Using the data from the Vulcain 2 engine, used on the Ariane-5 core stage, the specific impulse is 310 s at sea level and 432 s at vacuum, resulting in an average specific impulse of approximately 370-390 s dependant on the flight trajectory [41]. Advanced nozzle designs such as the dual-bell nozzle, expansion-deflection nozzle, and plug (aerospike) nozzle seek to reduce the losses of conventional conical and parabolic bell nozzles [42, 43].

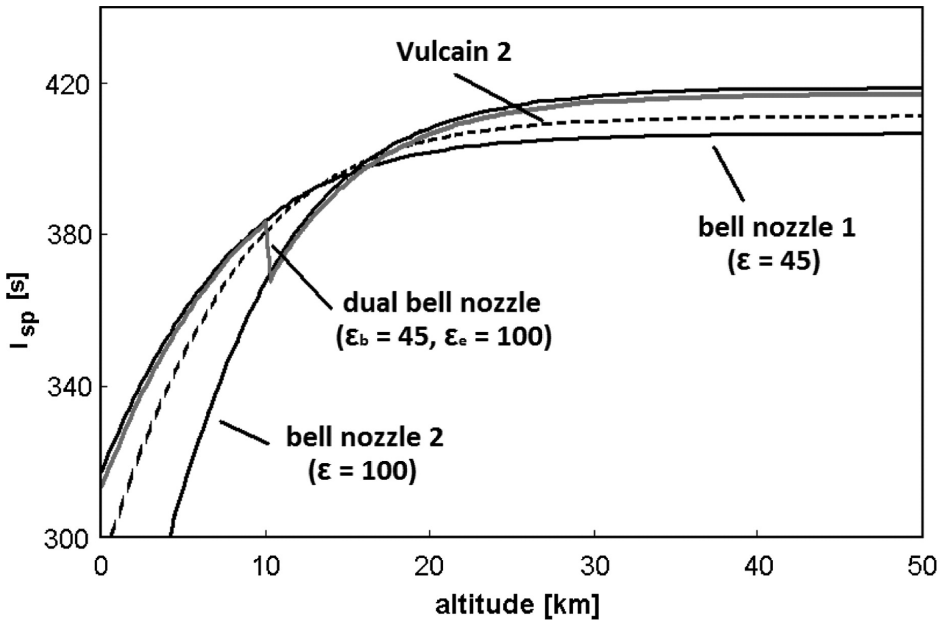

Fig. 2.3 Specific impulse as a result of altitude for three conventional bell-shaped nozzles and a dual-bell nozzle [40].

Dual-bell nozzles utilise a two-part nozzle (Fig. 2.4) that provides two-different operating modes for low and high altitude operation [40]. As shown previously in Fig. 2.3, at low altitudes, using a dual-bell nozzle can increase the specific impulse of a launch vehicle. This correlates to a reduction in fuel consumption of up to 25-30% [44]. However, dual-bell nozzles are larger in size and can increase the mass of the engine on the order of 20-30% [45].

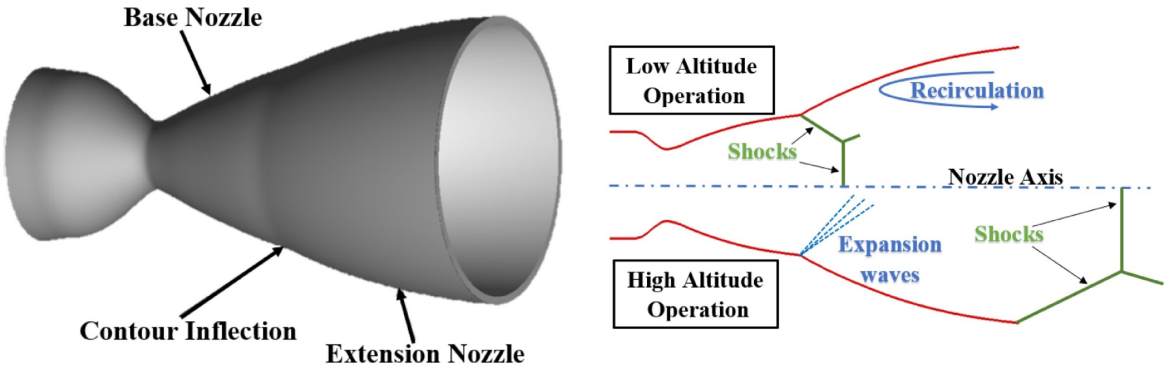

Fig. 2.4 Sketch of a dual-bell nozzle in low and high altitude operation [46].

Expanding-deflection (E-D) nozzles use a pintle architecture (Fig. 2.5), first proposed by Rao [47], to dynamically change the area ratio of the nozzle throughout the flight trajectory. A major benefit of the E-D nozzle is that it can reduce the overall nozzle length and reduce the structural mass of the engine. A study and numerical analysis done on the Ariane 5 upper stage found that shortening the nozzle increased the payload mass by 180 kg and the vacuum specific impulse by 2 s [48]. A recent experimental study, conducted by researchers at Chungnam National University, investigated the performance of two E-D nozzle designs, one designed to the same length as an 80% bell nozzle and the other with a 30% reduction to the nozzle extension length [49]. In an experiment setup at a 16 km altitude, the researchers found the performance of the engine with reduced nozzle length was within 1.0% of the

full-size nozzle. Therefore, E-D nozzles could offer an overall increase to performance while also reducing the total mass of the engine.

However, the E-D nozzle does have a significant weakness since there are a variety of parameters that must be selected in the design change based on assumptions. This can result in great variability between designs [50]. One experimental investigation, conducted by researchers at NASA Glenn Research Center, found that efficiencies of the E-D nozzle used in their tests were found to be 92.3% at sea level and 97.6% at the design point [51]. This was a net decrease in performance when compared to a conical converging-diverging nozzle used as a control which yielded nozzle efficiencies of 92.6% at sea level and 97.8% at the design point.

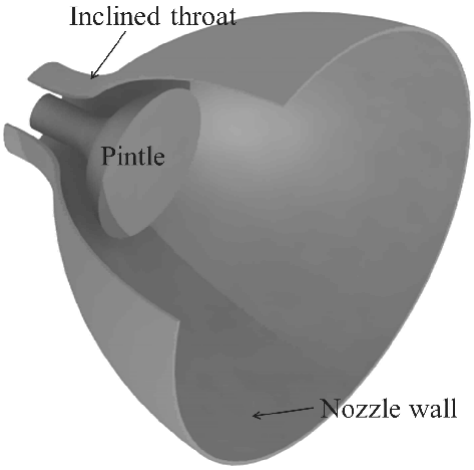

Fig. 2.5 Sketch of an expansion-deflection (E-D) nozzle [52].

The plug nozzle, also known as the aerospike, is the most promising in terms of theoretical performance increase. This is due to the aerospike architecture which uses an internal plug such that the exhaust plume is open to the atmosphere [53]. This allows the nozzle to dynamically adjust to an optimum expansion at all altitudes. A sketch of an aerospike nozzle and the resulting shock structure of the plume is shown in Fig. 2.6.

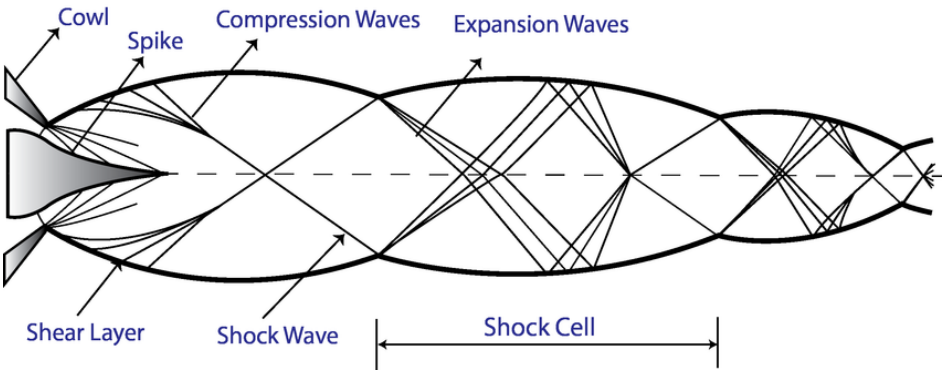

Fig. 2.6 Sketch of an aerospike nozzle and its shock structure [54].

Much like other altitude adaptive nozzles, aerospike nozzles have been found to increase average engine performance when operated across the full flight trajectory. According to one study, when compared to a bell nozzle in a hybrid rocket motor, aerospike nozzles yielded an increase in I_{sp} between 8.9%-23.4% [55]. Another study conducted by researchers at

the Beijing University of Aeronautics and Astronautics found that at sea level conditions, the thrust efficiency of an aerospike nozzle was 27% higher than a conventional bell nozzle [56]. Additionally, aerospike nozzles can be designed to be dramatically smaller than their conventional counterparts [57] with a numerical study finding that a truncation of 40% of the maximum length of an aerospike actually results in an increase in thrust due to the effect of recirculation zones in the plume [58]. Therefore, aerospike nozzles provide a significant benefit towards autophage propulsion systems because they not only offer an overall increase to I_{sp} but also minimally increase nozzle mass. Figure 2.7 considers the potential increase in launch vehicle performance when an aerospike nozzle is used in conjunction with an autophage architecture for the previously discussed example launch systems.

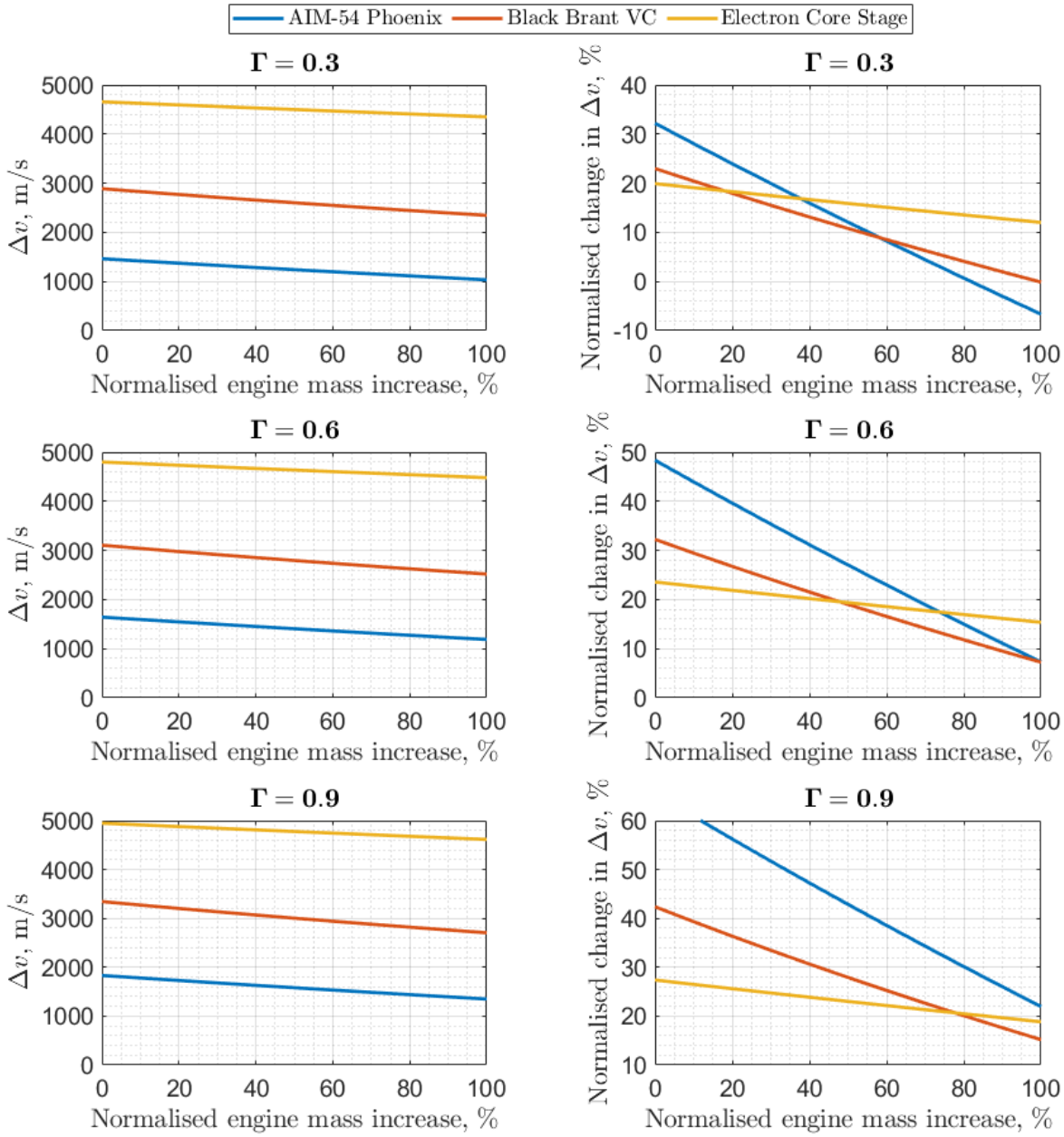

Fig. 2.7 Effect of a combined aerospike nozzle and autophage architecture on launch vehicle performance at various Γ.

2.3.2 Rotating Detonation Engines

Rotating detonation engines (RDEs) are an innovative class of propulsion systems that utilise continuous detonation waves in the combustion chamber rather than conventional, deflagration-based combustion. RDE performance has been empirically validated to show a 6-8% increase in specific impulse compared to deflagration combustors but increases of up to 10-15% are theoretically possible [59]. This specific impulse increase comes from the propellants being detonated instead of deflagrated, where the detonation shockwave increases the pressure and temperature at which combustion occurs. Figure 2.8 shows the cross-section of a typical RDE while Fig 2.9 shows a 3D model of the detonation wave propagation in an RDE combustion chamber.

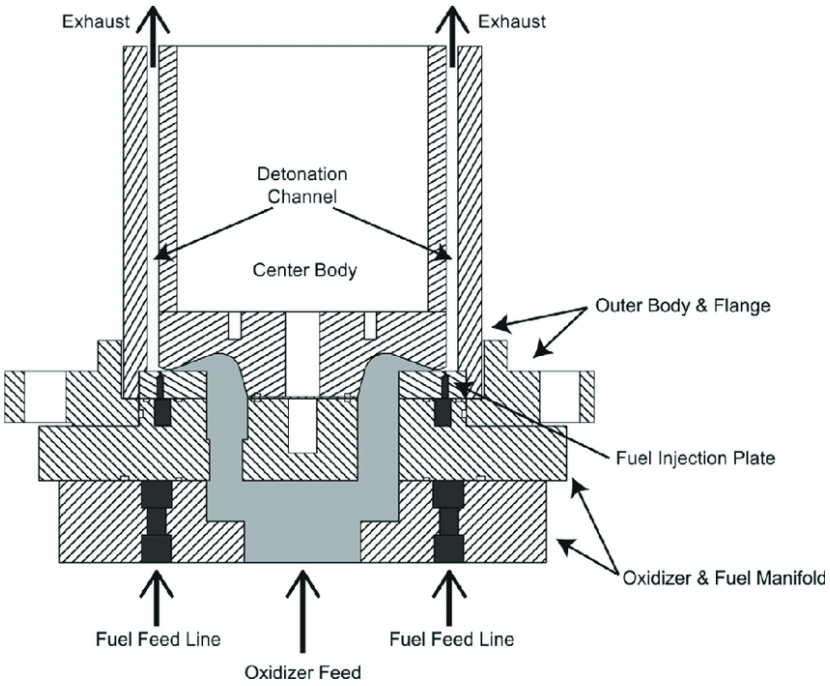

Fig. 2.8 Cross-section of a typical rotating detonation engine [60].

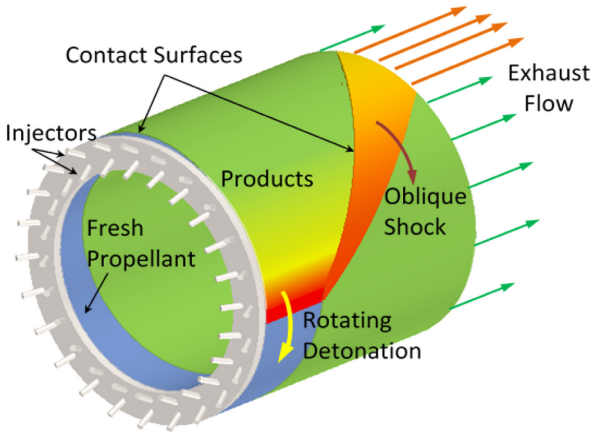

Fig. 2.9 Detonation wave propagation in an RDE combustion chamber [61].

While RDEs show potential to increase engine performance, the engines that have been experimentally validated thus far have been relatively small with insufficient thrust for

practical applications [62]. Some of the largest RDEs that have been successfully tested have been able to produce up to 6 kN of thrust while maintaing an outer chamber diameter of only 406 mm [63]. While not suitable for large-scale space launch vehicles, that thrust class of engine is in-line with many missile systems while being up to 50% smaller diameter than conventional rocket engines [62]. Therefore, it may be feasible to integrate rotating detonation engines (RDEs) into an autophage rocket for architectures similar to either the previously discussed AIM-54 Phoenix or Black Brant VC systems.

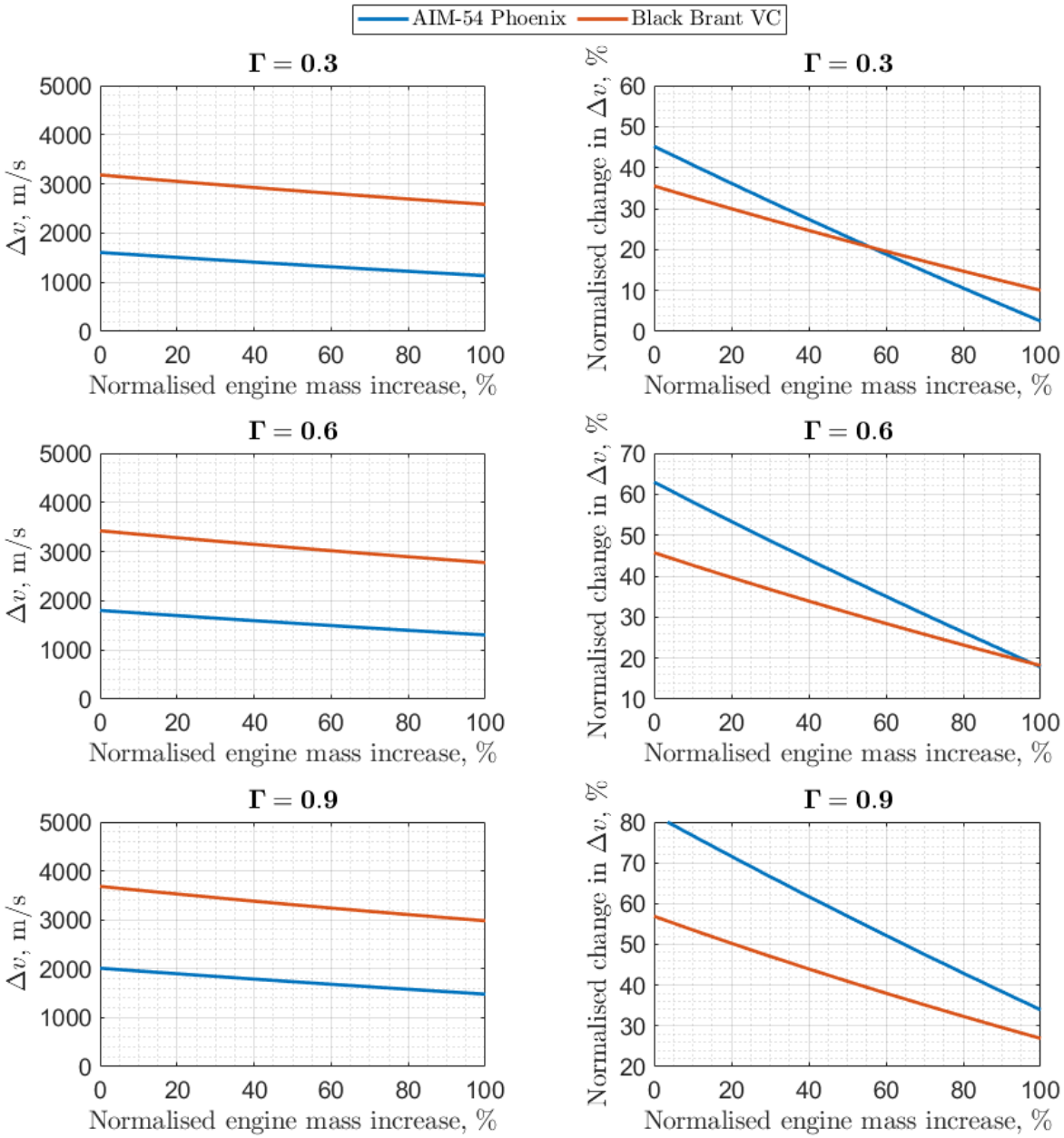

Fig. 2.10 Effect of a combined aerospike nozzle, rotating detonation engine, and autophage architecture on launch vehicle performance at various Γ.

However, given that RDEs have generally avoided the use of solid propellants, integrating an RDE into an autophage rocket engine will require a redesign of the combustion chamber. Thus, autophage combustion may need to occur either before the RDE as a gas generator [64], after the RDE in a two-stage combustion setup, or directly into the RDE as part of the

detonation combustion. The two-stage combustion cycle with a primary liquid bi-propellant RDE stage followed by a secondary autophage and RDE-products deflagration stage requires the least amount of modifications to current autophage engine designs and could prove to be the most effective.

Due to the center body in many RDE designs, the RDE also lends itself to be used in conjunction with aerospike nozzles [65]. This allows both technologies to be used synergistically on an autophage rocket to further improve performance over conventional propulsion systems. Figure 2.10 considers a further 10% improvement to autophage engine I_{sp} for the AIM-54 Phoenix and Black Brant VC architectures previously presented in Fig. 2.7.

2.3.3 Gel Monopropellants

Another emerging propulsion technology that can impact autophage rocket developments is the use of gel propellants. Smaller rocket architectures, like the AIM-54 Phoenix and Black Brant VC, primarily use solid propellants due to long-term storability requirements. While solid propellants have a high energy density, their I_{sp} is notoriously lower than liquid bi-propellant propulsion systems as can be seen in Table 2.1 when the AIM-54 Phoenix and Black Brant VC are compared to the Electron CS.

Gel propellants are able to combine the storability of solid propellants and the performance of liquid bi-propellants. They often operate by using a traditional propellant and a gellant. The gellant increases the viscosity which can be used to suspend energetic particles or additives that can enhance performance [66]. This produces a stable, yet high-energy density propellant which is also referred to as a slurry propellant. Slurry propellants have been investigated by NACA since the 1950s where researchers considered the idea of suspending boron and magnesium powders in JP fuel for enhancing the thrust and range of ramjets and turbofan engine afterburners with aluminum octoate as the gelling agent [67–69].

These types of gel propellants have the advantage of delivering higher specific impulse and energy density [70, 71] while also demonstrating long-term storability. Many gelled propellants are able to be stored for upwards of 10 years without settling or separation [72, 73]. Gel propellants also offer mission flexibility by their throttleability characteristics which allow for flight trajectory optimisation which is particularly valuable for maximising range when used in tactical missile applications [74].

Gel monopropellants are a subcategory that operate by using a single monopropellant. Historically, monopropellants, such as hydrazine, have advantages in storability and simplicity when compared to other propulsion systems. However, they have the disadvantage of lower performance [13] which has made them undesireable for launch applications. Recent advances in gel monopropellants have shown significant increases in performance through new formulations that aim to replace the use of hydrazine; these hydrazine replacements are known as green propellants [75, 76]. In particular, a new gel monopropellant has been developed at the US Air Force Research Lab known as AF-M315E which can provide an I_{sp} of 257 s, 50% higher energy density than hydrazine, and low-toxicity for safe handling [77, 78]. While the I_{sp} of AF-M315E is not significantly different than the I_{sp} of the AIM-54 Phoenix missile, it does provide the architecture required to make an autophage rocket possible which

can provide throttelability and mission flexibility that would improve upon the conventional architectures. The increase in I_{sp} does however have a significant impact on the performance of the Black Brant VC architecture. This effect is calculated and shown in Fig. 2.11 which takes into account the Black Brant VC using an autophage acrhitecture designed with an RDE, aerospike nozzle, and using the base I_{sp} of AF-M315E.

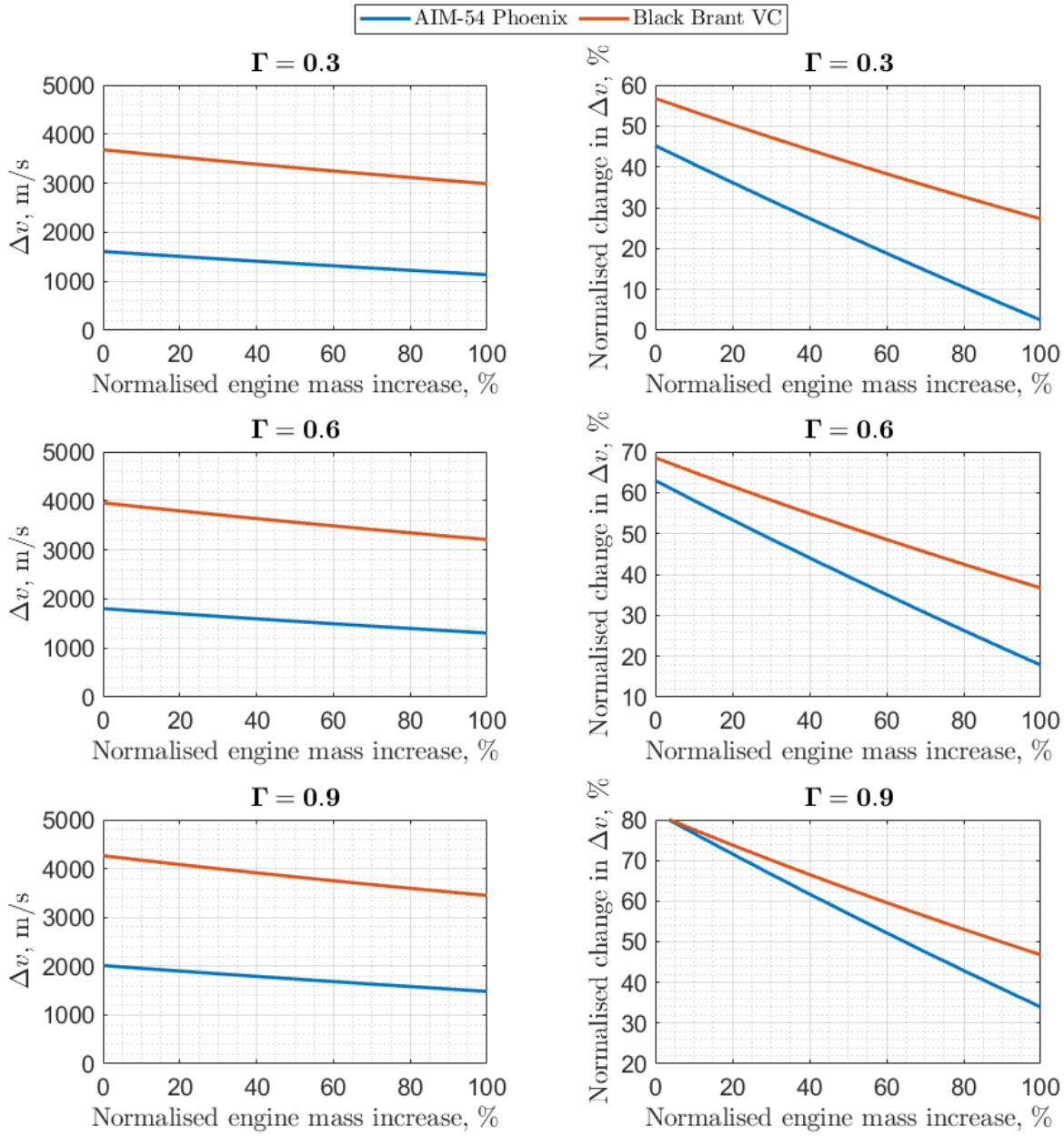

Fig. 2.11 Effect of a combined aerospike nozzle, rotating detonation engine, gel monopropellant and autophage architecture on launch vehicle performance at various Γ.

2.3.4 Air-Assisted Launch

Air-assisted launch configurations have been previously successful in increasing the total ΔV of rocket systems and delivering payloads to orbit on overall smaller launch vehicles. This architecture was best demonstrated by Pegasus, a launch vehicle developed by Northrup Grumman to deliver a payload of up to 443 kg to low-Earth orbit [79, 80]. The Pegasus

conducted 45 successful missions in delivering satellites to orbit. The design of it, and other air-assisted launch systems, seek to both reduce the gravitational and drag losses from ground launched rockets while also providing additional ΔV derived from the velocity of the carrier vehicle [81].

When accounting for the reduction in losses, as well as the addition of the velocity of the carrier vehicle, researchers at the University of California [82] calculated that the additional ΔV of an air-assisted launch system can reach between 400-1,200 m/s with a carrier velocity of only 340 m/s. For supersonic carriers, like fighter jets, which may be deploying air-to-air missiles, the additional ΔV reached up to 1,200-2,000 m/s when the carrier velocity was 1021 m/s. This represents a significant portion of the total ΔV of the AIM-54 Phoenix and Black Brant VC architectures which can extend the range of missile systems and altitude of sounding rockets. Autophage rockets can also be designed for air-assisted launch so long as the total mass of the system can be fastened to the carrier vehicle. For the architectures considered in this analysis, the AIM-54 Phoenix is in fact intended for air-launch and the Black Brant is well-suited to be launched using a subsonic carrier.

2.3.5 Theoretical Net Performance Increase from Combined Sources

Figure 2.12 considers the theoretical autophage performance of conventional launch vehicle architectures and applies all of the discussed sources of potential performance increases to the analysis. This provides a best case scenario of what an autophage system can achieve when used for a missile system, sounding rocket, and small satellite launch vehicle.

The net performance increase considers the use of aerospike nozzles for all architectures, as well as RDEs, gel monopropellants, and air-assisted launch for the AIM-54 Phoenix and Black Brant VC architectures. The analysis makes the following assumptions for the performance increase derived from each source:

1. Base I_{sp} of 257 s based on using AF-M315E propellant.
2. 15% increase to I_{sp} from the use of an aerospike nozzle.
3. 10% increase to I_{sp} from the use of an RDE.
4. ΔV increase of 400 m/s from air-assisted launch.

The results of the analysis show that if the theoretical performance increases from each of these technologies can be applied to an autophage architecture it can result in a substantial increase in overall performance. The analysis also shows that smaller launch vehicle architectures such as that of missiles and sounding rockets can leverage an autophage design for the highest performance increase. Even when accounting for an inert engine mass increase of 100% the total ΔV was calculated to increase by over 55% with an autophage ratio, Γ, of 0.6. Thus, combining an autophage launch vehicle architecture with other emerging technologies could provide a viable solution for significantly increasing the range and altitude of small launch vehicles for both civilian and military applications.

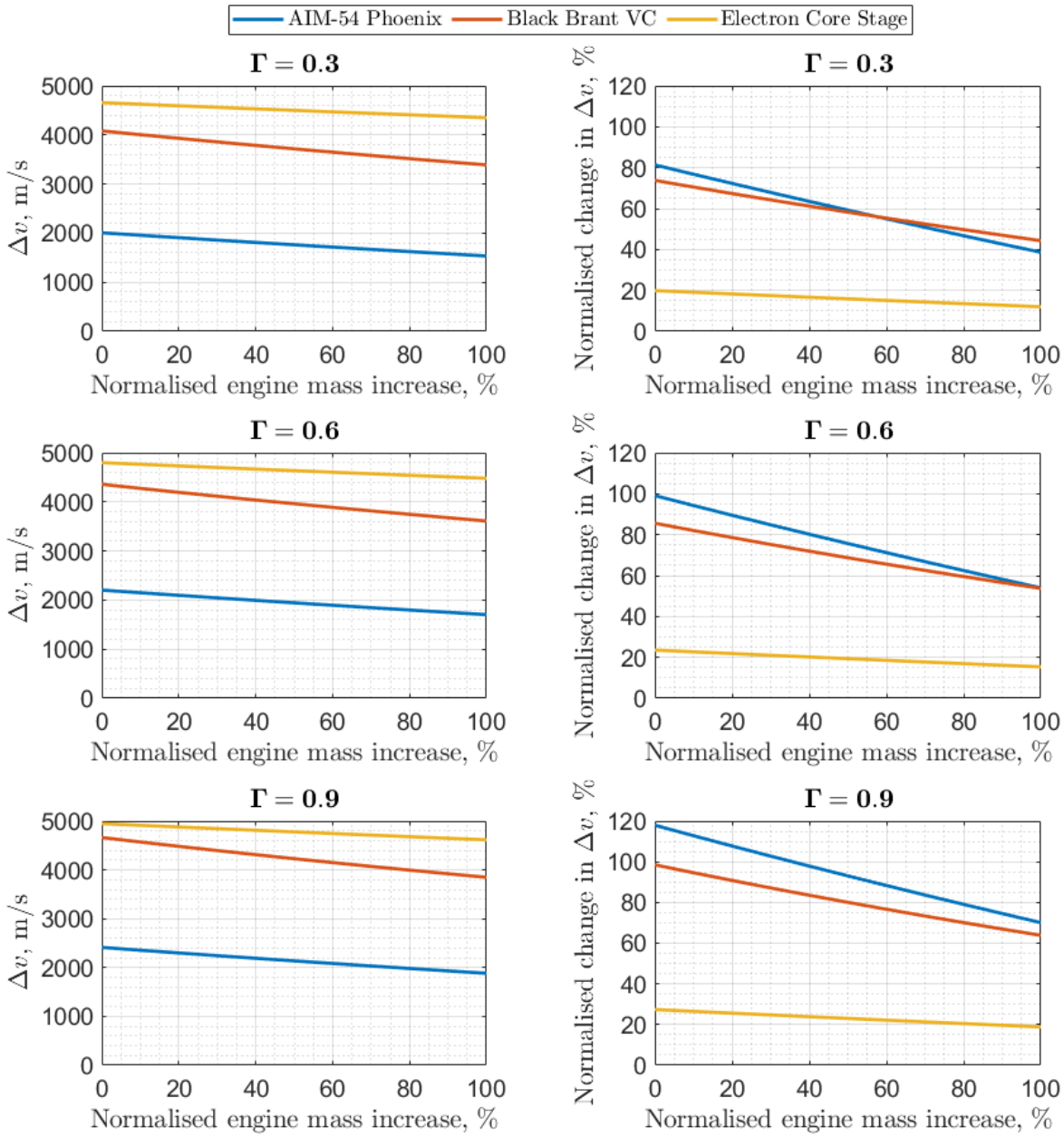

Fig. 2.12 Effect of a combined aerospike nozzle, rotating detonation engine, gel monopropellant, air-assisted launch, and autophage architecture on launch vehicle performance at various Γ.

Chapter 3

Hybrid Autophage Engine Design Methodology

3.1 Iterative Development of the Hybrid Autophage Ouroboros Engine

The development of the Ouroboros hybrid autophage engine programme was conducted under an iterative design philosophy in order to continue to improve the technology and achieve a TRL advancement through a series of validation tests over the duration of the programme. A total of three different engines were designed and tested; designated as Ouroboros-1, 2 and 3 with each improving upon lessons learned from the previous design. This approach was advantageous in order to rapidly evaluate multiple design features selected from the various historical records on autophage engine designs and improve upon them.

All three of the Ouroboros engines were designed to operate at the same standard inlet conditions (SIC) to provide a baseline comparison of the experimental results. Ouroboros-1 and 2 used two different architectures and were designed to be tested exclusively as bi-propellant engines with a plug in place of the polymer fuselage. This was done to reduce the number of experimental variables and to provide a control for the following autophage tests. The proposed initial designs of Ouroboros-1 and 2 were to investigate the feasibility of using a fuselage depolymerisation (or gasification) chamber versus a direct fuselage insertion method. The Ouroboros-2 design would then be improved upon; resulting in Ouroboros-3 which would be operated in the autophage configuration.

The specific hardware details used in the design and manufacture of the Ouroboros hybrid autophage engines is described in the following sections. The propellants chosen for these studies were gaseous oxygen (O_2), liquid propane (C_3H_8) and high density polyethylene (HDPE). The engine contour and standard inlet conditions were selected based on the results of a 1D chemical equilibrium analysis for the engines to achieve a target thrust of 100 N and chamber pressure of 5 bar. The chemical equilibrium analysis was conducted using Rocket Propulsion Analysis Software [83] with results verified using NASA Chemical Equilibrium Analysis (CEA) software [84].

The engines were mainly constructed out of 316 stainless steel with some initial Ouroboros-1 components being manufactured from Inconel 625. Stainless steel was used as the main material for manufacturing due to the relative low cost and high strength when compared to more exotic materials and alloys. The design of each of the components was based on the basic design guidance found in *Rocket Propulsion Elements* by G. Sutton and O. Biblarz [13] and *Modern Engineering for Design of Liquid-Propellant Rocket Engines* by D. Huzel and D. Huang [85] with additional references used for more complex components as required.

3.2 Depolymerisation Chamber Autophage Engine Based on Regenerative Cooled Bi-Propellant Systems

The first engine design was based in part on the published documentation from the Dnipro test campaigns as well as inspired by the well-studied concept of regenerative cooling in liquid bi-propellant engines. Regenerative cooling is a method of running propellants (usually fuel) through channels along the exterior of the engine in order to cool the nozzle and combustion chamber walls via convective heat transfer. An example of regenerative cooling can be seen in Fig. 3.1. This both reduces chamber wall temperature and increases the enthalpy of the propellant resulting in an increase in engine I_{sp} [85–87].

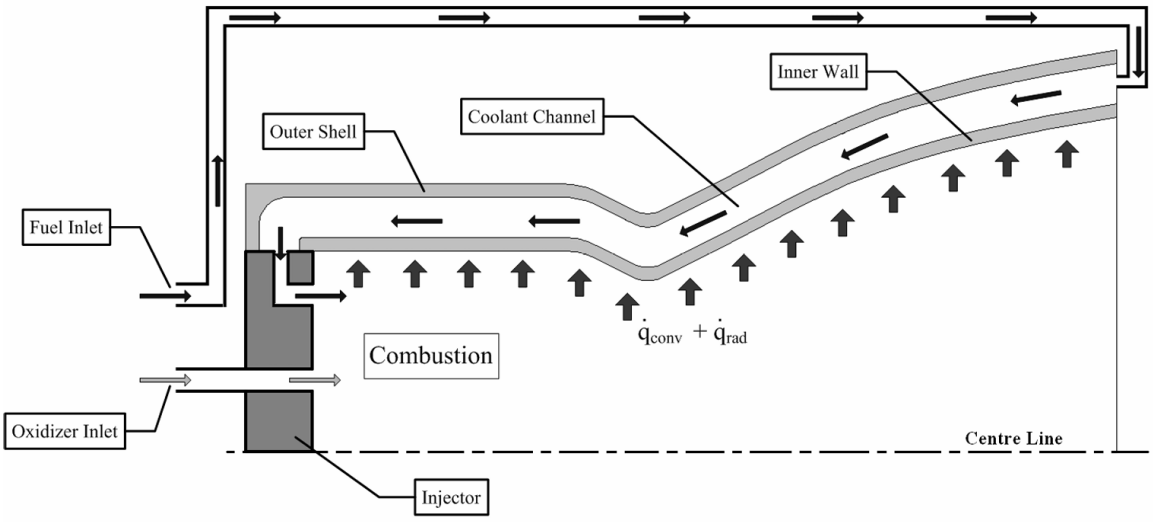

Fig. 3.1 Cross-section view of a regeneratively cooled liquid bi-propellant engine [88].

Fundamentally, autophage systems can be designed to operate on the same principles as regenerative cooling because they are both extracting thermal energy from the engine and into a propellant which is then injected into the engine. For a regeneratively cooled liquid bi-propellant engine the heat transfer is directed into a liquid propellant whereas for an autophage engine it would be directed into a solid polymer, the fuselage, which subsequently goes through a solid-liquid and liquid-gas phase change. This is similar in how the Dnipro engine used what was referred to as a "gasification chamber" where the heat from the combustion process sublimated the solid propellant which was then injected into the combustion chamber [18, 21, 89].

Ouroboros-1 was designed to evaluate the feasibility of this architecture for a bi-propellant autophage launch vehicle. The engine was built with a depolymerisation chamber as an outer shell that surrounded the combustion chamber. There the fuselage could be inserted along with liquid fuel in order to facilitate convective heat transfer from the combustion chamber to the fuselage followed by the fuel mixture then being injected into the combustion chamber.

The final design for the Ouroboros-1 engine is shown below in Fig. 3.2. It consisted of 4 major structural components: the combustion chamber, depolymerisation chamber, nozzle assembly and the injector assembly. The fuel tube plug (not pictured) was inserted into the gap at the depolymerisation chamber and was sealed using piston seals at the combustion chamber interface and rod seals at the outer shell interface; this allowed the engine to be operated solely as a bi-propellant system. The liquid propane fuel was fed into the depolymerisation chamber through a fuel inlet port on the side of the engine and the oxidiser was fed into a propellant manifold at the injector face. The fuel was injected via sidewall injector orifices that formed an impinging doublet with a corresponding oxidiser injector orifice. An additional self-impinging oxidiser triplet was used which intersected directly over the igniter. An electric spark igniter was used to ignite the propellants at engine start.

The combustion chamber and injector were built from Inconel 625 with the outer shell and nozzle bulkhead made from 316 stainless steel. The nozzle was built from graphite for its very high melting point and thermal conductivity which constitutes a heat sink engine architecture. The injector was fastened using Grade A2 M4 stainless steel cap screws and the chamber assembly with Grade 12.9 M6 bolts. The engine interfaces were sealed using a combination of silicon, PTFE encapsulated and FKM o-rings.

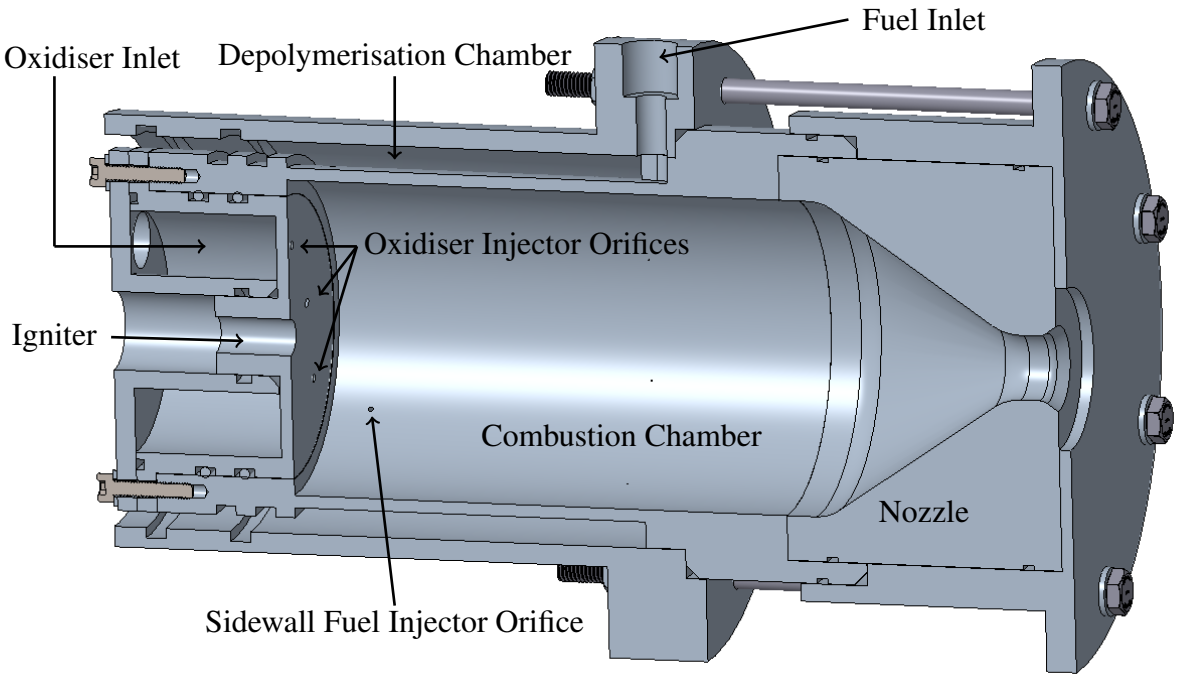

Fig. 3.2 Ouroboros-1 engine assembly cross-section view.

While the engine design was based on existing practices and technology, using it in a novel autophage configuration proved difficult and it was not selected as the architecture for the Ouroboros-3 design and tests. However, the lessons learned from the bi-propellant tests of

this architecture can still be used to eventually lead to a successful autophage engine design using this platform. The components and assembly of the Ouroboros-1 engine can be seen below in Fig. 3.3 and Fig. 3.4.

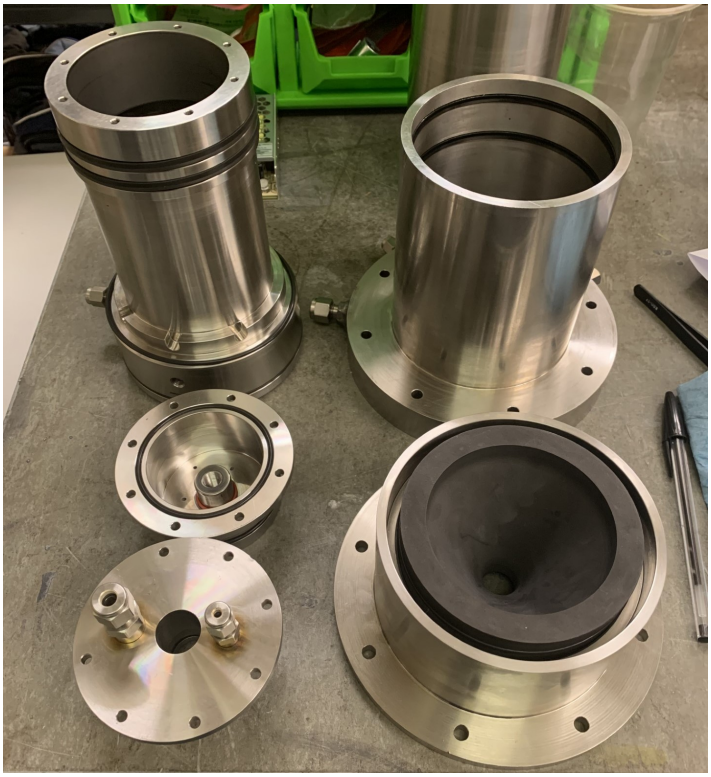

Fig. 3.3 Disassembled Ouroboros-1 components.

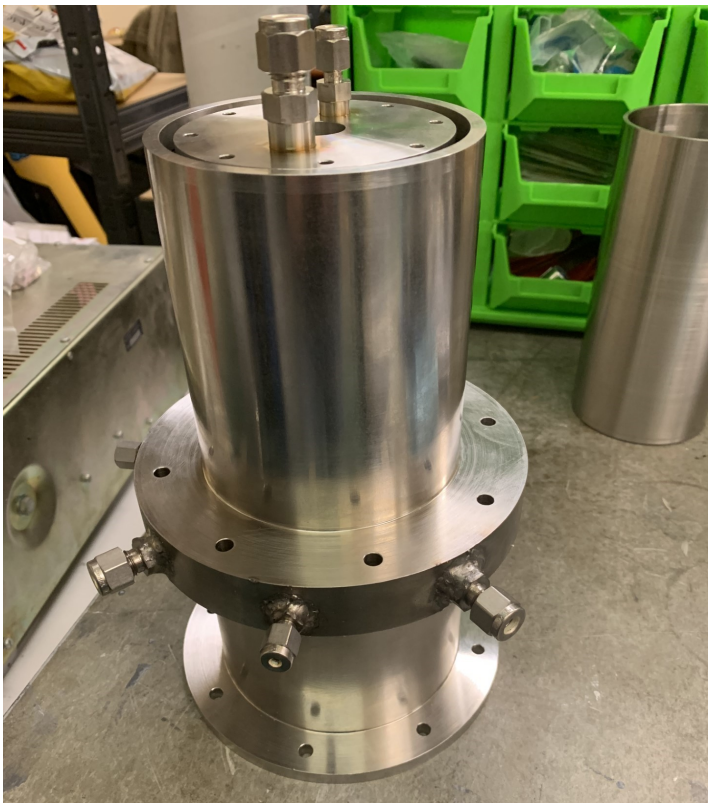

Fig. 3.4 Ouroboros-1 assembly fit-check.

3.2.1 Combustion Chamber

The purpose of the combustion chamber is to contain the combustion gases and facilitate the heat transfer from the combustion process to the HDPE fuel; a cross section of the Ouroboros-1 combustion chamber is shown in Fig. 3.5. For this reason, the Ouroboros-1 combustion chamber was designed to be constructed from Inconel 625 due to its strength at high temperatures. Combustion gases are capable of reaching temperatures of up to 2,500 K (far above the melting point of Inconel 625 at 1,600 K) which necessitates engine cooling in order to operate for long duration burns.

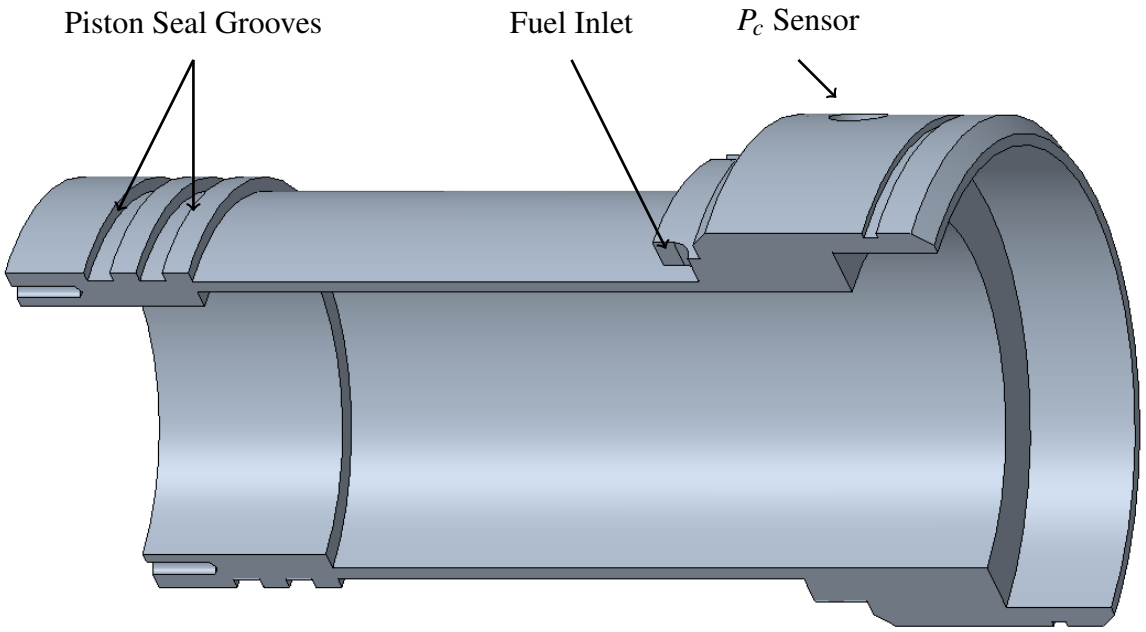

Fig. 3.5 Ouroboros-1 combustion chamber cross-section view.

The Ouroboros-1 architecture provides engine cooling through the previously discussed regenerative cooling mechanism where both the liquid fuel and HDPE fuselage are exposed to the outer combustion chamber wall. Therefore, the chamber wall must be sufficiently thin in order to maintain a high heat flux into the fuel to both effectively cool the engine and melt the HDPE fuselage. However, this requirement is juxtaposed by the need to have a thick chamber wall in order to provide structural strength to the combustion chamber.

Typical regeneratively cooled engines use channels rather than a shell to route the fuel around the engine. This allows for relatively thin chamber walls which make regenerative cooling very effective by optimising the heat flux into the propellant. The required minimum thickness will be determined by the hoop stress of the chamber walls, σ_θ. The hoop stress is a function of the combustion chamber pressure, P_c multiplied by the mean diameter, D_m, and divided by half the chamber wall thickness δ as shown in Eq. (3.1).

$$\sigma_\theta = \frac{P_c D_m}{2\delta} \tag{3.1}$$

However, the Ouroboros-1 autophage design was unable to use such channeling due to the inherent nature of the HDPE fuselage needing to fully encompass the combustion chamber. Additionally, the depolymerisation chamber is pressurised to a minimum of 1.2x the

combustion chamber pressure in order to inject and atomise the fuel. This creates an external pressure that drives the thickness of the combustion chamber via the hoop stress buckling load equation, Eq. (3.2).

$$P_{fuel} - P_c = \frac{2E}{3}\left(\frac{\delta}{D}\right)^3 \tag{3.2}$$

Using the nominal combustion chamber pressure of 5 bar, the thickness was designed to be 2 mm which corresponds to a maximum fuel inlet pressure of 21 bar. This results in a factor of safety of 3.5 bar over the nominal fuel inlet pressure of 6 bar. Of course, elevated temperatures would reduce the strength of the combustion chamber making it more susceptible to a hoop stress buckling failure while operating in steady state for an extended duration. Inconel 625 is able to maintain its yield strength relatively well for temperatures up to 1,000 K; however, as shown in Fig. 3.6, the yield and ultimate strength sharply drop off over 1,075 K [90].

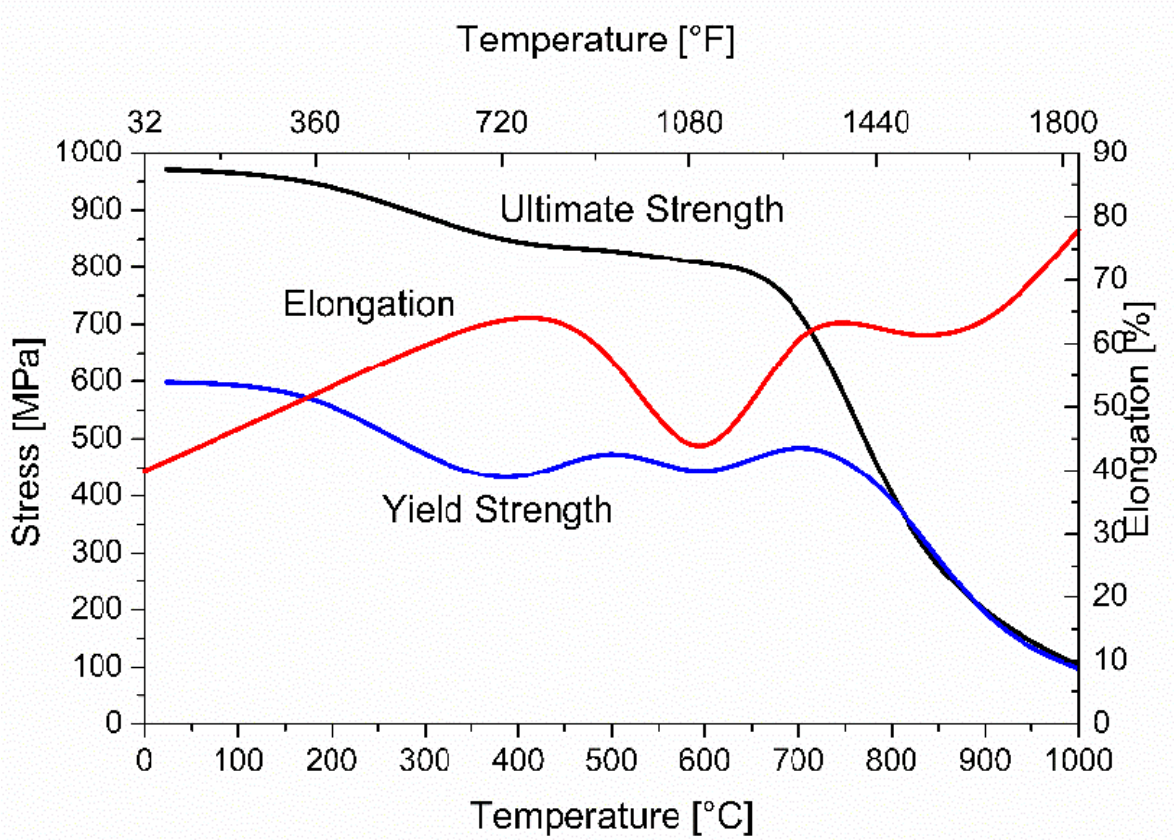

Fig. 3.6 Yield strength, ultimate strength and elongation of Inconel 625 at elevated temperatures [90].

Therefore, a thermal analysis was conducted on the combustion chamber to determine the steady state operating temperature of the chamber walls and verify that even at elevated temperatures the wall thickness would be sufficient to prevent hoop stress buckling failure. The thermal analysis also considered the convective cooling of the propane fuel as it traveled through the depolymerisation chamber to the sidewall injector orifices. The analysis was conducted using the thermal and cooling suite of the 1D chemical equilibrium software: *Rocket Propulsion Analysis* [83]. This would also verify that the fuel in the depolymerisation chamber would reach a sufficiently high temperature to also melt the HDPE fuselage. The

thermal analysis of the engine contour was conducted for both the combustion chamber and the nozzle. A section of the combustion chamber is regeneratively cooled and the remainder of the engine is cooled via conductive heat transfer; results shown in Fig. 3.7.

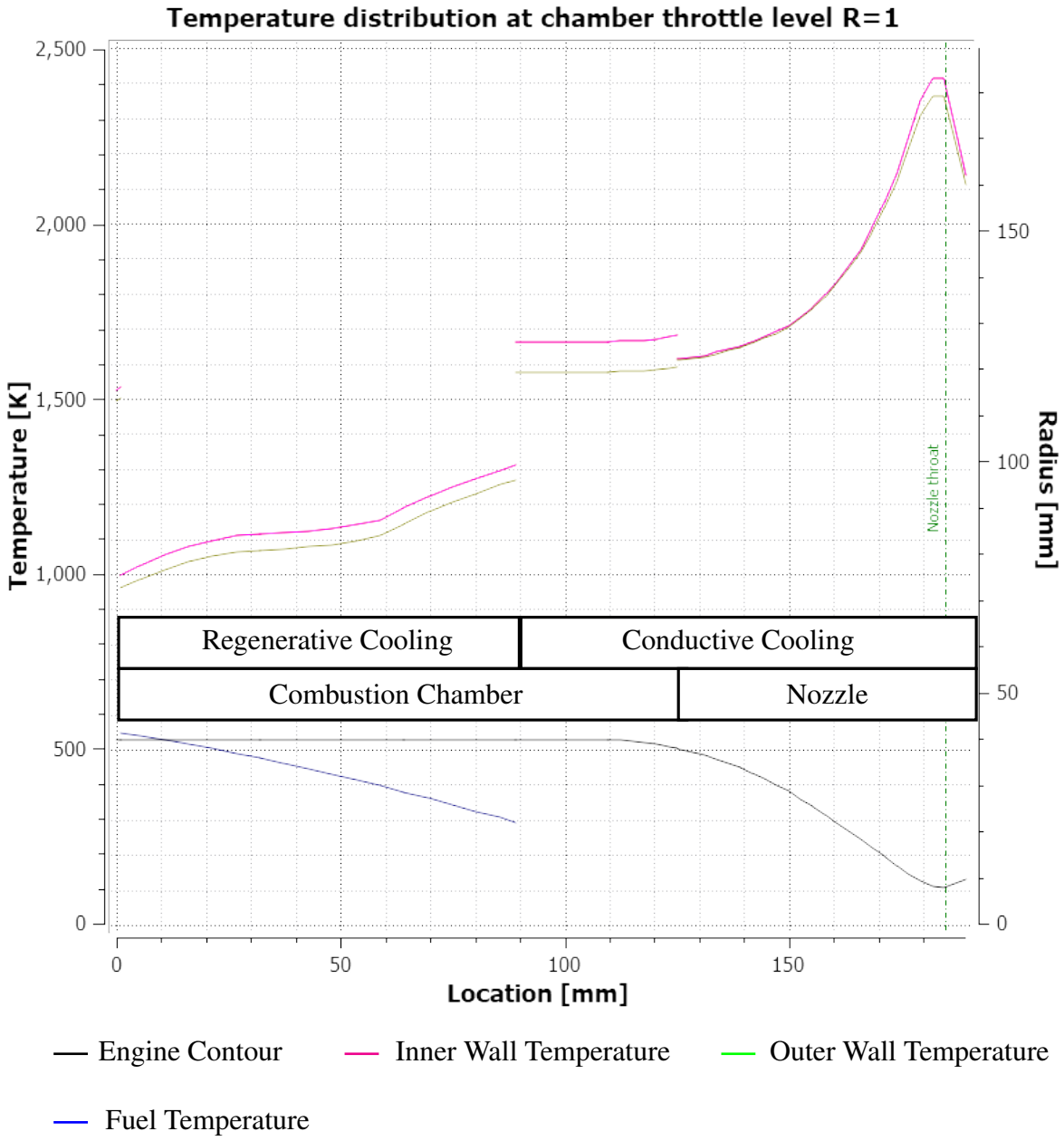

Fig. 3.7 Equilibrium thermal profile of the Ouroboros-1 autophage engine.

The thermal analysis conducted by *Rocket Propulsion Analysis* uses the Bartz equation derived by D.R. Bartz [91]. It is a semi-empirically derived formula that predicts the heat-transfer coefficient in jet engine turbines and rocket engines. The equation is generally expressed as:

$$h_g = \frac{0.026}{{d_t}^{0.2}} \left(\frac{\mu^{0.2} C_p}{{Pr_c}^{0.6}} \right) \left(\frac{P_c}{C^*} \right)^{0.8} \left(\frac{A_t}{A} \right)^{0.9} \sigma \tag{3.3}$$

Where d_t is the diameter of the throat, μ is viscosity, C_p is the specific heat at constant pressure, Pr is Prandtl number, P is the chamber pressure, C^* is characteristic velocity, A_t is

area at the throat, and A is the area at the selected axial location. σ is a correction factor that accounts for property change across the boundary layer and is given by Eq. 3.4.

$$\sigma = \frac{1}{\left[0.5\frac{T_{wg}}{T_0}\left(1+\frac{\gamma-1}{2}M^2+0.5\right)\right]^{0.68}\left[1+\frac{\gamma-1}{2}M^2\right]^{0.12}} \tag{3.4}$$

Where T_0 is the stagnation temperature of the combustion gas, and M is the local Mach number.

This process shows the non-constant nature of the heat flux of a rocket engine, reaching a maximum value in the vicinity of the throat. To perform a heat transfer analysis, the non-linear behaviour is discretised into 'stations' which can be individually analysed. The Bartz equation is generally regarded as a conservative approximation [92] and is used throughout industry for first order analyses [93, 94]. The Bartz equation makes several assumptions to simplify the complexity of heat transfer calculations in practical applications: steady state flow, constant properties, fully developed turbulent flow, circular cross-section, and homogeneity of the fluid.

Due to the complexity of rocket combustion, empirical data is necessary to validate more accurate models for specific propellants and propulsion systems [95]. The tri-propellant, autophage engine architecture is novel and does not have any available empirical data; therefore, the Bartz equation and thermal analysis conducted by *Rocket Propulsion Analysis* was determined to be a sufficient approximation for the purposes of this research which aims to supply the first sets of empirical data for autophage engine performance.

In this thermal analysis the *Rocket Propulsion Analysis* software has discritised the system into 200 stations and used the Bartz equation to estimate the heat transfer throughout the combustion chamber. One shortfall of this analysis is that the software does not consider axial heat transfer between engine components, this results in a piecewise thermal profile at the interface of the combustion chamber and graphite nozzle. Empirically, this would be a continuous curve; however, this result is the conservative approximation.

As can be seen in Fig. 3.7, the fuel temperature increases past 473 K (200°C) which is higher than the melting point of HDPE [20]. This indicates that the fuselage should contribute to the total fuel mass flow rate during steady state engine operation. However, the combustion chamber wall temperatures in the regenerative cooling section reach up to 1,300 K (1,027°C). While below the melting point, the reduction in yield strength of Inconel 625 is significant at those temperatures according to Fig. 3.6. The results indicate that the engine is likely to fail due to hoop stress buckling as it approaches the equilibrium operating temperature. Nevertheless, when running the thermal analysis for various chamber wall thicknesses, an increase in chamber wall thickness both increased the chamber wall temperature and reduced the fuel temperature below the melting point of HDPE. On the other hand, decreases in chamber wall thickness corresponded to a reduction in chamber wall temperature and increased the effectiveness of the regenerative cooling; however, the factor of safety for the hoop stress buckling was reduced.

Due to this analysis, it was hypothesised that the engine design was likely to fail due to hoop stress buckling unless chamber wall temperature was reduced by using different

materials or another cooling method. Using copper or another material with high thermal conductivity could reduce chamber wall temperature; however, the yield strength of the chamber wall would be significantly reduced and susceptible to hoop stress buckling due to the lower young's modulus of copper. Further cooling of the engine wall via film or transpiration cooling [96] could be effective but it would also reduce the heat flux into the fuselage making autophage operation unfeasible.

To verify these conclusions experimentally, the Ouroboros-1 engine and combustion chamber were built as specified with the intention of monitoring engine performance, combustion chamber temperature and depolymerisation chamber temperature during steady state operation at standard inlet conditions. The engine would still operate nominally, for a time, from ignition until reaching the hoop stress buckling failure mode as chamber wall temperature approached equilibrium. This would validate the analysis methods used in the design of the regeneratively cooled autophage combustion chamber and confirm the likely failure mode for this architecture. Thus, future development could build on these results and target research into regenerative cooled combustion chamber designs for autophage engines.

3.2.2 Depolymerisation Chamber

The depolymerisation chamber consisted of an outer shell which created the seal at the outer wall of the engine fuselage. A cross section of the depolymerisation chamber shell is shown in Fig. 3.8. It was constructed of 316 stainless steel due to the fact that it was not designed to be directly exposed to any combustion gases and it was the main structure that fastened the engine to the test stand. Stainless steel also offered sufficient corrosion resistance to propane fuel and melted HDPE.

The chamber also had four inlets for fuel and sensors. The first was a fuel inlet to provide propane fuel for Ouroboros-1 and the second was a fuel outlet for engine purge in the event of over-pressurisation of the depolymerisation chamber. The outlet was outfitted with both a pressure relief valve and a manual purge valve to allow for both automatic and manual venting. This was implemented due to the risk of the sidewall injectors becoming blocked and over-pressurisation in the depolymerisation chamber, which would cause a larger external pressure on the combustion chamber walls and risk a hoop stress buckling failure as described in the previous section. The sensor inlets were for both a pressure and temperature sensor to measure the fuel inlet/depolymerisation chamber conditions. All inlets and outlets going to the depolymerisation chamber were interfaced with a lip machined into the combustion chamber (visible in Fig. 3.5) to prevent the outlets from being covered by the HDPE fuel.

The seals on both the combustion chamber and depolymerisation chamber were unidirectional FKM piston and rod seals which reduced the friction to drive the HDPE fuselage into the depolymerisation chamber while still sealing the interface between the engine and the fuselage.

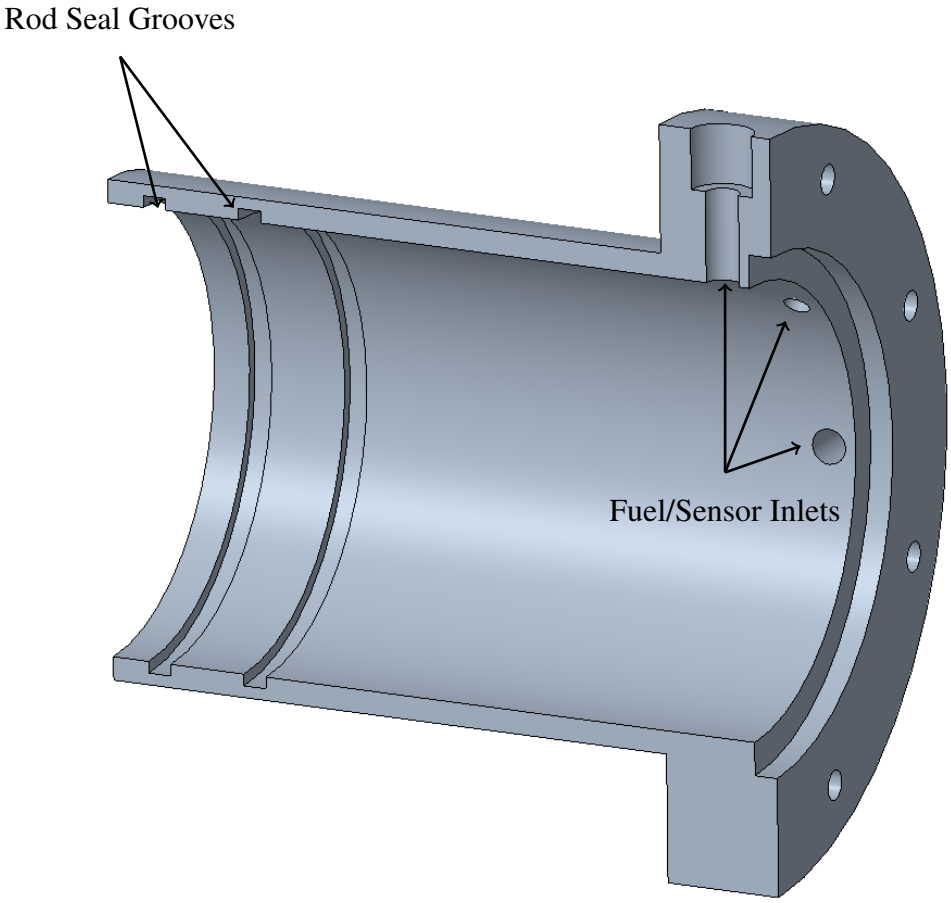

Fig. 3.8 Cross-section view of the depolymerisation chamber outer shell.

3.2.3 Injector and Propellant Manifolding

Propellant injection is a vital component of successful engine design in order to maximise the combustion efficiency and performance of the propulsion system. The injector and propellant manifolding of the Ouroboros-1 engine consisted of multiple components: the combustion chamber and the depolymerisation chamber which facilitated the fuel injection, while the oxidiser injection was conducted using a dedicated injector face which was fastened to the combustion chamber.

The depolymerisation chamber acts as the fuel inlet manifold which injects the fuel mixture into the combustion chamber. The injection is performed via the sidewall injector orifices located on the combustion chamber walls per Fig. 3.2. There are three 1mm injector orifices located on the combustion chamber walls spaced 120 degrees apart around the firing axis. These injector orifices are perpendicular to the firing axis which also intersect perpendicularly with the oxidiser injector orifices; the two-stream fuel and oxidiser intersection classifies these as doublet injectors.

As shown in Fig. 3.9, the oxidiser injector has a total of 6 orifices that are 2mm in diameter. Due to gaseous oxidizer being used rather than liquid oxidizer, more orifices are needed to maintain nominal oxidizer mass flow rate at standard inlet conditions. The flow from three of these orifices intersects with the flow from the sidewall fuel injector to facilitate mixing. The remaining three orifices are angled at 30°in order for the flow to converge directly above the

igniter; this is referred to as a self-impinging triplet and creates an oxygen rich environment which encourages ignition from the spark igniter at engine start. This oxidiser injector was manufactured from Inconel 625 using the same rationale as the combustion chamber due to being exposed directly to the combustion gases. The oxidiser manifold is also an important part in the design of injectors as it even distributes the oxidiser across all of the orifices such that each orifice has the same mass flow rate.

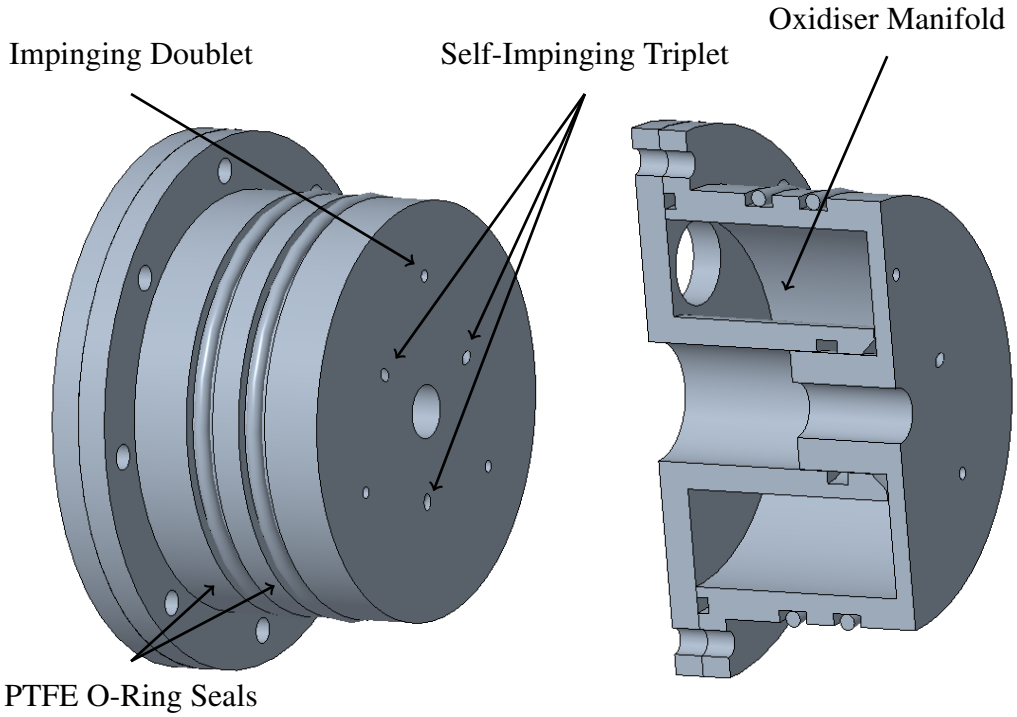

Fig. 3.9 Ouroboros-1 oxidiser injector and propellant manifolding

The main function of the injector assembly is to atomise propellants and facilitate mixing between the oxidiser and fuel. This maximises the contact area between the propellant molecules and the combustion efficiency of the engine. For gas injection, propellant atomisation is not a concern. And the gaseous oxidiser injector orifices of the engine are able to be designed using a single phase incompressible (SPI) model [97] given by Eq. (3.5). A discharge coefficient of 0.6 is used as it corresponds with an approximation for a short tube injector with sharp corners.

$$\dot{m}_{SPI} = C_d A \sqrt{2\rho\Delta P} \tag{3.5}$$

However for liquid propellants, there are multiple factors that will impact atomisation and droplet size (I.e. surface tension forces, inertial forces, and viscous forces). This leads to two-phase, non-homogeneous flow which creates difficulty in accurately modeling and designing liquid injector orifices [98]. However, experimental validation has identified five main spray structures for propellants as they are injected through an orifice; these spray structures are depicted in Fig. 3.10.

The preferred structure is complete atomisation which minimizes droplet diameter and is a function of pressure differential, orifice sizing and fluid properties. In order to achieve

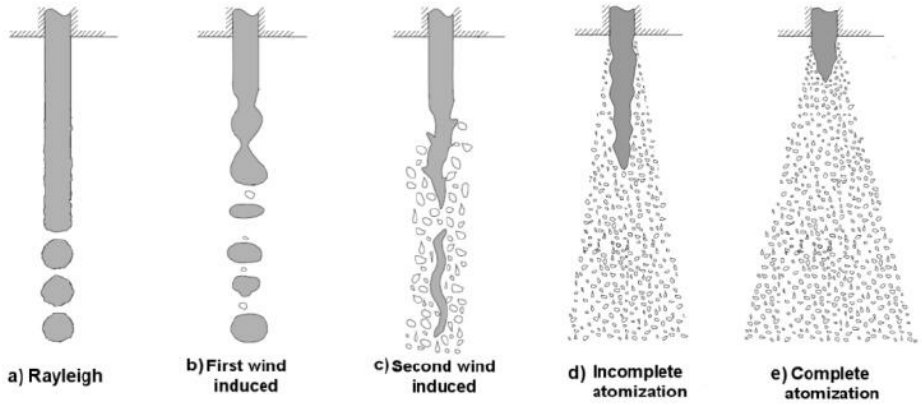

Fig. 3.10 Spray structure for different atomisation regimes [99].

this, the fuel orifices were sized using a homogeneous equilibrium model (HEM) and the two-phase Dyer model (DYER) per Eq. (3.6) and Eq. (3.7) respectively.

$$\dot{m}_{HEM} = C_d A \rho_2 \sqrt{2(h_1 - h_2)} \tag{3.6}$$

$$\dot{m}_{DYER} = A \left(\frac{k}{1+k} \dot{m}_{SPI} + \frac{1}{1+k} \dot{m}_{HEM} \right) \tag{3.7}$$

The homogeneous equilibrium model is commonly used to predict two-phase critical flow rate through an injector orifice and assumes thermal equilibrium between the liquid and vapor phases, no velocity difference between the liquid and vapor phases and isentropic flow across the injector. This provides a maximum critical mass flow rate in terms of entropy based on the first law of thermodynamics. However, the HEM is only a limiting case for the critical mass flow rate and it often under predicts the mass flow rate for short tube injectors. The Dyer model provides a correction to the HEM by relating it to the single-phase flow model and includes non-equilibrium effects which are primarily driven by two mechanisms: the super-heating of the liquid during expansion and finite vapor bubble growth rates [100]. These are represented by a relationship between the bubble growth time and the liquid residence time k, a non-equilibrium parameter defined by Eq. (3.8).

$$k = \sqrt{\frac{P_1 - P_2}{P_0 - P_2}} \tag{3.8}$$

Using the Dyer model, a mass flow rate per injector orifice is determined based on a set orifice diameter. In this case, a 1mm diameter orifice is used for the sidewall fuel injectors since an orifice diameter below 0.8mm risks blockages and larger orifices will result in lower injection velocities which can affect fuel atomisation. In order to determine whether the orifice design is sufficient to atomise the fuel the Reynolds number (Eq. (3.9)) and Weber number (Eq. (3.10)) are calculated.

$$Re = \frac{\rho v l}{\mu} \tag{3.9}$$

$$We = \frac{\rho v^2 l}{\sigma} \tag{3.10}$$

The Weber and Reynolds numbers are then used to calculate the Ohnesorge number which relates the inertial, viscous and surface tension forces in a fluid and is the main metric for determining the spray structure of a flow.

$$Oh = \frac{\sqrt{We}}{Re} \tag{3.11}$$

When related to the Reynolds number the Ohnesorge number shows a logarithmic correlation which describes the atomisation level of flow as it passes through an orifice. These regions have been experimentally validated and provide a non-dimensional metric for determining a flows atomisation through an injector orifice [101]. The resulting Ouroboros-1 fuel injector orifice conditions are included in Fig. 3.11 and complete atomisation of the fuel was predicted.

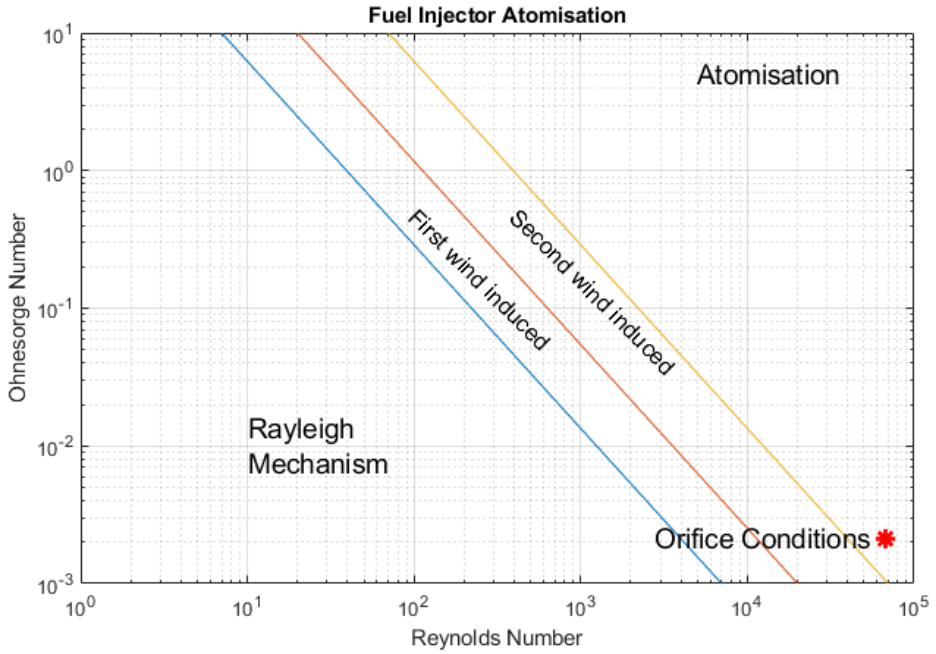

Fig. 3.11 Ouroboros-1 fuel orifice atomisation analysis.

Assembly of the injector to the combustion chamber used PTFE encapsulated o-rings and various silicone and FKM o-rings at the manifold and oxidiser inlets. These were selected due to material compatibility with the propellants as well as high temperature operating ranges.

3.2.4 Nozzle and Nozzle Block

The Ouroboros-1 nozzle consists of two components: a graphite nozzle insert and a 316 stainless steel nozzle block shown in Fig. 3.12. This allowed for interchangeability across all Ouroboros engine designs, meaning that the same nozzle block section could be reused. Also, if the same engine was to be tested at differing inlet conditions, only a new graphite nozzle insert would have to be manufactured, rather than an entire engine.

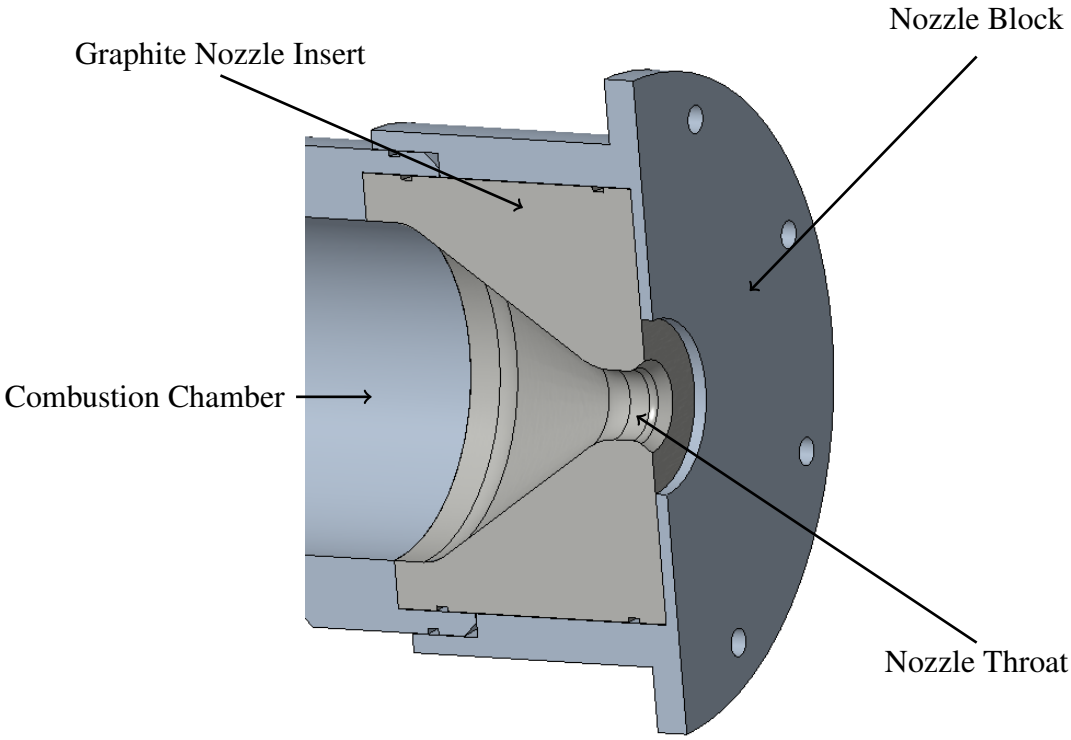

Fig. 3.12 Ouroboros-1 nozzle and nozzle block cross-section view.

The nozzle converts pressure into thrust by compressing the combustion gases and accelerating the flow to Mach 1 at the throat; this exposes the nozzle to very high temperatures. Therefore, special consideration for the nozzle material was taken and a graphite insert was selected due to its very high working temperatures (up to 3,000 K). Additionally, graphite has heritage as being used for nozzles in rocket engine design [102, 103] and referencing Fig. 3.7 shows that the expected throat temperature will be approximately 2,400 K which is within typical ranges for a graphite nozzle.

Like the combustion chamber, the optimum geometry of the nozzle was designed using the *Rocket Propulsion Analysis* software package. The nozzle is a converging-diverging conical nozzle design. The diverging section was selected to be conical due to the minimal effect a bell nozzle would have on engine performance. This is due to the relatively small change in exit area of the nozzle when compared to the throat since combustion chamber pressure for standard inlet conditions was quite low at only 5 bar. The characteristics of the nozzle are shown in Table 3.1.

The nozzle block was designed to keep the nozzle secured in place whereby the nozzle fits within the combustion chamber collar and the nozzle block collar. It is then fastened to the depolymerisation chamber via eight M6x140mm bolts that are fastened through the M6 clearance holes. This supplies a compressive force across the depolymerisation chamber, combustion chamber, nozzle and nozzle block which keep all components fastened and compress all crushing seals at the interfaces.

Overall, the nozzle block was expected to experience moderate temperatures as heat is transferred via conduction from the nozzle. Additionally, due to slight exposure of combustion gases at the interface with the combustion chamber, 316 stainless steel was selected as the

Table 3.1 Nozzle characteristics of the Ouroboros autophage engine design.

Parameter	Value
Throat diameter	16.00 mm
Exit diameter	19.39 mm
Combustion chamber diameter	80.00 mm
Contraction area ratio	25.00
Expansion area ratio	1.47
Contraction angle, degrees	30.0°
Conical nozzle half angle	25.0°
Combustion chamber pressure	5.0 bar
Exit pressure	1.013 bar
Mach number	1.736
Exhaust velocity	1932 m/s

material for the nozzle block. For the Ouroboros-1 design, silicone and PTFE encapsulated seals were used to seal the nozzle; these were later replaced with copper gaskets for Ouroboros-2 and 3.

3.2.5 Igniter

The auto-ignition temperature of propane is 723 K and thus requires an igniter to provide the required energy to initiate the combustion process [104]. The initial energy to begin ignition was provided via a high voltage electric spark from a Denso RU01-34 spark plug as shown in Fig. 3.13. This plug has been selected due to its low profile and high temperature compatibility.

The igniter is a cold-type spark plug with a high rating of 34 on the Denso thermal scale. This corresponds to a very high operating temperature of over 1,000°C which aligns with the nominal operating temperature of the injector plate where the igniter is fastened. The electrode is also an iridium surface gap design which contributes to the very high operational temperature and is not expected to show significant wear throughout the total cumulative lifetime of the engine

Fig. 3.13 Image of the RU01-34 igniter used for engine ignition.

The electric spark igniter itself is operated through a circuit that has been designed to deliver a high voltage spark of up to 30,000 V. The schematic and manufactured PCB are shown in Fig. 3.14 and 3.15 respectively.

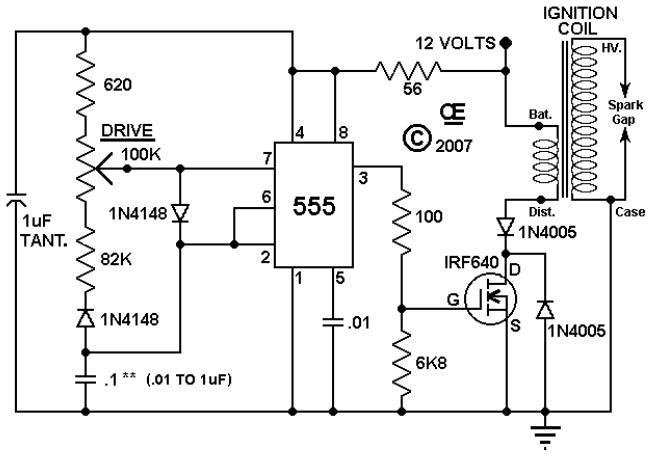

Fig. 3.14 Electric spark igniter circuit schematic.

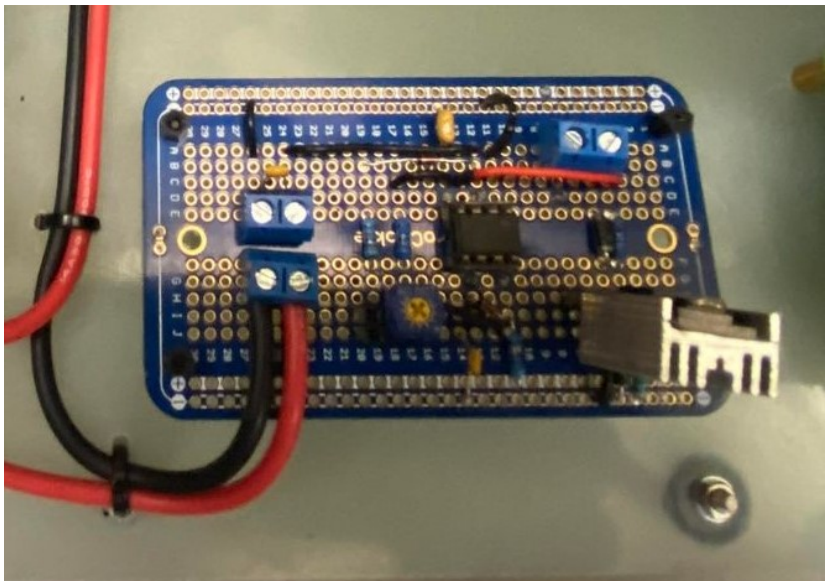

Fig. 3.15 Electric spark igniter circuit PCB.

The ignition circuit is thus able to deliver a high voltage spark using a 12 VDC input in order to start the engine. The cable used to deliver the high voltage current to the igniter was an EMI suppressed cable to reduce any potential interference caused by the ignition cable with engine instrumentation. Tests of the ignition circuit and igniter showed success in ignition tests and no significant additional noise for sensors. Figure 3.16 shows the igniter integrated and operating on the injector face. Once ignition begins, the combustion chamber temperatures exceeds the autoignition temperature and combustion process is self-sustaining.

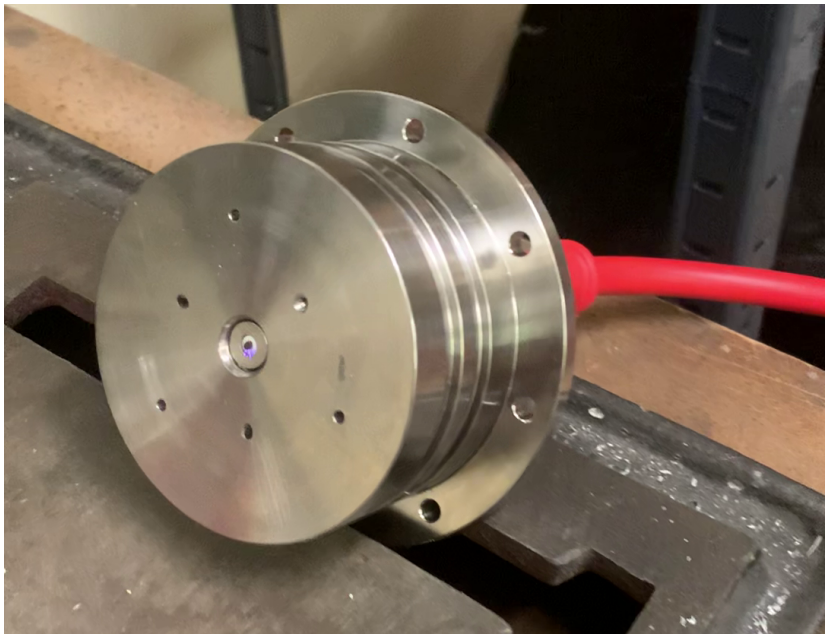

Fig. 3.16 Integrated igniter and injector test.

3.3 Direct Fuselage Insertion Based On Hybrid Propulsion Systems

The second engine, Ouroboros-2, was designed to use a direct fuselage insertion method instead. In this architecture, rather than using a separate depolymerisation chamber, the fuselage is inserted directly into the combustion chamber and is burned similar to a traditional hybrid propulsion system design. A classic hybrid propulsion system consists of two components: a liquid oxidiser and a solid fuel grain. The fuel grain is bored and inserted into a combustion chamber. There, liquid oxidiser is injected and the combustion process propagates radially outward along the fuel grain at a designed regression rate. An example of a hybrid propulsion system is shown in Fig. 3.17.

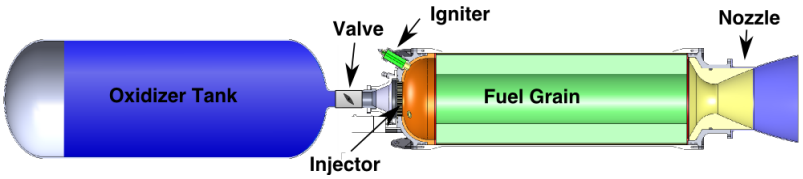

Fig. 3.17 Cross-section view of a typical hybrid rocket motor [105].

The direct fuselage insertion autophage engine operates similarly by exposing the fuselage directly to the combustion gases. This causes the solid fuel to be directly burned rather than first being depolymerised and mixed with liquid bi-propellant fuel before injection into the engine as a fuel mixture. However, unlike a classic hybrid motor where the diameter of the inner fuel grain increases, the hybrid autophage motor has a thin fuel grain that remains the same diameter as it is continuously inserted into the thrust chamber as shown in Fig. 3.18.

Ouroboros-2 was built based on this architecture and used a slotted inner combustion chamber to expose the fuselage to the combustion gases while still securing the injector to

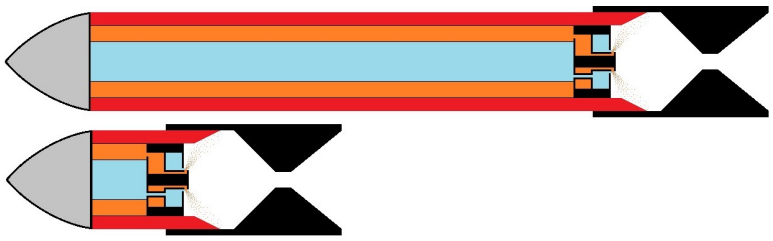

Fig. 3.18 Cross-section view of a hybrid autophage motor.

the combustion chamber and nozzle. To contain the combustion gases, an external steel shell was used as the outer chamber wall surrounding the fuselage at the engine interface. The injector itself injected both liquid fuel and oxidiser through the forward end of the combustion chamber allowing for liquid bi-propellant ignition. In the autophage configuration, this would shift to a tri-propellant burn as the fuselage would begin to contribute to the total fuel mass flow rate.

A cross-section view of the Ouroboros-2 and 3 engine can be seen in Fig. 3.19. Using the direct fuselage insertion method, the HDPE fuel tube was inserted directly into the combustion chamber and eliminated the need for a separate depolymerisation chamber. However, the outer chamber shell was still necessary to form the structural wall of the engine. Similarly to the Ouroboros-1 design, the HDPE fuselage was sealed between the combustion chamber and the outer shell using a combination of piston and rod seals. Due to the direct fuselage injection, the liquid propane fuel was routed through the HDPE fuselage and injected through the face at the end of the combustion chamber alongside the oxidiser.

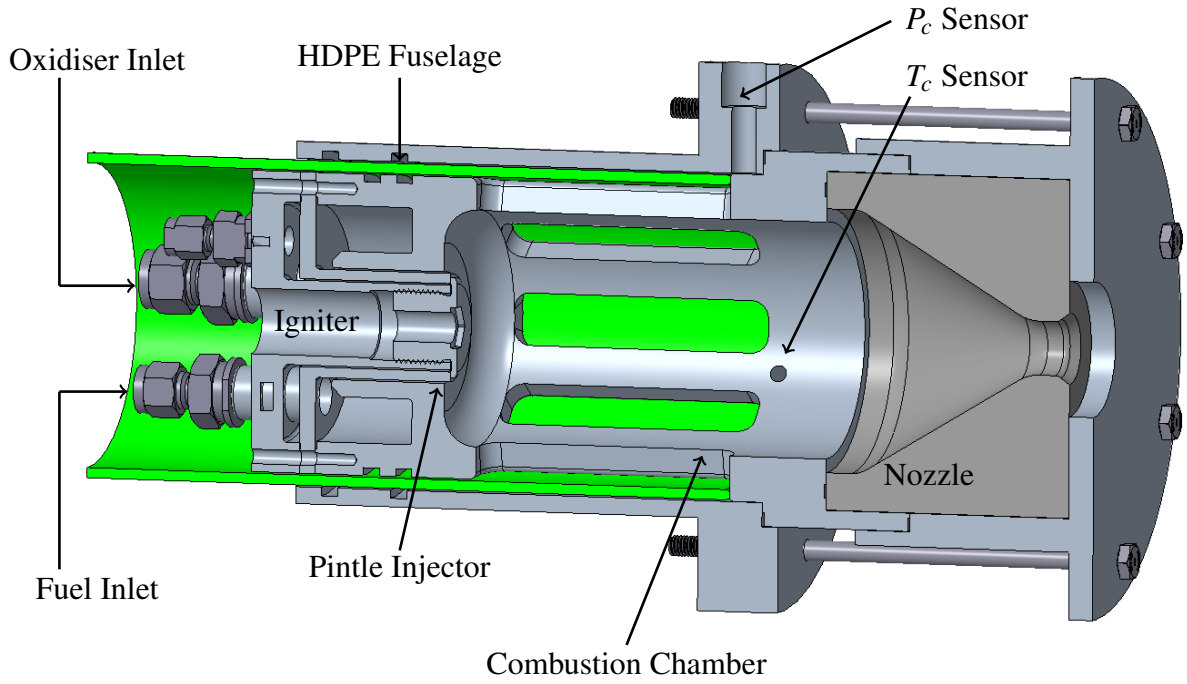

Fig. 3.19 Ouroboros-2 and 3 engine assembly cross-section view.

The diameter of the engine was driven by the required mass flow rate of the propellants as well as the limited injector face area for accommodating all propellant lines, sensors and the igniter. Due to the limited volume, a pintle injector was selected as the preferred

injection method. Propellant manifolding was also required to evenly distribute the propellant around the pintle. As in the previous design, an electric spark igniter was used to ignite the propellants. As the engine temperature rapidly increased after ignition, it would melt and vaporise the exposed HDPE fuel. In order to manufacture multiple engines for repeated tests, the combustion chamber and injector manifold were manufactured from 316 stainless steel. All other seals, with the exception of propellant manifolding were replaced with copper gaskets due to lessons learned form the Ouroboros-1 tests.

From the Ouroboros-2 test results, the direct fuselage insertion architecture operated successfully in the bi-propellant configuration and showed promise to be used as the design architecture for the Ouroboros-3 autophage tests with some minor improvements. The lessons learned were based mainly around the pintle injector design which caused combustion instabilities and elevated engine operating temperatures during the Ouroboros-2 bi-propellant tests; the injector was modified to add channels on the oxidiser which reduced combustion instabilities and added film cooling to the internal combustion chamber walls. Thus, the final Ouroboros-3 autophage tests used a direct fuselage insertion architecture. The sub-assemblies of the Ouroboros-2 injector and inner combustion chamber can be seen in Fig. 3.20 and Fig. 3.21. Table 3.2 defines the major dimensions of the Ouroboros-2 and 3 combustion chambers.

Table 3.2 Dimensions of the Ouroboros autophage engine design.

Parameter	Value
Combustion chamber inner diameter	80.00 mm
HDPE fuel inner diameter	90.00 mm
Combustion chamber outer diameter	96.00 mm
Outer engine diameter	110.0 mm
Combustion chamber length	165.0 mm
Combustion chamber support length	80.00 mm
Characteristic length	1.0 m

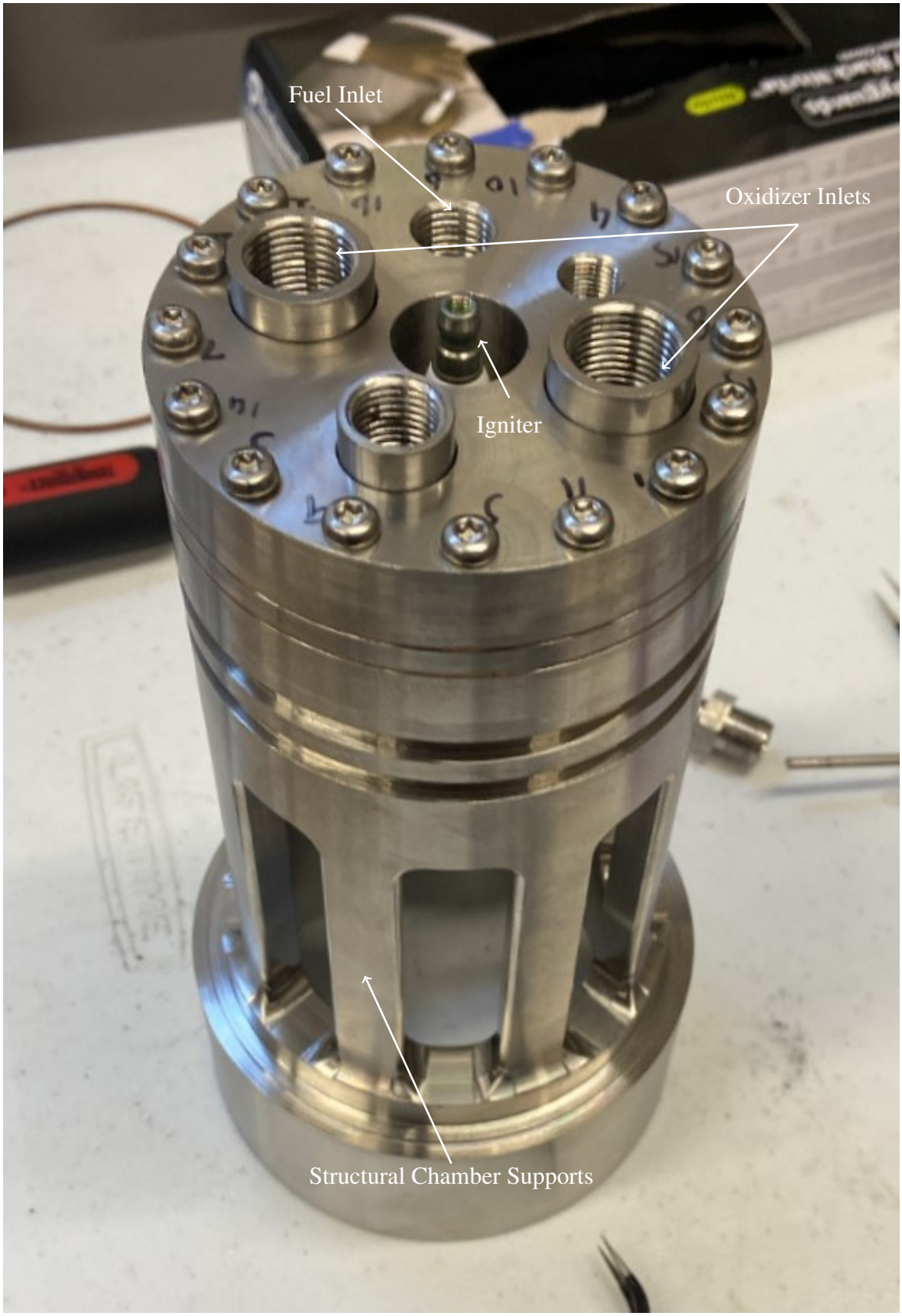

Fig. 3.20 Ouroboros-2 integrated injector and inner combustion chamber.

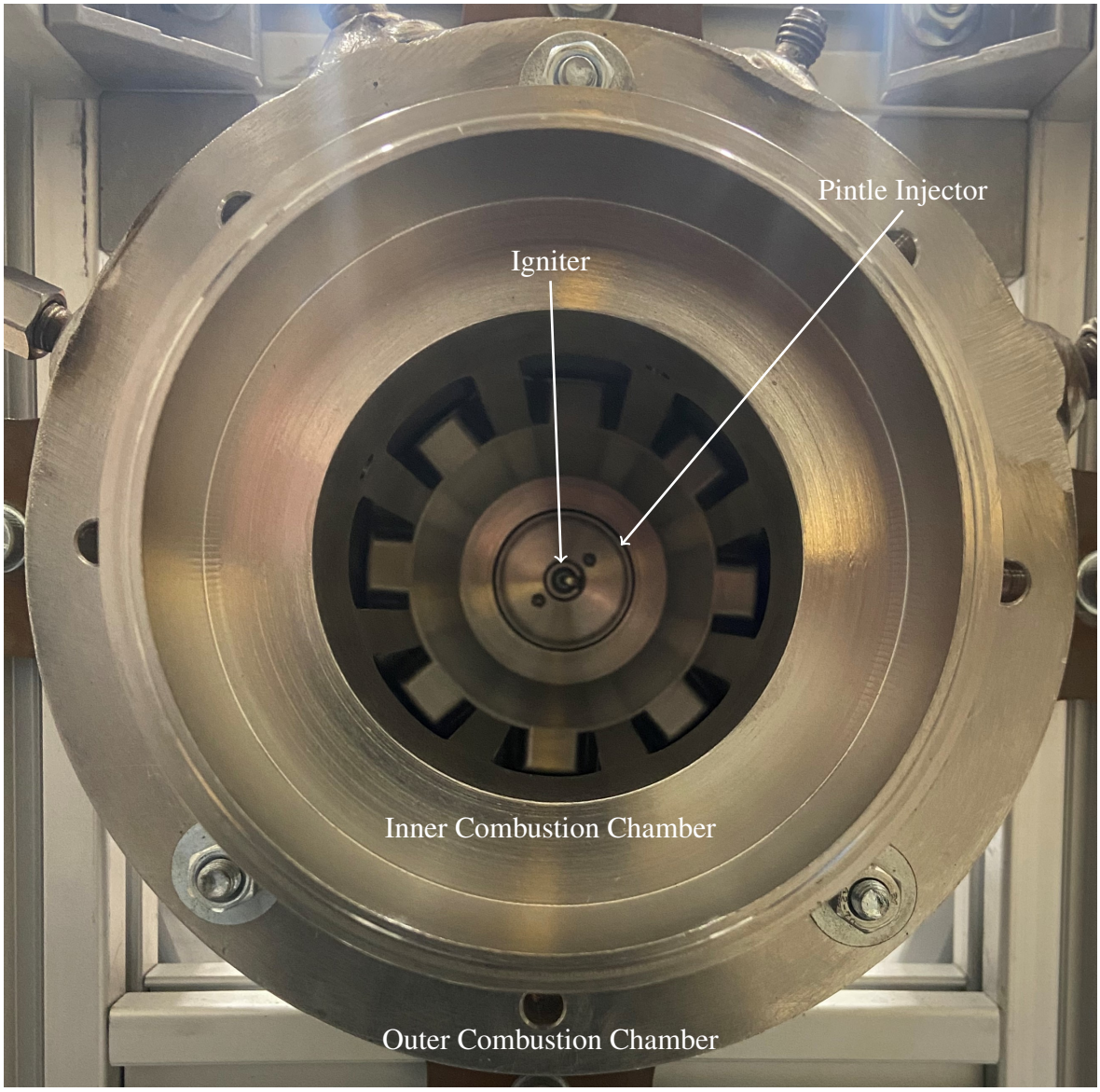

Fig. 3.21 Ouroboros-2 integrated inner and outer combustion chamber assemblies.

3.3.1 Inner Combustion Chamber

The direct fuselage insertion architecture required a different combustion chamber design in order to facilitate both the HDPE fuselage being burned in the chamber as well as allowing bi-propellant injection at the injector face. In order to meet these requirements, a slotted combustion chamber was proposed which would create the structural support for injector fastening while providing an exposed area for the fuselage to melt and burn; the cross section of the Ouroboros-2 and 3 combustion chamber is shown in Fig. 3.22. As the combustion process occurred along the chamber slots, the melted HDPE would also contributed to engine cooling since it would create a film boundary layer around the inner combustion chamber structural components.

Building on the results of Ouroboros-1, film cooling was introduced in order to reduce the chamber wall temperature and reduce the risk of engine failure. As a whole, film cooling is a very effective method for reducing engine wall temperature and it operates by creating a thin boundary layer at the chamber wall. Heat flux from the combustion process enters this

boundary layer and causes the fuel to evaporate; therefore, the maximum temperature that the chamber wall is exposed to is limited to the boiling point of the fuel at the combustion chamber pressure [96] so long as the film covers the chamber wall. In the autophage engine architecture, the HDPE film cooling is self regulating: as engine temperature increases, the HDPE fuselage will melt faster and provide a higher mass flow rate which should further cool the engine. Therefore, the direct fuselage insertion combustion chamber design could provide a dynamic method for regulating engine temperature even if it is operated outside of its nominal inlet conditions. In an effort to characterise this, the combustion chamber temperature sensor was placed directly downstream of the chamber slots to investigate the effectiveness of the dynamic autophage film cooling.

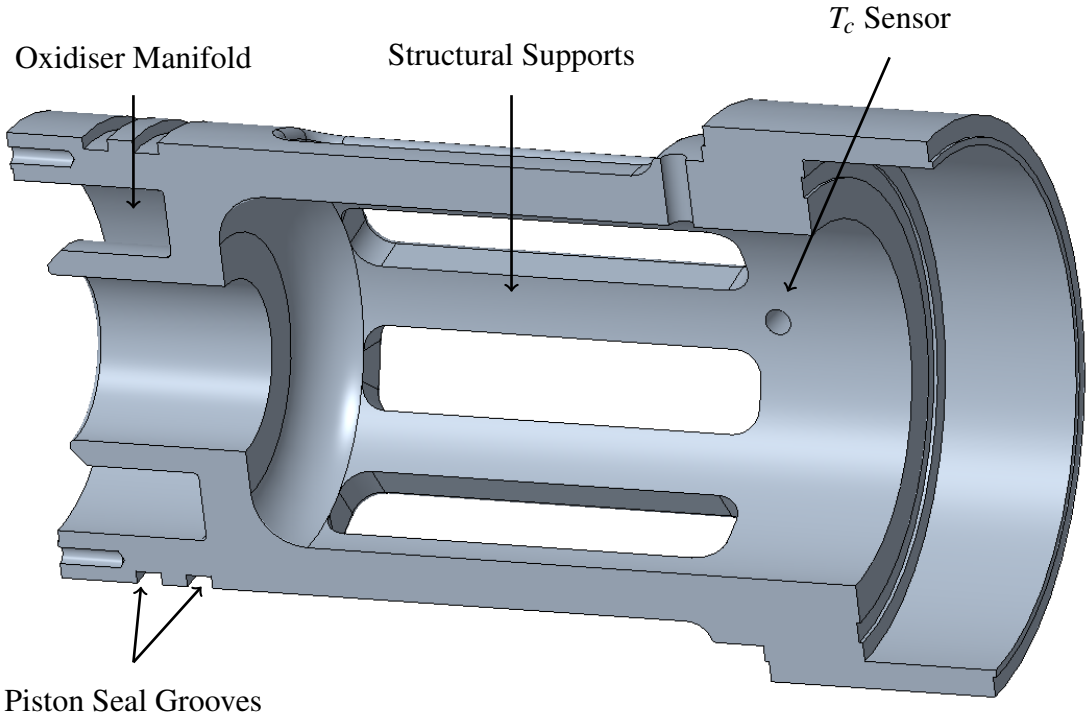

Fig. 3.22 Ouroboros-2 and 3 combustion chamber cross-section view.

Unlike the previous design, the Ouroboros-2 and 3 combustion chambers also included the oxidiser manifold and injector face as a single machined part. This allowed for the number of required seals and fasteners to be reduced. However, due to the increased manufacturing complexity, the combustion chambers were built from 316 stainless steel instead of Inconel 625 which allowed for multiple combustion chambers to be tested. Nevertheless, stainless steel has a reduced yield strength at elevated temperatures when compared to Inconel 625 and the yield strength significantly decreases at temperatures above 975 K [106]. Therefore, the stainless steel chambers have a lower threshold for reaching engine failures due to excessive chamber wall temperature. The most likely failure mode for this design was identified to be the midpoints of the structural supports where there might not be sufficient HDPE film to fully coat the chamber. For this reason the Ouroboros-3 injector was designed to also contribute liquid propane as a film coolant on the combustion chamber structure.

As in the previous design, the HDPE fuselage was the same diameter and sealed using FKM piston and rod seals. However, all other combustion chamber seals were switched to

copper gaskets for a wider operating temperature range. The combustion chamber was also designed to interface with the same depolymerisation chamber, nozzle and nozzle block as Ouroboros-1 in order to reduce the cost and manufacturing schedule.

3.3.2 Outer Combustion Chamber

The outer combustion chamber used in the direct fuselage insertion architecture was the same component as the outer shell of the Ouroboros-1 depolymerisation chamber described in Section 3.2.2. The only difference was that both the fuel inlet and outlet were plugged in the Ouroboros-2 and 3 tests and copper gaskets were used at the combustion chamber interface. The partial engine assembly of Ouroboros-2 is shown in Fig. 3.23.

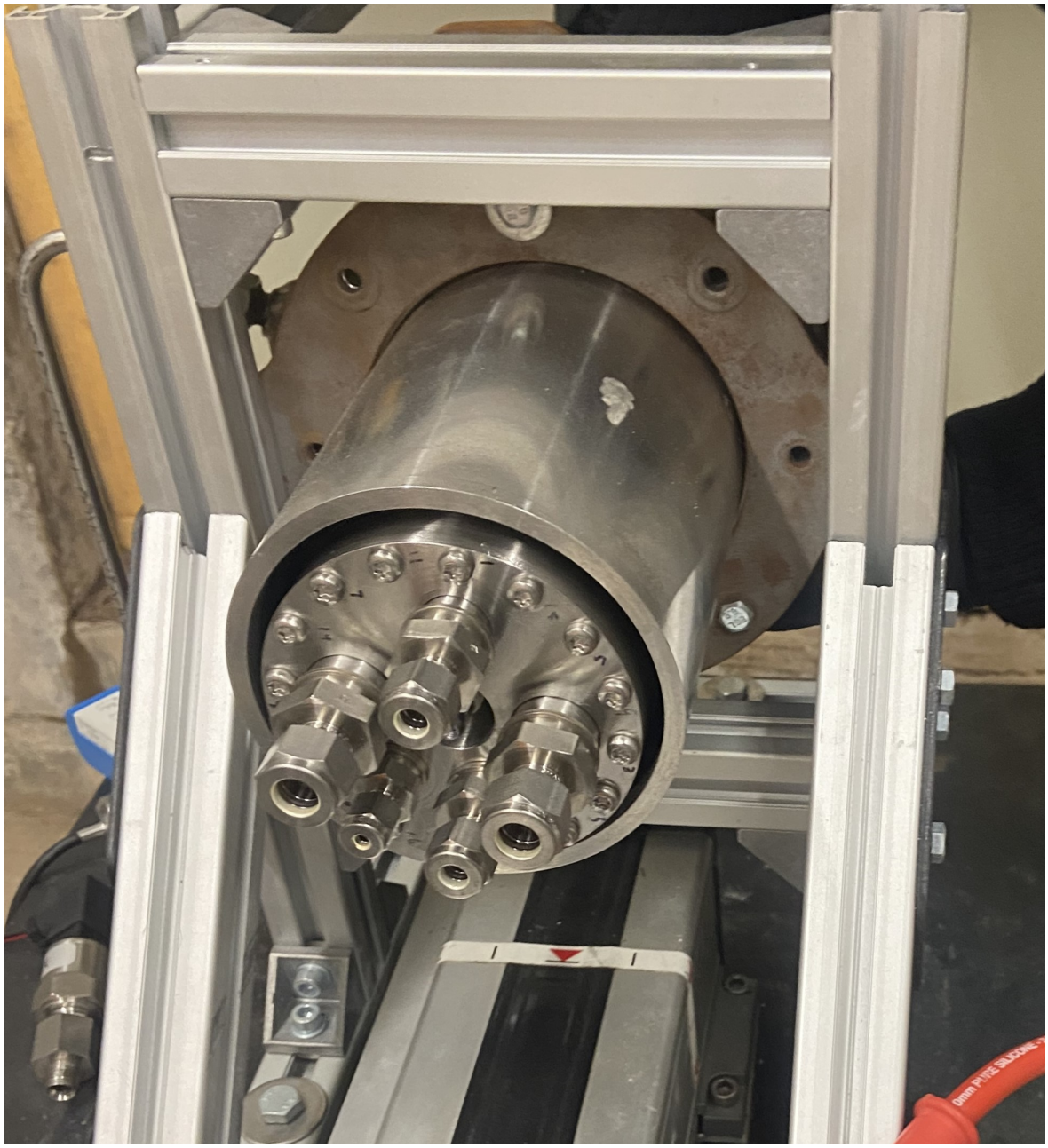

Fig. 3.23 Ouroboros-2 engine integration to the test stand.

3.3.3 Pintle Injector and Propellant Manifolding

Significant changes were made to the propellant injection method between the autophage engine depolymerisation chamber architecture and the direct fuselage insertion architecture. In the first instance, rather than the fuel being injected through sidewall injectors, the direct fuselage insertion architecture necessitated that both the oxidiser and fuel be injected through the injector face. This would require complex machining and manifolding such that the two fluids remained isolated within the form factor until being symmetrically injected into the combustion chamber.

It was determined that an injector design using impinging doublets and triplets was not possible to be machined within budget and time constraints; thus, a different injector design was needed. The proposed change was to use a single variable area (pintle) injector with the igniter placed inside the pintle; an example of a pintle injector is shown in Fig. 3.24. This would offer radially symmetric injection as well as significant face cooling at the injector. Additionally, a pintle injector can offer control over the mass flow rate and mixture ratio of the propellants by moving the pintle element [107, 108]. This can be a particularly valuable tool for autophage engines where adjusting inlet conditions and engine performance can allow for engine throttling [109] and influence the feed rate of the fuselage.

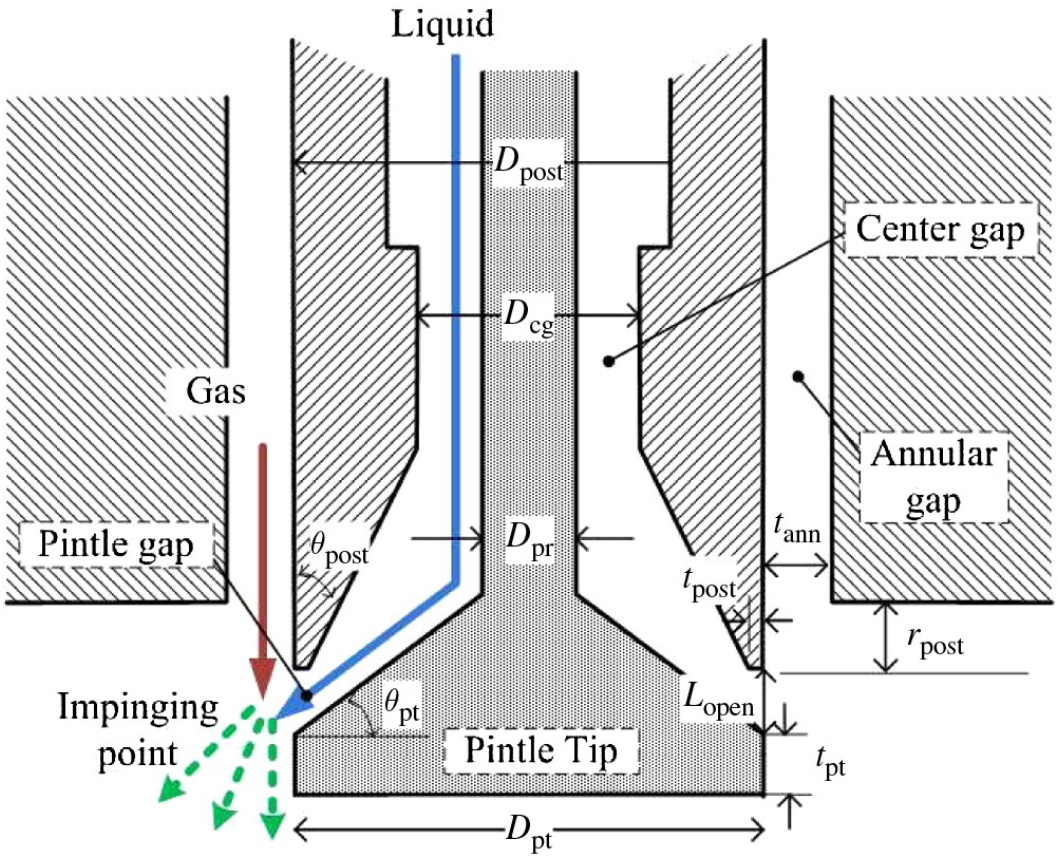

Fig. 3.24 Example of a pintle injector using gaseous and liquid propellants [107].

The pintle injector of the Ouroboros-2 engine was designed using a set pintle diameter and adjusting the pintle and annular gaps in order to provide the required mass flow rates of the propellants. The area of the pintle and annular gaps was determined using the previously mentioned Dyer model (Eq. (3.7)) for the fuel and the single-phase incompressible model

(Eq. (3.5)) for the oxidiser [108] using a discharge coefficient of 0.65 which is consistent with other pintle injectors [110]. It was determined that the fuel would be injected through the pintle gap and the oxidiser through the annular gap as shown in Fig. 3.25. This is considered a fuel-centered pintle injector.

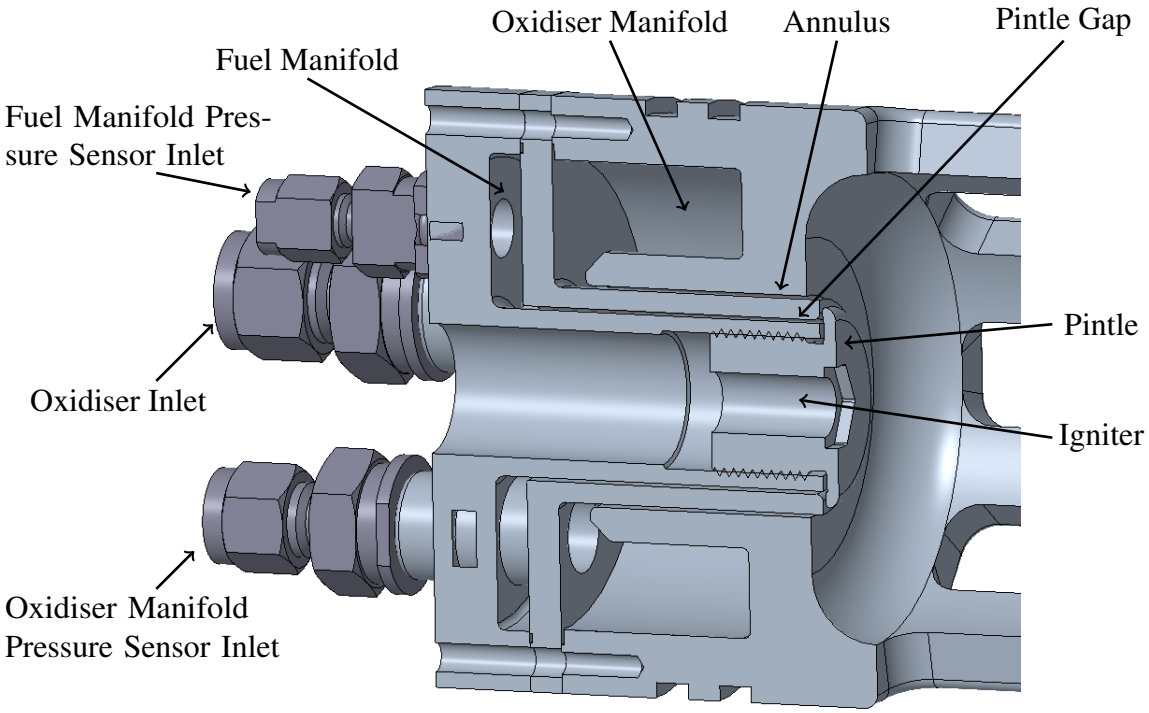

Fig. 3.25 Ouroboros-2 pintle injector assembly CAD model.

This configuration provides multiple benefits to the engine design. First, it results in more complete atomisation of the liquid fuel. By injecting the fuel radially, the pintle creates a thin liquid sheet that collides with the annular gas flow which effectively breaks apart the droplets and atomises the fuel as shown in Fig. 3.26 [111].

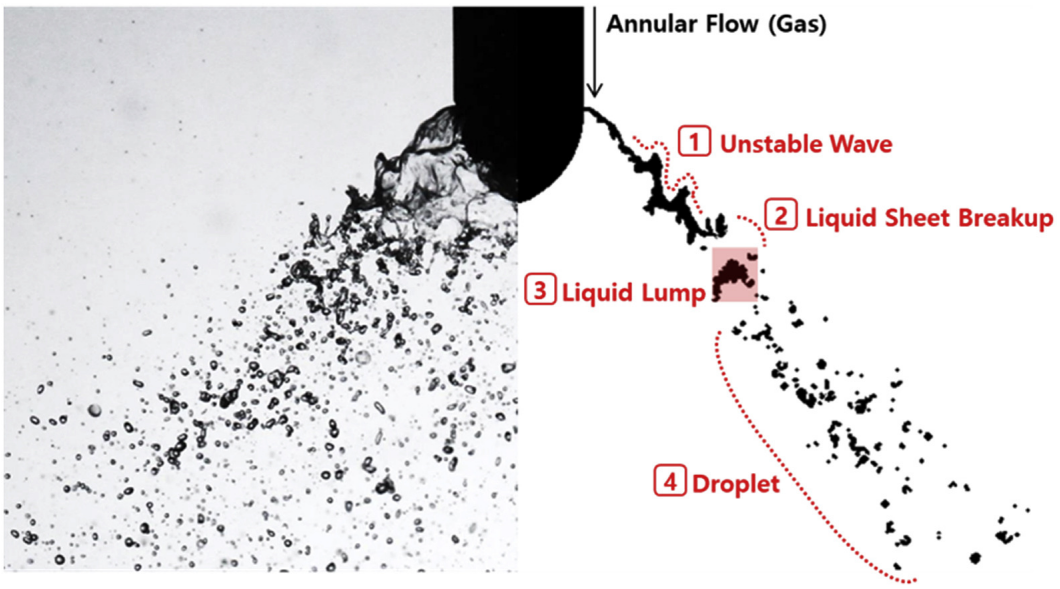

Fig. 3.26 Atomisation process of a pintle injector with a radially injected liquid propellant and a gaseous annular flow [111].

Additionally, in the Ouroboros-2 injector design, the pintle deflects the fuel at a 90 degree angle. Such a sharp angle induces turbulence into the flow which facilitates mixing. The radially injected liquid fuel also contributes to a favorable total momentum ratio (TMR) of the propellants given by Eq. (3.12).

$$TMR = \frac{(\dot{m}v)_{radial}}{(\dot{m}v)_{annular}} \tag{3.12}$$

TMR is a critical parameter of pintle injector performance as it directly influences the spray angle as well as the Sauter mean diameter (SMD) which is a measure of droplet size [112]. A lower TMR correlates with a narrow spray angle and a smaller SMD [111]. For the Ouroboros-2 injector, the TMR was calculated using the propellant mass flow rates and velocities at standard inlet conditions. As can be seen in Table 3.3, the TMR with the fuel at the pintle is significantly lower than if the propellants were reversed.

Table 3.3 Ouroboros-2 pintle injector TMR comparison at standard inlet conditions

Injector path	Propellant	MR	P_c	P_{inlet}	$A_{injector}$	$\dot{m}$	v	TMR	θ
			bar	bar	m^2	g/s	m/s		
Pintle	Fuel	1.00	5.00	6.00	$4.0\ e^{-5}$	37.65	2.40	0.026	9.24°
Annulus	Oxidiser		5.00	6.00	$5.1\ e^{-5}$	37.65	92.3		
Pintle	Oxidiser	1.00	5.00	6.00	$4.0\ e^{-5}$	37.65	92.3	38.5	$\sim 90°$
Annulus	Fuel		5.00	6.00	$5.1\ e^{-5}$	37.65	2.40		

The TMR and SMD are used as the indicator of the quality of atomisation in pintle injectors [113] rather than the Ohnesorge number which is used in orifice injectors. Atomisation and spray angle of pintle injectors are typically either numerically or experimentally derived for specific geometries, inlet conditions, and propellants; however, some generalised models have been developed including the Boettcher model for gas-gas pintle injection [114], the experimentally validated liquid-liquid model derived by Peng et al. [113] as well as the Heister model [115]. For this analysis, the Heister model was used given by Eq. (3.13).

$$\theta = \frac{180}{\pi} TMR^{0.5} \tag{3.13}$$

The result predicts a small angle of 9.24 degrees for the fuel-centered injector while the oxidiser-centered injector approaches a 90 degree angle; near perpendicular to the center axis of the engine. Thus, the fuel-centered design is preferred from an atomisation standpoint and is consistent with other small thrust engines as noted in the *Handbook of Atomization and Sprays* [115].

Additionally, a small spray angle is preferred from a thermal management perspective in order for the bulk of the combustion process to occur in the middle of the combustion chamber. In general, pintle injectors in rocket engines facilitate the creation of two recirculation zones shown in Fig. 3.27. The mantle recirculation zone is typically made up of the propellant injected through the annulus while the core recirculation zone consists mainly of the pintle propellant. The size and composition of these two zones can influence the cooling of both the

injector face and the pintle and is primarily dependant on the spray angle. Additionally, the size of the mantle and core recirculation zones have an inverse relationship such that when the size of one increases the other decreases.

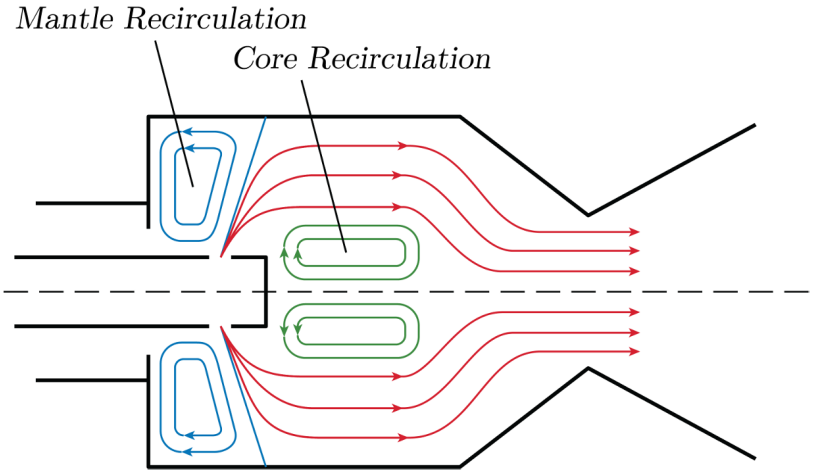

Fig. 3.27 Typical pintle injector engine recirculation zones [116].

Numerical modeling conducted by Min et al. [117] has shown that a large spray angle will create a very small mantle recirculation zone and consequently a large core recirculation zone. Furthermore, such a large spray angle directs the injection streamlines directly at the combustion chamber walls leading to a critically high wall heat load that could lead to an engine burn-through. On the other hand, a small spray angle will expand the mantle recirculation zone and shrink the core recirculation zone. Examples of the streamlines and thermal gradient across three cases of spray angle for a fuel-centered methane pintle injector are shown in Fig. 3.28.

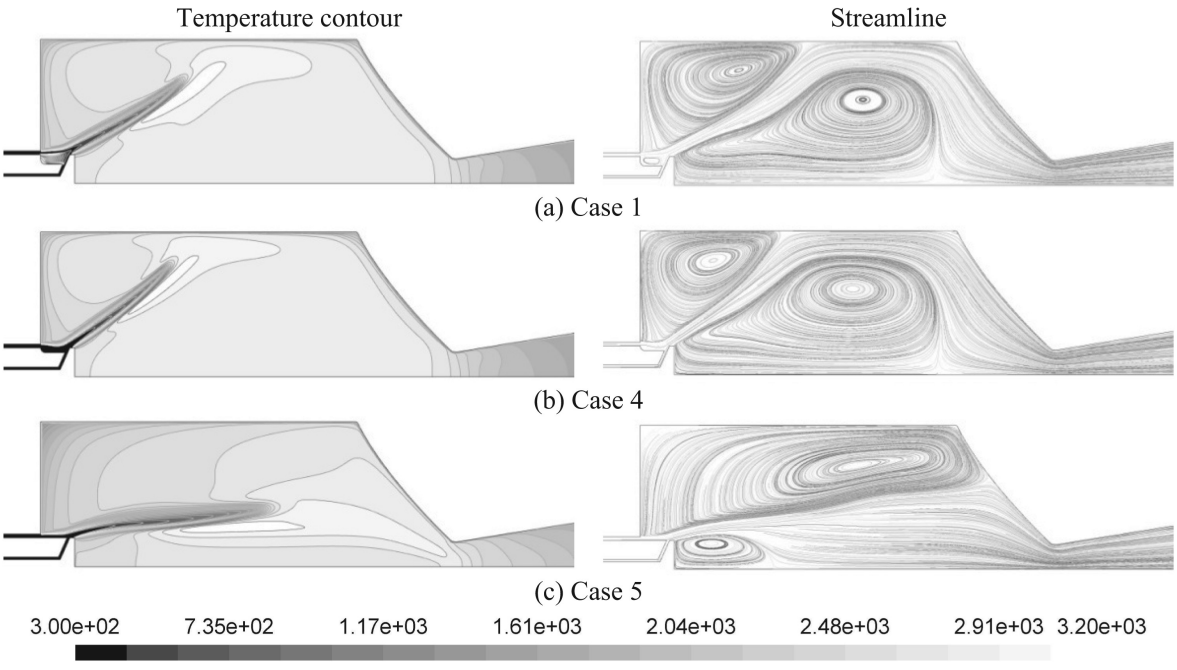

Fig. 3.28 Model of spray angle influence on variation in streamlines and temperature contour of pintle injector combustion chamber flow [117].

No computational fluid dynamics or other first-order modeling was conducted on the Ouroboros pintle injector design due to time constraints to manufacture the engine for experimental testing. The 1-dimensional analysis conducted using the Heister model to determine spray angle was considered to be a sufficient approximation for the pintle injector performance due to its heritage as an empirically validated model [115].

While a small spray angle is preferable for maintaining a favorable chamber wall temperature, it can cause the pintle tip to be prone to overheating due to the core recirculation zone [118]. Additionally, it results in a shorter combustion chamber residence time of the gases which can reduce the combustion efficiency of the engine. Thus, the spray angle can be optimised in a way to maximise the combustion chamber efficiency while maintaining chamber wall temperature below a set constraint; however, doing so was outside the scope of this research and minimising the chamber wall temperature was a priority in order to extend the operating time of the engine. Therefore, a very small spray angle was preferred and selected for the Ouroboros-2 and 3 injector design.

In order to address the risk of the pintle tip overheating, it was made to be as flush as possible with the injector face to limit its exposure to the combustion gases (visible in Fig. 3.25). It was also hypothesized that the relatively large diameter of the pintle compared to the chamber diameter (driven by the igniter diameter) could contribute to a larger core recirculation zone thereby resulting in lower gas temperature at the pintle tip.

Another consideration was the effect that the melting HDPE fuselage would have on the mantle recirculation zone since no previous research into pintle injectors had considered an autophage architecture. Based on the design of the inner combustion chamber detailed in Section 3.3.1, the majority of the HDPE fuel would melt and vaporise downstream of the structural supports and prior to the graphite nozzle insert. Due to the small spray angle, this section of the combustion chamber would be in the mantle recirculation zone meaning that the vaporised HDPE fuel would be traveling upstream along the mantle zone streamlines in Fig. 3.27. This could change the shape of the streamlines as well as the temperature contour since the HDPE mass flux would theoretically contribute to combustion within the mantle recirculation zone; corresponding to an increase in wall temperature at the combustion chamber structural supports. This hypothesis was the leading rationale in the design of the Ouroboros-3 pintle injector which was a modified design from Ouroboros-2.

The only difference in the new injector design was the introduction of channeling into the annulus which would block off the flow of oxidiser corresponding to the locations of the inner combustion chamber structural supports as shown in Fig. 3.29.

In typical fuel-centered pintle injectors, it is often the pintle tip that is channeled rather than the annulus, this allows for the TMR of the fuel to be increased such that it can penetrate the axial oxidiser annulus sheet and impact the wall in order to provide film cooling [115]. As discussed in Section 3.3.1, film cooling is a mechanism for providing a boundary layer (film) along the chamber wall in order to limit the exposure of the chamber to the combustion gases. Even minor increases in the percentage of film coolant used can significantly reduce the maximum chamber wall temperature while only slightly reducing the characteristic velocity of pintle injector engines [119].

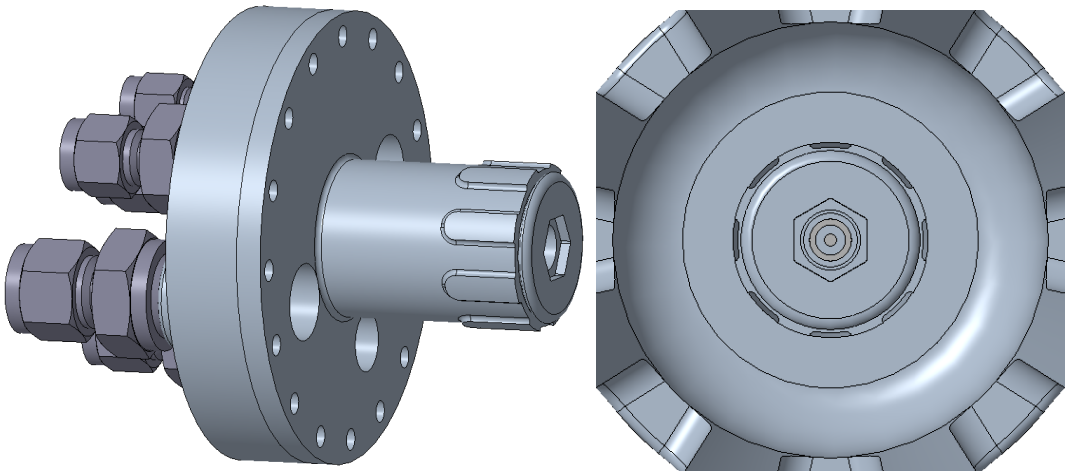

(a) (b)

Fig. 3.29 Ouroboros-3 pintle injector assembly model.

However, for the Ouroboros-3 injector design, the fuel injection velocity is unable to reach sufficient values to increase the TMR enough to penetrate the oxidiser sheet. Thus, the oxidiser annulus has been blocked using a blocking factor of 0.5 in order to permit fuel penetration and film cooling along the combustion chamber structural supports. The resulting TMR and spray angle are given in Table 3.4.

Table 3.4 Ouroboros-3 pintle injector TMR and θ at standard inlet conditions

Injector path	Propellant	MR	P_c	P_{inlet}	$A_{injector}$	$\dot{m}$	v	TMR	θ
			bar	bar	m^2	g/s	m/s		
Pintle	Fuel	1.00	5.00	6.00	$4.0\ e^{-5}$	37.65	2.40	0.013	6.54°
Annulus	Oxidiser		5.00	6.00	$2.55\ e^{-5}$	37.65	184.6		

In order to ensure uniform flow through all orifices for both injector designs, propellant manifolds were used. Propellant manifolding is a standard practice for most injector designs as it allows for even distribution of the propellants across the injector [110]. The propellant manifolds can be seen in Fig. 3.25. The interfaces between these manifolds were sealed using annealed copper gaskets. Additionally, both the oxidiser and fuel manifold used pressure sensors to monitor and record the propellant inlet pressures.

3.3.4 Nozzle and Nozzle Block

There was no change to the nozzle contour or the nozzle block design used in Section 3.2.4 except for the removal of the seal grooves on the exterior of the graphite nozzle insert. Seals between the nozzle block and combustion chamber were replaced with copper gaskets due to the higher temperature range of copper; these gaskets were annealed prior to installation.

3.3.5 Igniter

There was no major changes to the design of the igniter and ignition system from Section 3.2.5. However, the ignition circuit reliability was improved by using a printed PCB as shown in Fig. 3.31; the circuit schematic remained the same.

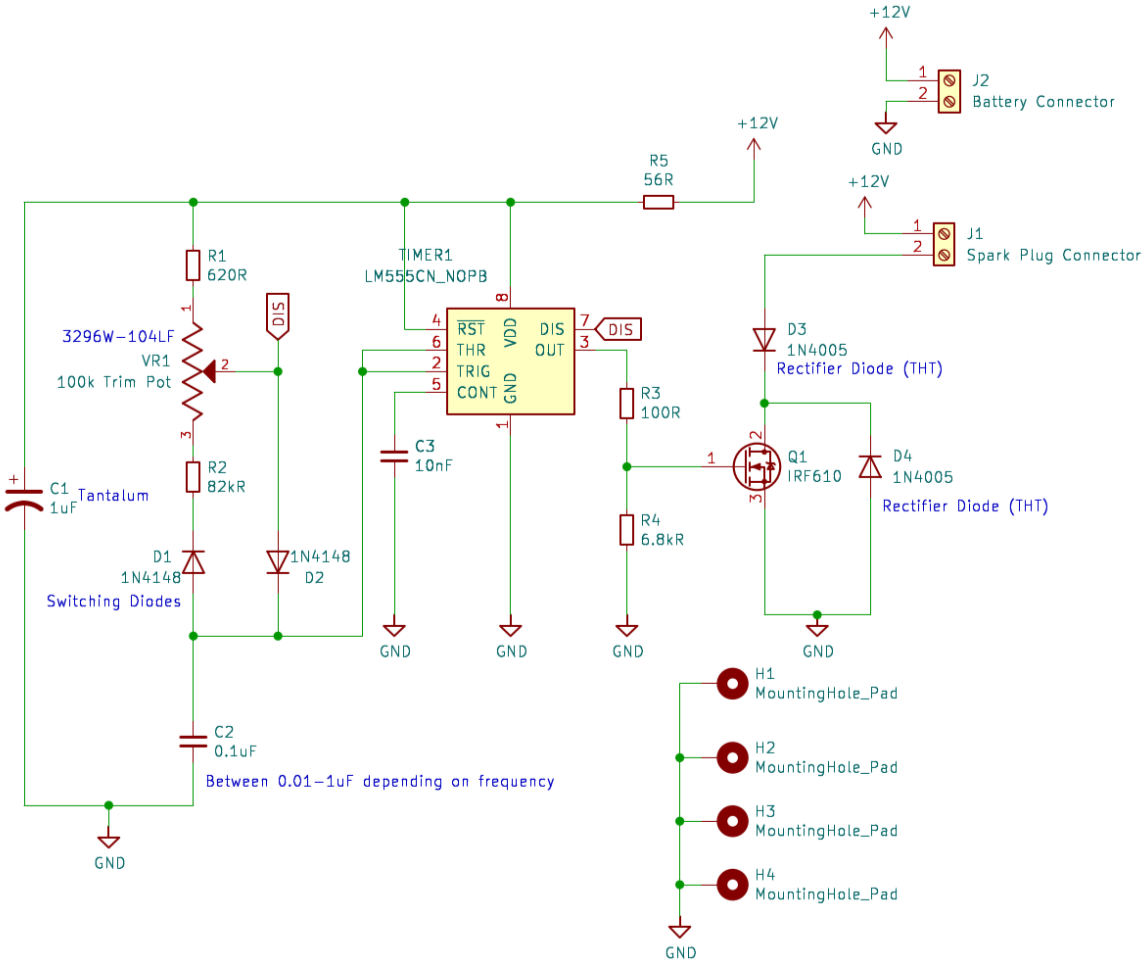

Fig. 3.30 Ignition circuit PCB schematic

Fig. 3.31 Printed PCB of the ignition circuit.

Chapter 4

Test Apparatus and Experimental Setup

The unique conditions required for autophage engine operation necessitated the development of a custom test stand that could support both a linear feed force to drive the HDPE fuselage into the engine while still being able to measure resulting engine thrust. No such test facilities or capabilities previously existed in the UK and so the test apparatus was developed as part of this research programme. The following sections detail the test facilities, Khepri test stand, propellant feed system, instrumentation, and data acquisition system which were designed and developed for the express purpose of testing the Ouroboros autophage engines.

Additionally, the Ouroboros autophage engines were tested across a range of general test conditions and specialised conditions which were used to characterise the performance within a wide operating box. These test conditions and the rationale behind selecting them are detailed herein.

4.1 Test Facilities

All experimental test campaigns were conducted at Machrihanish Airbase facilitated by Discover Space UK Ltd. and Machrihanish Airbase Community Company. The research programme consisted of three separate test campaigns which operated the Ouroboros-1, 2, and 3 engines at a range of test conditions. The test campaigns were as follows:

1. June 6 to 9, 2022 (Ouroboros-1)
2. February 13 to 17, 2023 (Ouroboros-2 and Ouroboros-3)
3. July 10 to 14, 2023 (Ouroboros-3)

Machrihanish Airbase was selected as an ideal testing location due to being an ex-Royal Air Force military base with a substantial amount of suitable and empty infrastructure in a remote location. The first test campaign was conducted in a temporary test facility while later test campaigns were moved to the MachLab Propulsion Test Facility which consisted of modified infrastructure to accommodate experimental propulsion system testing on a permanent basis at the airbase.

4.1.1 Temporary Test Facility

The first test campaign (conducted from June 6 to 9, 2022) operated the regeneratively cooled Ouroboros-1 engine in the bi-propellant configuration. These tests were conducted at the 076 Refueling Vehicle Shelter (RVS) shown in Fig. 4.1.

Fig. 4.1 076 Refueling Vehicle Shelter (RVS) used as a temporary propulsion test facility.

The engine was assembled and tested outside the shelter with a safe distance of well over 100 m from any occupied buildings. All personnel, as well as the data acquisition and control systems, were located inside the shelter. This allowed for a minimum length of data cables and propellant feed system tubing to be used. This was a temporary test facility which required all equipment to be assembled on-site at the start of the test campaign and disassembled at its conclusion. For this reason, the test stand, data acquisition, and control systems, were developed to be mobile as well as to fulfill their performance requirements.

4.1.2 MachLab Propulsion Test Facility

The subsequent test campaigns were conducted at the newly built MachLab Propulsion Test Facility shown in Fig. 4.2 which was developed jointly by the University of Glasgow and Discover Space UK Ltd. under a UK Space Agency grant in order to create a permanent location for experimental propulsion system testing. Similar to the temporary facility, all test equipment was still assembled and disassembled during the course of each test campaign; however, using a facility with a fixed layout allowed for quicker assembly and the dedicated test chamber reduced the risk of testing being impacted by weather conditions.

The facility consisted of a test chamber where the test stand, propellant feed system, and engine were mounted and a separate control room where the control systems and the test operators were located (Fig. 4.3). The propellant run tanks were located in the test chamber annexe (outside of the main test chamber). This provided another layer of separation from the engine and test operators. All data transfer from the test instruments was conducted using hardwired connections from the test chamber to the control room. Downstream of the test chamber, the area was covered with gravel and included a berm in order to reduce the risk of

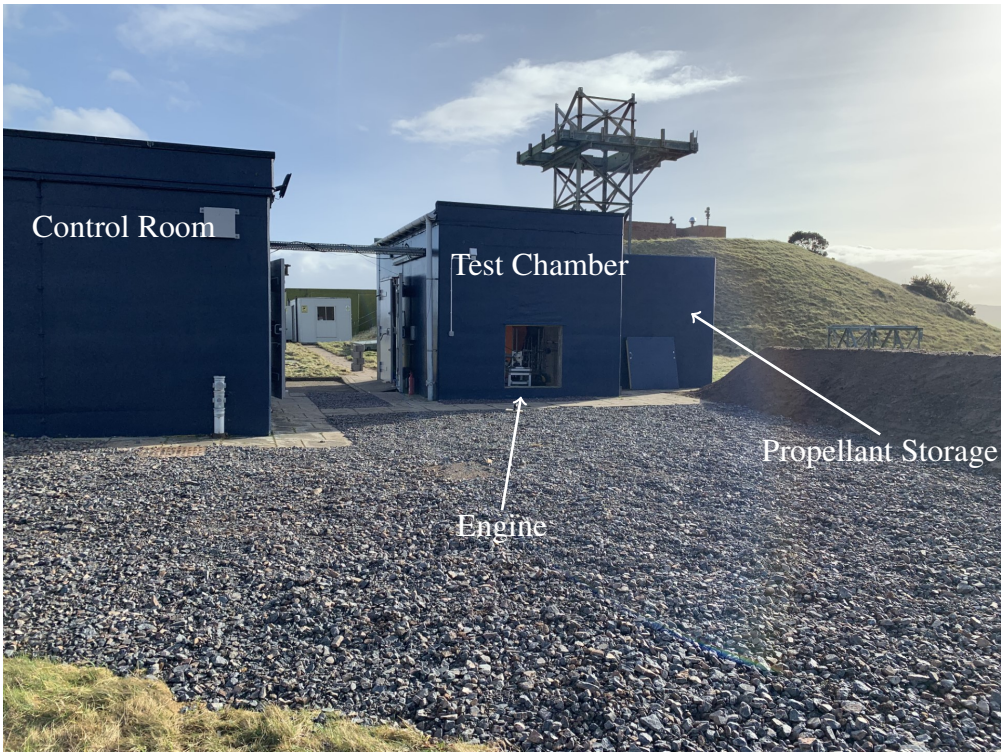

Fig. 4.2 MachLab propulsion test facility with test chamber and control room building.

debris, fire and noise. Additionally, the entire area was secured behind a locked security fence to prevent unauthorised personnel from accessing the area.

Fig. 4.3 Inside view of the MachLab propulsion test facility control room.

The new facility coupled with the multiple layers of reinforced concrete between the test chamber and control room offered a safe environment to test the experimental autophage engines at both nominal and off-nominal conditions. This allowed the later tests of the Ouroboros-3 engine to intentionally test the system to destruction in order to push the operating limits leading to a better understanding of the performance and parameters of successful autophage engine design.

4.2 Test Stand

Due to the unique architecture of operating an autophage engine, a dedicated test stand was required to be built. This was done in order to have a method of exerting a large force on the engine while isolating and maintaining a method for measuring the resulting engine thrust.

This was done by separating the test stand into two sections: the engine mounting platform and the frame structure. The engine mounting platform was designed as a rigid body where both the engine and a linear actuator could be mounted with enough length to accommodate a 1 m long HDPE fuselage. Thus, the linear actuator would be capable of exerting a force on the engine fuselage while the entire mounted assembly remained stationary; feeding the HDPE fuselage into the engine. This force was controlled by specifying the current provided to the linear actuator from the data acquisition and control systems. The engine platform could then be mounted to the main structure using linear bearings with a load cell at the interface. Thus, allowing engine thrust to be measured. The specifics of the test stand were designed, built, and acceptance tested as part of an associated Masters in Engineering project by Jack Tufft [120]. The final CAD model and integrated assembly of the test stand is shown in Fig. 4.4.

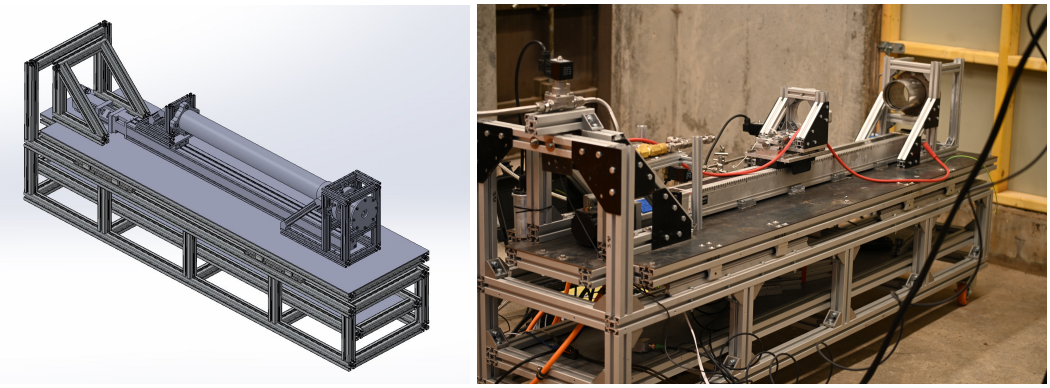

(a) (b)

Fig. 4.4 Test stand (a) CAD model and (b) integrated assembly.

4.2.1 Frame Structure

The test stand frame was constructed from Matara 45x45 aluminium extrusion [121] to provide a lightweight but stiff structure. It was comprised of a cuboid structure of beams, reinforced at intervals along its length of 2 meters. This length was selected to provide an adequate distance to both mount the engine, linear actuator and provide sufficient HDPE fuselage feed to reach a minimum test time of 60 seconds. The frame was mounted on wheels to provide mobility at the test facility; during hot-fire tests, brakes were applied to prevent the test stand frame from moving (no movement was observed throughout the campaigns). Linear bearing rails were fastened to the frame to provide a frictionless interface between the frame and the engine mounting platform.

4.2.2 Engine Mounting Platform

The engine mounting platform has been designed as a rigid body allowing both the engine and linear actuator to be fastened to it. This allows the linear actuator to exert a feed force on the engine fuselage without influencing thrust measurement. The platform is constructed from Matara 45x45 aluminium extrusion to provide a stiff frame structure topped with a 3 mm thick sheet of S275 low carbon steel; providing a flat platform for fastening equipment. Linear bearings are secured to the bottom of the platform to interface with the rails on the test stand frame.

4.2.3 Linear Actuator Driven Fuselage Feed

The engine fuselage feed force was provided by a *Heason* 207-08831 ball guided, screw driven linear actuator that was powered by a servo motor and controlled by a *Kollmorgen* PCMM controller. The linear actuator assembly was selected due to its capability of providing up to 2 kN of force with a capability of reaching a linear speed of up to 0.1 m/s. This was sufficient margin to provide both the maximum feed force and feed rate. This system was used to provide the required feed force for the Ouroboros-1, 2, and 3 engine designs for all test campaigns.

4.3 Propellant Feed System

The propellant feed system was designed to be a self-pressurised gaseous oxygen and pressure regulated liquid propane blowdown system. The overall objective was to provide the propellants across a range of inlet pressures and mass flow rates in order to test the autophage engines at various operating conditions. Additionally, the feed system was designed to hold enough propellant to continuously operate for up to 120 seconds with precise control over rapid-response control valves in order to have the capability of testing the engines in a pulsed operating mode as well as in continuous steady state. The design requirements and resulting system capabilities are listed in Table 4.1.

Table 4.1 Earth-storable propellant feed system capabilities.

Capability	Value
Operational thrust range	0-500N
Available oxidizers	Gaseous Oxygen
Available fuels	Liquid Propane
Operating temperature range	-10°C to 40°C
Maximum oxidizer delivery pressure	30 bar
Maximum fuel delivery pressure	30 bar
Maximum oxidizer delivery flow rate	150 g/s
Maximum fuel delivery flow rate	75 g/s
Oxidizer pressurization method	Self pressurized oxygen tanks
Fuel pressurization method	Dry nitrogen pressurization blowdown
Maximum oxidiser storage mass	20kg
Maximum fuel storage mass (propane)	10kg
Maximum run time	120 seconds
Pressure regulation	Manual spring-loaded pressure regulators
Mass flow rate regulation	Manual needle valves
Valve control	Solenoid actuated

In addition to the oxidiser and fuel propellant lines there is also a nitrogen pressurisation line in order to provide the blowdown pressure to deliver the liquid fuel at high pressure. A separate inert nitrogen line is also used to provide purge gas to both the oxidiser and fuel lines; this is a safety feature in order to be able to both flush the engine with inert nitrogen prior to testing and to also purge the lines of all propellants at the end of the test (or in the event of an emergency stop).

The final piping and instrumentation diagram of the propellant feed system is shown in Fig. 4.5; the oxidiser line is shown in blue, fuel line in red, and inert nitrogen lines in gray. Each of the lines was outfitted with standard components detailed in the following sections.

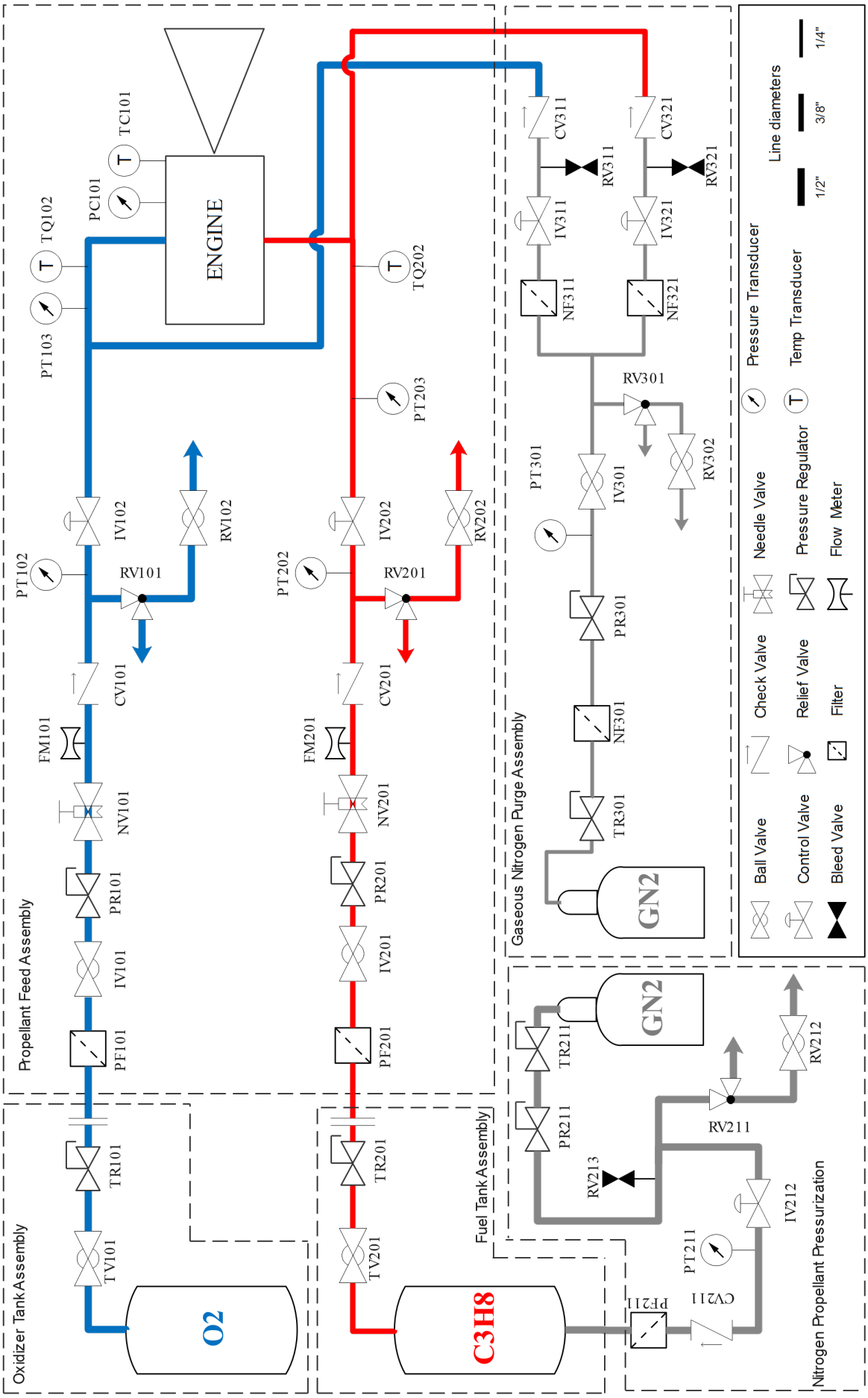

Fig. 4.5 Propellant feed system piping and instrumentation diagram

Gas Panels

Both the pressure regulators and needle valves (used for mass flow rate regulation) were mounted on a gas panel in order to provide a central location for the operator to set the engine inlet conditions from. The gas panels are shown in Fig. 4.6. Also visible in the figure are some of the other feed system components including the solenoid control valves and flow meters. Each of the lines connects to the test stand using flexible hoses to reduce thrust measurement error due to spring, inherent in standard tubing.

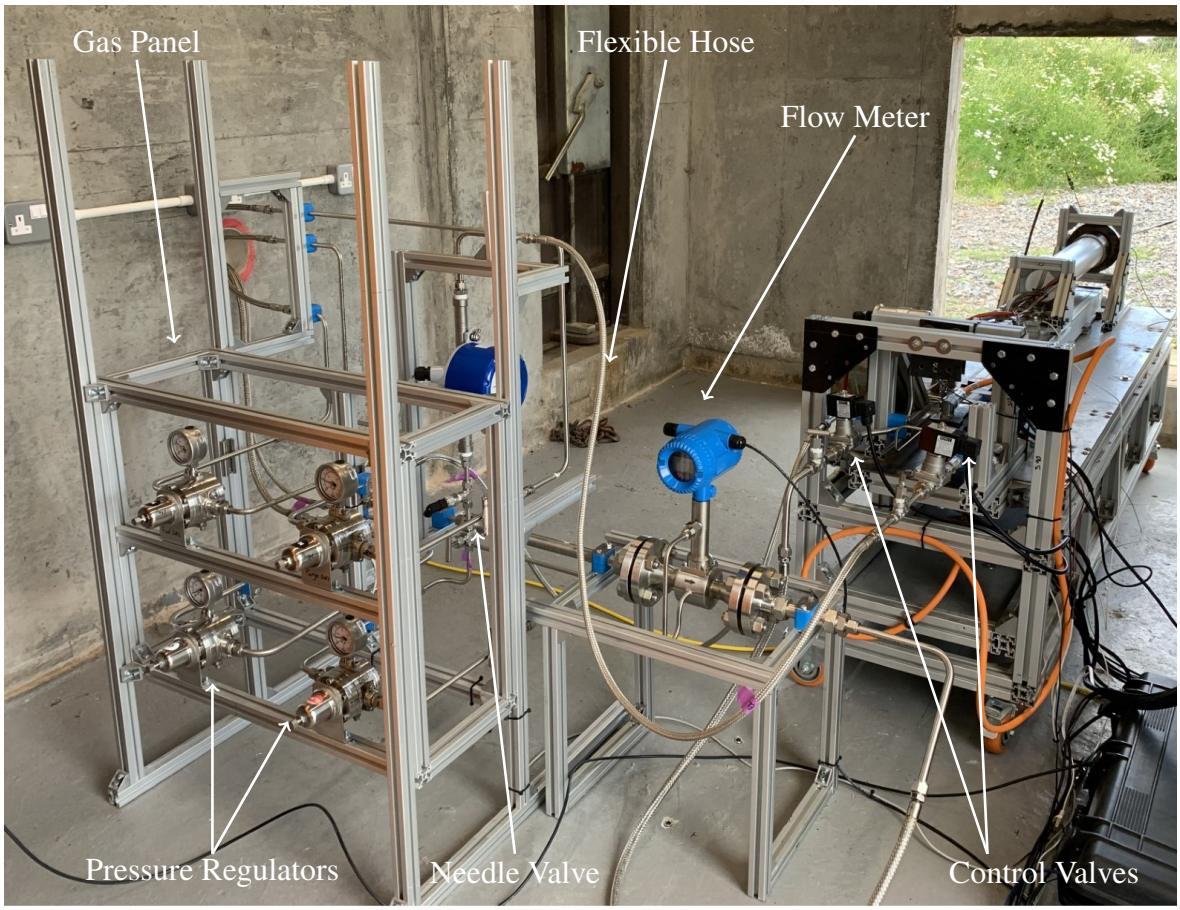

Fig. 4.6 Propellant feed system gas panels.

Pressure Regulation

The feed system utilizes in-line spring loaded pressure regulators to monitor and regulate propellant pressure directly. These are preset to the desired pressure using the analog pressure gauges by the operator prior to test start.

As mentioned, the gaseous oxygen propellant tank was self-pressurised and the propellant line was pressure regulated upstream of the engine inlet. This allowed for manual setting of the desired engine inlet pressure in order to deliver the oxidiser at a constant pressure. On the other hand, the liquid propane fuel used a blowdown system whereby the run tank was pressurised using inert gaseous nitrogen and liquid propane was extracted from the run tank at high pressure using a dip tube.

A potential challenge with such blowdown systems is that the liquid fuel can drain from the run tank at a higher mass flow rate than the pressurising gas can fill the volume while

maintaining a steady pressure. Therefore for this system design, the propane run tank was designed to be pressurised up to 50 bar using pressure regulated gaseous nitrogen flow and the fuel output was again pressure regulated upstream of the fuel engine inlet. This allowed for the fuel inlet pressure to be maintained throughout the required run time duration of 120 seconds.

Mass Flow Rate Regulation

In order to vary the oxidiser to fuel mixture ratio of the engines, the propellant feed system required a method for controlling the mass flow rate in addition to the inlet pressures. This was done using manual needle valves located downstream of the pressure regulators. Of course, using a needle valve to adjust the orifice area in a propellant line will cause a pressure drop and change the engine inlet pressure if the pressure regulator setting remains constant.

Since both the pressure regulators and needle valves needed to be manually set prior to test start this introduced a source of error in achieving the desired engine inlet conditions. Therefore the inlet conditions describe in Section 4.5 were considered targets rather than requirements to be met. However, the inlet pressures and mass flow rates were heavily varied during the Ouroboros-2 tests in order to provide an accurate estimation of the gas panel settings to deliver the propellants at the desired inlet conditions.

Control Valves

The propellant feed system used solenoid controlled ball valves in order to provide rapid response time control of the engine. These were controlled via the data acquisition and control system detailed in Section 4.4. The solenoid valves and the control system allowed for both manual control over the valves and ignition circuit as well as pre-programmed operation; this capability correlated with the ability to both operate the engines in continuous steady state as well as pulsed operating modes at a desired frequency and duty cycle.

Check Valves

The feed system was outfitted with check valves at key locations on the propellant lines in order to prevent any backflow of the propellants or gases. This would reduce the risk of an engine failure propagating upstream through the propellant feed system.

Isolation Valves

Each propellant line utilised a manual ball valve as an isolation valve which was used as a safety measure to prevent accidental propellant delivery to the engine until the operators were ready for test start at which point the isolation valves were opened.

Pressure Relief, Vent, and Bleed Valves

To both prevent over-pressurisation of the propellant lines, and create a way to vent the propellant lines, pressure relief and vent valves were implemented on each line. An additional

pressure relief and vent valve were also located at the depolymerisation chamber for the Ouroboros-1 engine design to prevent over-pressurisation of the fuel inlet. Bleed valves were used immediately before the solenoid actuated control valves in order to fill the propellant lines with propellant and allow any residual purge gases to escape from the lines prior to engine start. This would reduce the engine start transient by minimising the line length required for the propellants to travel before reaching the engine.

Piping, Hoses, Filters and Fittings

The feed system was constructed using 316 stainless steel tubing in order to meet material compatibility of both propellants and used a combination of standard twin-ferrule compression, NPT, and BSPP fittings at each component interface. Delivery of the propellants to the test stand platform and engine was performed using stainless steel braided flexible hoses to effectively eliminate the effect of spring constant in the propellant lines when measuring engine thrust. Filters were fitted at the outlet of each propellant tank in order to remove any debris which could cause blockages or damage to any of the feed system components.

4.4 Instrumentation and Data Acquisition and Control System (DACS)

The instrumentation and data acquisition and control system, or DACS, was specifically developed to meet the needs of the autophage engine hot-fire tests. This included the capability to remotely control the engine operation and measure certain performance parameters. In order to precisely characterise the engine performance a minimum number of parameters were required to be measured including: thrust, inlet pressures, combustion chamber wall temperature, combustion chamber pressure and fuselage feed rate.

Over the course of the three test campaigns, additional instrumentation was added and the capabilities of the DACS were improved due to lessons learned. The following sections detail the evolution of the DACS throughout the course of the research.

4.4.1 Baseline Test Campaign (Ouroboros-1)

The baseline DACS (Fig. 4.7) was designed to interface with both the propellant feed system control valves, ignition, and instrumentation. Control of the solenoid valves and ignition circuit was performed through a *Raspberry Pi* controller which operated a relay switch, providing power to the systems when required. The control system was designed such that the propellant control valves would fail closed and purge valves would fail open in the event of a control system failure to be able to safely shut off the engine.

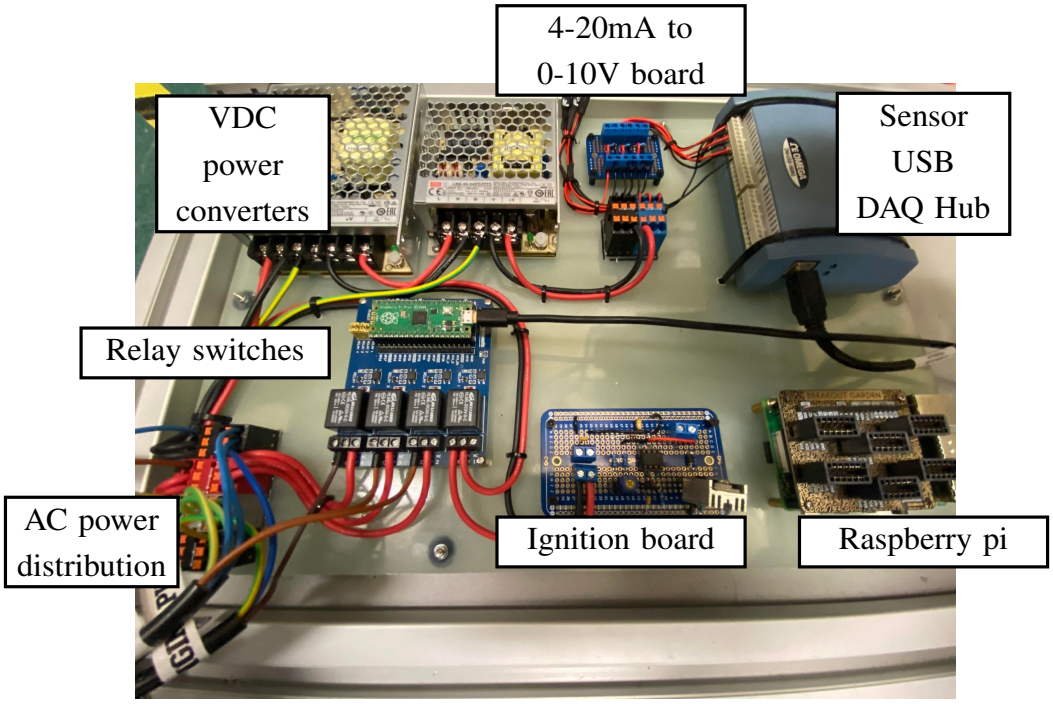

Fig. 4.7 First iteration of the data acquisition and control system.

To power the instrumentation and ignition circuit, VDC power converters were used to supply both 12 and 24 VDC where required. The various instruments used to measure engine performance had a variety of outputs including charge, 0-10V, and 4-20mA outputs. The charge outputs were converted to 0-10V output using charge amplifiers and the 4-20mA outputs were converted to 2-10V via a current signal to voltage output conversion board. This standardised the instrument output to be compatible with 0-10V data collection and used an OM-USB-1608G hub connected to the control room. With this setup, a maximum of 8 differential channels of up to 250,000 combined samples per second with a live remote data display were able to be operated during the tests. Data recording and display was performed using *DAQami* data acquisition companion software.

The only instrumentation that did not use the USB hub were the engine thermocouples. These were connected to thermocouple junctions that interfaced with the *Raspberry Pi* controller for the Ouroboros-1 tests and a dedicated USB thermocouple converter that connected directly to the control room for subsequent tests.

Control System Graphic User Interface

In order to control the engine valves and ignition a program was written using *LabVIEW* [122] which was uploaded to the *Raspberry Pi* mounted on the DACS. This allowed the system to be both manually controlled or with a pre-programmed frequency and duty cycle for pulsed mode operation. The graphic user interface of the program is shown in Fig. 4.8. This was done to minimise the complexity of the system during active hot-fire testing to reduce the likelihood of operator errors occurring that could otherwise damage the engine or influence the data.

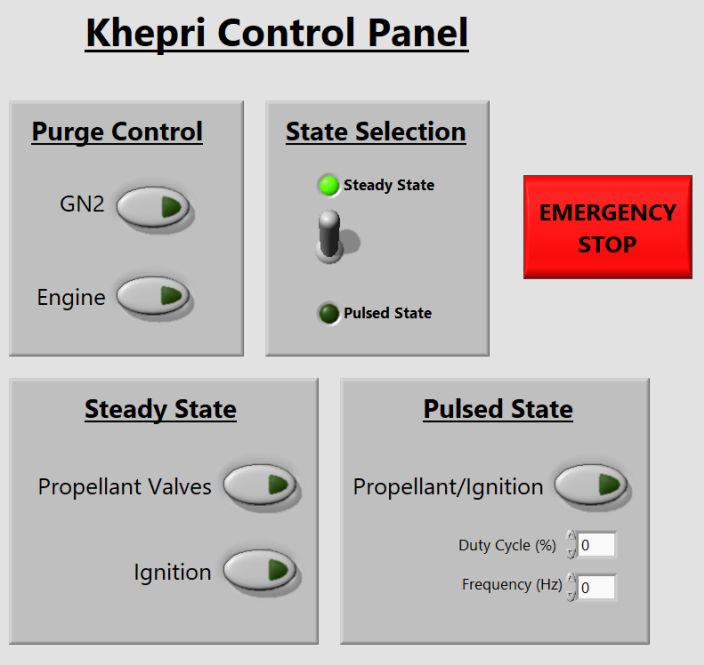

Fig. 4.8 Data acquisition and control system user interface in LabVIEW.

Linear Actuator Control and Feed Force Measurement

The linear actuator, which delivered the fuselage feed force, was controlled using a separate controller that interfaced with *Kollmorgen Workbench* software [123] and allowed the operator to control the amount of current supplied to the actuator servo motor. This supplied current range was calibrated to correlate with the desired feed force that the actuator would exert on the fuselage. This system was connected to the control room using RJ45 connections and a CAT6 network cable. The feed force measurement was done using a Burster 8477 force transducer located at the linear actuator and engine fuselage interface.

Pressure Measurement

Pressure measurement of both the propellant inlets and the combustion chamber are some of the most useful parameters to evaluate propulsion system performance. Oxidiser inlet pressure was measured using an Omega PX119-300AI resistive pressure sensor due to compatibility with oxygen and no requirement for high temperature use. The depolymerisation chamber pressure was measured using a Kistler 4260A piezoresistive sensor due to likely exposure to a higher temperature range. Finally, a Kistler 601CAA piezoelectric sensor was used to measure combustion chamber pressures. This sensor was selected due to its high operational temperature range of up to 350°C and the capability of recording data at sampling rates of up to 20 kHz. The pressure transducer was fixed to the engine using 1/8-inch stainless steel instrument tubing for a total standoff distance of 150 mm to reduce the temperature at the pressure transducer interface to below 350°C. This method of incorporating a standoff distance to reduce the temperature experienced by the pressure transducer is standard practice; however, this strategy does have the disadvantage of delays in pressure propagation [124]. The high sampling rate of the selected Kistler 601CAA sensor was critical in detecting high frequency combustion instabilities.

Temperature Measurement

Two K-type thermocouples were used for the Ouroboros-1 engine with one located at the depolymerisation chamber wall and one at the combustion chamber wall. Each thermocouple was an Omega TJ1-CAXL capable of operating up to 1335°C. The thermocouple locations were selected to verify the temperature in the depolymerisation chamber being sufficiently high to melt the HDPE fuselage and to compare the experimental combustion chamber wall temperature to the predicted temperature based on the thermal model in Fig. 3.7.

Thrust Measurement

The engine thrust was measured using a piezoelectric HBM U9C force transducer. This load cell was mounted at the interface between the engine mounting platform and the frame structure as shown in Fig. 4.9. Treating the engine mounting platform as a rigid body, the resulting engine thrust would drive the platform into the test stand frame allowing thrust measurement while the linear actuator was also being capable of exerting a feed force on the engine.

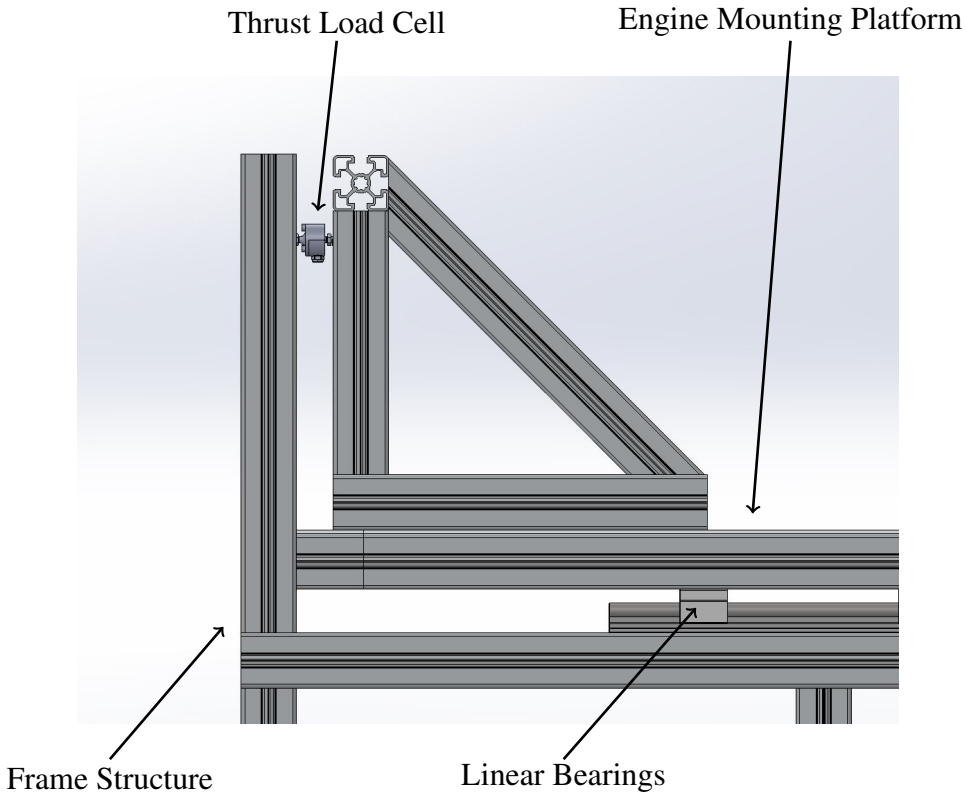

Fig. 4.9 View of the thrust load cell mounting location on the test stand.

A minor issue observed with this setup was that a linear oscillation of the platform was observed at engine ignition which dampened out within 1 second. For continuous steady state tests this did not impact the measurement of engine performance; however, it did impact the thrust measurement in later pulsed operating mode tests. The analysis of the pulsed mode operation includes filtering out this harmonic since it is a result of the method of which the thrust cell was attached to the test stand structure and engine mounting platform. Future tests, should include a method of reducing or dampening this oscillation.

Sampling Frequency

Temperature data was taken at a sampling frequency of 1 Hz due to not being susceptible to high frequency oscillations. All other data was taken at a sampling frequency of 1 kHz; this encompassed the frequency range needed to detect low-frequency combustion instabilities such as chug which could be an indicator of coupling or issues between the engine and propellant feed system [125].

4.4.2 Second Test Campaign Modifications (Ouroboros-2 and 3)

Following the Ouroboros-1 test campaign multiple modifications were made to the DACS assembly in order to facilitate a faster setup time. A control box was designed and built which offered IEC connector plugs for power distribution, M12 connectors for sensor connections, and data output connectors. The resulting DACS control box is shown in Fig. 4.10. In addition to reducing setup time, these quality of life changes to the DACS reduced the risk of operator error connecting the sensors incorrectly. These changes were a direct result of the lessons learned from the Ouroboros-1 test campaign whereby the combustion chamber pressure sensor failed and resulted in a skewed result for other sensors.

Besides the quality of life changes to the DACS control box, the thermocouples from the depolymerisation chamber was removed and mass flow rate meters were added in order to measure flow rate data of the propellants. An optical camera was also used in order to provide a method of measuring the HDPE fuselage feed rate for the Ouroboros-3 tests. All other instrumentation and settings remained consistent with the previous test campaign.

Fig. 4.10 Second iteration of the DACS control box.

Temperature Measurement

The thermocouple located at the depolymerisation chamber was removed for the direct fuselage insertion Ouroboros-2 and 3 engine test campaigns. This was done because in this architecture, there is no separate depolymerisation chamber/regenerative cooling channels; just the combustion chamber wall temperature was needed to evaluate the effectiveness of the HDPE film cooling and pintle injector film cooling.

Mass Flow Rate Measurement

In order to better evaluate engine performance and verify the mixture ratio during testing, flow meters were implemented on both the gaseous oxygen and liquid propane propellant lines. Both the oxidiser and fuel lines each used a Swagelok variable area VAF-M4 meter calibrated for each medium. Unfortunately, the oxidiser flow meter was improperly sized and was not used during the test campaign.

HDPE Fuselage Feed Rate Measurement

To measure the HDPE fuselage feed rate, an optical camera was mounted for a side view of the test stand and marks were placed at 1 cm intervals along the linear actuator. Thus, as the linear actuator inserted the fuselage into the engine the recorded video could be used to provide the feed rate (and by extension the HDPE mass flow rate) during data analysis after the test. This side view is shown in Fig. 4.11.

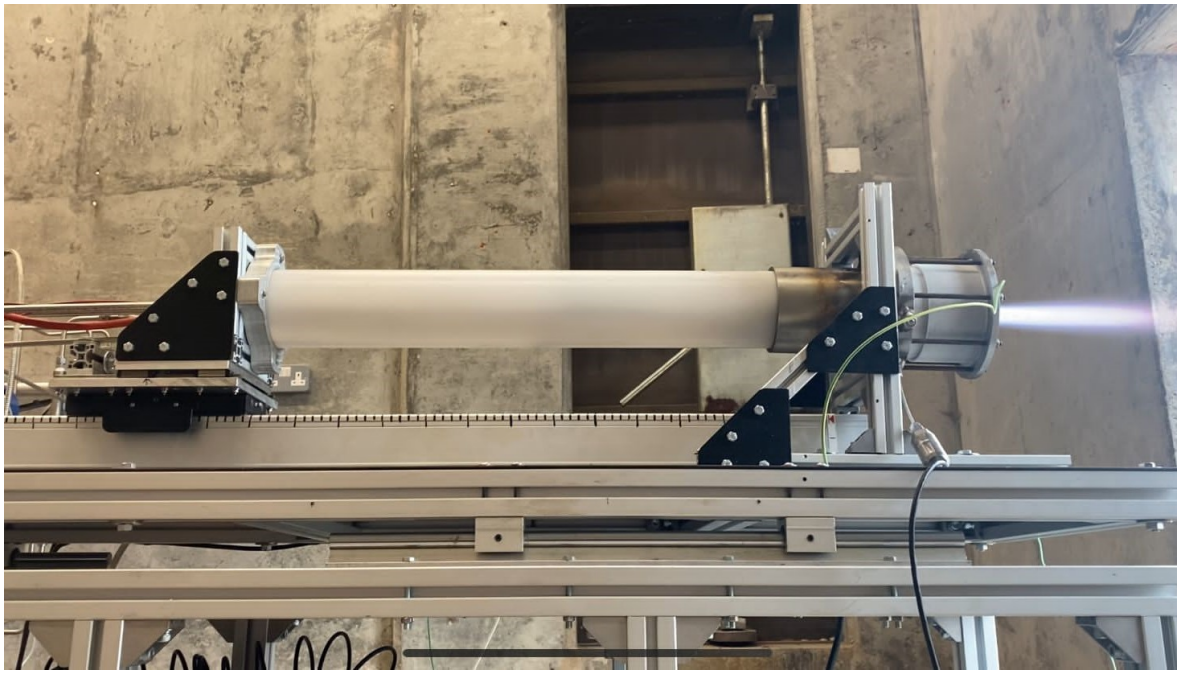

Fig. 4.11 Side view of the Ouroboros-3 engine showing 1 cm markings on the linear actuator used to measure HDPE fuselage feed rate.

4.4.3 Third Test Campaign Modifications (Ouroboros-3)

No major modifications were made to the DACS control box leading up to the third test campaign; however, additional instruments were implemented. A thermal camera was added to measure external engine wall temperature and a vortex flow meter was used to replace the previous non-functional variable area flow meter on the gaseous oxygen propellant line. Additionally, the sampling frequency of all instruments (excluding the thermocouples and cameras) was changed to 10 kHz.

Thermal Camera

In addition to the optical cameras, a FLIR A50 thermal camera was used to gather data on external engine temperature but mainly to detect any gas leaks at the combustion chamber and HDPE fuselage interface during hot-fire testing. The camera was set to measure object temperature from -20 to 175°C in order to detect hot spots and the development of the thermal gradient as the engine reached thermal equilibrium. While not a sufficient temperature range to measure plume temperature, the thermal camera can still detect variations in the plume which can be useful in evaluating qualitative engine performance.

Mass Flow Rate Measurement

The oxidiser variable area flow meter was replaced with a VFM60 vortex flow meter (shown in Fig. 4.6) which could measure a much higher range of flow rates and included both pressure and temperature compensation for more accurate measurements of the flow rate.

Sampling Frequency

Following the previous test campaigns, the sampling frequency was increased to 10 kHz in order to have the capability of detecting high frequency combustion instabilities such as screech [126].

4.5 Test Operating Conditions

4.5.1 Bi-Propellant Tests (Ouroboros-1 and 2)

While both the regeneratively cooled depolymerisation chamber engine (Ouroboros-1) and the direct fuselage injection engine (Ouroboros-2) were designed to use three propellants as an autophage engine, they were first operated as bi-propellant engines. This was done to reduce the complexity of the engine tests and to first set a performance baseline such that the Ouroboros-3 autophage engine performance could be directly compared to the equivalent bi-propellant engine.

Therefore, these bi-propellant engines replaced the HDPE fuselage with a stainless steel (SS 316) plug that was machined to the dimensions of the fuselage. This plug was inserted into the engine and secured in place using the linear actuator. Thus, during hot-fire testing

there was no HDPE contribution to the fuel mass flow rate and no feed rate. This reduced the number of variables to better evaluate the designs and performance before proceeding to fully integrate autophage tests.

The bi-propellant hot-fire test campaigns for Ouroboros-1 and Ouroboros-2 were designed to first test the engines at standard inlet conditions (SIC) with additional off-nominal tests prepared if the SIC tests were successful. The target standard inlet conditions were defined by Fig. 4.2.

Table 4.2 Ouroboros engine hot-fire test campaign target standard inlet conditions.

Parameter	Value
Throttle Setting, %	100
Thrust, N	100.4
MR	2.00
P_c, bar	5.00
P_{fuel}, bar	6.00
P_{ox}, bar	6.00
$\dot{m}_{fuel}$, g/s	19.63
$\dot{m}_{ox}$, g/s	39.25
v_e, m/s	1705
I_{sp}, s	197
T, K	2928

The Ouroboros-1 engine was only operated at standard inlet conditions before engine failure; however the Ouroboros-2 engine was operated for two tests at standard inlet conditions, two tests at a slightly higher fuel inlet pressure (lower mixture ratio), and one test at both high oxidiser and fuel inlet pressures (high throttle setting). All tests were conducted at a continuous steady state operating mode, but in each case, the engines were also intentionally shutdown and restarted mid-burn. This was done to verify that the propellant feed system and ignition system would be able to operate the engine in a pulsed mode during the later Ouroboros-3 tests.

4.5.2 Autophage Tests (Ouroboros-3)

While the Ouroboros-1 and 2 designs were operated as exclusively as bi-propellant engines, the Ouroboros-3 engine was operated in the autophage configuration. However, due to both the Ouroboros-1 and Ouroboros-2 bi-propellant engines experiencing overheating leading to combustion chamber failures. The Ouroboros-3 autophage engine was first operated at a lower, fuel-rich mixture ratio (which corresponds with a lower engine temperature) before being tested at SIC. This would verify the autophage engine architecture before conducting hot-fire tests that could overheat the engine and increase the likelihood of achieving multiple successful tests.

The target inlet conditions are listed in Fig. 4.3. The test plan for the Ouroboros-3 engine was designed to determine the effect of throttle setting and mixture ratio on engine performance and fuel tube feed rate.

Table 4.3 Ouroboros-3 engine hot-fire test campaign target inlet conditions.

Parameter	Test No.				
	1	2	3	4	5 (SIC)
Operating Mode[1]	SS	SS	SS	SS/PM	SS/PM
Throttle Setting, %	100	50	50	75	100
Thrust, N	100.4	49.38	50.84	75.89	101.7
MR	1.00	0.75	1.00	2.00	2.00
P_c, bar	5.00	3.00	3.00	4.00	5.00
P_{fuel}, bar	6.00	3.60	3.60	4.80	6.00
P_{ox}, bar	6.00	3.60	3.60	4.80	6.00
$\dot{m}_{fuel}$, g/s	37.65	20.62	22.76	30.23	37.73
$\dot{m}_{ox}$g/s	37.65	27.59	22.76	15.11	18.87
v_e, m/s	1457	1148	1213	1805	1932
I_{sp}, s	149	99	124	184	197
T_c, K	1233	1102	1205	2913	2928

[1] Operating modes can be either steady state (SS), pulsed mode (PM), or both (SS/PM).

While the previous bi-propellant engines were only tested in continuous steady state operating modes, they both demonstrated successful engine shutdowns and restarts. Tests 2 and 3 of the Ouroboros-3 engine were also designed to do the same shutdown and restart procedure to verify that the autophage engine was capable of being restarted after a period of time; during which the HDPE fuel was still being fed into the combustion chamber. In addition to these steady state tests, a set of pulsed mode tests were also designed to evaluate the engine performance across a range of frequencies and duty cycles.

These pulsed operating modes were added at the end of the final two steady state tests to evaluate how pulsed mode influenced both the engine performance, fuselage feed force, and fuselage feed rate when compared to the same steady state operating conditions. It was theorised that pulsed mode could reduce the required feed force during engine off-time when combustion chamber pressure was low, due to the fuel tube being inserted directly into the combustion chamber. Additionally, pulsed operating modes are known to have an affect on engine operating temperature and could provide a method for controlling the fuel tube feed rate without changing the bi-propellant inlet conditions. Instead, the combustion chamber wall temperature could be changed by operating the engine at various frequencies and duty cycles.

The resulting test plan is shown in Fig. 4.4. With a minimum number of tests we can demonstrate how throttle settings, mixture ratios, frequencies and duty cycles can affect both engine performance and fuel tube feed rate.

Table 4.4 Ouroboros-3 hot-fire test plan target chamber pressure, mixture ratio, and operating frequencies.

Test no.	Throttle, %	MR	Burn Time, s	Operating Mode	f, Hz	Duty cycle, %
1	100	1.00	25	SS	-	-
2	50	1.00	45	SS	-	-
3	50	1.00	45	SS	-	-
4	75	2.00	30	SS	-	-
4.a			15	PM	0.5	50
4.b			15	PM	1.0	50
4.c			15	PM	1.0	75
5	100	2.00	30	SS	-	-
5.a			15	PM	1.0	50
5.b			15	PM	1.0	75
5.c			15	PM	0.5	75
5.d			15	PM	2.0	75
5.e			15	PM	2.0	50

Chapter 5

Depolymerisation Chamber Architecture, Bi-Propellant Test Results

5.1 Ouroboros-1 Operational Modes and Test Campaign Overview

As detailed in Section 3.2 the first iteration of the Ouroboros-1 engine was designed using a depolymerisation chamber architecture where the HDPE fuselage was melted and mixed with the propane fuel before being injected into the engine as a fuel mixture. This engine was tested on June 8th, 2022 in its bi-propellant configuration at steady state, standard inlet conditions for approximately 51 seconds. It achieved a maximum sustained steady state thrust of approximately 90.39 N, slightly below the target thrust of 100 N.

While additional tests where planned across a wider operating box, the test campaign was terminated after the first hot-fire due to damage of the combustion chamber which underwent a burn-through of the chamber wall. This burn-through was determined to be caused by a buckling hoop stress on the chamber wall due to the both the higher pressure within the depolymerisation chamber and high combustion temperatures which weakened the chamber wall strength.

While the engine experienced a failure, results showed that components of the autophage design are feasible. Mainly: the fuel tube seals are effective, fuel tubes are capable of being inserted into the engine, autophage engine performance can be effectively modeled as a bi-propellant fuel mixture, and depolymerisation chamber temperatures are sufficient to melt the fuel tube. The tests also characterised potential failure modes of autophage engines such as the buckling hoop stress failure and cavitation within the depolymerisation chamber which may have restricted the fuel mass flow rate, reduced the effectiveness of cooling within the depolymerisation chamber, and contributed to the engine burn through.

Overall, the results of this test campaign showed that the regeneratively cooled, depolymerisation chamber architecture was not feasible for engines of this scale; but it does not exclude the possibility of using this architecture for larger scale engines. In order for this architecture to be viable it was determined that the combustion chamber should be manufac-

tured from a material with high thermal conductivity and the topology of the depolymerisation chamber would need to be optimised in order to maximise the heat transfer from the combustion chamber to the fuselage. Additionally, turbomachinery or electric pumps should also be employed downstream of the depolymerisation chamber prior to fuel injection; this would reduce the depolymerisation chamber pressure and prevent the compressive buckling failure mode of the combustion chamber. Implementing these design considerations could be viable for engine thrust classes of 1 kN or higher and can be considered for future work. Nevertheless, the lessons learned from testing this system were used in driving the design of the direct fuselage insertion architecture for Ouroboros-2 and 3 which proved to be a more effective architecture for operating an autophage engine at the 100 N thrust class.

5.1.1 Test Data

The following describes the key events of the Ouroboros-1 hot-fire test which are reflected in the performance data shown in Fig. 5.1.

Timeline of the hot-fire test

T - 05s Engine countdown begins.

T - 00s Control valves open, oxidizer reaches nominal pressure, engine ignition.

T + 02s Fuel inlet reaches nominal pressure. Long rise time suggests either gaseous or two-phase fuel flow.

T + 08s Engine reaches steady state with a thrust of approximately 40N. Lower thrust than expected, suggests fuel mass flow rate is constrained which could be due to gaseous rather than liquid fuel injection.

T + 19s Engine experiences a sudden 1.4 bar drop in fuel pressure and 30N increase in thrust. This may indicate a transition from gaseous fuel injection to liquid fuel injection through one or more fuel injector orifices.

T + 24s Engine experiences a second sudden drop in fuel inlet pressure to 5 bar (combustion chamber design pressure) and an increase in thrust to 90N. A large flame burst is seen in the plume and a major oscillation is shown in the thrust data. Fuel inlet pressure roughness increases. These factors are indicative of an engine burn-through as the depolymerisation chamber (fuel inlet) pressure is now effectively gathering combustion chamber pressure.

T + 38s An emergency stop is initiated. Nitrogen purge valves open, propellant feed system control valves fail to close.

T + 43s After a 5 second engine purge, the nitrogen purge valves close and the engine restarts and resumes steady state operation.

T + 48s A second emergency stop is initiated. Nitrogen purge valves open, propellant feed system valves fail to close again.

T + 51s Propellant feed system valves are manually shut off.

T + 54s Nitrogen purge completes.

T + 58s A final nitrogen purge is initiated.

T + 63s Nitrogen purge complete. Engine is shut down.

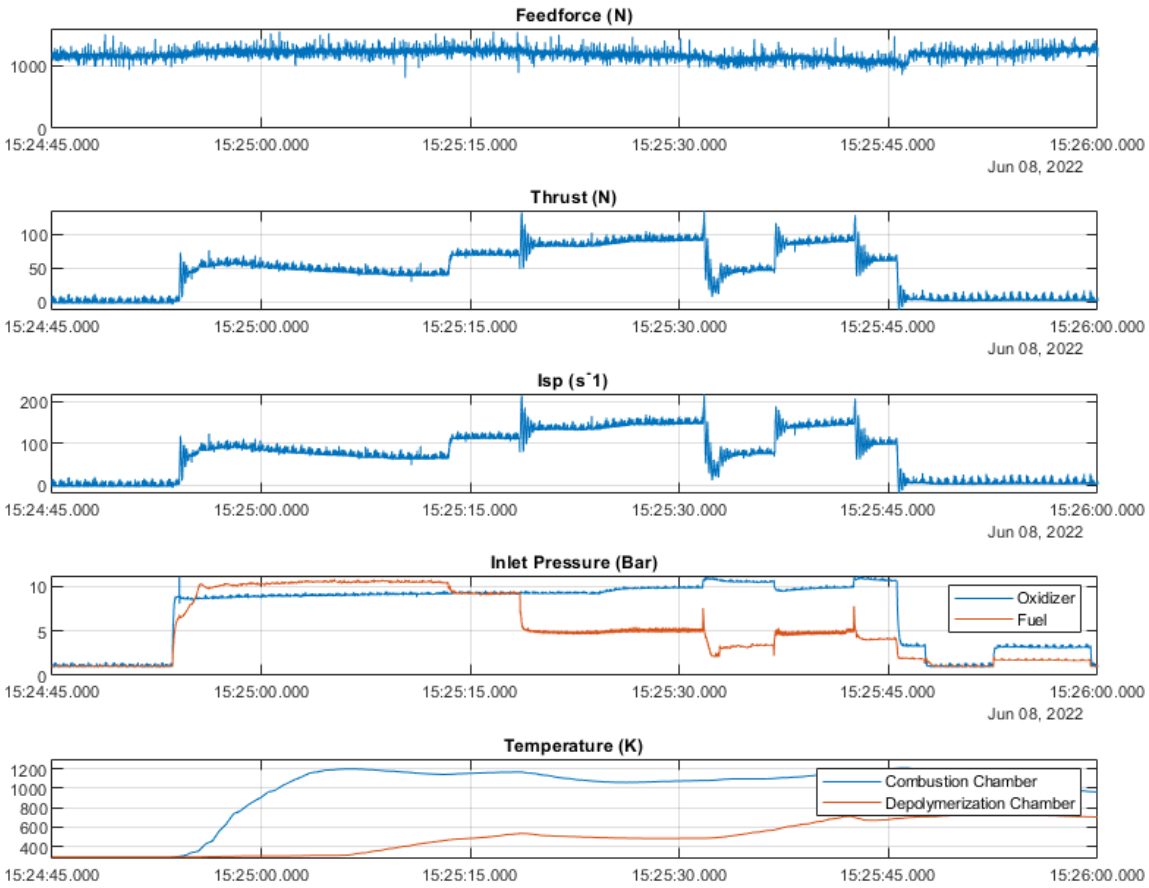

Fig. 5.1 Ouroboros-1 full run performance data

5.2 Performance Analysis

When analyzing the performance data in Fig. 5.1 we can separate the hot-fire test into 3 key phases of interest:

1. **Phase 1:** First instance of steady state operation from T+08s to T+19s.
2. **Phase 2:** Second instance of steady state operation from T+19s to T+24s; after the slight drop in fuel inlet pressure and rise in thrust.

3. **Phase 3:** Third instance of steady state operation from T+24s to T+38s; following the large drop in fuel inlet pressure to the design combustion chamber pressure (5 bar).

Each phase corresponds with a different mode of operation which was determined via analysis of the available data. There were seven sensors on the engine as show in Table 5.1.

Table 5.1 Ouroboros-1 sensors and sampling frequencies.

Location	Type	Units	Frequency, f_s
Actuator, F_F	feed force load cell	N	1 kHz
Test stand, F_T	thrust load cell	N	1 kHz
Depolymerisation Chamber, P_f	pressure transducer	Bar	1 kHz
Oxidizer Inlet, P_o	pressure transducer	Bar	1 kHz
Combustion Chamber, P_c	pressure transducer	Bar	1 kHz
Depolymerisation Chamber, T_{DC}	thermocouple	K	1 Hz
Combustion Chamber, T_{CC}	thermocouple	K	1 Hz

During the course of the run it was discovered that there was a software error which failed to turn on the combustion chamber pressure transducer. Therefore, the combustion chamber pressure data has been omitted from the analysis.

5.2.1 Phase 1: Steady State Operation With Constrained Fuel Injection

Phase 1 encompasses the first steady state mode initially after engine startup. Prior to the start of the test, the propellant lines were flushed with gaseous nitrogen. This was done to remove as much atmospheric air as possible from the system prior to connecting the propellants. Thus, when the propane fuel tank valve was opened there was a mixture of both liquid propane, gaseous propane and gaseous nitrogen in the fuel lines. Similarly, there was also a mixture of gaseous oxygen and nitrogen in the oxidiser lines.

When the propellant feed system control valves were opened, a liquid fuel and gaseous nitrogen mixture was delivered to the depolymerisation chamber and the fuel injected into the combustion chamber was likely a mixture of two-phase flow. The horizontal test bed would have caused the liquid propane to settle at the bottom of the depolymerisation chamber which may have resulted in liquid injection through some of the fuel orifices and gaseous injection through the top orifices. This can be observed in Fig. 5.1 with the slow rise time of fuel inlet pressure as the fuel is filling the depolymerisation chamber. Additionally, the fuel injectors were designed for liquid injection and if there was gaseous injection it would create a significant flow restriction which would greatly reduce the fuel mass flow rate and in turn engine thrust. This is the case with the visibly low engine thrust of approximately 40N and the grossly over-expanded plume seen in Fig. 5.2 which shows a contracting plume with visible shock diamonds; indicative of over-expansion [127, 128].

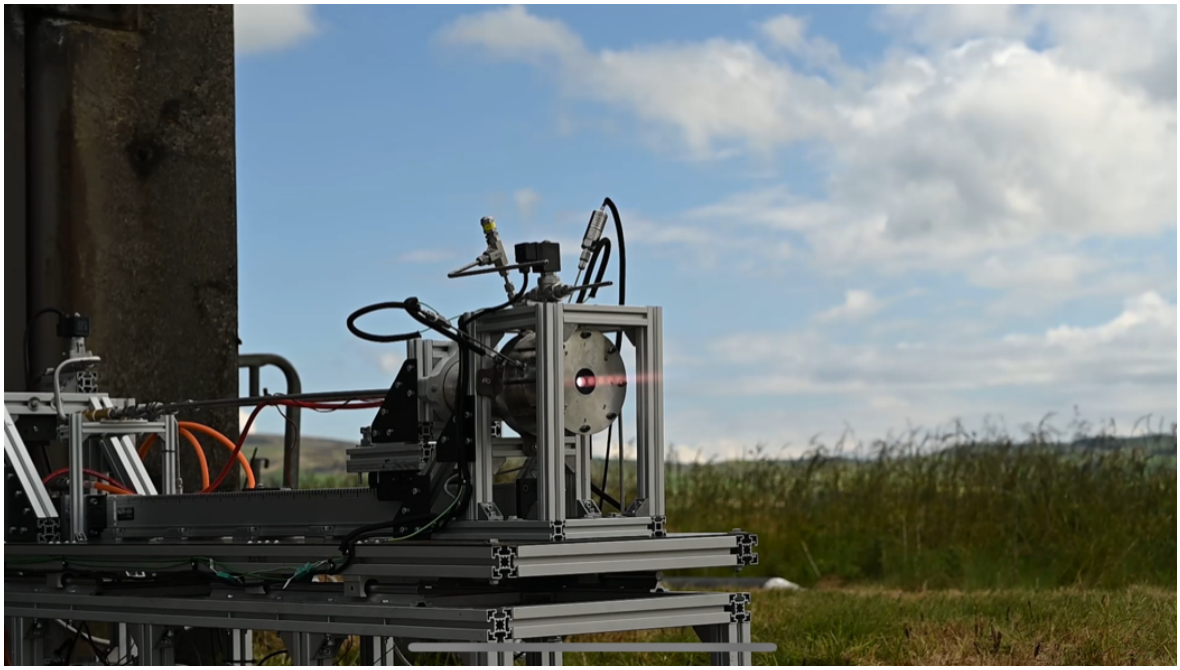

Fig. 5.2 Ouroboros-1 over-expanded plume during initial steady state operation.

The temperature data also supports the hypothesis of gaseous or two-phase fuel in the depolymerisation chamber. As the fuel mixture entered the depolymerisation chamber the liquid would have initially expanded into the larger chamber volume and vaporised, reducing chamber temperature. This is reflected in the thermal data from T+00s to T+12s where the rate of change of the depolymerisation chamber temperature is only 1.4 K/s compared to the time interval of T+12s to T+19s where the rate of change climbs to 23.1 K/s. This delay in depolymerisation chamber temperature rise time can be both attributed to vaporisation of the liquid fuel near the thermocouple as well as the low thermal conductivity of the chamber wall material (Inconel 625). At that point the temperature at the depolymerisation chamber thermocouple exceeds the boiling point of propane at 10 bar indicating the presence of gaseous propane at the top of the chamber (where the thermocouple is located) this however does not exclude the presence of liquid propane at the bottom of the chamber leading to partial liquid injection occurring in Phase 2. This is confirmed by inspection of the combustion chamber wall following the hot-fire test.

Taking a closer look at the data in Fig. 5.3, we can see both the thrust roughness and the inlet pressure roughness. It is important to note that there are some clear outliers in the data, particularly for thrust which appears to have a beat and oscillation. A frequency analysis was run in Section 5.3 which found repeating frequencies across all sensors which were connected to the 4-20mA to 0-10V sensor conversion board; it was concluded that the outliers and frequencies were artificially induced due to the electronics.

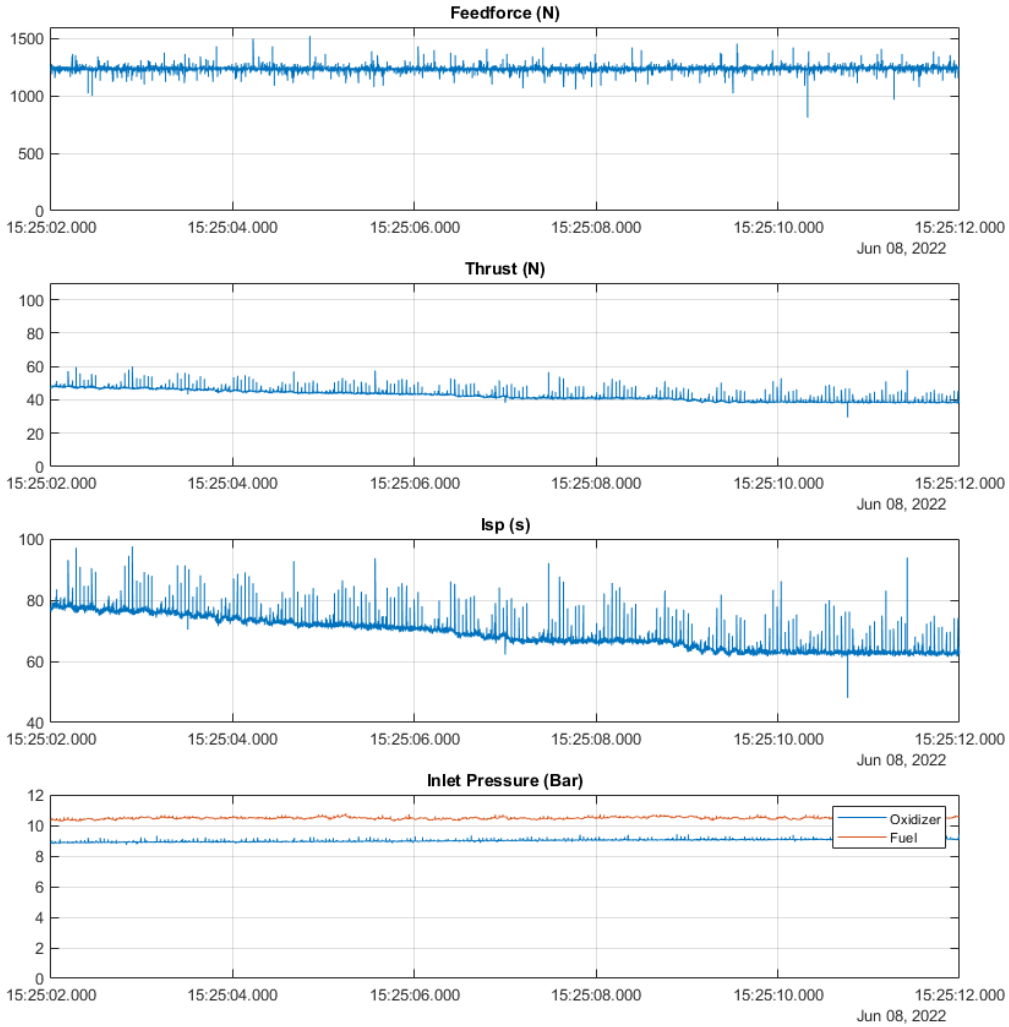

Fig. 5.3 Ouroboros-1 performance data during phase 1 steady state operation.

Excluding those outliers data roughness was found and detailed in Table 5.2. The data shows generally steady state behavior; however, average thrust was observed to decrease by approximately 12%. This can again be attributed to a changing fuel mass flow rate due to the vaporisation of propane within the depolymerisation chamber.

Table 5.2 Ouroboros-1 phase 1 steady state operation data roughness.

Data	Mean	Roughness	Units
Depolymerisation chamber pressure, P_f	10.48	+/- 0.87%	Bar
Oxidiser inlet pressure, P_o	9.04	+/- 0.44%	Bar
Thrust, F_T	42.42	+/- 1.70%	N

5.2.2 Phase 2: Steady State Operation With Liquid Fuel Injection

Phase 2 is considered to be the point at which the engine operated with at least partial liquid fuel injection. The start of the phase is marked with an increase in engine thrust and a slight decrease in fuel inlet pressure; seen at T+19s in Fig. 5.1. The thrust rise time is calculated to be 0.32 seconds and there is no indication of an overshoot and subsequent roughness in the data. Thus, it is unlikely that any engine damage or burn-through occurred at that time, rather it is indicative of a sudden increase in propellant mass flow rate within the constraints of the nominal design which is best explained by a transition of at least one of the fuel injection orifices from injecting gaseous propane to liquid propane.

Analysis of the thrust and pressure roughness during phase 2 (Fig. 5.3) supports this hypothesis as it does not significantly vary from the data roughness of phase 1. In fact, the thrust roughness decreased to below 1% of full scale thrust which indicates stable combustion, good atomisation, and effective mixing of the propellants.

Table 5.3 Ouroboros-1 phase 2 steady state operation data roughness.

Data	Mean	Roughness	Units
Depolymerisation chamber pressure, P_f	9.09	+/- 0.79%	Bar
Oxidiser inlet pressure, P_o	9.13	+/- 0.59%	Bar
Thrust, F_T	69.30	+/- 0.99%	N

Additionally, the plume in Fig. 5.4 appeared to still be slightly over-expanded likely due to a low combustion chamber pressure leading to the lower than expected thrust. A closer look at the plume shock structure in Fig. 5.5 showed a mach disc immediately after the nozzle exit this is indicative of an over-expanded flow rather than an under-expanded flow which would instead have expansion waves at that location [129]. However, the plume was not as over-expanded as the phase 1 plume which indicated a higher combustion chamber pressure during phase 2 operation and supports the hypothesis of more liquid fuel being injected and an overall higher propellant mass flow rate.

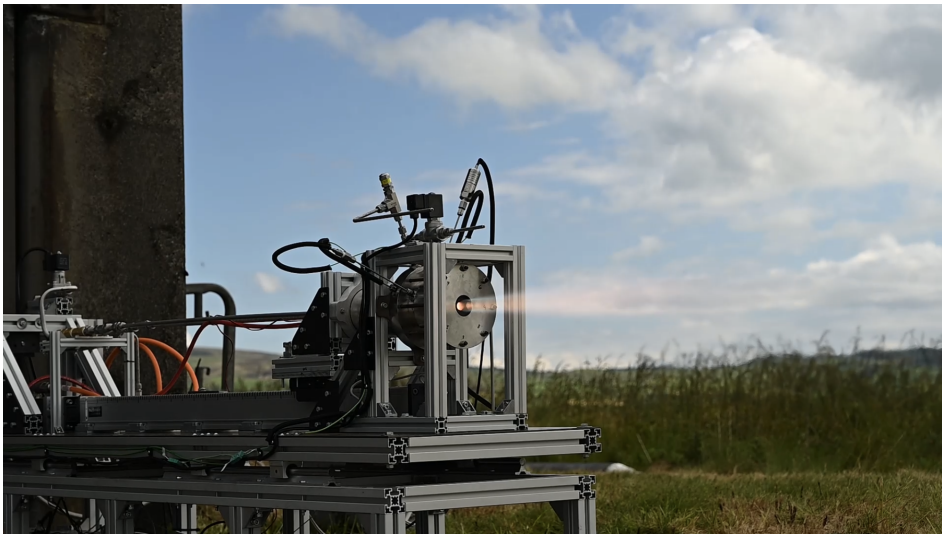

Fig. 5.4 Ouroboros-1 over-expanded plume during phase 2 steady state operation.

Fig. 5.5 Ouroboros-1 plume shock structure during phase 2 steady state operation.

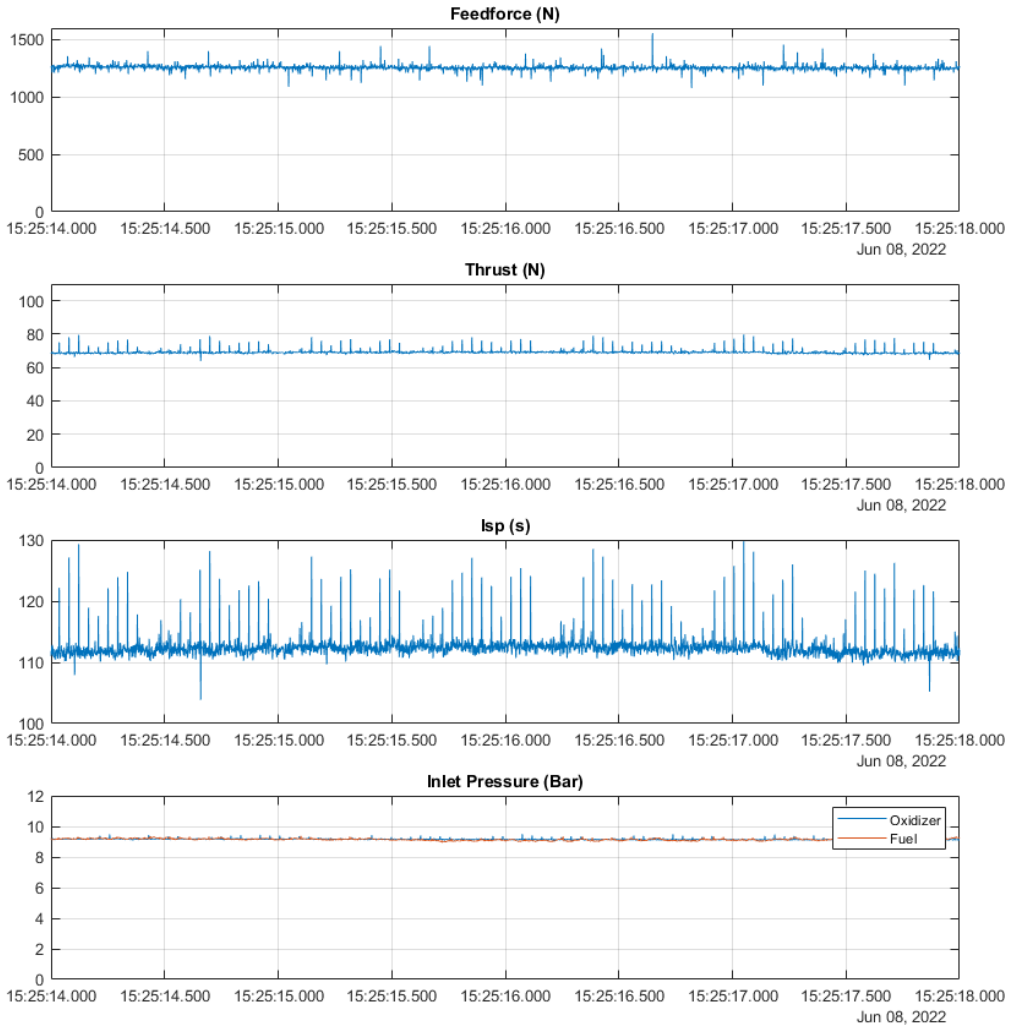

Fig. 5.6 Ouroboros-1 performance data during phase 2 steady state operation.

Nevertheless the engine was still not operating at the design point of 100 N; as can be seen in Figure 5.6, the full scale thrust output was approximately 70 N which is 70% of the designed thrust for standard inlet conditions. Since the inlet pressures for both the oxidiser and fuel were nominal, the only reasonable explanation for the off-nominal thrust would be due to a fuel mass flow restriction caused by one of the orifices injecting gaseous propane rather than liquid propane.

As observed in phase 1, the depolymerisation chamber temperature exceeded the boiling point of liquid propane indicating that the top of the depolymerisation chamber was still filled with gaseous fuel rather than liquid fuel. This corroborates that there was still at least one fuel orifice conducting gaseous injection during phase 2.

Considering the thermal profile of the engine, when compared to the predicted thermal analysis for steady state (Figure 3.7) the combustion chamber wall temperature at the sensor location, 116mm, was approximately 400 K lower than the predicted value of 1,600 K. However, as discussed in Section 3.2.1, the analytically calculated thermal profile of the engine did not take into account the thermal gradient between the regenerative cooled section of the engine and the nozzle which skewed the predicted temperature to a higher value. Additionally, the engine had not yet reached a thermal equilibrium.

Of note, however, is the discrepancy between the predicted temperature of the regenerative coolant (propane) and the measured depolymerisation chamber temperature. As mentioned previously, the measured depolymerisation chamber temperature exceeded the boiling point of propane at 10 bar of pressure causing gaseous propane to be present in the depolymerisation chamber. Moreover, the fuel injection orifices were designed to inject liquid fuel and the presence of a gas in the depolymerisation chamber would have caused gaseous injection, choked flow and a fuel mass flow rate constriction. Exceeding the boiling point of the propane fuel in the depolymerisation chamber was a design oversight which resulted in gaseous fuel injection through orifices designed for liquid fuel, constrained fuel mass flow rate, and off-nominal engine performance.

Overall, in phase 2, the Ouroboros-1 engine was operated near its standard inlet conditions and its design point but failed to meet nominal performance targets due to a fuel mass flow rate constraint. This is further verified when the Ouroboros-1 engine enters phase 3 steady state operation following an engine burn-through where the combustion chamber wall is compromised.

5.2.3 Phase 3: Steady State Operation With Unconstrained Liquid Fuel Injection Following Combustion Chamber Burn-Through

The steady state operation of the Ouroboros-1 engine during phase 2 was cut short with a sharp and significant drop in fuel inlet pressure as well as an increase in thrust which marked the start of phase 3. This event was determined to be the burn-through of the combustion chamber wall with post hot-fire inspection of the combustion chamber verifying the burn-through shown in Fig. 5.11.

The most significant indication that the burn-through occurred at this point was a visible burst in the plume (Fig. 5.7) followed by an increase, overshoot and oscillation of the thrust.

This indicated a detonation within the engine likely caused by a sudden increase in fuel mass entering the combustion chamber at that time.

Following the initial burst, the engine entered a steady state operating mode generating approximately 90N of thrust; slightly below the engine design point and standard inlet conditions. Figure 5.7 shows the plume burst and subsequent steady state plume. The plume still had some visible shock diamonds; however, it appeared closer to nominal expansion when compared to phase 1 and phase 2 exhaust plumes.

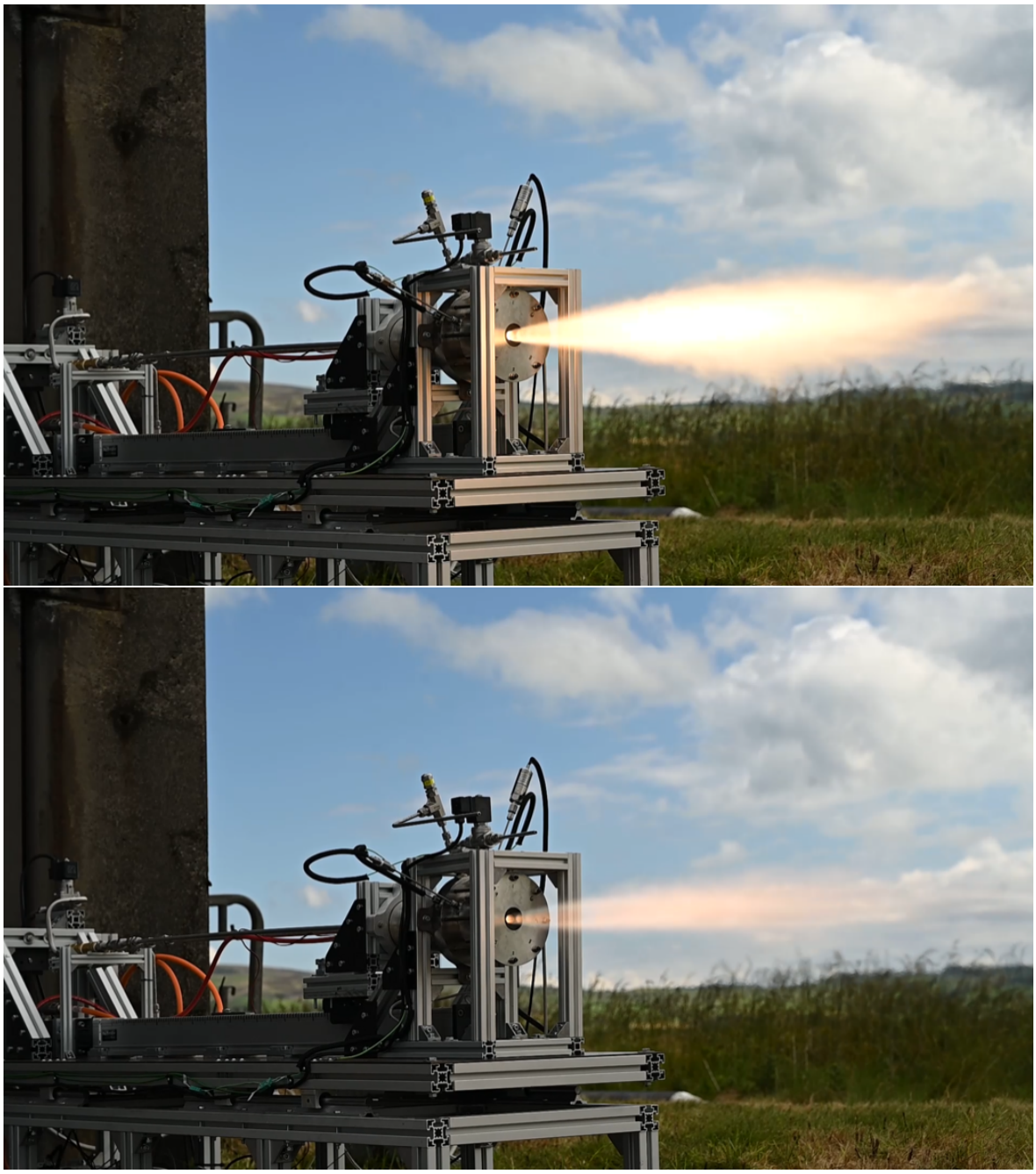

Fig. 5.7 Ouroboros-1 burst (top image) and plume during Phase 3 (bottom image).

Taking a closer look at the performance data in Fig. 5.8, the depolymerisation chamber pressure was noted as sharply decreasing and remaining steady at approximately 5.04 bar. This was the target combustion chamber pressure in order to operate at a nominal 100 N

of thrust. Due to the burn-through of the combustion chamber wall it was deduced that the depolymerisation chamber pressure sensor was effectively measuring combustion chamber pressure throughout phase 3 steady state. The burn-through hole was found to be near the propane fuel inlet; thus, fuel mass flow rate would be unrestricted through the perforation and effectively bypass the depolymerisation chamber and fuel injection orifices.

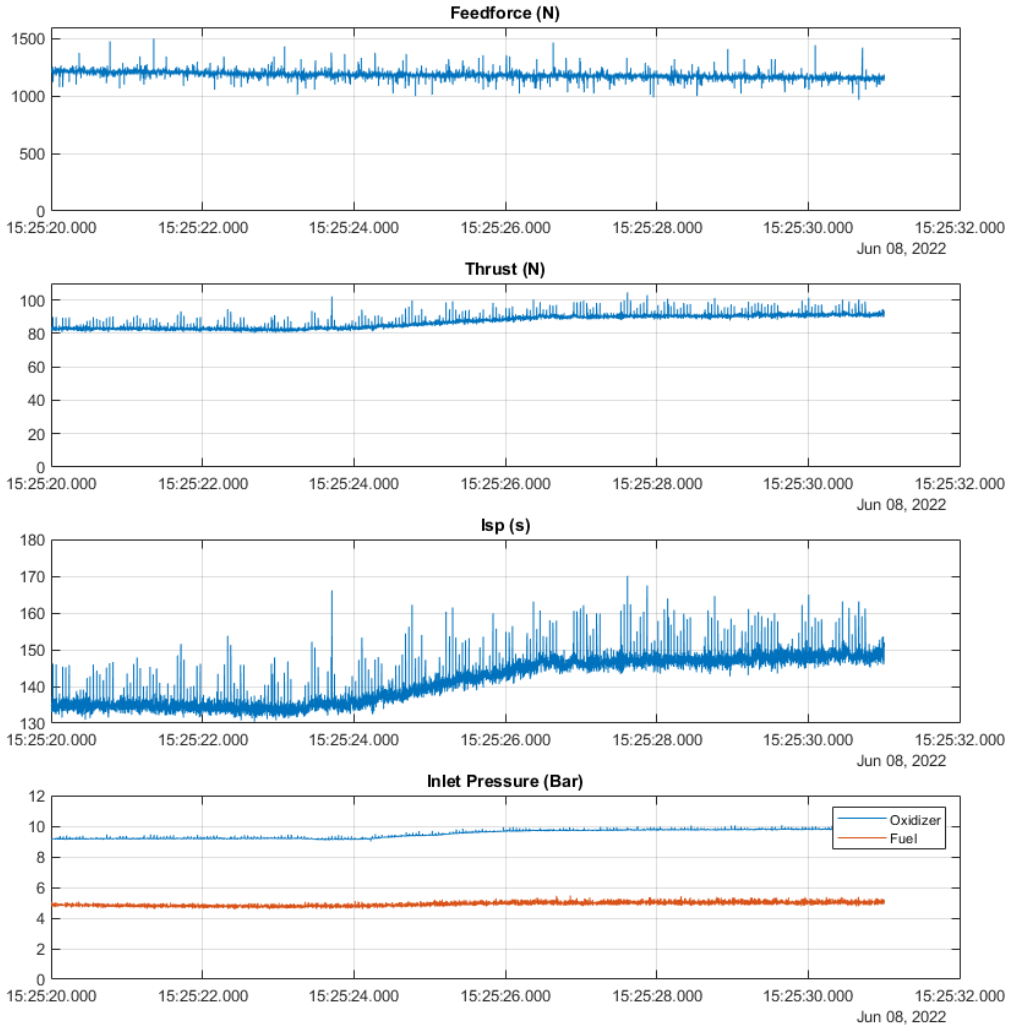

Fig. 5.8 Ouroboros-1 performance data during phase 3 steady state operation.

Additionally, seen in the performance data was a significant increase in thrust and depolymerisation chamber pressure sensor roughness while oxidizer pressure sensor roughness remained similar to the previous phases shown in Fig. 5.4. This is an indicator of unsteadiness and potential combustion instabilities likely caused by the burn-through and unrestricted flow of fuel through the combustion chamber hole.

Taking into account the change in data roughness for the thrust and depolymerisation chamber pressure, a frequency analysis was conducted in Section 5.3 to determine if any combustion instabilities were detected. Further analysis of the temperature data also showed a

Table 5.4 Ouroboros-1 phase 3 steady state operation data roughness.

Data	Mean	Roughness	Units
Depolymerisation chamber pressure, P_f	5.04	+/- 5.60%	Bar
Oxidiser inlet pressure, P_o	9.77	+/- 0.35%	Bar
Thrust, F_T	90.39	+/- 2.59%	N

decrease in both combustion chamber temperature and depolymerisation chamber temperature immediately following the engine burn-through. This further supports that the engine did indeed suffer a burn-through at that moment since unrestricted fuel flow would result in a fuel rich mixture ratio which typically decreases engine operating temperatures [130].

While the burn-through demonstrated a failure of the engine it did supplement the Ouroboros-1 performance with combustion chamber pressure data due to the fact that the depolymerisation chamber pressure sensor was effectively logging combustion chamber pressure during phase 3 steady state operation. Using that data we are able to determine that the engine was operating near the design point of 100 N of thrust at a chamber pressure of approximately 5.0 bar.

Furthermore, this supports the previous hypothesis of a flow restriction of the fuel mass flow rate causing a lower combustion chamber pressure during phases 1 and 2 since the burn-through allowed the fuel to bypass the injectors; resulting in performance closer to the design point. While still a lower thrust than the design point, this can be explained by a high likelihood of incomplete combustion of the fuel and a low combustion efficiency.

First, following the burn-through event, propane fuel would have had a tendency to travel through the burn-through hole into the combustion chamber with no atomisation of the liquid fuel. This would cause inadequate mixing and lower the combustion efficiency of the engine. Furthermore, the burn-through hole occurred halfway down the length of the combustion chamber, thereby, any fuel entering the chamber through the hole would have its residence time significantly reduced. This reduction in residence time would significantly reduce the combustion efficiency of the engine [131] reflected by a reduction in measured engine thrust.

5.3 Frequency Analysis

A frequency analysis was done on the available data to determine if there were any low frequency instabilities during the hot-fire test of Ouroboros-1. Low frequency combustion instabilities in liquid propellant engines are typically within the range of 0-500 Hz and are typically caused due to a coupling between the combustion process and the propellant feed system. When data roughness is less than +/-5% we can typically consider the combustion as "smooth" while roughness in excess of +/-10% can be an indicator of the manifestation of an instability [132].

Thus, prior to running the frequency analysis for the full test duration it was determined that instabilities during steady state phases 1 and 2 were unlikely because of the relatively smooth data. However, due to the depolymerisation chamber pressure exceeding a roughness of +/-5% during phase 3 steady state operation (and the evident engine burn-through) it was

determined that an instability may be present. All pressure and load sensors were operated at 1 kHz, thus the frequency analysis was conducted between 0-500 Hz. This range is only capable of detecting low-frequency combustion instabilities with high-frequency instabilities being capable of reaching up to 5,000 Hz.

The frequency analysis can be seen in both the spectrograms and persistence diagrams of the pressure and force transducers in the below figures. One thing of note for the thrust, depolymerisation chamber, and oxidiser inlet pressure sensors is a repeating oscillation at approximately 23 Hz intervals. This was been determined to be interference due to the 4-20 mA to 0-10 V sensor conversion board which interfaces with those three sensors but not the feed force load cell. That information was used to remove outliers from the performance data.

The spectrograms are time dependant and show that there were no major frequencies present across the sensors for most of the duration of the test. The exceptions are the fuel inlet pressure sensor during both phases 2 and 3 as well as the thrust load cell during phase 3.

There is a slight frequency peak at 125 Hz in the depolymerisation chamber pressure that appears during phase 2 which was the period of partial liquid injection into the engine. This peak is not present in the thrust sensor which supports that the engine was operating with partial liquid fuel injection and that the frequency could be a result of boiling of the propane within the depolymerisation chamber causing fluctuations.

During phase 3, the thrust sensor also developed a frequency peak from 80-120 Hz which corresponded to the same frequency range of the depolymerisation chamber pressure sensor. This is expected as the burn-through is hypothesized to have occurred at the start of phase 3 which would cause the fuel to enter the engine asymmetrically. This frequency is not present on the oxidizer inlet though which indicates there is no coupling of the instability with the oxidiser inlet.

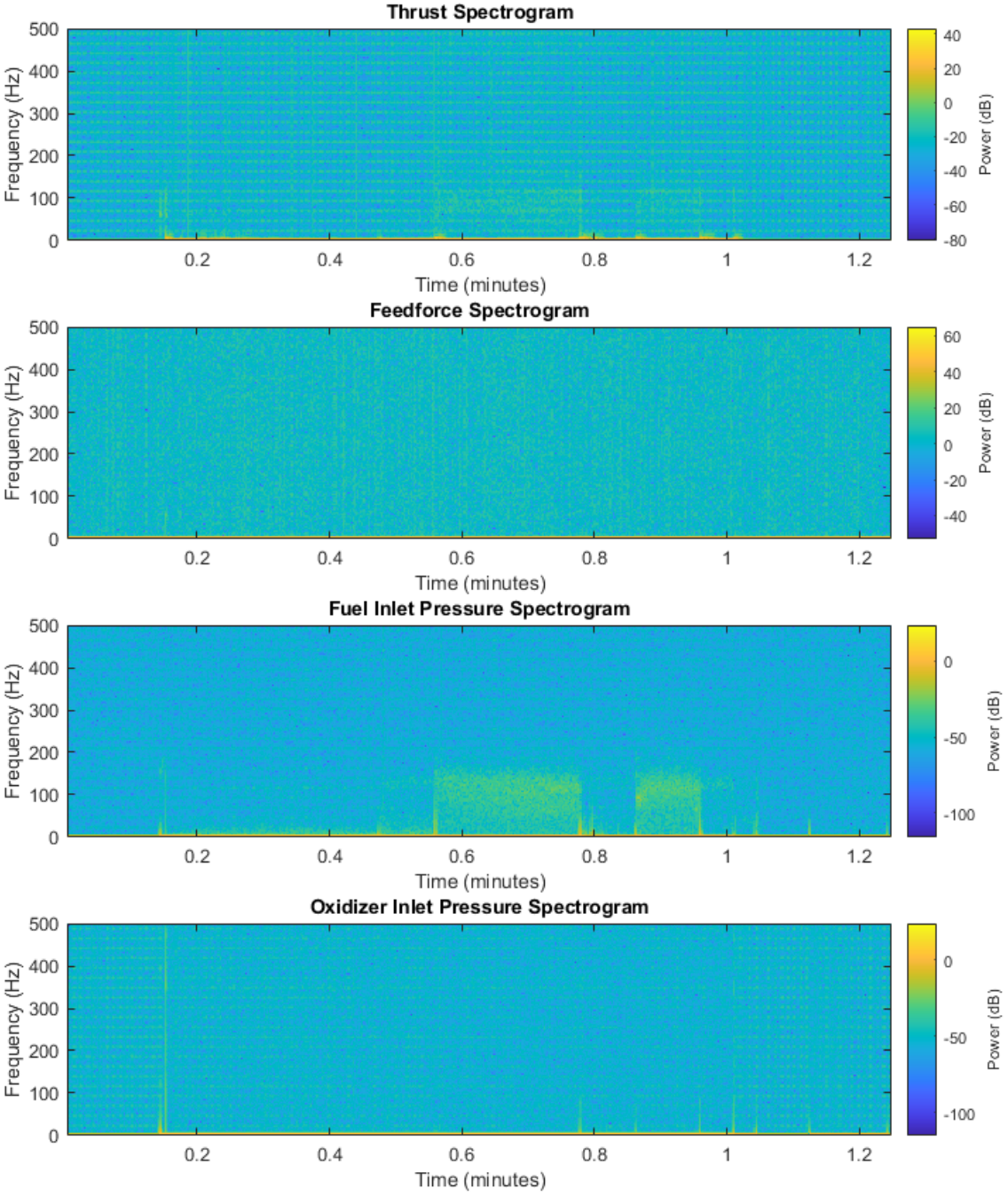

Fig. 5.9 Ouroboros-1 spectrogram of pressure and force sensors analyzed across the duration of the burn from 0-500 Hz. Repeating frequencies can be seen across both thrust, depolymerisation chamber, and oxidizer inlet pressure sensors but not the feed force; these frequencies are induced by the 4-20 mA to 0-10 V sensor conversion board on the DAQ. There is a slight frequency at 125 Hz for both the depolymerisation chamber pressure sensor and the thrust sensor during phase 3 operation; this corroborates the hypothesis that burn-through occurred at the start of phase 3.

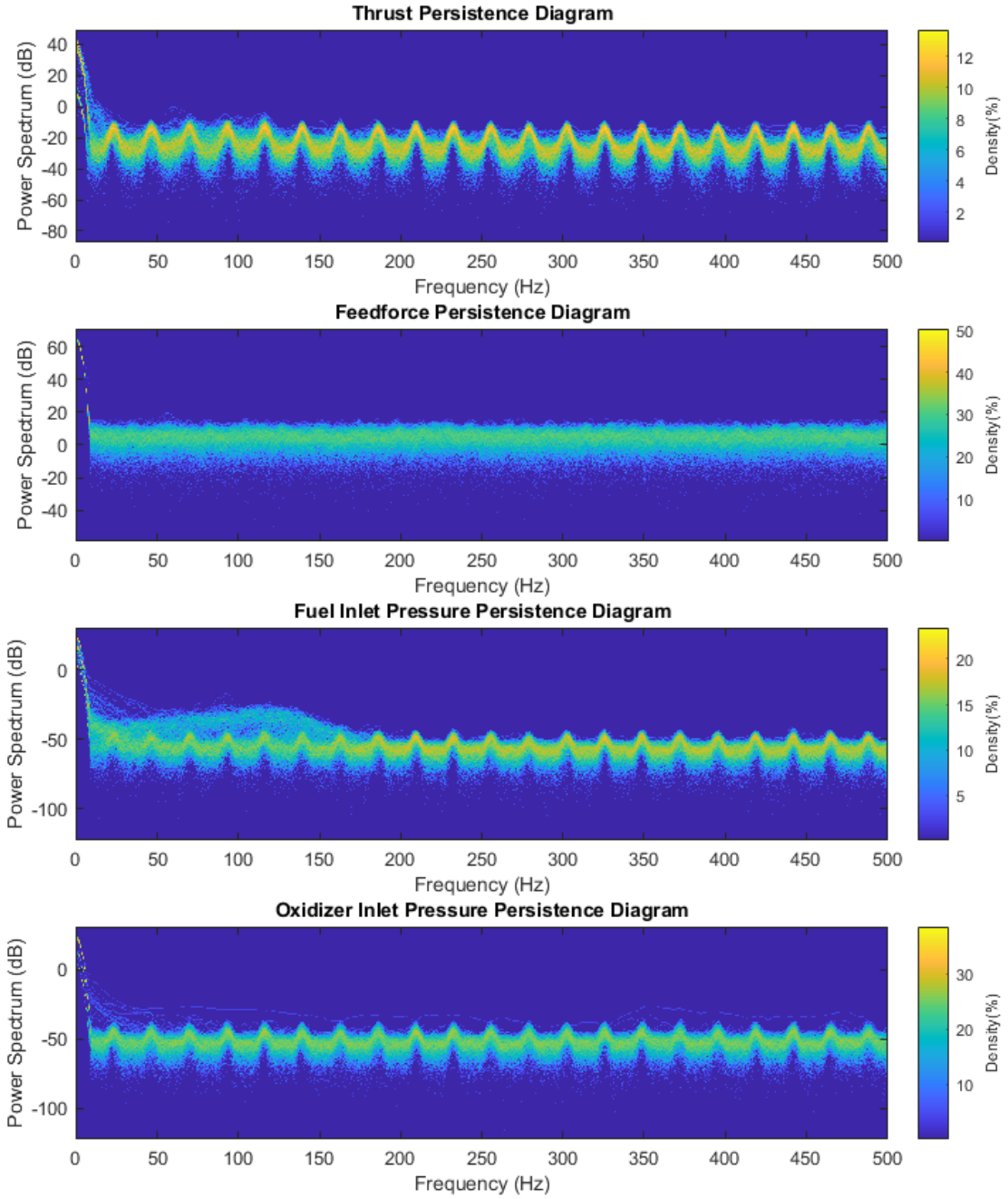

Fig. 5.10 Ouroboros-1 persistence diagram analyzed from 0-500 Hz. The alternating frequency in some of the graphs corresponds to electrical interference from the DAQ. The power spectrum of the thrust and depolymerisation chamber pressure sensor indicate a very low power and distributed frequency which correlate to the asymmetric fuel injection caused by the burn-through rather than an inherent combustion instability of the engine.

5.4 Post-Firing Inspection and Analysis

Following the hot-fire test, the engine was disassembled and inspected. Major damage was found on both the combustion chamber and the injector. The combustion chamber showed signs of hoop stress buckling, a 16 mm diameter burn-through hole, as well as evidence of

cavitation on the outer wall and micro-perforations. Meanwhile, the injector was heavily damaged at the igniter fastening point located directly above the self-impinging triplet.

The interior of the combustion chamber and the graphite nozzle were coated in shards of molten steel. While there were shards of steel stuck to surfaces on the inside of the combustion chamber there were no blockages present at the nozzle throat which could have restricted the flow and reduced engine performance. A measurement of the throat diameter after testing yielded a diameter of 16.0 mm which was consistent with the initial throat diameter. The injector, nozzle and combustion chamber seals were damaged and burnt; however the fuel tube seals were undamaged. Other engine components including the depolymerisation chamber, nozzle bulkhead, oxidizer inlet and fuel tube plug were also undamaged.

5.4.1 Combustion Chamber

The combustion chamber sustained the worst damage and the chamber walls failed during the hot-fire test. This is evident by the buckling of the chamber walls and the burn-through hole. The combustion chamber walls were designed with a 4x hoop stress factor of safety based on heritage design of regenerative cooling channels. However, this proved to be insufficient as the high temperature likely weakened the chamber walls which succumbed to the higher fuel inlet pressure leading to crushing the chamber walls.

This failure was likely to have been compounded by the fact that combustion chamber pressure may have been lower than expected as determined in the performance analysis. A lower combustion chamber pressure would have increased the difference in pressure between the fuel inlet and the combustion pressure significantly increasing the hoop stress on the chamber walls.

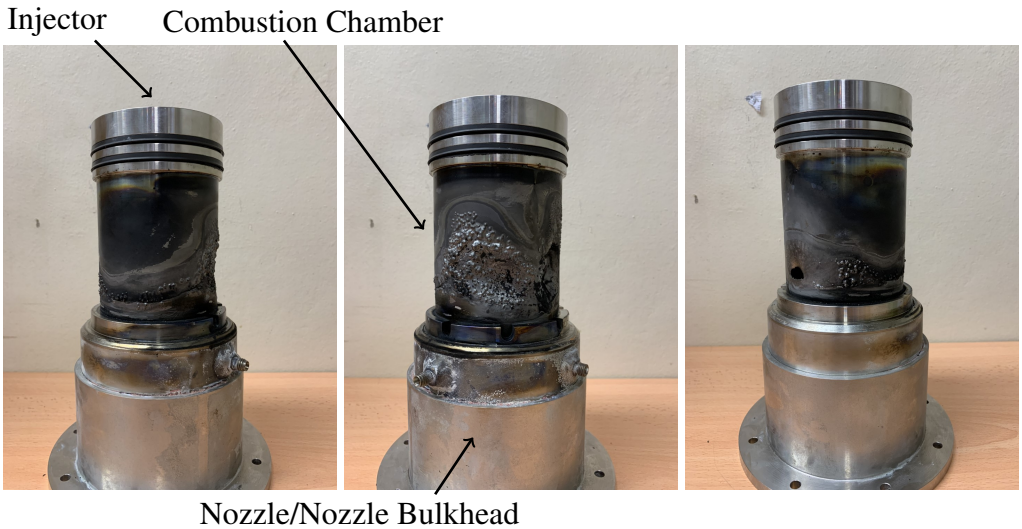

Fig. 5.11 A 360°view of the Ouroboros-1 combustion chamber post hot-fire. The leftmost figure shows the bottom of the engine which would have filled with liquid propane first due to gravity, keeping it cooler; it shows the least amount of thermal damage. The middle photo figure shows the top of the engine near the fuel inlet and shows the flow-path of the fuel. There are visible signs of melting of the chamber walls. The rightmost photo shows the side of the engine where the burn through occurred.

The crushing of the chamber walls would have resulted in the formation of a crack which exposed the fuel within the depolymerisation chamber directly to the combustion chamber. This is likely how the hole in the combustion chamber wall propagated as the thin wall was exposed directly to the hot combustion chamber gases as shown in Fig. 5.12.

The molten steel is thought to then have coated the interior walls of the combustion chamber and nozzle as it was burned. The steel shards seen in Fig. 5.13 include both steel from the injector and the combustion chamber. There also does not appear to be any evidence of the beading on the interior walls as there was on the exterior walls which is believed to be caused by cavitation and boiling of the liquid propane. Further investigation and consultation with materials experts yielded that the engine failure could have been a result of cavitation erosion.

Fig. 5.12 Ouroboros-1 combustion chamber burn-through hole. Diameter of the hole is measured at 16 mm at the widest point. The metal surrounding the hole shows visible signs of melting and re-solidifying as well as splatter; this is indicative of a hot-spot on the engine which caused the chamber wall to melt.

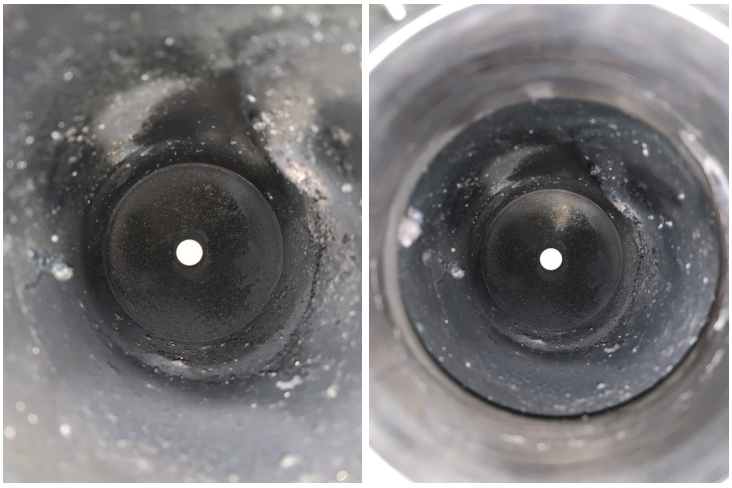

Fig. 5.13 Interior view of the Ouroboros-1 combustion chamber post-hot fire. Splatter of molten Inconel can be seen along the combustion chamber interior as well as the nozzle. The splatter appears to be a combination of both the injector as well as the combustion chamber.

With the combustion chamber wall breached, combustion gases entered the depolymerisation chamber. This was characterised by a decrease in fuel inlet pressure. Furthermore, soot on the exterior of the combustion chamber walls indicates pyrolysis of the propane and combustion within the depolymerisation chamber. Also of note is the presence of cavitation on the surface of the exterior wall and upon closer inspection there are perforations within those areas. These traits suggest cavitation occurring within the depolymerisation chamber as the liquid propane is rapidly vaporized.

Cavitation erosion is a physical process of rapid bubble formation, expansion, and collapse in the liquid field with pressure fluctuation. The rapid formation and collapse of bubbles can result in localised temperatures of up to 5,000 K, pressures of up to 100 MPa inside the bubble, and shockwaves in the liquid field [133, 134]. The results of cavitation erosion can lead to melting of materials with relatively low melting points, high-temperature creep, and even fracture [135]. Typically, cavitation erosion is a result of a region of localised low-pressure in a liquid caused by motion of a body through the liquid such as a propeller or impellar. However, it is possible that in the Ouroboros-1 engine rapid vaporisation of the propane fuel occurred due to the heat transfer from the combustion chamber to the fuel. This would have raised the vapor pressure of the propane fuel and caused it to rapidly boil within the depolymerisation chamber. The result of which is the pitting and fracture shown in Fig. 5.14.

Fig. 5.14 Evidence of propane boiling/cavitation and flow-path within the Ouroboros-1 depolymerisation chamber. The sections with visible cavitation indicate hot-spots on the engine which failed to be effectively cooled by the liquid propane. The route of the liquid fuel flow can be mapped via the cooled sections. The chamber walls are also marked as being porous in the areas of cavitation indicating chamber walls were molten and re-solidified.

The cavitation also mapped out the hot spots along the combustion chamber walls. There is a clear path leading from the fuel inlet of the right image of Figure 5.14 which indicates the route and mixing of liquid propane fuel. It is evident that the fuel flowed quickly to the

injectors causing hot spots to form with limited cooling. This is typically not a failure mode for regeneratively cooled engines as the channels are designed to evenly cool the surface and add strength to the chamber walls rather than an open chamber like Ouroboros-1 which failed to do so.

The location of the hole does not show those same cavitation; the surface is however melted so it is likely that the majority of the present cavitation occurred after the burn-through. Once compromised, the hole would see in influx of fuel which would cool the surface around the hole; however, the other hot spots would experience a sudden drop in fuel pressure resulting in the rapid boiling of the liquid propane. This rapid boiling may have caused an increase in localised pressure which could have contributed to the crushing of the chamber walls at the other locations as well as deforming the weakened chamber walls.

5.4.2 Injector

The injector suffered a different failure which was due to its design. In particular, the self-impinging triplet was identified as the root cause of the oxidiser injector overheating. The injector was designed such that three streams of oxygen intersected directly above the igniter which would facilitate mixing and rapid ignition. However, an unexpected result was that during combustion the self-impinging triplet created a recirculation zone which consisted of a high concentration of oxygen directly above the igniter. This recirculation zone and the highly reactive nature of oxygen likely melted and burned the Inconel of the injector face around the igniter resulting in the crater visible in Fig. 5.15.

Fig. 5.15 View of injector post hot-fire. The center of the injector, where the igniter is located, shows an approximately 15mm crater where the injector face was melted and burned. This crater is likely due to a concentrated area of oxygen reacting with the Inconel injector face caused by the self-impinging triplet oxidizer injector design.

5.5 Ouroboros-1 Conclusions and Lessons Learned

While the Ouroboros-1 engine did not perform as expected, the tests were still useful in terms of lessons learned to be applied to Ouroboros-2 and 3. Additionally, the Ouroboros-1 tests proved to be vital in verifying the nominal operation of the propellant feed system, test stand, linear actuator feed, and data acquisition system. Most importantly, these tests identified that the depolymerisation chamber architecture for autophage engines at the 100 N thrust class is not feasible.

This architecture adds significant complexity that makes the engines prone to failure even when operating in a bi-propellant configuration. In order for this architecture to be feasible, it would require increasing the thrust class of the engine by multiple orders of magnitude in order to utilise turbomachinery or electric pumps. This would allow for the fuselage to be inserted into the depolymerisation chamber at pressures below the combustion chamber pressure and the melted fuel then having its pressure increased by the pumps prior to injection, this would both reduce the required feed force and eliminate the risk of compressive hoop stress failure of the combustion chamber walls. However, this type of design would also require research into topology optimised cooling channels in order to both maximise and control steady melting of the fuselage. This design should also consider the use of hydrocarbon fuels with high boiling points such as RP-1 or Jet-A.

Overall, the direct fuselage insertion architecture was considered to be a more likely candidate for a successful autophage burn than the Ouroboros-1 design. Thus, research regarding the depolymerisation chamber architecture was concluded after this test campaign. Nevertheless, the lessons learned were implemented into the design and test procedures of the subsequent Ouroboros-2 and 3 engines.

Mainly the addition of flow meters to the propellant lines in order to calculate mixture ratio, the addition of bleed valves to reduce gases in the fuel line, a verification procedure of combustion chamber pressure sensor operation prior to testing, spare engines to allow for multiple tests, and the replacement of the impinging jet injectors with a pintle injector.

Chapter 6

Direct Fuselage Insertion Architecture, Bi-Propellant Test Results

6.1 Ouroboros-2 Operational Modes and Test Campaign Overview

The Ouroboros-2 engine was designed according to the proposed direct fuselage insertion architecture detailed in Section 3.3. It was operated solely as a bi-propellant system and used a stainless steel (SS316) plug as a substitute for the HDPE fuselage. By operating the engine in a bi-propellant configuration rather than in autophage, a performance baseline could be set prior to the Ouroboros-3 autophage tests which used the same direct fuselage insertion architecture. Thus, Ouroboros-2 functioned as a control group leading up to the later autophage test campaigns and data analysis comparing the two configurations was used to identify the impact of introducing a third propellant in the form of an HDPE rocket fuselage.

A total of 5 steady state tests were run at 3 target inlet conditions shown in Table 6.1. The Ouroboros-2 tests were to be operated in short bursts based on the lessons learned from Ouroboros-1 to reduce combustion chamber wall temperature and extend the life of the engine. The first two tests were designed to operate the engine at fuel rich inlet conditions for 10 seconds followed by a 2 second off-time and then an engine restart for an additional 10 seconds of steady state operation. The decision was made to test the engine in fuel rich conditions because it would decrease the combustion chamber temperature and again extend the life of the engine. This test was done to both set a performance baseline at those inlet conditions and demonstrate that the engine was capable of an engine restart. The engine restart would verify that the engine both had a sufficient chamber pressure rise time and decay time such that the Ouroboros-3 could be operated in a pulsed operating mode for later tests.

Tests 2a & 2b each operated the engine for a burn time of approximately of 5 seconds with slightly adjusted inlet conditions based on the results from tests 1a & 1b (the target inlet conditioned remained the same, however, the feed system pressure regulators and needle valves were adjusted such that the inlet conditions were closer to the targets). There would also be a long dwell time of approximately 40 seconds between firings. This would not only

Table 6.1 Ouroboros-2 steady state target inlet conditions.

			Pressure, bar				Mass Flow Rate, g/s	
Test no.	t_b, s	F_t, N	P_c	P_{ox}	P_{fuel}	MR	$\dot{m}_{ox}$	$\dot{m}_{fuel}$
1a & b	10.0	101.2	5.00	6.00	6.00	1.25	40.52	32.41
2a & b	5.0	101.2	5.00	6.00	6.00	1.25	40.52	32.41
3	10.0	154.5	7.00	8.40	8.40	1.25	56.51	45.20

drive engine operation closer to the desired inlet conditions but also provide a performance baseline for an engine restart after a long dwell time between firings. This was particularly important as a control group which could be compared to future Ouroboros-3 autophage tests with long dwell times between engine restarts (allowing the fuselage to melt and settle inside the combustion chamber).

The final Ouroboros-2 test operated the engine at a high throttle setting to set the upper limit of the operating box. This was also done to verify that the engine and engine seals would operate nominally at higher combustion chamber pressures and temperatures; it was considered a possibility that the additional HDPE fuel in the subsequent Ouroboros-3 autophage tests could require a longer burn time for the engine to reach a nominal engine temperature that could melt the HDPE fuel. Thus, this test was intended to test the engine to destruction and use the results to set an upper limit of the engine operating box.

In summary, the Ouroboros-2 autophage tests were very successful in verifying the direct fuselage insertion architecture. They demonstrated both nominal propellant injection through the pintle injector, nominal engine thrust at standard inlet conditions, engine restart capabilities with low chamber pressure rise and decay times, engine throttling, and set performance baselines that the Ouroboros-3 autophage engines could be evaluated against.

The Ouroboros-2 engine was operated using the same propellant feed system as the previous Ouroboros-1 tests; however, it included modifications that allowed mass flow rate control and measurement for both the oxidiser and fuel propellant lines. A table of all the Ouroboros-2 sensors can be seen in table 6.2. Unfortunately, the oxidiser mass flow rate was unable to be calculated due to an error with flow meter installation so it has been omitted from the sensor list and performance analysis. However, due to all of the other performance data gathered, both the approximate oxidiser flow rate and mixture ratio can be calculated using a chemical equilibrium analysis at the measured chamber pressure and fuel mass flow rate for each test. The combustion chamber thermocouple was also omitted due to an error with the cold-junction compensation.

Table 6.2 Ouroboros-2 sensors and sampling frequencies.

Location	Type	Unit	Frequency, f_s
Actuator, F_F	feed force load cell	N	1 kHz
Test stand, F_T	thrust load cell	N	1 kHz
Fuel Inlet, P_f	pressure transducer	Bar	1 kHz
Oxidizer Inlet, P_o	pressure transducer	Bar	1 kHz
Combustion Chamber, P_c	pressure transducer	Bar	1 kHz
Fuel Mass Flow Rate, $\dot{m}_{fuel}$	flow meter	g/s	1 kHz

6.2 Tests 1a & 1b: Fuel Rich Inlet Conditions with Engine Restart

6.2.1 Test Data

The first test of the Ouroboros-2 engine was programmed to operate in steady state for 10 seconds, followed by a 2 second shutdown, restart, and another 10 seconds of steady state operation. Each ignition event was designated as its own sub-test (Tests 1a & 1b). This particular sequence was chosen to ensure the engine reached steady state and to verify engine restart capabilities. The test timeline and resulting performance data are shown below in Fig. 6.1.

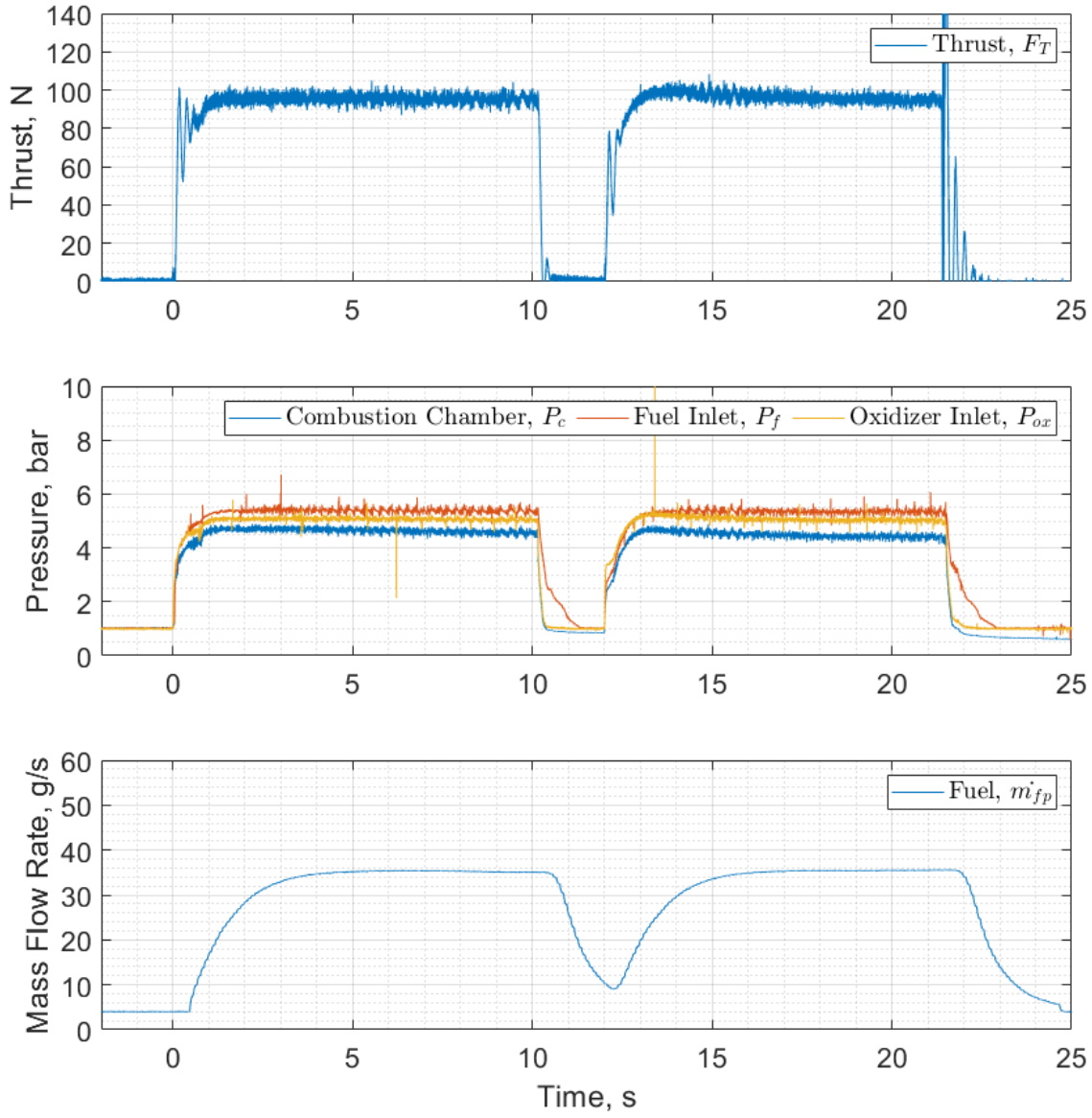

Fig. 6.1 Ouroboros-2 10 second steady state bi-prop test performance chart at fuel rich inlet conditions. Engine performance appears to be nominal. Steady state thrust is approximately 95.54 N with a combustion chamber pressure of 4.65 bar.

Test Timeline

T - 05.0 s Engine countdown begins.

T - 00.0 s Control valves open, oxidizer reaches nominal pressure, engine ignition.

T + 00.8 s Combustion chamber pressure reaches 90% of full scale output.

T + 01.0 s Engine reaches steady state combustion with an average thrust of 95.54 N.

T + 05.0 s Fuel mass flow rate reaches steady state.

T + 10.2 s Propellant control valves are closed, initiating engine shutdown.

T + 10.4 s Combustion chamber pressure decays to ambient pressure.

T + 12.0 s Control valves are opened for the second time, the engine ignites and is successfully restarted.

T + 12.6 s Combustion chamber pressure reaches 90% of full scale output.

T + 13.0 s Engine reaches steady state combustion with an average thrust of 96.58 N.

T + 21.5 s Propellant control valves are closed for the second time, initiating engine shutdown.

T + 21.7 s Combustion chamber pressure decays to ambient pressure.

6.2.2 Performance Analysis

Experimental Results

The data provided in Table 6.3 shows the mean engine performance compared to the target inlet conditions of tests 1a & 1b. Both the inlet conditions and resulting thrust were slightly below the target; however, the engine performance was generally nominal and within measurement error. It was noted that the calculated mixture ratio had the largest discrepancy compared to the target, this result would drive the decision of starting Ouroboros-3 autophage tests at a mixture ratio of 1.00 to correlate with the bi-propellant test conditions.

Table 6.3 Ouroboros-2 tests 1a & 1b mean performance data.

			Pressure, bar				Mass Flow Rate, g/s	
Test no.	t_b, s	F_t, N	P_c	P_{ox}	P_{fuel}	MR[1]	$\dot{m}_{ox}$	$\dot{m}_{fuel}$
Target	10.0	101.2	5.00	6.00	6.00	1.25	40.52	32.41
1a	10.2	95.54	4.65	5.07	5.38	1.07	37.53	35.24
1b	9.5	96.58	4.49	5.07	5.34	1.01	35.35	35.41
CEA	-	90.97	4.65	-	-	1.07	37.53	35.24

[1] As discussed in Section 6.1, an issue with the installation of the oxidiser mass flow meter prevented the recording of oxidiser mass flow rate and experimental mixture ratio. However, using a chemical equilibrium analysis with the recorded combustion chamber pressures and fuel mass flow rates as inputs yielded a calculated oxidiser mass flow rate and mixture ratio which have been included in the table.

There was minimal variation between the inlet conditions of tests 1a & 1b and the resulting chamber pressure and thrust were similar. The higher thrust of test 1b can be attributed to a warm engine start whereas test 1a was conducted as a cold start. Albeit, the measured mean combustion chamber pressure of test 1b was lower than 1a which contradicts the thrust measurement; however, the combustion chamber pressure was also observed to decrease below atmospheric pressure at the conclusion of test 1b which could be an indicator of possible sensor drift or a partial blockage of the combustion chamber pressure sensor port. Thus, it is reasonable to conclude that the actual combustion chamber pressure of test 1b was higher than the measured 4.49 bar. A chemical equilibrium model was also conducted at the operating conditions and resulted in a theoretical thrust of 90.97 N; thus, the actual engine thrust is within a +/-5% margin of error.

Specific Impulse Calculation

The specific impulse of the engine was calculated using the recorded engine thrust, mean fuel mass flow rate and the calculated mean oxidiser mass flow rate with Eq. (6.1).

$$I_{sp} = \frac{F_T}{(\dot{m}_{ox} + \dot{m}_{fuel})\, g_0} \tag{6.1}$$

This resulted in a live estimation of the specific impulse shown in Figure 6.2 and an average I_{sp} of 135 s across the entire operating time. This aligned closely to the theoretical sea level expansion I_{sp} of 130 s when the same mixture ratio and engine thrust are put into the chemical equilibrium analysis model. This is within a margin of error for variations in atmospheric pressure, temperature, and density as well as the uncertainty in the actual oxidiser mass flow rate.

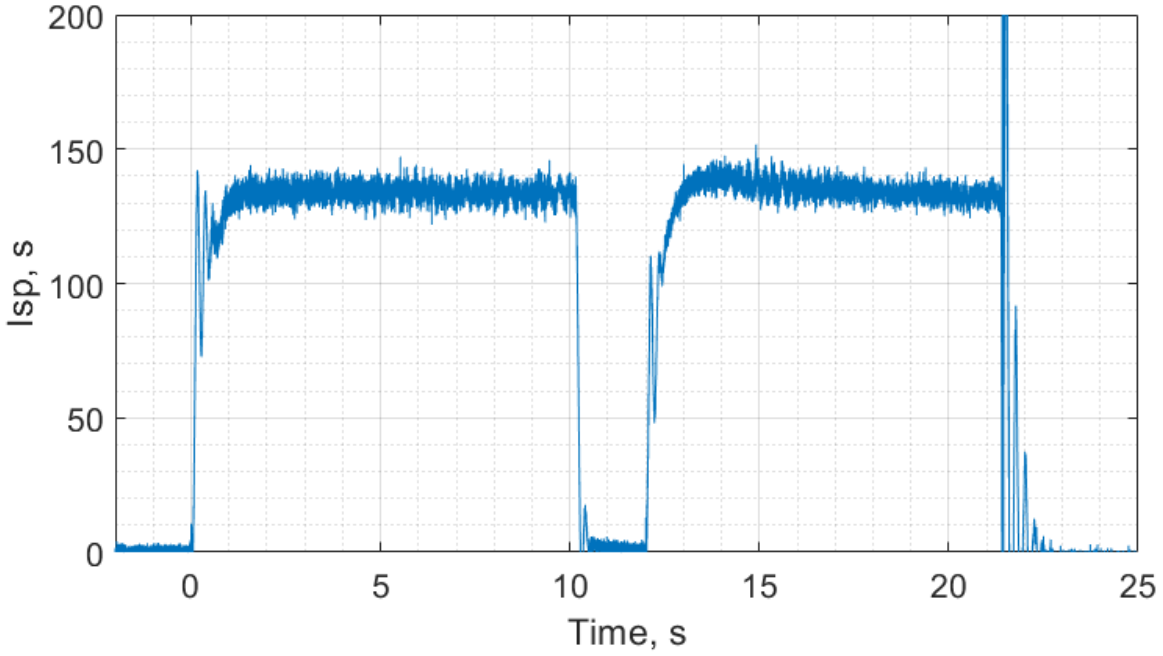

Fig. 6.2 Ouroboros-2 specific impulse from test 1 performance data.

Engine Restart and Chamber Pressure Rise/Decay Time

One of the other major results from this test was a demonstration of a successful engine shutdown and restart to prove the feasibility of testing the subsequent Ouroboros-3 autophage engine in a pulsed operating mode. Pulsed mode was considered as a possible method for operating autophage engines due to the off-time reducing the combustion chamber pressure which could theoretically reduce the required feed force to drive the fuselage into the engine. Therefore, determining the combustion chamber pressure rise and decay times would characterise a range of potential frequencies and duty cycles to test at which could control the feed rate of the autophage fuel.

The chamber pressure rise time, t_r, was defined as the time it takes in milliseconds for chamber pressure to reach 90% of full scale output; decay time, t_d was defined as the time in milliseconds for the chamber pressure to reach 10% of full scale output from valve shutoff. Figure 6.3 compares the rise and decay times of tests 1a & 1b respectively with both 10% and 90% of combustion chamber pressure full scale output shown in red and the calculated results are shown in Table 6.4.

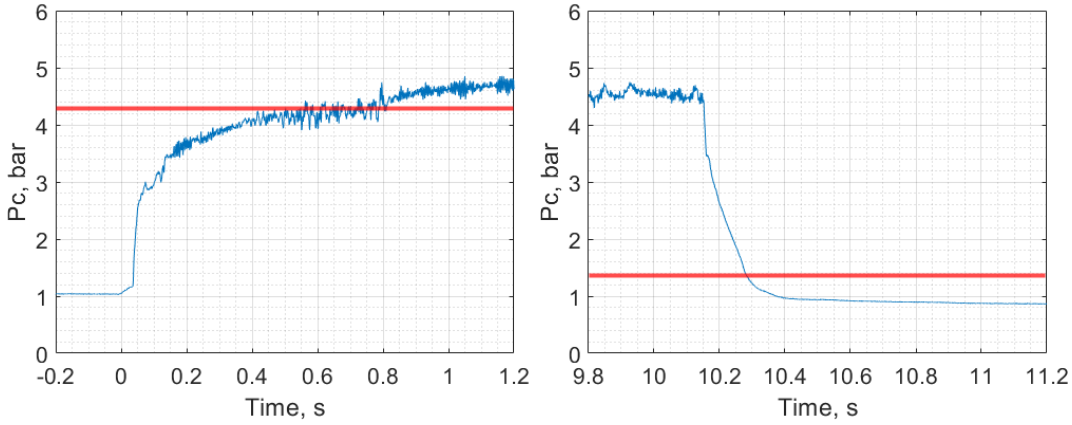

(a) Test 1a rise time

(b) Test 1a decay time

(c) Test 1b rise time

(d) Test 1b decay time

Fig. 6.3 Comparison of the Ouroboros-2 combustion chamber pressure rise and decay times between a cold and warm engine start for tests 1a & 1b.

The observed rise time is noticeably longer for the cold start of the engine while there is no significant difference between the decay times. This behavior is as expected since a warmer

Table 6.4 Ouroboros-2 tests 1a & 1b chamber pressure rise and decay times.

Test no.	F_t, N	P_c	MR	t_r, ms	t_d, ms
1a	95.54	4.65	1.07	750	125
1b	96.58	4.49	1.01	600	150

engine will correlate with faster propellant ignition. In any case, the engine demonstrated an effective ability to reignite and reach nominal operating pressures faster than the initial ignition. This verifies that pulsed mode operation may be feasible.

Considering both the maximum rise time of 750 ms and the decay time of 150 ms at these inlet conditions, we can make an approximation that to successfully operate in pulsed mode the engine should have a minimum on-time of 750 ms and a minimum off-time of 150 ms. This would allow the engine to both reach performance targets while gaining the benefits of a lower chamber pressure for fuselage insertion during the off-time. Ideally, the off-time should be longer than the minimum in order to increase the duration when the fuselage can be inserted at low chamber pressures.

This analysis of the chamber pressure rise and decay times was used to set the minimum feasible frequency and duty cycle of pulsed mode operation. Using a 750 ms on-time and a 250 ms off-time (including a 100 ms delay for fuselage insertion) correlates with an operating frequency of 1 Hz at a 75% duty cycle. This operating mode was thus identified as the feasible limit for standard inlet conditions and all other pulsed modes detailed in Section 4.5.2 and Table 4.4 were derived from this analysis.

Observed Combustion Instability (Chug)

Analysis of the test footage (Fig. 6.4) showed a low-frequency oscillation both visually in the plume and over audio throughout the steady state burn of both Test 1a and 1b. No shock diamonds were visible in the plume suggesting close to nominal expansion; however, there was clearly a combustion instability present.

Referencing the performance data in Figure 6.1 we saw the resulting thrust and combustion chamber pressure were in line with the theoretical performance for standard inlet conditions. The engine was nominally generating 95.45 N of thrust with a chamber pressure of approximately 4.65 bar. However, the oscillation seen in the test footage can also be seen in the performance data; particularly in the combustion chamber and fuel inlet pressure. An instability that shows a coupling between the combustion chamber pressure and propellant feed system is typically an indication of chug [125]. Chug is a low frequency combustion instability occurring below 500 Hz that is described as having pulsed-combustion. It can be caused by low throttle settings and low pressure-drop injectors [136]. The presence of this combustion instability is confirmed by the frequency analysis in Section 6.2.3.

The chug instability is likely to have manifested due to the design of the pintle injector whereby the oxidiser was injected at high pressure through the annulus with the oxidiser streamlines covering the pintle gap. This may have created an area of higher pressure at the pintle gap preventing the injection of the fuel into the combustion chamber. Increasing the inlet pressures was determined to be a possible solution that could eliminate the chug. This

was a secondary driver for slightly increasing the propellant feed system settings of tests 2a & 2b; the main driver being to reach the target combustion chamber pressure of 5.00 bar. However, the chug was a significant driver in increasing inlet conditions for test 3 to see if the instability would dissipate at higher throttle settings.

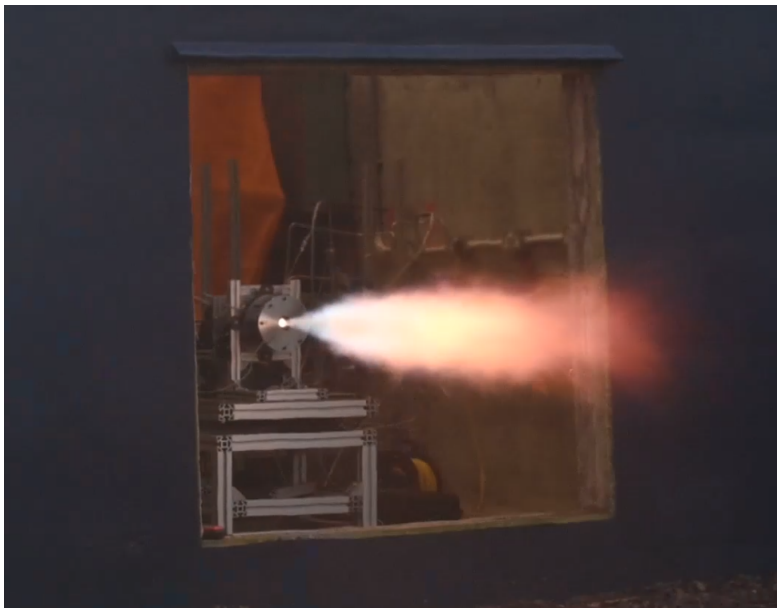

Fig. 6.4 Ouroboros-2 10 second steady state bi-prop test photo. A large plume can be seen coming from the engine due to a low-frequency combustion instability in the engine (chug) caused by the coupling of the propellant feed system and the combustion processes.

6.2.3 Frequency Analysis

A frequency analysis was conducted to verify the oscillation and identify what frequency range the engine is operating in. The results are shown in Figures 6.5 and 6.6. The data was collected at a sampling frequency of 1 kHz resulting in a maximum frequency analysis range of 500 Hz for the bi-propellant tests. This was sufficient in detecting low-frequency instabilities; however, the sampling frequency was insufficient to detect any high-frequency instabilities which occur at over 1 kHz [137, 138]. Additionally, the frequency analysis was only conducted on the thrust, combustion chamber pressure, fuel inlet pressure and oxidiser inlet pressure; the fuel mass flow rate was not considered since the sensor used was a variable area flowmeter which does not have the required sensitivity to detect instabilities.

The results of the spectrogram clearly indicate a combustion instability at approximately 200 Hz. This pattern is indicative of the previously discussed engine chug. However, the inlet pressure sensors did not detect any instabilities which suggests that the chug is likely coupling with the pintle injector rather than the feed system upstream of the injector manifolds which is where both inlet pressure sensors are located. Overall, the engine chug is likely due to the low inlet pressures and results in the unstable engine plume seen in the videos; eliminating the combustion instability could likely be achieved by increasing the inlet pressures or operating at off-nominal inlet conditions.

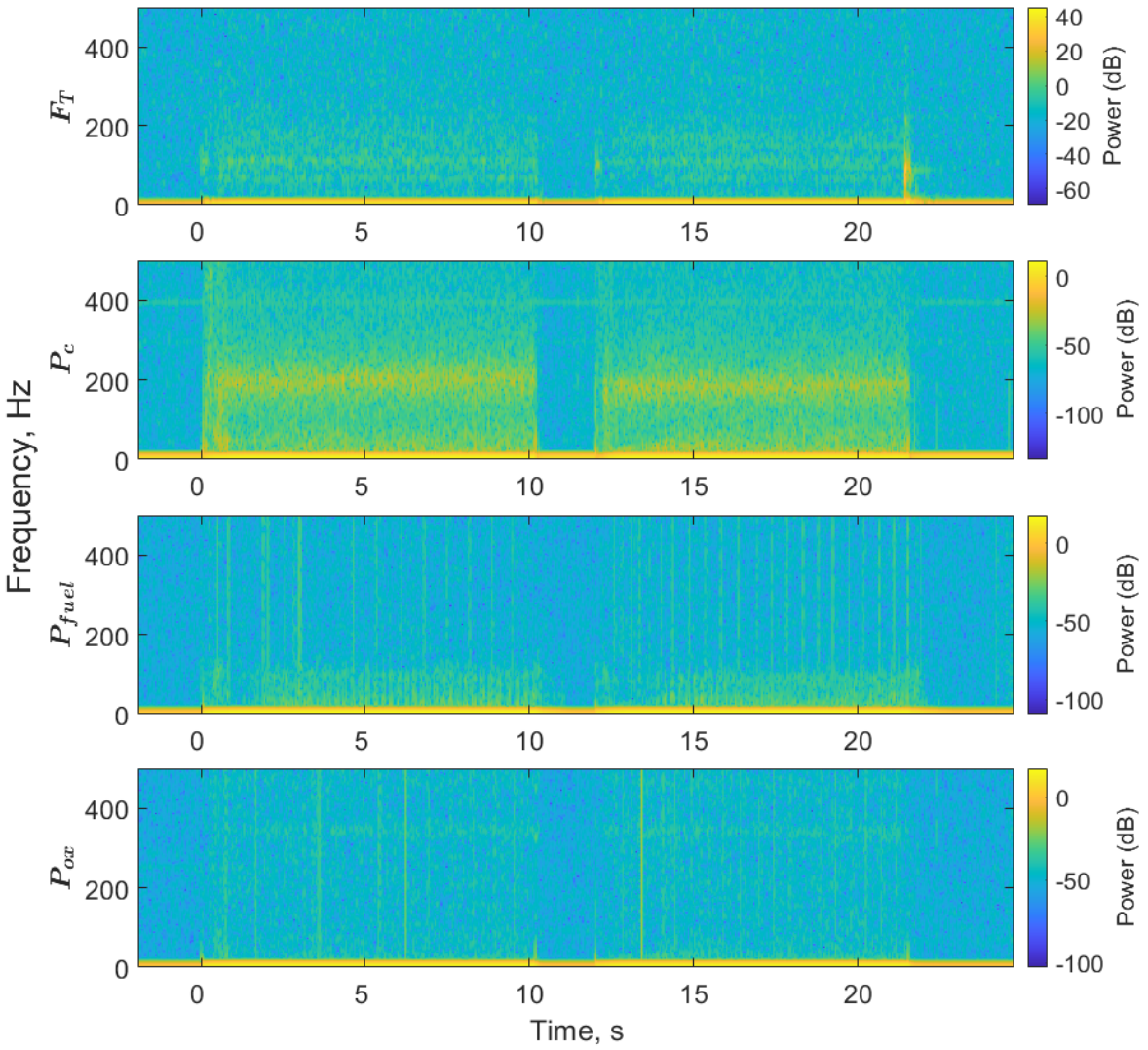

Fig. 6.5 Ouroboros-2 test 1 spectrogram. A low frequency combustion instability is seen at approximately 200 Hz in the combustion chamber pressure. This confirms previous indications of a combustion instability known as engine chug and is likely due to low inlet pressures.

The persistence diagram also confirmed chug occurring at 200 Hz. While chug is generally non-destructive to engine components due to its low power, it can also induce or be an indicator of higher frequency combustion instabilities. High frequency instabilities such as screech can lead to rapid engine failure and disintegration. The Ouroboros-2 tests did not consider high-frequency combustion instabilities; however, after detecting chug, it was determined to increase the sampling frequency range for the later autophage Ouroboros-3 tests to allow for the detection of high-frequency instabilities up to 5 kHz.

Additionally, of note for all subsequent frequency analyses is the lack of a repeating oscillation such as what was observed in the Ouroboros-1 frequency analysis in Section 5.3. That oscillation was verified to be an issue caused by a grounding loop in the 4-20 mA to 0-10 V sensor conversion board and was corrected for this test campaign.

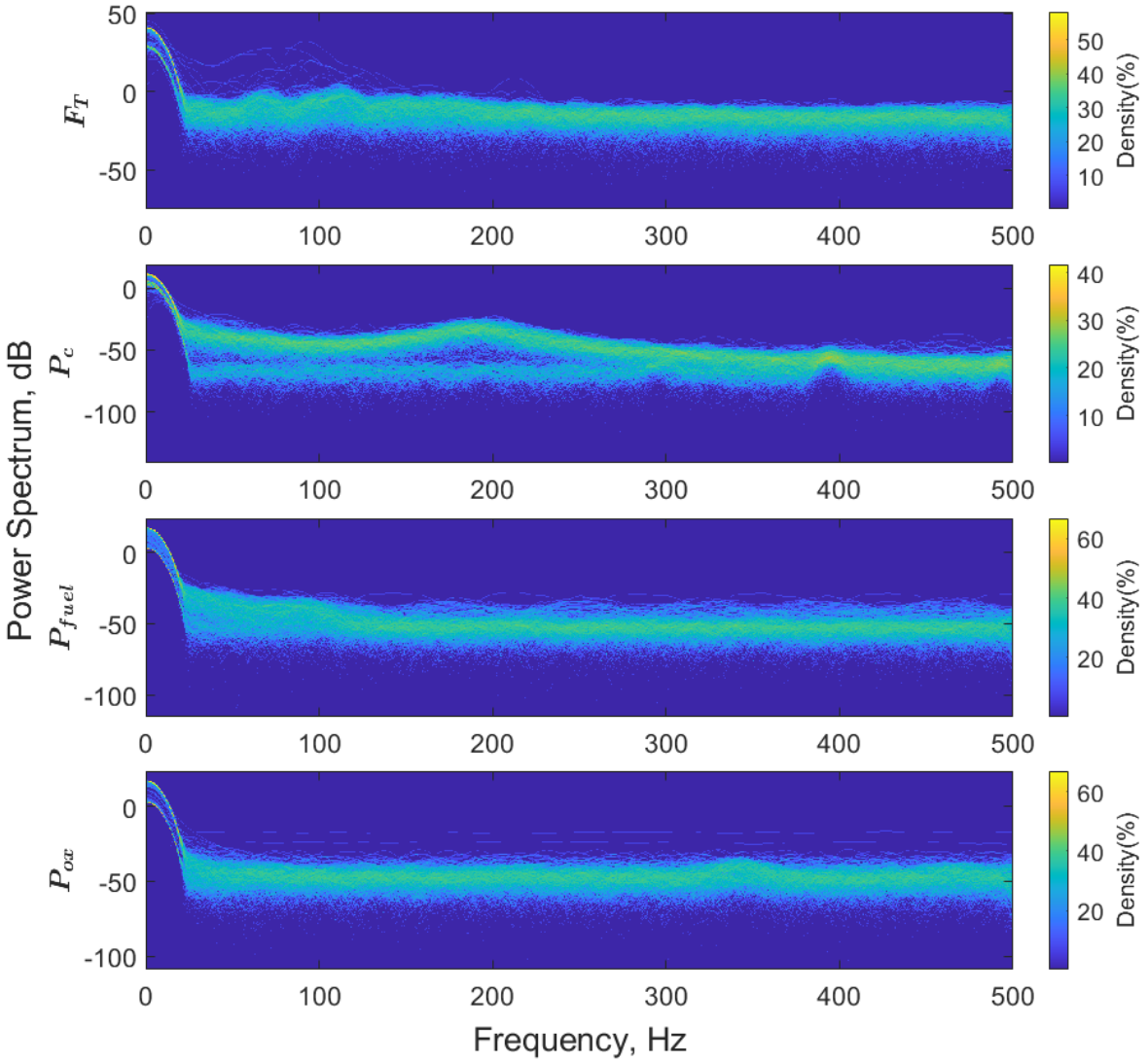

Fig. 6.6 Ouroboros-2 tests 1a & 1b persistence diagram. The sensor sampling frequency was set to 1 kHz so only low-frequency combustion instabilities were capable of being detected. The combustion chamber pressure sensor showed a clear peak at 200 Hz corroborating that the engine was experiencing chug at these inlet conditions. While the other sensors showed general roughness in the spectrogram, the persistence diagram did not indicate any clear power spectrum peaks in the data.

6.3 Tests 2a & 2b: Adjusted Inlet Conditions with Long Dwell Time Engine Restart

6.3.1 Test Data

The second set of tests of the Ouroboros-2 engine were designed to operate the engine in steady state for two, 5 second firings with a long dwell time of at minimum 40 seconds between ignitions; these were designated as sub-tests 2a & 2b. The upstream propellant feed system pressure regulators and needle valves were slightly adjusted from the previous tests

in an effort to dial into the target inlet conditions (which were the same for tests 1 and 2). Performance results can be seen in Figure 6.7 below.

This particular sequence was chosen to again verify engine restart capabilities and the chamber pressure rise and decay times; but the long dwell time was implemented in order to set a performance baseline which could then be compared to an autophage engine test with a long dwell-time during which the HDPE fuselage could melt and fill the combustion chamber.

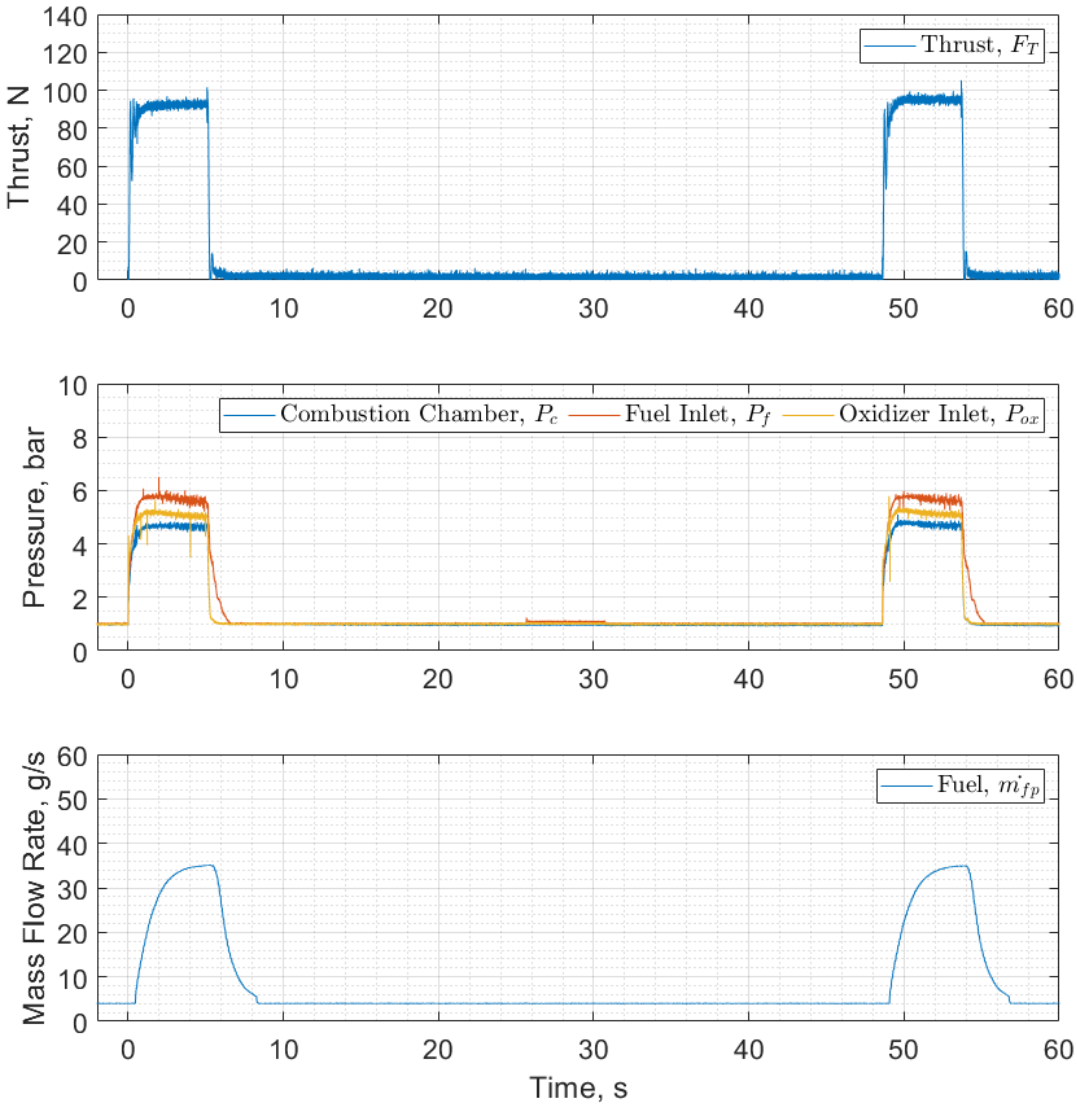

Fig. 6.7 Ouroboros-2 tests 2a & 2b performance chart at adjusted fuel rich inlet conditions with a long dwell time.

Test Timeline

T - 05.0 s Engine countdown begins.

T - 00.0 s Control valves open, oxidizer reaches nominal pressure, engine ignition.

T + 00.6 s Combustion chamber pressure reaches 90% of full scale output.

T + 01.0 s Engine reaches steady state combustion with an average thrust of 92.25 N.

T + 05.1 s Propellant control valves are closed, initiating engine shutdown.

T + 05.3 s Combustion chamber pressure decays to ambient pressure.

T + 26.0 s Purge valves are opened for a 5.0 second duration.

T + 48.6 s Control valves are opened for the second time, the engine ignites and is successfully restarted.

T + 49.2 s Combustion chamber pressure reaches 90% of full scale output.

T + 49.5 s Engine reaches steady state combustion with an average thrust of 94.94 N.

T + 53.7 s Propellant control valves are closed for the second time, initiating engine shutdown.

T + 53.9 s Combustion chamber pressure decays to ambient pressure.

6.3.2 Performance Analysis

Experimental Results

The data provided in Table 6.5 shows the mean engine performance compared to the target inlet conditions of tests 2a & 2b. While the upstream propellant feed system controls were adjusted slightly to increase the inlet pressures, the adjustments were insufficient to significantly change the engine performance from tests 1a & 1b. Both the inlet conditions and resulting thrust were slightly below the target, and the mean measured engine thrusts were actually lower than tests 1a & 1b even though the combustion chamber pressures were approximately equal.

This could be a result of the engine operating at a lower mass flow rate than what was calculated due to skewed results. Previous tests showed that the fuel mass flow rate reached steady state after approximately 5 seconds post engine ignition (which would correlate with the total burn time of these tests). Additionally, the flow rate still showed a slight positive slope at engine shutdown indicating that the true fuel mass flow rate was not recorded. Rather than taking the mean fuel mass flow rate of the last 100 ms of the burn if we instead integrate the area under the curve we can calculate the total fuel mass to pass through the flow meter. However, it is important to consider that this is an approximation and that the flow meter data has a delayed response since it is upstream of the engine, a minimum measurement limit of 4.00 g/s, and this calculation method will overestimate the total propellant used due to including losses in filling the propellant lines from the control valves to the engine.

Nevertheless, the total fuel mass used during test 2a was calculated to be 186.2 g. When divided by the total burn time the fuel mass flow rate was calculated at 36.50 g/s. This same process was used to estimate the total fuel mass used across both tests 1a & 1b and then divided by the cumulative engine burn time which yielded a total fuel mass of 710.4 g and a mean fuel mass flow rate of 36.06 g/s.

Compared to the measured mean fuel mass flow rate of tests 1a & 1b, this calculation method yielded a 2% overestimation; thus, a correction factor for this calculation method

can be defined as $C_{f(\dot{m})} = 0.98$. Applying this correction factor to the calculated fuel mass flow rate of test 2a yielded a corrected fuel mass flow rate of 35.77 g/s which was noticeably higher than that of tests 1a & 1b. Using the corrected value resulted in a lower mixture ratio which supports the hypothesis that the lower thrust was a result of higher fuel mass flow rates. However, the thrust was still lower than the previous tests even with this correction.

Another factor which may have impacted the recorded test 2 thrust under-performance could be ablation of the graphite nozzle causing a slight increase in the nozzle throat area which would reduce engine thrust. However, after the tests were concluded, the nozzle throat diameter was measured to be 16.0 mm, matching the pre-test throat diameter, and showed no ablation or significant change in geometry that would have affected performance. Other sources of error could include a slight shift in the alignment of the test stand or thrust load cell resulting in off-axis thrust measurement. When compared to the results of a chemical equilibrium analysis at the operating conditions though, the thrust is within +/-2% of the theoretical thrust. Thus we can conclude that the results are within a small margin of error such that engine performance during these tests was considered nominal.

Nevertheless, the slight adjustments to the upstream propellant feed system were inadequate to significantly change the engine inlet conditions. This resulted in lessons learned that would be applied to test 3 in order to experimentally determine the pressure drop across the propellant feed system such that we would have greater control and likelihood of achieving the desired inlet conditions for the Ouroboros-3 autophage tests. As mentioned in Section 6.2.2, since all of these tests operated the engine at a mixture ratio near 1.00 it was decided to start the Ouroboros-3 autophage tests at a mixture ratio of 1.00 to correlate with the bi-propellant test conditions.

Table 6.5 Ouroboros-2 tests 2a & 2b mean performance data.

			Pressure, bar				Mass Flow Rate, g/s	
Test no.	t_b, s	F_t, N	P_c	P_{ox}	P_{fuel}	MR[2]	$\dot{m}_{ox}$	$\dot{m}_{fuel}$
Mean Fuel Mass Flow Rates								
Target	5.0	101.2	5.00	6.00	6.00	1.25	40.52	32.41
2a	5.1	92.25	4.66	5.10	5.69	1.08	37.78	34.95
2b	5.1	94.94	4.73	5.16	5.69	1.11	38.55	34.92
Corrected Fuel Mass Flow Rates								
Target	5.0	101.2	5.00	6.00	6.00	1.25	40.52	32.41
2a	5.1	92.25	4.66	5.10	5.69	1.05	37.46	35.77
2b	5.1	94.94	4.73	5.16	5.69	1.07	35.71	35.77
CEA	-	93.03	4.73	-	-	1.07	35.71	35.77

Specific Impulse Calculation

As covered in Section 6.2.2, the specific impulse of the test was calculated and a live estimation is shown in Figure 6.8; for the calculation, the corrected fuel mass flow rates were used. The engine demonstrated an average I_{sp} of 130 s across the entire operating time which closely matched a theoretical sea level expansion I_{sp} of 127 s calculated via the chemical equilibrium

[2]See footnote 1 from Table 6.3.

analysis model. Additionally, I_{sp} was slightly lower than that of tests 1a & 1b which can be explained by the lower mixture ratio.

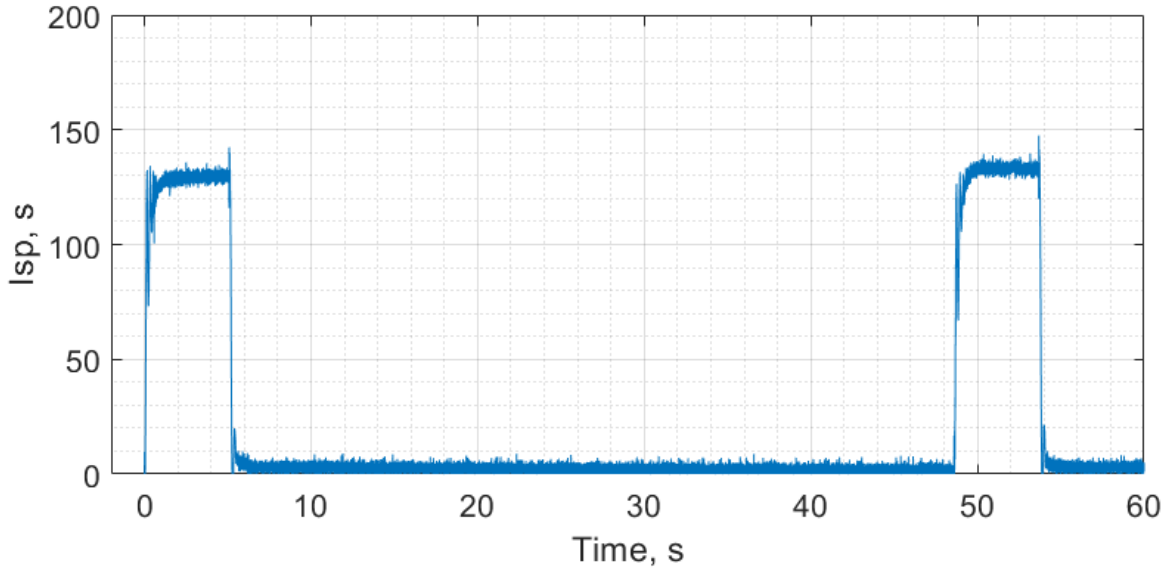

Fig. 6.8 Ouroboros-2 specific impulse from test 2 performance data.

Long Dwell Time Engine Restart and Chamber Pressure Rise/Decay Time

For the start of test 2, the Ouroboros-2 engine had already been warmed up since there was only a 10 minute delay from the previous tests. Therefore it was expected that the chamber pressure rise and decay times should closely match that of test 1b. Analysis of the data shown in Fig. 6.9 and Table 6.6 confirmed this and showed no major variations between tests 1b, 2a, & 2b.

However, an interesting feature was discovered across these charts. During tests 2a & 2b there was an oscillation from approximately 400-600 ms after engine start. This oscillation was present in test 1a with a longer duration from 400-800 ms but it was not observed during test 1b. Thus, this result was classified as an indicator of a potential combustion instability occurring at startup whereby the flame propagated from the igniter to the rest of the combustion chamber before reaching steady state and the instability being dampened out. This could be an area of concern for future engine designs and tests because even short duration combustion instabilities (specifically the transverse instability mode) can result in rapid engine failure as was seen in the development of the F-1 engine for the Saturn V launch vehicle [132]. These results served as additional justification to increase the sampling frequency to 10 kHz for the Ouroboros-3 autophage tests in an effort to characterise any instabilities during the ignition transient.

Overall, the long dwell time between tests had no significant impact on engine performance. This was expected but nonetheless verified in order to set a performance baseline for Ouroboros-3 tests to be compared against.

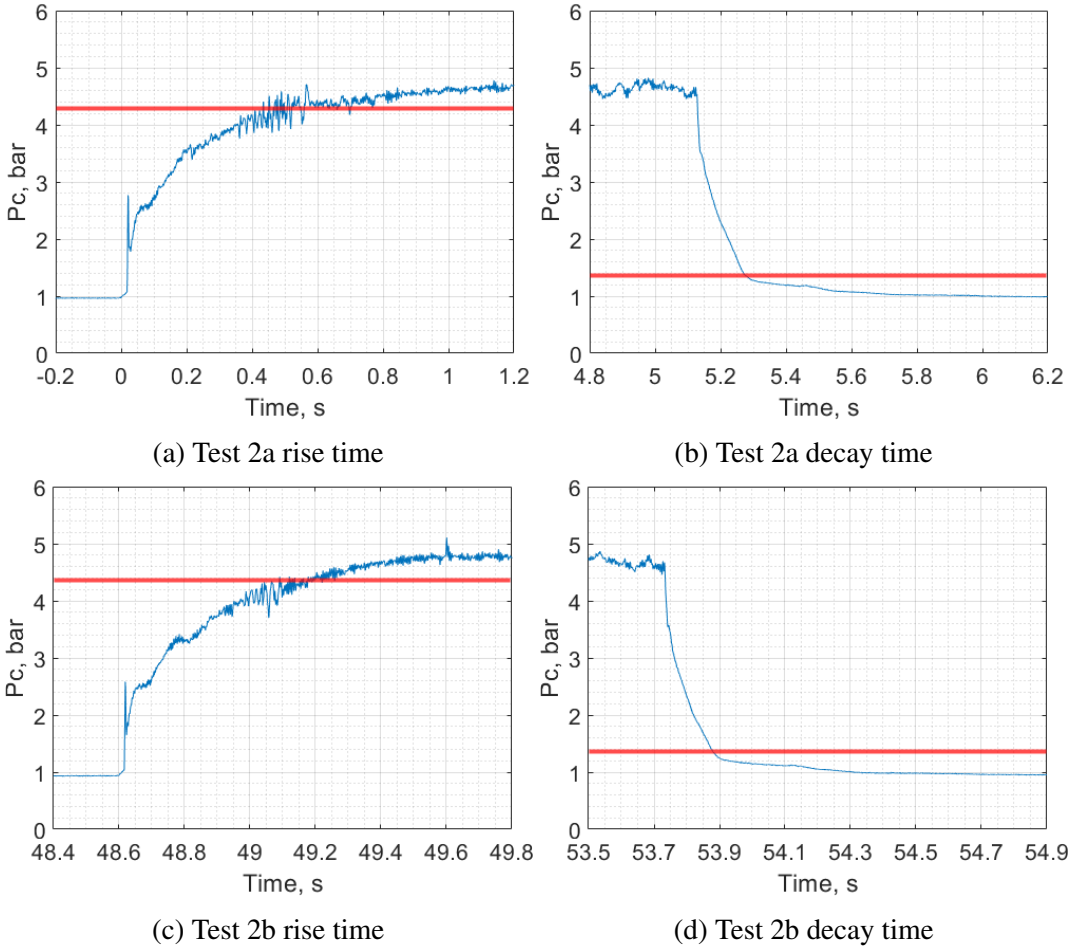

(a) Test 2a rise time

(b) Test 2a decay time

(c) Test 2b rise time

(d) Test 2b decay time

Fig. 6.9 Comparison of the Ouroboros-2 combustion chamber pressure rise and decay times for tests 2a & 2b.

Table 6.6 Ouroboros-2 tests 2a & 2b chamber pressure rise and decay times.

Test no.	F_t, N	P_c	MR	t_r, ms	t_d, ms
2a	92.25	4.66	1.05	600	150
2b	94.94	4.49	1.07	600	150

Plume Analysis and Combustion Instability (Chug)

The plume of these tests was noticeably different from that of the previous tests. There was very little visible plume which suggests complete combustion within the chamber and a high combustion efficiency; however, sets of sparks were also emitted from the nozzle intermittently. These were indications of some sort of ablation occurring within the engine; either steel within the combustion chamber melting or an ablation of the graphite nozzle resulting in debris being expelled from the engine.

The engine also did not exhibit the characteristic plume flashing and sound of chug that was observed during tests 1a & 1b. The lack of these observations does not however exclude the existence of chug which can manifest differently even under the same test conditions. Moreover, the frequency analysis in Section 6.3.3 later confirmed that chug was still present.

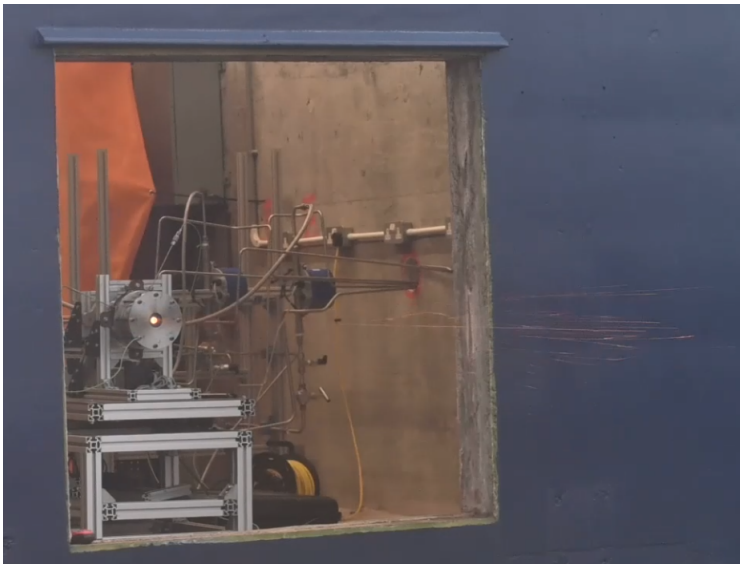

Fig. 6.10 Ouroboros-2 5 second steady state bi-prop test photo. No plume is visible; however, sparks were intermittently emitted from the nozzle suggesting ablation of either the combustion chamber or nozzle.

6.3.3 Frequency Analysis

As for previous tests, a frequency analysis was conducted on the data to detect and verify the presence of any combustion instabilities. Due to the similarity between the performance results of tests 2a & 2b, the spectrogram was a close up of only test 2a in order to provide a shorter duration and see the potential combustion instability at engine ignition discussed in Section 6.3.2.

The first thing of note regarding the spectrogram was the presence of an instability at 200 Hz which again confirmed the presence of chug at these inlet conditions. However, the power density of the instability was characteristically lower than it was for tests 1a & 1b which correlated with the lack of visual and audio indicators as described in Section 6.3.2. Thus, we can conclude that the instability had a lower intensity at these inlet conditions whereby the fuel and oxidiser inlet pressures were slightly higher. Nevertheless, chug is known to reduce engine performance by up to 8% [136], and since these tests had lower recorded thrust than tests 1a & 1b (even at similar inlet conditions) this difference in manifestation of the instability could also be a factor in the performance variation.

In addition to engine chug, the spectrogram also clearly indicates unstable behavior of both the thrust and combustion chamber pressure approximately 400-600 ms after the test start. This was identified as an area of interest in Section 6.3.2 where an oscillation was observed in the chamber pressure which could be due to unstable propogation of the flame throughout the combustion chamber at ignition. The spectrogram confirmed this as a combustion instability by the tell-tale increase in power within the 400-600 ms range. The instability appeared to mainly be between 0-200 Hz and it did quickly dampen out which suggests that it is unlikely to lead to catastrophic engine failure. However, a higher sampling frequency was implemented for the subsequent Ouroboros-3 tests.

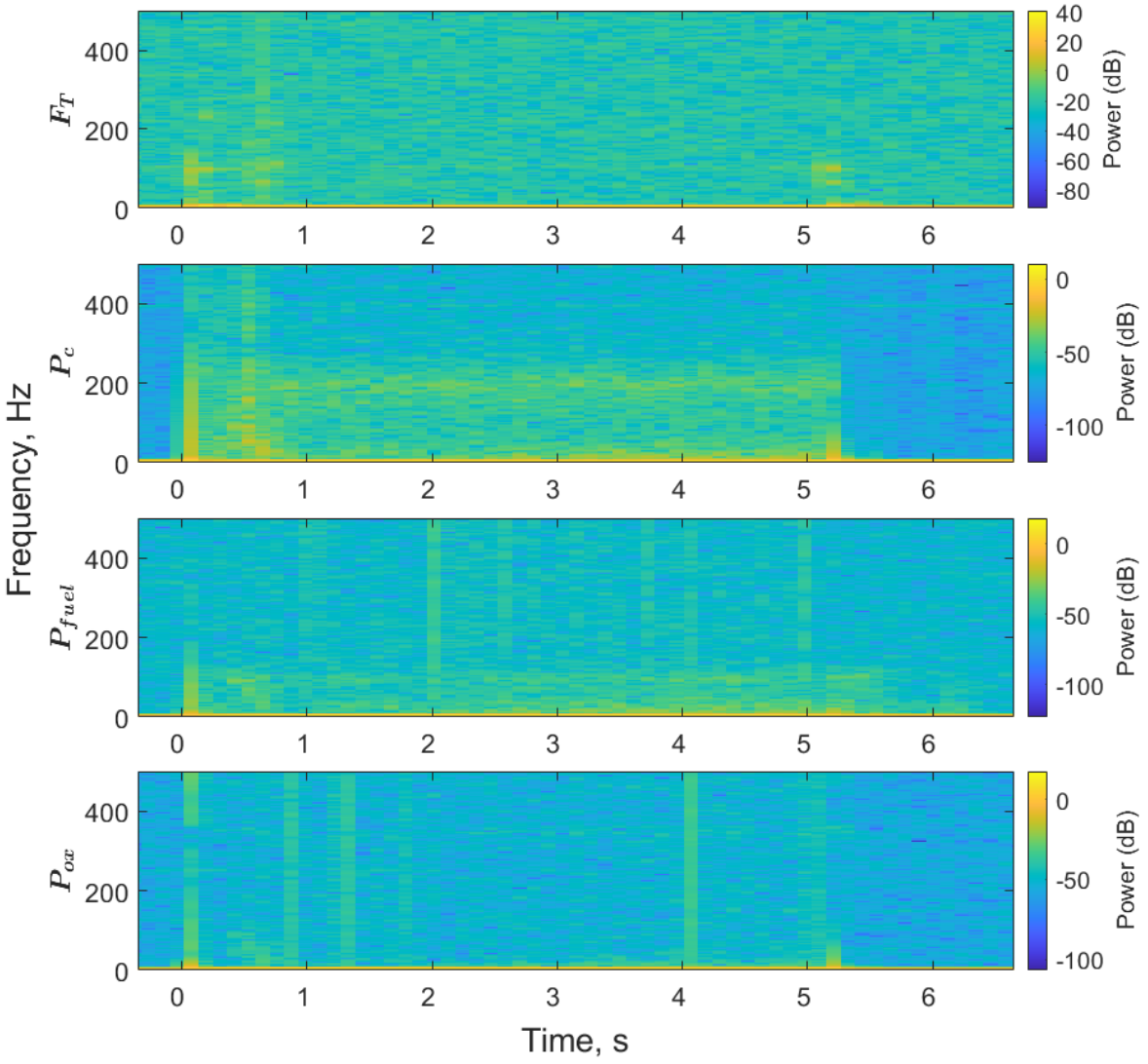

Fig. 6.11 Ouroboros-2 test 2a spectrogram. A low frequency combustion instability is seen at approximately 200 Hz in the combustion chamber pressure. This confirms the presence of chug, albeit at a lower power than it was observed in tests 1a & 1b. Another instability can be seen between 400-600 ms after engine ignition which is likely the flame propagating through the combustion chamber.

While the spectrogram analysis was only conducted on one of the tests, the persistence diagram covers the full duration of tests 2a & 2b including the long dwell time. Of note are frequency peaks at 300, 400 and 500 Hz for the chamber pressure sensor data. The peaks have a very high density which means that they occurred throughout the data recording (including the aforementioned dwell time). Moreover, the power spectrum of these peaks is relatively low as well. These conditions indicate that those frequencies are not related to engine combustion and could be a result of electrical interference.

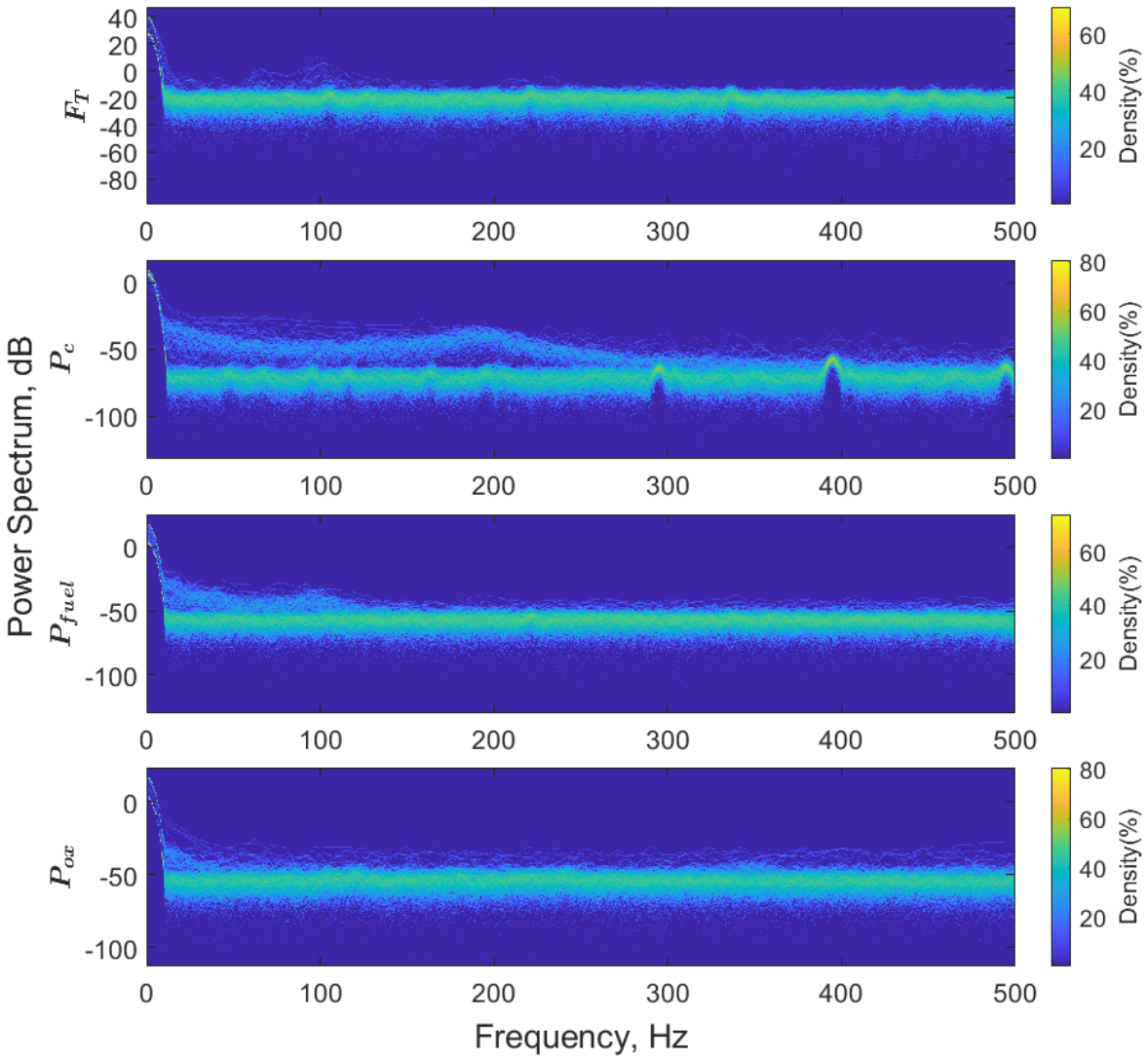

Fig. 6.12 Ouroboros-2 tests 2a & 2b persistence diagram.

6.4 Test 3: High Pressure Inlet Conditions

6.4.1 Test Data

The final test conducted with the Ouroboros-2 engine was a target 10 second burn at high pressure inlet conditions to demonstrate throttleability and expand the operating box. Additionally, the higher throttle setting could eliminate the low-frequency combustion instability known as chug which was observed during the previous tests. However, the test was only operated for 7.4 seconds before an emergency shutdown was initiated due to a rapid change in thrust data at approximately 5.6 seconds into the burn. An inspection of the system after the test determined that it was an engine mount failure at the test stand interface rather than a failure of the engine.

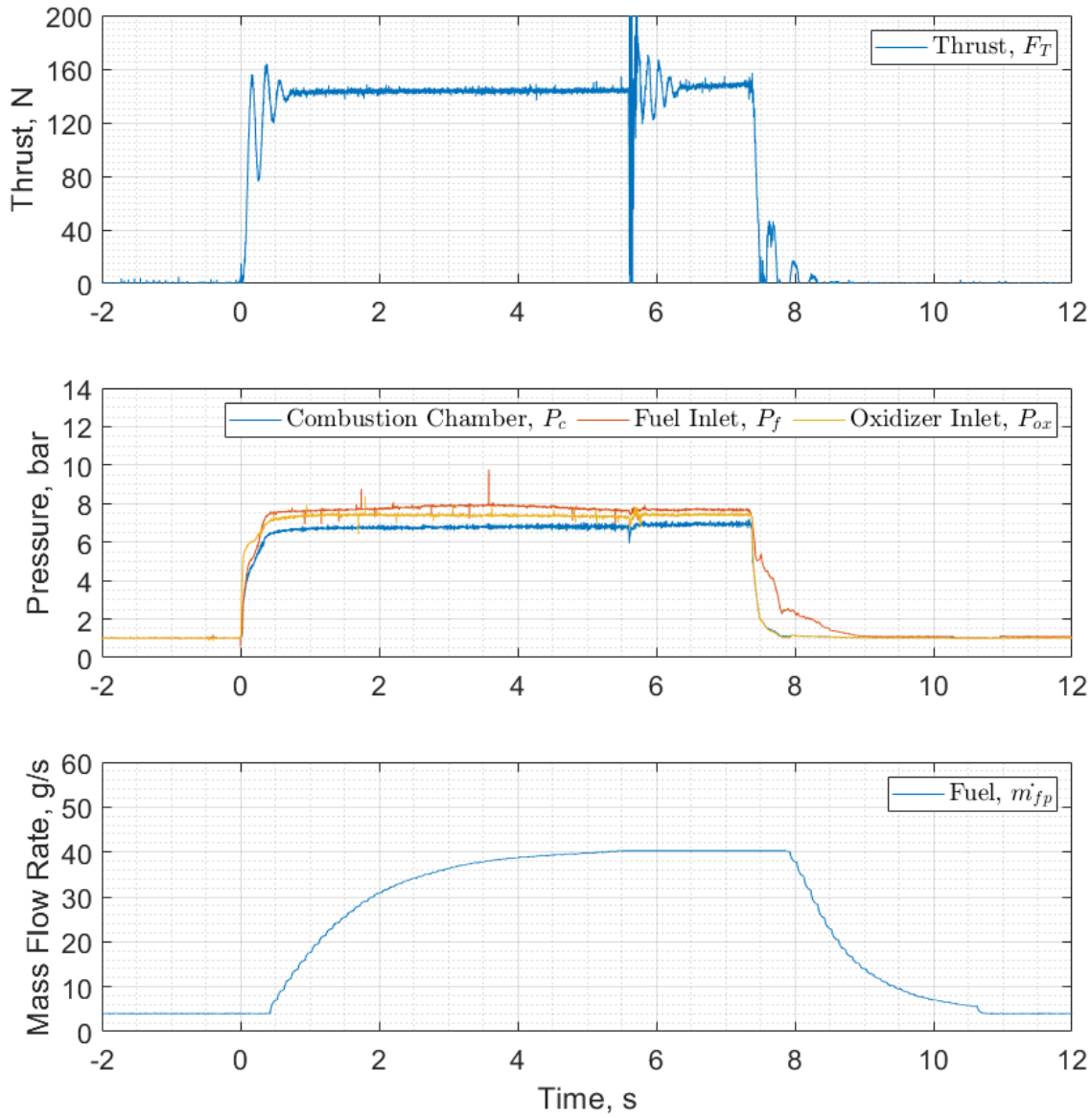

Fig. 6.13 Ouroboros-2 test 3 high inlet pressure performance chart. Steady state thrust is approximately 143.5 N with a combustion chamber pressure of 6.76 bar. Approximately 5.6 seconds into the test an engine mount failure occurs and is marked by the sudden change in feed force and thrust.

Test Timeline

T - 05.0 s Engine countdown begins.

T - 00.0 s Control valves open, oxidizer reaches nominal pressure, engine ignition.

T + 00.4 s Combustion chamber pressure reaches 90% of full scale output.

T + 00.5 s Engine reaches steady state combustion with an average thrust of 143.5 N.

T + 05.0 s Fuel mass flow rate reaches steady state.

T + 05.6 s Sudden step increase and large oscillation observed in the thrust and feed force load cells. Later identified as an engine mount failure.

T + 07.4 s Propellant control valves are closed, emergency stop initiated.

T + 07.6 s Combustion chamber pressure decays to ambient pressure.

6.4.2 Performance Analysis

Experimental Results

The experimental engine performance was once again within a small margin of error from the target shown in Table 6.7. In this test, the calculated mixture ratio was the closest to the target out of all previous tests. All other performance data was slightly below the nominal targets; however, the resulting engine thrust was within +/-3% of the expected thrust according to the chemical equilibrium analysis model.

Table 6.7 Ouroboros-2 test 3 mean performance data.

			Pressure, bar				Mass Flow Rate, g/s	
Test no.	t_b, s	F_t, N	P_c	P_{ox}	P_{fuel}	MR[3]	$\dot{m}_{ox}$	$\dot{m}_{fuel}$
Target	10.0	154.5	7.00	8.40	8.40	1.25	56.51	45.20
3	7.4	143.5	6.76	7.38	7.77	1.33	53.63	40.26
CEA	-	147.3	6.76	-	-	1.33	53.63	40.26

Moreover, the engine successfully demonstrated throttleability to significantly higher combustion chamber pressures than originally designed. In general, the data roughness also appeared to decrease which was considered an indicator that there might no longer be a low-frequency combustion instability present. Although this was later disproved in the frequency analysis (Section 6.4.3) where chug was still detected.

Much like tests 2a & 2b, the plume was not visible and behaved similarly with a steady stream of sparks that exited through the nozzle. This was again an indication of ablation of either the combustion chamber walls or the graphite nozzle.

Another outcome of this test was the observed oscillation of the thrust at engine ignition. This oscillation was not present in the combustion chamber pressure and from analysis of the video it appeared to be a harmonic of the test stand itself whereby the momentum of the engine platform and the thrust load cell interface caused the structure to oscillate. While not a significant issue for steady state operation, the time it took to dampen the oscillation was noted as approximately 750 ms which could prevent accurate thrust measurement at certain pulsed operating mode frequencies and duty cycles unless the frequency was filtered from the data.

Overall, the performance results of test 3 showed good correlation with expected values and set a performance baseline for high inlet pressure operation. Furthermore, the variation in propellant feed system settings allowed for an interpolation of the feed system pressure drop which could be used for dialing in on the required settings for the Ouroboros-3 autophage tests to be closer to their target inlet conditions. This proved to be useful and resulted in a wider operating box that the Ouroboros-3 engine was able to be tested across, including tests with higher mixture ratios.

[3] See footnote 1 from Table 6.3.

Specific Impulse Calculation

As covered in Section 6.2.2, the specific impulse of the test was calculated and a live estimation is shown in Figure 6.8. The average I_{sp} across the steady state operating time was found to be 156 s this is higher than the previous tests due to the higher mixture ratio which is closer to the ideal mixture ratio for maximum specific impulse. The results also align closely to the theoretical sea level expansion I_{sp} of 160 s using a chemical equilibrium analysis at the operating conditions. Like the previous Ouroboros-2 tests, this is within a small margin of error which could be a result of variations in atmospheric pressure, temperature, and density as well as the uncertainty in the actual oxidiser mass flow rate.

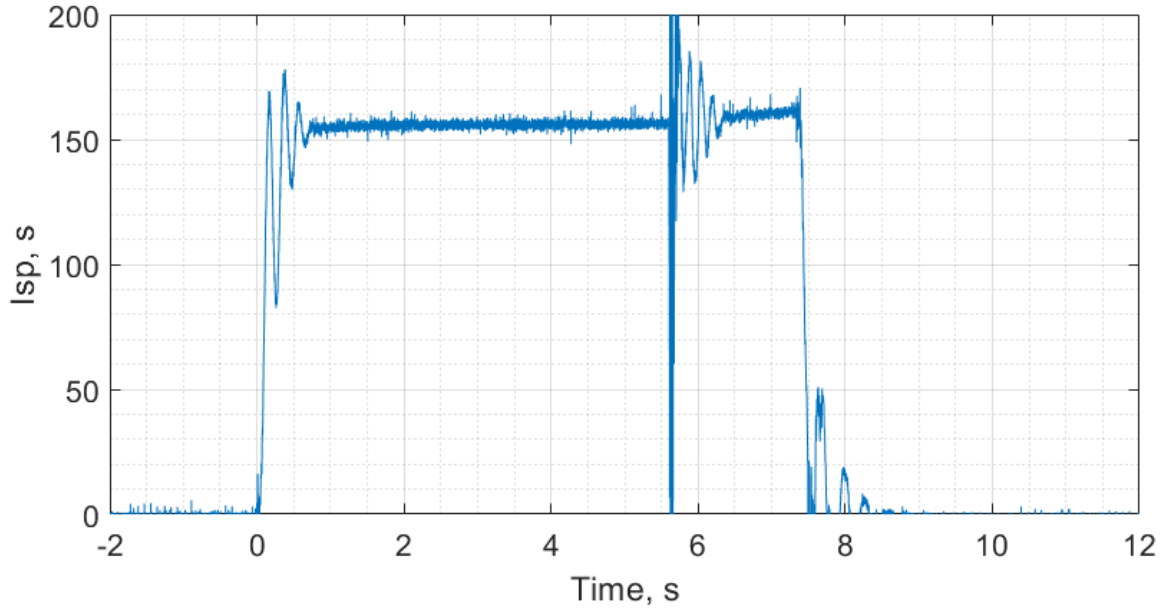

Fig. 6.14 Ouroboros-2 specific impulse from test 3 performance data.

High Inlet Conditions Chamber Pressure Rise/Decay Time

When compared to the previous tests, the results of the combustion chamber pressure rise and decay time showed a significant difference shown in Fig. 6.15 and Table 6.8 below. First, the rise time was recorded as being only 350 ms, nearly half the time it took the previously warmed engines to reach 90% of the full scale chamber pressure and less than half the time for the cold engine start.

Table 6.8 Ouroboros-2 test 3 chamber pressure rise and decay time at high inlet pressures.

Test no.	F_t, N	P_c	MR	t_r, ms	t_d, ms
3	143.5	6.76	1.33	350	225

There are multiple factors which could have contributed towards this faster rise time. For instance, a higher pressure drop across the fuel injector would have resulted in better atomisation of the propellant which would correlate with a faster ignition. The increase in mixture ratio would also aid in accelerating the ignition by introducing relatively more

oxidiser. Finally, the higher throttle setting may have eliminated the instability present during the previous engine ignitions which may have contributed to a steadier propagation of the flame throughout the combustion chamber. In fact, unlike the previous tests, there is not a significant oscillation visible in the combustion chamber pressure data during the transient ignition period. In either case, the combination of these factors resulted in a significantly faster rise time which could be leveraged to operate the engine in a wider range of pulsed mode frequencies and duty cycles.

The decay time on the other hand was observed to actually be 50% longer than previous tests. This was likely due to the inherently higher combustion chamber pressure such that once the flow through the nozzle was subsonic, it took slightly longer for the gases within the chamber to exit at the end of the test.

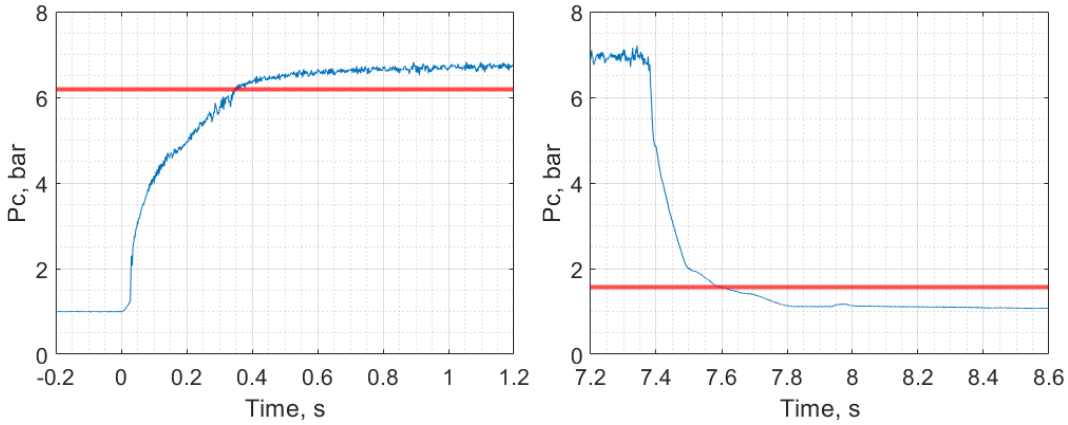

(a) Test 3 rise time

(b) Test 3 decay time

Fig. 6.15 Comparison of the Ouroboros-2 combustion chamber pressure rise and decay times at high inlet pressures.

6.4.3 Frequency Analysis

The frequency analysis was repeated for test 3 in order to verify the elimination of the 200 Hz chug instability and the combustion instability at engine ignition for previous tests. Even though the test 3 performance data showed decreased roughness and there were no visual nor audio indicators of chug, it was nonetheless still detected in both the spectrogram (Fig. 6.16) and persistence diagram (Fig. 6.17) of the combustion chamber pressure data.

The persistence of this combustion instability was highly unusual. First, because it typically only manifests at lower throttle settings [136] and this test was operated at a very high throttle. And second, because pintle injectors are known to be highly resistant to combustion instabilities [139]. While there are some identified instability modes for pintle injectors, low-frequency modes such as the one observed for these tests are noted to occur at high TMR values [140]; whereas the design of the Ouroboros-2 injector had a notably low TMR (Table 3.3) using a fuel-centered pintle design.

However, the continued presence of this instability prompted an analysis to determine what could be causing it. The leading theory was that the pressure drop across the oxidiser inlet was too low. In fact, the typical recommendation for injector design is to design for

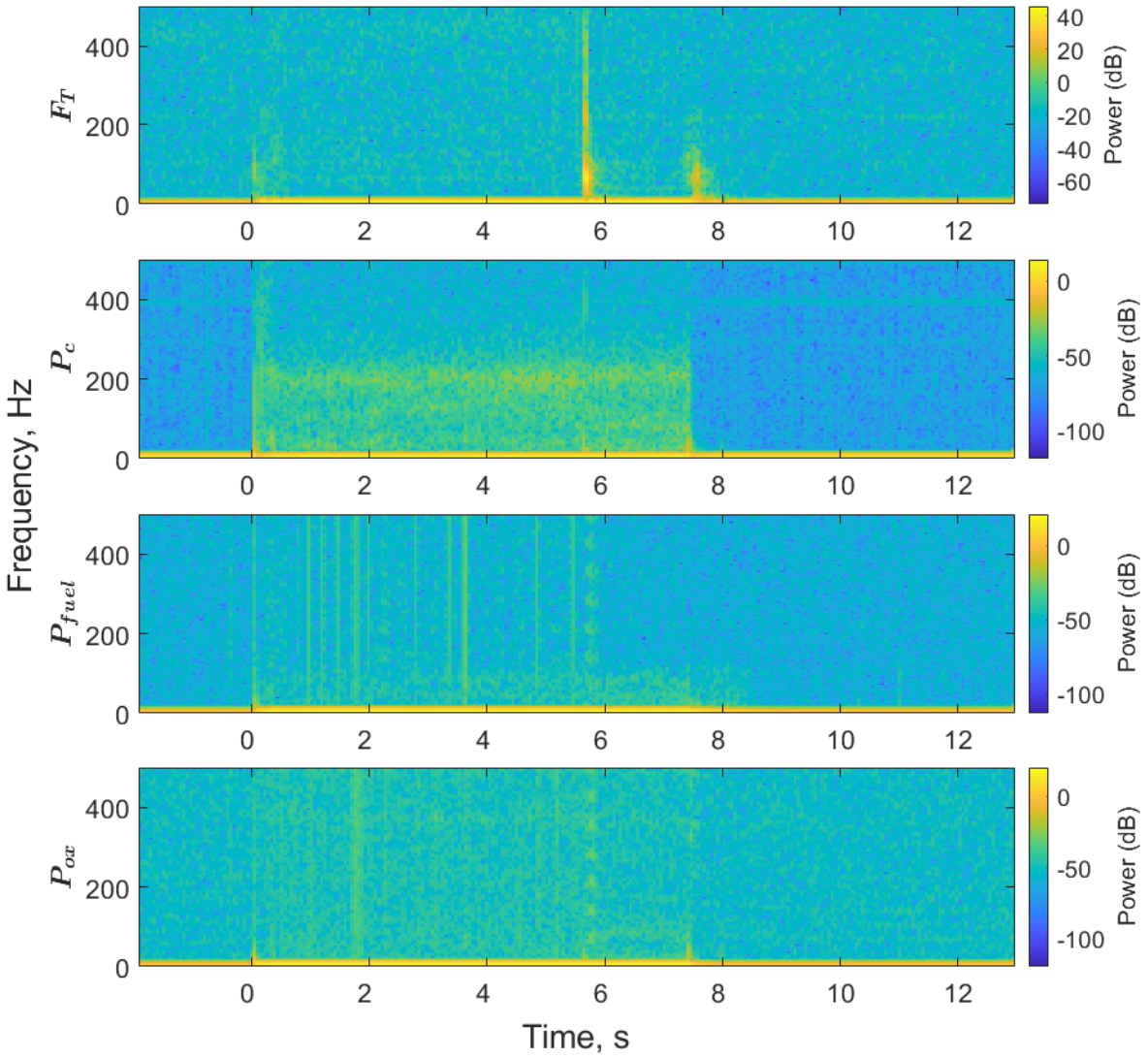

Fig. 6.16 Ouroboros-2 test 3 spectrogram. The power and energy of the 200 Hz chug instability is still present even at high throttle settings. This is highly unusual due to the resilience of pintle injectors to combustion instabilities.

a 15-20% pressure ratio between the inlet and combustion chamber [141]. In the case of Ouroboros-2, the fuel injector ratios across all the tests were approximately 15-20% whereas the oxidiser injector ratios ranged from 9-12% (Table 6.9). Therefore, increasing the oxidiser injector ratio could eliminate the low frequency instability.

Fortunately, the Ouroboros-3 injector design used a blockage to restrict the oxidiser flow through the annulus (Fig. 3.29). This design was originally intended as a method that would allow the fuel to penetrate the oxidiser flow and introduce film cooling at the combustion chamber supports. A bi-product of the annulus blockage was that the pressure drop across the oxidiser injector would also increase since the diameters of all the injector components, as well as the pintle and annular gaps, remained constant for both designs. The results of the Ouroboros-3 tests using the annulus blocked injector are further discussed in Section 7.6.4.

Nevertheless, the combustion instability identified to have been occurring at engine ignition for the previous Ouroboros-2 tests was not observed during test 3. There is still uncertainty whether the instability was causing the longer rise times described in Section

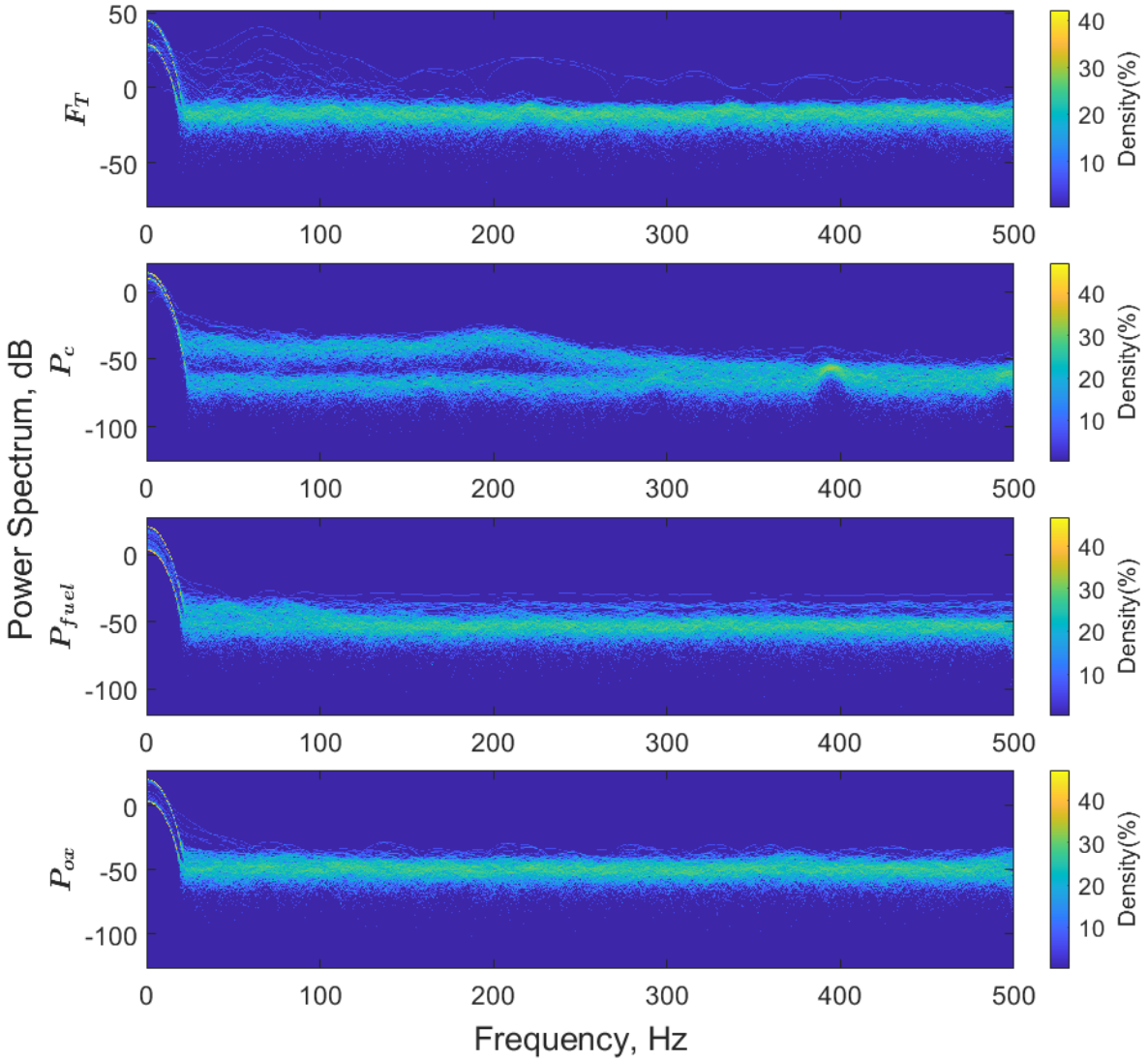

Fig. 6.17 Ouroboros-2 test 3 persistence diagram. The power and energy of the 200 Hz chug instability is functionally identical to the previous tests indicating that the high throttle setting did not have the expected effect of eliminating the instability.

6.4.2 or whether the rise times were causing the instability. In either case, the two conditions are likely correlated but additional testing and analysis should be done prior to assigning causation to the relationship.

As mentioned in previous frequency analyses, a higher sampling frequency was used for the subsequent Ouroboros-3 tests in order to include a method for detecting high frequency instabilities up to 5 kHz.

6.5 Post Hot-Fire Test Inspection and Analysis

At the conclusion of the test campaign the Ouroboros-2 engine was disassembled and inspected. Photographs showed that the stainless steel plug (which was put in place of the HDPE fuselage) had been welded to the inner combustion chamber under the high combustion temperatures and unable to be separated. However, the combustion chamber outer shell

Table 6.9 Ouroboros-2 test 3 chamber pressure rise and decay time at high inlet pressures.

	Pressure, bar					Ratio, %	
Test no.	P_c	P_{ox}	P_{fuel}	ΔP_{ox}	ΔP_{fuel}	O_2	C_3H_8
1a	4.65	5.07	5.38	0.42	0.73	9.03	15.7
1b	4.49	5.07	5.34	0.58	0.85	12.9	18.9
2a	4.66	5.10	5.69	0.44	1.03	9.44	22.1
2b	4.73	5.16	5.69	0.43	1.01	9.09	20.3
3	6.76	7.38	7.77	0.62	1.01	9.17	14.9

showed no damage and was able to be separated, cleaned, and used again on Ouroboros-3. As for the inner combustion chamber, the supports were melted all the way through and had the engine operated for any longer it was likely to have resulted in a catastrophic failure with the injector face being ejected through the top of the engine. The injector itself showed no major damage though which was a significant improvement over the Ouroboros-1 injector.

6.5.1 Combustion Chamber

When the engine was first removed from the test stand, the stainless steel plug (which was used in place of the HDPE fuselage to operate the engine solely as a bi-propellant system) was unable to be separated from the inner combustion chamber. The outer combustion chamber shell, injector, and graphite nozzle were all easily removed, leaving behind the inner combustion chamber and fuel plug assembly shown in Fig. 6.18.

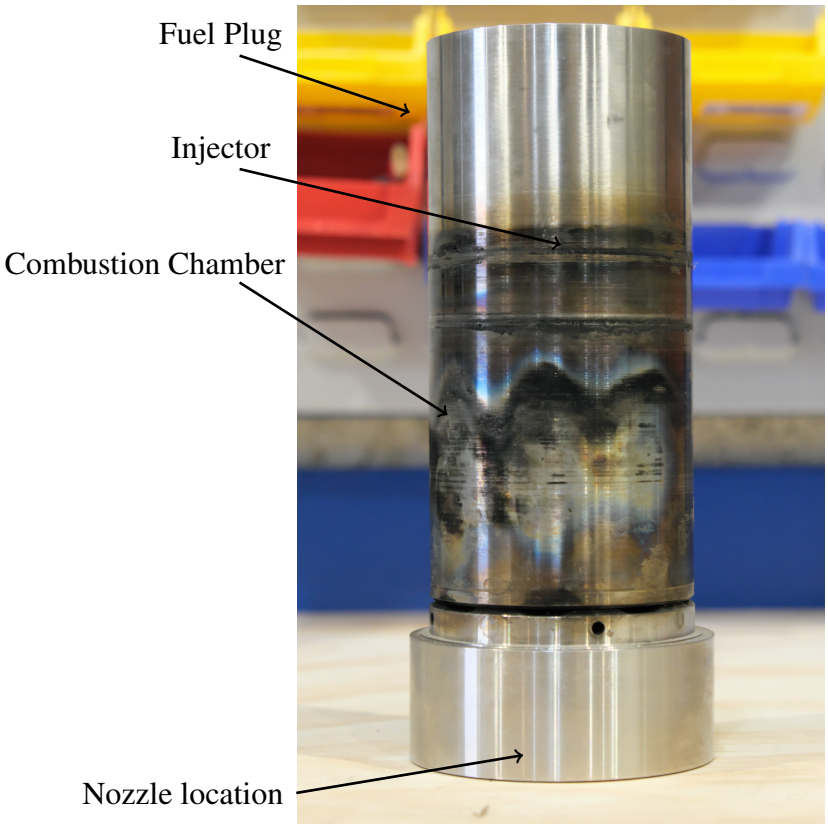

Fig. 6.18 Exterior view of the Ouroboros-2 combustion chamber and fuselage plug post hot-fire testing.

The pattern visible on the exterior of the plug corresponds with the alignment of the combustion chamber structural supports. This pattern also acts as a heat map, showing evidence of the angle of the main combustion streamline which traveled from the injector. The fuel plug acted as a barrier between the high temperature combustion gases and the outer combustion chamber shell. This resulted in the outer shell remaining intact and undamaged after the test campaign.

However, the inner combustion chamber of the Ouroboros-2 engine was significantly damaged. Figure 6.19 shows the extent of the damage, which was significant. The combustion chamber supports were fully melted through which caused the injector to effectively no longer be fastened to the engine; any additional tests would have resulted in the injector face being ejected through the top of the engine. This had already been considered the most likely failure mode for this engine due to the overall lack of cooling mechanisms at the chamber supports and these tests confirmed the assumption. We can also rightfully conclude that the sparks that were ejected through the nozzle during tests 2a, 2b, & 3 were in fact molten steel.

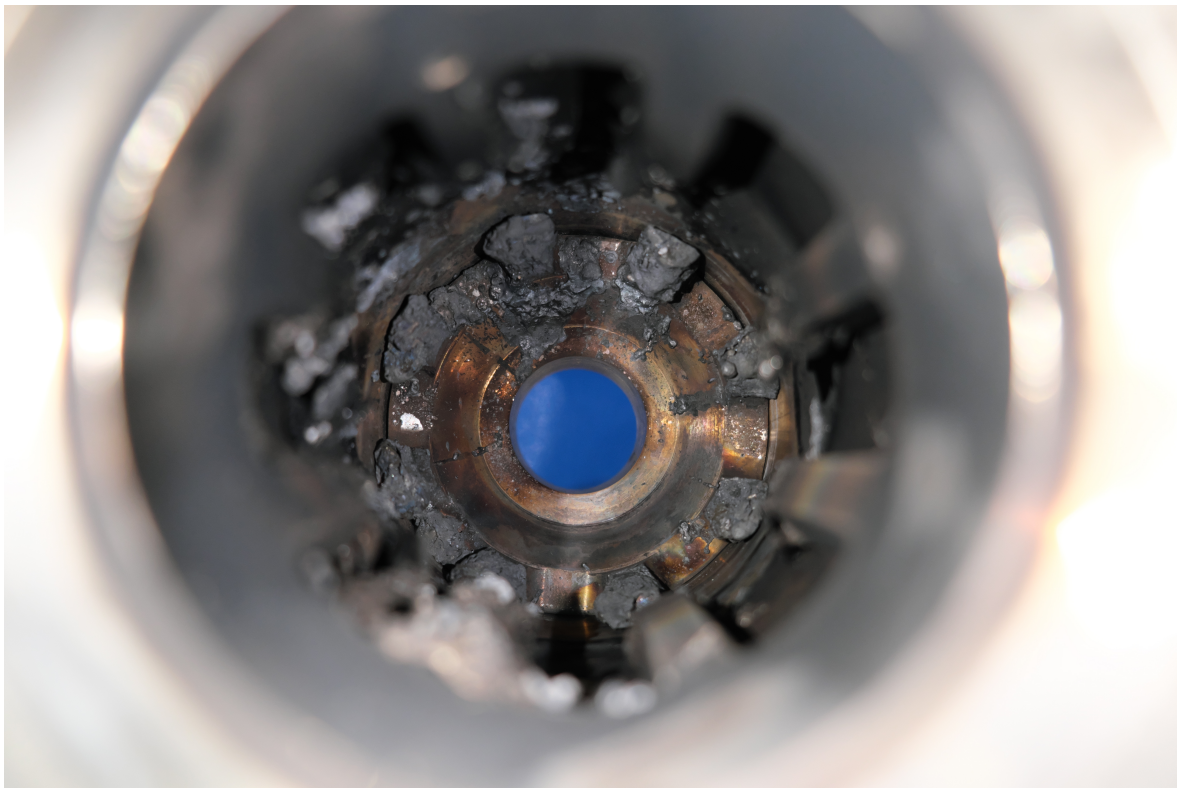

Fig. 6.19 Interior view of the Ouroboros-2 combustion chamber post hot-fire testing.

This complete melting of the inner combustion chamber also only occurred at approximately 37.3 seconds of cumulative burn time. Therefore, this was considered the minimum achievable test duration that Ouroboros-3 could be tested at those inlet conditions before being at risk of a failure. Furthermore, these tests drove the decision to start the autophage test campaign at low mixture ratios and low pressures in order to extend the test duration and life of the engine since low throttle settings correlate with lower engine temperatures. Nevertheless, the Ouroboros-3 engine was also expected to have a generally longer cumulative lifetime due

to both the propane film cooling which would target the combustion chamber supports, and also the HDPE film which would cool the nozzle side of the combustion chamber.

6.5.2 Injector

The injector, on the other hand, performed well and had no signs of any damage. Upon disassembling the injector though, a significant amount of soot was detected within the pintle channel as shown in Fig. 6.20. At first, there was a concern that some combustion processes may have occurred within the channel during the hot-fire testing. However, this was deemed unlikely since the propellant lines were first purged with gaseous nitrogen, filled with propane and then any excess gas bled from the lines up to the test stand; there was still a potential that some air could have been present within the propellant lines or injector manifold but it would have been rapidly cleared from the injector manifold at engine start.

Fig. 6.20 Soot deposition on the Ouroboros-2 pintle injector.

Further investigations concluded that the soot could be a result of pyrolysis of the propane fuel at temperatures over 970 K which would result in soot formation within a fuel rich environment and without an oxidiser present [142]. Even though the injector showed no signs of thermal damage, it would have been capable of reaching those temperatures and pyrolyzing the propane after each hot-fire test due to thermal soak-back. Typically, the injector face is the coolest part of the combustion chamber during steady state operation due to the constant influx of cold propellants. However, after engine shutdown, the system will experience thermal soak-back whereby there is a heat flux that will flow from the nozzle and combustion chamber to the rest of the engine [143].

The Ouroboros engines also used control valves with approximately 1.25 meters of propellant line between the valves and the engine inlet. Thus, even at engine shutdown there would still be a brief period of propellant mass flow that would have continued to combust (and with no upstream inlet pressure this could have resulted in some soot deposition within

the injector). According to this analysis, the soot deposition would be even more likely due to the multiple tests and engine restarts of the engine. Moreover, propane in general has a high incidence of soot deposition [144]. Therefore, it was determined that the soot deposition was most likely nominal under the specific conditions and not a sign of poor engine performance or combustion within the injector.

Another interesting, but not unexpected result, was that the chamber supports were melted very close to the injector side rather than the nozzle side of the engine. This indicated that the mantle recirculation zone was quite small. By measuring the remaining lengths of the melted combustion chamber supports and applying them to the Ouroboros-2 drawings, we were also able to estimate the angle of the main combustion reaction streamline originating from the injector (Fig. 6.21) as being approximately 30°from the center axis of the engine.

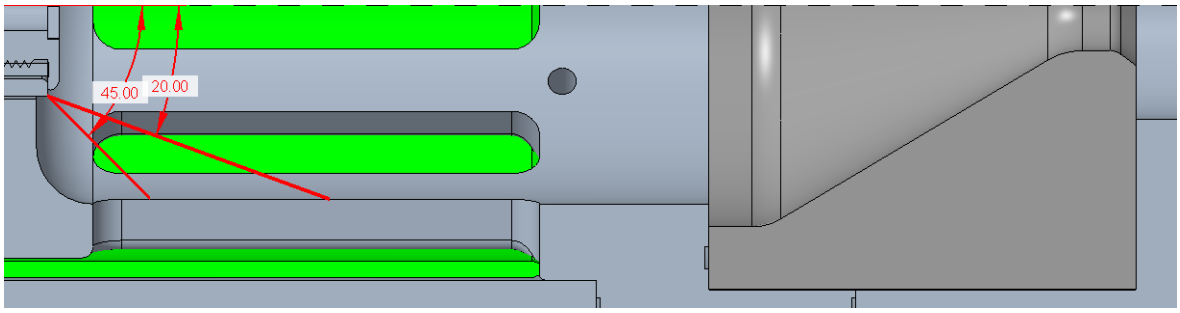

Fig. 6.21 Estimated angle of the Ouroboros-2 main combustion streamline based on post hot-fire testing analysis.

6.6 Conclusions and Lessons Learned

Overall, both the Ouroboros-2 design and test campaign were very successful. The direct fuselage insertion proved to be operationally far more effective than the depolymerisation chamber architecture. It also met performance targets within a very small margin of error when compared to the theoretical performance estimates based on a chemical equilibrium analysis (CEA) which can be seen in Fig. 6.10. The only outlier in the data was test 1b where the combustion chamber pressure sensor exhibited either drift or a blockage and resulted in off-nominal data, otherwise the engine performance was within +/-5% of theoretical values.

Table 6.10 Ouroboros-2 thrust data vs. theoretical performance.

	Actual			CEA			
Test no.	F_t, N	P_c, bar	MR	F_t, N	P_c, bar	MR	Thrust Error, %
1a	95.54	4.65	1.07	90.97	4.65	1.07	+4.8
1b	96.58	4.49	1.01	86.42	4.49	1.01	+10.5
2a	92.25	4.66	1.05	91.07	4.66	1.05	+1.3
2b	94.94	4.73	1.07	93.03	4.73	1.07	+2.0
3	143.5	6.76	1.33	147.3	6.76	1.33	-2.6

These results set a clear performance baseline that were used as a control for the autophage Ouroboros-3 tests to be compared to which would identify any impacts on performance that

the introduction of a third propellant (the HDPE fuselage) may have caused. The high inlet pressure test (test 3) also verified throttleability of the engine and substantially expanded the operating box by varying both inlet pressures and mixture ratio. Additionally, the tests operated the engine for a cumulative burn time of 37.3 seconds setting a minimum duration for which the Ouroboros-3 engines should be confidently operated for without a catastrophic failure of the combustion chamber.

The engine also exhibited no issue with multiple engine shutdowns and restarts with minimal variation in performance for both short and long duration dwell times. Combustion chamber pressure rise and decay times were also consistent across tests 1a, 1b, 2a, & 2b (which all shared approximately the same inlet conditions); however, a significantly faster rise time and longer decay time was recorded for test 3 at the high throttle setting. A comparison of all the chamber pressure rise and decay time is shown in Fig. 6.11. The longer rise time for test 1a was also attributed to it being the first and only cold start of the engine.

Table 6.11 Ouroboros-2 chamber pressure rise and decay times across all test conditions.

Test no.	F_t, N	P_c	MR	t_r, ms	t_d, ms
1a	95.54	4.65	1.07	750	125
1b	96.58	4.49	1.01	600	150
2a	92.25	4.66	1.05	600	150
2b	94.94	4.49	1.07	600	150
3	143.5	6.76	1.33	350	225

These rise and decay times were used to approximate the minimum feasible conditions to operate the Ouroboros-3 autophage engine in pulsed modes. Effectively, the engine should have an off-time of at minimum 250 ms in order to allow for complete decay of the combustion chamber pressure and an on-time of 750 ms to reach nominal performance. This correlates to operating at a frequency of 1 Hz at a 75% duty cycle which was the baseline used to create the target operating modes of the hot-fire test plan (Fig. 4.4). The test plan varied both the frequencies and duty cycles around this baseline in order to evaluate the effect of pulsed mode on the feed rate of the HDPE fuselage.

Frequency analyses of all performance data also detected the presence of a low-frequency combustion instability of approximately 200 Hz across all test conditions. This instability was identified as chug due to the characteristic pulsed combustion which was visible during tests 1a & 1b as well as the sound of the engine during the tests. The instability persisted and was detected within the combustion chamber pressure data throughout each test including the high throttle settings of test 3 which was particularly unexpected since low-frequency instabilities will usually only occur at low throttle settings. After analysis, it was concluded that this instability was likely a result of an insufficient pressure drop across the oxidiser injector.

Injectors are typically designed to have an inlet pressure 15-20% higher than combustion chamber pressures in order to facilitate both atomisation and prevent instabilities. However, the oxidiser inlet pressure for all Ouroboros-2 tests was found to only be approximately 10% higher than the combustion chamber pressures (fig. 6.9). This instability would be addressed by using a modified pintle injector design which used blockages in the annulus to block oxidiser flow correlating with the combustion chamber support structures. Replacing the

injector with this modification would not only raise oxidiser inlet pressures and eliminate the instability but also provide film cooling to the support structures and significantly increase the maximum achievable test duration of the direct fuselage insertion architecture. This was the only change made to the design between the Ouroboros-2 and 3 engines, other than the introduction of the HDPE fuselage, and was deemed to not be significant enough to warrant retesting the engine in the bi-propellant configuration. The injector modification should not effect the performance baseline since the engine design was already operating within a small margin of error of its theoretical performance and it should only influence the stability and thermal management of the inner combustion chamber walls.

In addition to the conclusions regarding engine performance, a number of other outcomes also resulted from this test campaign. One of these outcomes was an experimentally validated approximation of the propellant feed system pressure drop; this would allow for better control over delivery pressures in order to meet the target inlet conditions for each test. The tests also identified a need for a suitable oxidiser flowmeter in order to verify mixture ratio as well as a procedure for ensuring thermocouple data was correctly recorded and stored. Additional optical and thermal cameras were also implemented in the Ouroboros-3 tests for additional monitoring and data recording.

To summarise, the Ouroboros-2 test campaign provided a valuable set of data to effectively characterise the direct fuselage insertion architecture across multiple metrics. The results verified that the design was ready to progress to autophage tests and introduce the HDPE fuselage as a third propellant.

Chapter 7

Direct Fuselage Insertion Architecture, Autophage Test Results

7.1 Ouroboros-3 Operational Modes and Test Campaign Overview

Building on the lessons learned and successful bi-propellant tests of the direct fuselage insertion architecture ultimately resulted in the design and test of the Ouroboros-3 autophage engine. This engine was designed to start operations as a bi-propellant system, and as engine temperature increased, it would then transition into operating as a tri-propellant hybrid engine whereby the HDPE fuselage was inserted and burned as a supplementary fuel. The feed force across all tests was set at a constant 2 kN of force.

The Ouroboros-3 autophage tests were conducted over the course of two separate test campaigns for a cumulative total of 5 hot fire tests. The first three tests were conducted during the same period as the previous Ouroboros-2 tests and attempted to operate the engine at the same inlet conditions. Unfortunately, during the Ouroboros-2 test campaign there was a failure of a burst disc in the oxygen tank pressure regulator which led to a limited supply of high pressure oxygen. The remaining supply was used efficiently in order to conclude the Ouroboros-2 tests and the first Ouroboros-3 test; however, tank pressure dropped below nominal operating conditions leading to the reduction in engine performance during test 1, this can be seen in Fig. 7.1 where all of the sensors show a gradual decline in performance. For tests 2 and 3 a different oxygen pressure regulator was sourced at the test site that could supply the gas at lower pressures so that the engine could at least be tested at low throttle settings. Thus, tests 2 and 3 were conducted at fuel rich and low throttle inlet conditions. It is also important to note that all three of these tests were conducted using the same engine assembly.

While tests 1-3 were successful and demonstrated engine operation, they were unable to maintain the engine at standard inlet conditions and only operated the engine in a steady state operating mode. Thus, another test campaign was scheduled which continued to test the

Ouroboros-3 engine at higher mixture ratios and standard inlet conditions, the complete set of steady state target inlet conditions is shown in Table 7.1.

Table 7.1 Ouroboros-3 steady state target inlet conditions.

			Pressure, bar				Mass Flow Rate, g/s	
Test no.	t_b, s	F_t, N	P_c	P_{ox}	P_{fuel}	MR	$\dot{m}_{ox}$	$\dot{m}_{fuel}$
1	30.0	100.4	5.00	6.00	6.00	1.00	37.65	37.65
2	30.0	50.84	3.00	3.60	3.60	1.00	22.76	22.76
3	30.0	50.84	3.00	3.60	3.60	1.00	22.76	22.76
4	30.0	75.89	4.00	4.80	4.80	2.00	30.23	15.11
5	30.0	101.7	5.00	6.00	6.00	2.00	37.73	18.87

The two additional tests (tests 4 and 5) also included steady state and pulsed operating modes which were very effective at characterising the autophage engine performance. The second test campaign also introduced the use of a vortex flowmeter on the oxidiser propellant line which was able to confirm oxidiser flow rate and propellant mixture ratios; a K-type thermocouple (located at the inner combustion chamber wall) was also incorporated to monitor engine wall temperature for all tests. The rationale for this was to verify the threshold for which engine temperature could promote the melting of the HDPE fuselage, validate the presence of film cooling provided by the HDPE, and characterise the effect of the different operating modes on wall temperature.

The data acquisition system was also set to collect data at a sampling frequency of 10 kHz for the autophage tests which would allow the detection of high frequency combustion instabilities up to 5 kHz. However, this setting was only useful to the pressure sensors and load cells since the flow meters did not have the required sensitivity nor minimum hysteresis to operate within that sampling frequency. Table 7.2 shows the sensors and sampling frequencies used during the Ouroboros-3 tests.

Table 7.2 Ouroboros-3 sensors and sampling frequencies.

Location	Type	Unit	Frequency, f_s
Actuator, F_F	feed force load cell	N	10 kHz
Test stand, F_T	thrust load cell	N	10 kHz
Fuel Inlet, P_f	pressure transducer	Bar	10 kHz
Oxidizer Inlet, P_o	pressure transducer	Bar	10 kHz
Combustion Chamber, P_c	pressure transducer	Bar	10 kHz
Combustion Chamber, T_c	Thermocouple	K	1 Hz
Fuel Mass Flow Rate, $\dot{m}_{fuel}$	flow meter	g/s	1 kHz
Oxidiser Mass Flow Rate, $\dot{m}_{ox}$[1]	flow meter	g/s	1 kHz

Contrary to tests 1-3, a fresh combustion chamber and nozzle were used for each additional test which proved to be an effective method of testing the engines both to, and past, their operational limits. This resulted in each Ouroboros-3 combustion chamber having a cumulative life of over 90 seconds, nearly 3x the cumulative life of the sole Ouroboros-2

[1] The oxidiser flow rate data was only collected during tests 4 and 5 using a vortex flowmeter. No mass flow rate data was collected during tests 1-3 due to not having a suitable oxidiser flow meter during that test campaign.

engine. Moreover, the injector showed even greater resilience one of which was used for tests 1-4. Table 7.3 shows the distribution and cumulative life of each major Ouroboros-3 component. Impressively, both the combustion chamber outer shell and nozzle bulkhead remained unchanged and were used for each test, from the first Ouroboros-1 test until the conclusion of the Ouroboros-3 campaign.

Table 7.3 Ouroboros-3 component list and cumulative life.

	Cumulative Life, s						
		Ouroboros-3 Tests					
Component	Heritage Tests	1	2	3	4	5	Total
Combustion Chamber 1	-	23.6	53.0	50.0	-	-	126.6
Combustion Chamber 2	-	-	-	-	61.25	-	61.25
Combustion Chamber 3	-	-	-	-	-	72.25	72.25
Nozzle 1	-	23.6	53.0	50.0	-	-	126.6
Nozzle 2	-	-	-	-	61.25	-	61.25
Nozzle 3	-	-	-	-	-	72.25	72.25
Injector 1	-	23.6	53.0	50.0	-	72.25	198.9
Injector 2	-	-	-	-	61.25	-	61.25
Chamber Shell	88.3	23.6	53.0	50.0	61.25	72.25	348.4
Nozzle Bulkhead	88.3	23.6	53.0	50.0	61.25	72.25	348.4

The wide range of operating conditions were also developed in such a way as to evaluate the effect of both throttle setting, mixture ratio and pulsed modes on both fuselage feed rate and performance within a small number of total tests. All in all, these were identified as key metrics for characterising the potential contribution of the autophage fuel to engine performance and in determining methods of controlling the autophage burn. As a whole, these tests were very successful in not only demonstrating a novel, autophage propulsion system but also the first instance in effectively measuring and characterising the performance of a tri-propellant autophage engine. The following sections evaluate the steady state performance of the engine during each test, compare the results to the bi-propellant performance where applicable, define the influence of multiple different variables on the autophage feed rate and explore the use of pulsed operating modes with an autophage engine.

7.2 Test 1: Benchmark Test at Ouroboros-2 Baseline, Fuel Rich, Inlet Conditions

The initial Ouroboros-3 test was designed to target the same mixture ratio and throttle setting as the results from the baseline Ouroboros-2 tests. These results would then be compared to evaluate the influence of introducing a third propellant, HDPE, into the system. The intent was to operate the engine for a total duration of 30 seconds in steady state mode or until oxidiser tank pressure dropped below sustainable levels. This maximum test duration was based on the results of the cumulative life of the Ouroboros-2 engine to ensure the autophage engine was not operated past its estimated maximum life. In fact, due to the previously discussed issues with the availability of high pressure oxygen, the test duration was limited to 23.6 s.

Nevertheless, this was an exceptionally successful test as a demonstration of the first-of-its-kind hybrid autophage propulsion system operating on three different propellants. Figure 7.2 shows the first successful firing of the Ouroboros-3 engine and Fig. 7.1 shows the resulting performance data.

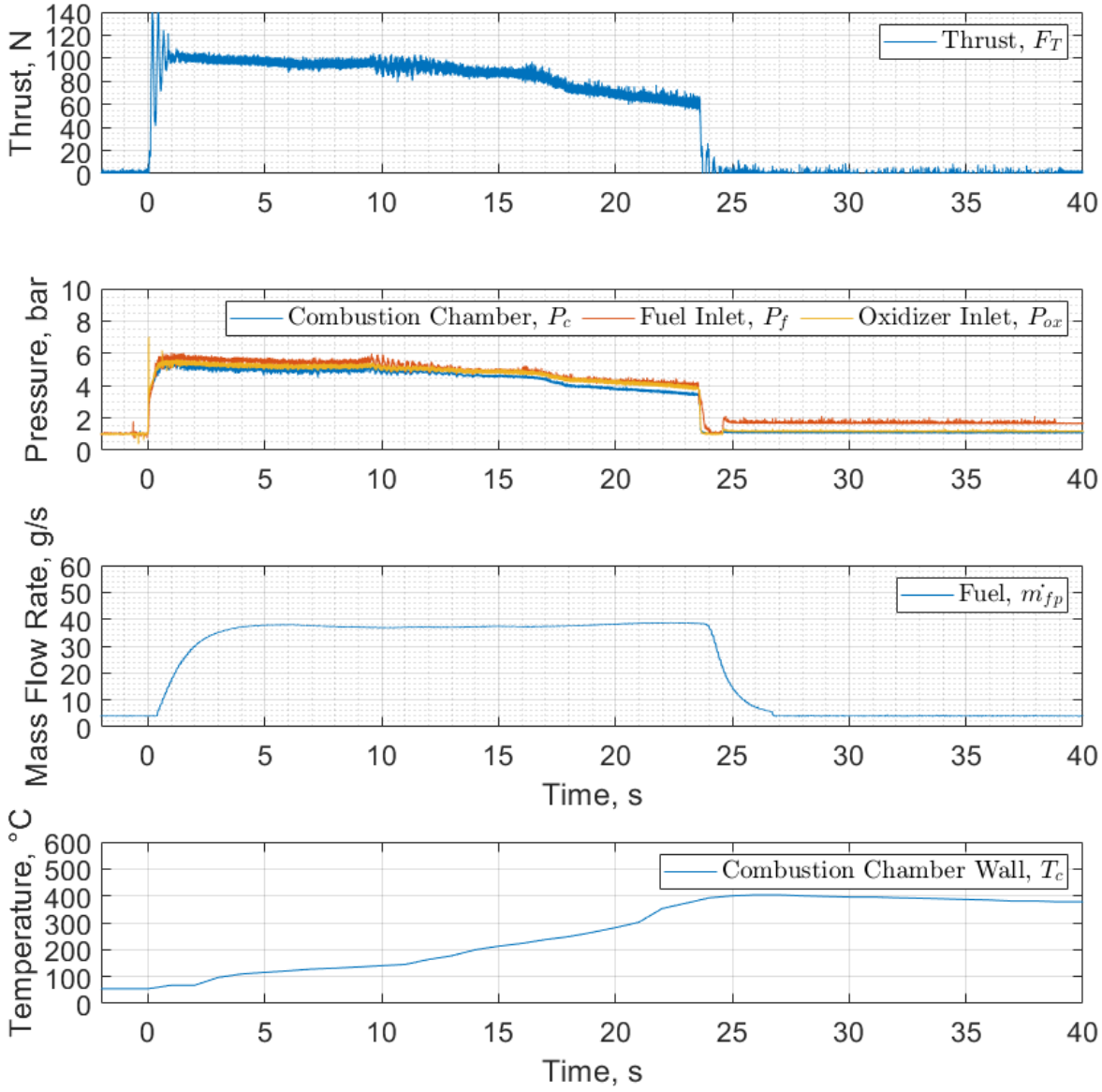

Fig. 7.1 Ouroboros-3 autophage test 1 performance results at fuel rich inlet conditions.

Test Timeline

T - 05.0 s Engine countdown begins.

T - 00.0 s Control valves open, oxidizer reaches nominal pressure, engine ignition.

T + 00.3 s Combustion chamber pressure reaches 90% of full scale output.

T + 00.5 s Engine reaches steady state combustion with an average thrust of 96.54 N.

T + 05.0 s Fuel mass flow rate reaches steady state.

T + 10.0 s A low-frequency oscillation is observed in both inlet pressure data, chamber pressure data and thrust.

T + 14.0 s The low-frequency oscillation is dampened out from all sensors.

T + 17.0 s A steady decline in inlet pressures and engine performance is observed, indicating reduction in oxidiser tank pressure below nominal values.

T + 23.6 s Propellant control valves are closed, initiating engine shutdown. The HDPE fuel tube is observed to begin moving into the engine.

T + 23.8 s Combustion chamber pressure decays to ambient pressure.

T + 24.6 s Purge valves are activated to rapidly cool the engine with gaseous nitrogen to prevent excess HDPE fuel from being melted in the engine chamber.

T + 37.0 s The HDPE fuel is observed to stop moving and the actuator feed force is released. A total of 6 cm of HDPE was observed as inserted into the engine during this period.

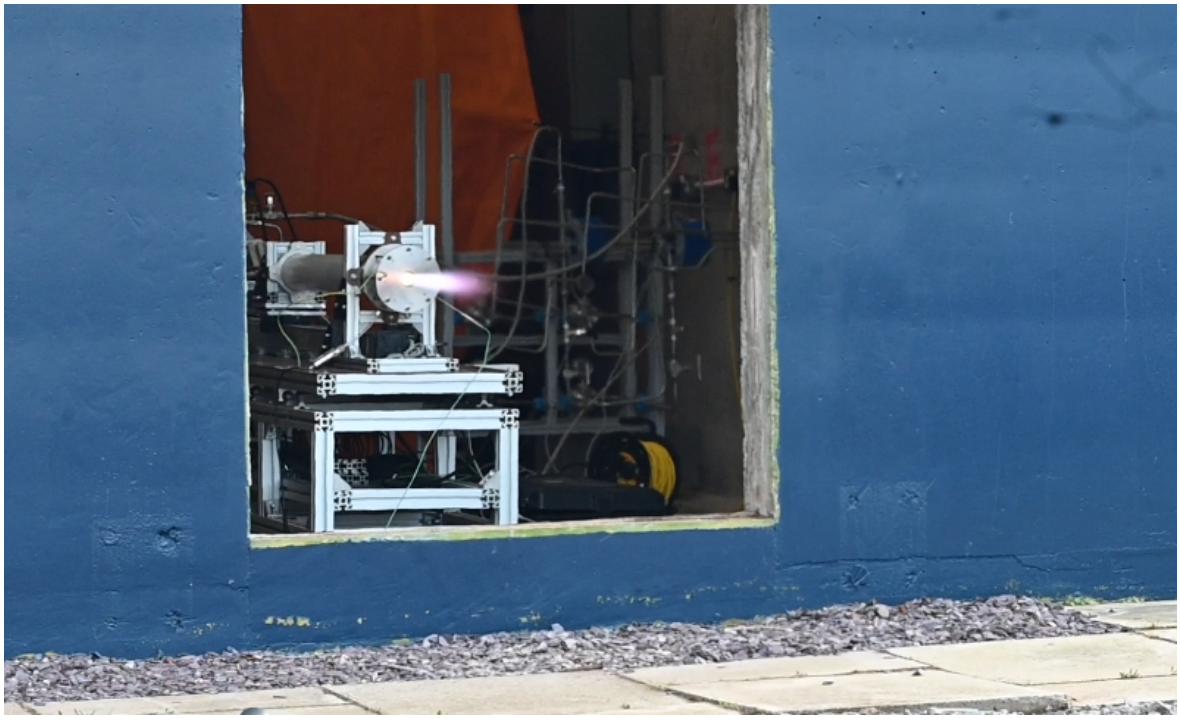

Fig. 7.2 Ouroboros-3 test 1 with the engine operating in the autophage mode.

7.2.1 Experimental Results

As with the Ouroboros-2 tests, there was no suitable oxidiser flowmeter in order to measure oxidiser flow rate. Therefore, the estimated flow rate and mixture ratio were determined using a chemical equilibrium analysis. However, unlike the Ouroboros-2 tests, the HDPE fuselage now contributed to the total fuel mass flow rate. This flow rate was originally to be determined by recording the linear rate of displacement of the end of the fuselage as it was inserted into

the engine during steady state operation. Using the dimensions and density of the fuselage we could then determine the HDPE fuel mass flow rate. However, for test 1, the engine was shut down right as the HDPE fuselage began to move and so a steady state feed rate was unable to be determined.

While we were unable to record real time measurement of the fuselage feed rate due to the short test duration, the fuselage was observed to have been inserted 6 cm into the chamber during engine cooldown. Considering the dimensions and density of the fuselage, this corresponded to a total HDPE fuel mass of 50 g; and when applied over the burn time yielded an estimated HDPE mass flow rate of 2.10 g/s. This was considered an upper limit of the HDPE contribution to the total fuel mass flow rate and was used to calculate the corrected fuel mass flow rates shown in Table 7.4. Overall, the true HDPE fuel mass flow rate falls within these performance bounds.

Table 7.4 Ouroboros-3 autophage test 1 mean performance data.

			Pressure, bar				Mass Flow Rate, g/s			
Test no.	t_b, s	F_T, N	P_c	P_{ox}	P_{fuel}	MR[2]	$\dot{m}_{ox}$	$\dot{m}_{fuel}$	$\dot{m}_{fp}$	$\dot{m}_{ft}$
Mean Fuel Mass Flow Rates										
Target	30.0	100.4	5.00	6.00	6.00	1.00	37.65	37.65	37.65	-
1	23.6	96.54	5.04	5.24	5.54	1.10	40.99	37.39	37.39	-
CEA	-	101.4	5.04	-	-	1.10	40.99	37.39	37.39	-
Corrected Fuel Mass Flow Rates										
1	23.6	96.54	5.04	5.24	5.54	1.01	39.99	39.49	37.39	2.10
CEA	-	100.6	5.04	-	-	1.01	39.99	39.49	37.39	2.10

The performance results considering both no HDPE contribution and the maximum HDPE contribution were within 5% of the theoretical performance based on the chemical equilibrium analysis and within an even smaller margin from the target performance. Of note though is the comparison of the autophage tests to the Ouroboros-2 bi-propellant tests. Table 7.5 shows the performance results of this test compared to that of Ouroboros-2 test 2b which was the closest in terms of inlet conditions and combustion chamber pressure. While the Ouroboros-2 test thrust exceeded the theoretical thrust, the autophage test instead failed to meet the theoretical thrust by a small margin.

Table 7.5 Ouroboros-3 autophage test 1 mean performance data.

			Pressure, bar				Mass Flow Rate, g/s			
Test no.	t_b, s	F_T, N	P_c	P_{ox}	P_{fuel}	MR	$\dot{m}_{ox}$	$\dot{m}_{fuel}$	$\dot{m}_{fp}$	$\dot{m}_{ft}$
Ouroboros-2 Bi-Propellant Performance										
2b	5.1	94.94	4.73	5.16	5.69	1.07	35.71	35.77	-	
CEA	-	93.03	4.73	-	-	1.07	35.71	35.77	-	
Ouroboros-3 Autophage Performance										
1	23.6	96.54	5.04	5.24	5.54	1.01	39.99	39.49	37.39	2.10
CEA	-	100.6	5.04	-	-	1.01	39.99	39.49	37.39	2.10

In each case, the margin of error was less than +/-5%; this could be attributed to a slight misalignment of the thrust load cell between tests, a tilt in the test stand or evidence of

[2]See footnote 1 from Table 6.3.

autophage operation causing a slight reduction in engine performance. However, one data point is not conclusive enough to deduce whether autophage operation actually caused a reduction in engine performance.

Meanwhile, the combustion chamber wall temperature reached a maximum of 403°C immediately after engine shutdown, right as the HDPE fuselage began feeding into the engine. This was determined to likely be an indicator of the minimum engine wall temperature required for the fuselage feed to begin.

7.3 Tests 2 &3: Fuel Rich and Low Throttle Inlet Conditions with a Long Dwell Time Engine Restart

The following set of tests was conducted at a very low throttle setting as well as fuel rich inlet conditions. This was a direct result of needing to use a low pressure and low flow rate oxygen pressure regulator due to an exhausted supply of usable high pressure oxygen tanks. A bi-product of the fuel-rich conditions was cooler engine temperatures which allowed the engine to operate for those extended durations with no damage to the combustion chamber nor the injector. Thus, even at extreme throttle settings, the Ouroboros-3 autophage engine was able to demonstrate fuselage feed for long duration burns as well as a successful engine shutdown and restart after a long dwell time. No specific dwell time was set prior to the test; however, the engine restart was to be initiated immediately after detecting that the combustion chamber wall temperature fell below 400°C which was the previously determined minimum temperature to achieve fuselage feed.

The complete test sequence is shown below in Fig. 7.3. Of note was the unusual transient at engine startup whereby the inlet conditions were unexpectedly higher than the later steady state conditions. This was a result of the procedure by which the previous high pressure oxygen tank and regulator (that was used for test 1) were replaced with the lower pressure tank and regulator. During the replacement procedure only the propellant lines near the tank were depressurised, everything downstream of the pressure regulator had not been depressurised and the feed system check valves maintained the line pressure during the tank replacement. Thus, at engine start, the initial feed pressures were higher than expected and resulted in the higher performance. This was a procedural oversight and the propellant lines should have been purged prior to the test start. However, for the purposes of the performance analysis, only the steady state portion of test 2 (from 20-53 seconds) is considered.

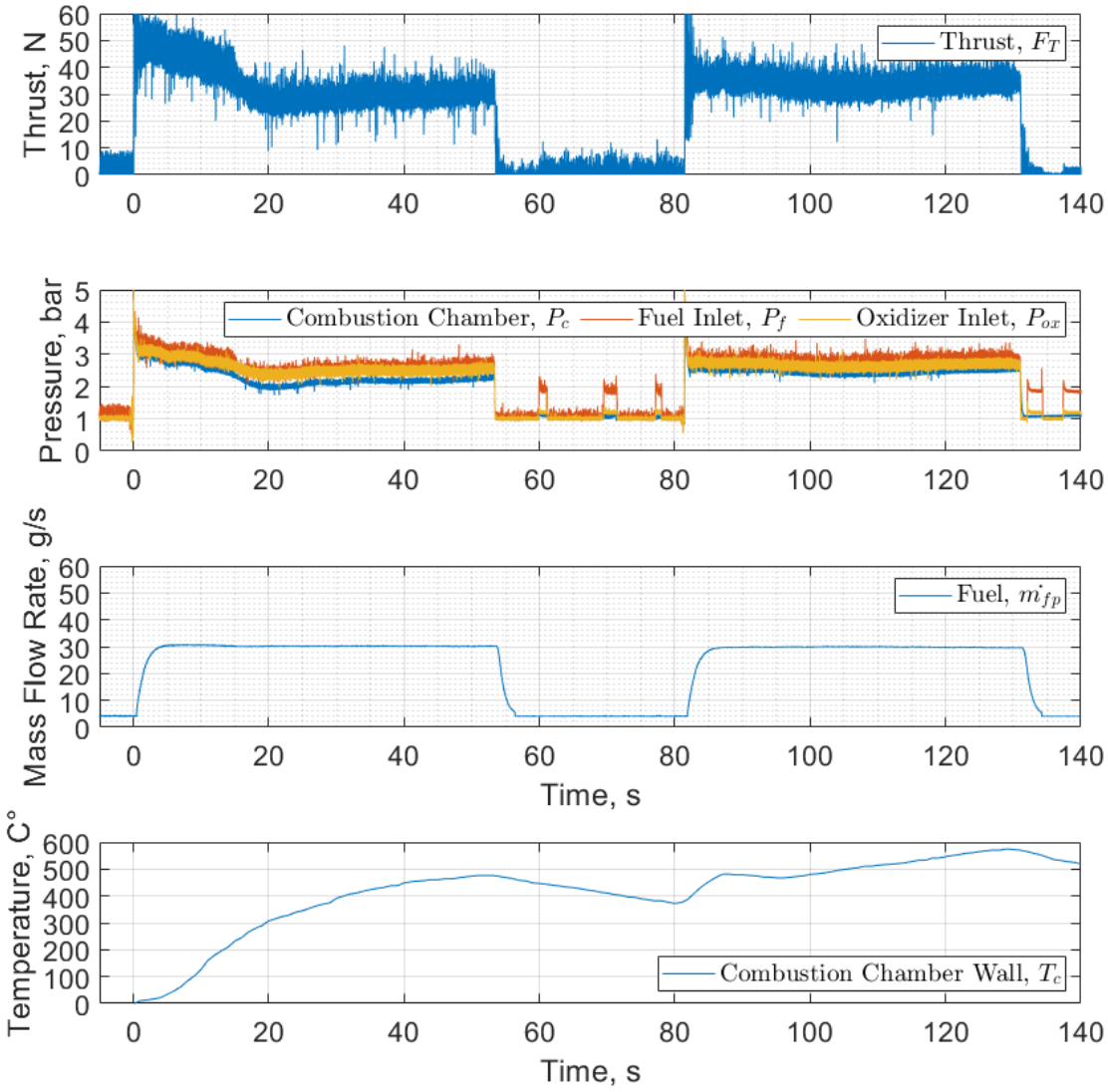

Fig. 7.3 Ouroboros-3 autophage tests 2 & 3 performance results at low throttle, fuel rich inlet conditions.

Test Timeline

T - 05.0 s Engine countdown begins.

T - 00.0 s Control valves open, oxidizer reaches nominal pressure, engine ignition.

T + 00.3 s Combustion chamber pressure reaches 90% of full scale output.

T + 00.5 s Engine thrust peaks at approximately 50 N before steadily declining.

T + 05.0 s Fuel mass flow rate reaches steady state.

T + 20.0 s The HDPE fuselage is observed to begin moving into the engine. From this point onward, steady state thrust is observed at 31.93 N.

T + 53.0 s Propellant control valves are closed, initiating engine shutdown. Long dwell time begins, the HDPE fuel rod continues to be inserted into the engine for a total insertion of 8 cm, or 70 g of HDPE. Purge valves are activated in three short bursts during the dwell time.

T + 81.0 s Control valves are opened and the engine is restarted immediately after chamber wall temperature reaches below 400°C.

T + 81.5 s Steady state is reached with an average thrust of 34.35 N.

T + 131 s Control valves are closed and Purge valves are activated to rapidly cool the engine with gaseous nitrogen to prevent excess HDPE fuel from being melted in the engine chamber.

7.3.1 Experimental Results

As a whole, the Ouroboros-3 engine performed exceptionally well at these inlet conditions and verified the capability to operate for long durations under a continuous steady state feed rate of the fuselage (Fig. 7.4). Evaluating the mean performance of the Ouroboros-3 engine at these steady state inlet conditions yielded the results detailed in Table 7.6.

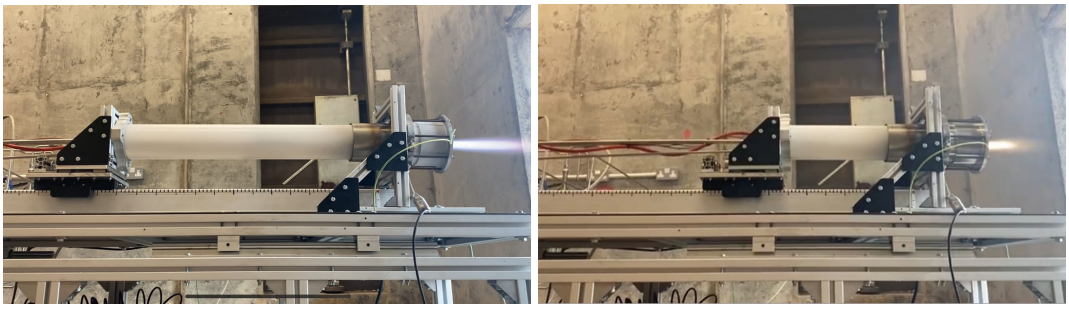

(a) (b)

Fig. 7.4 Steady state operation of the Ouroboros-3 autophage propulsion system at a) ignition and b) shutdown.

Table 7.6 Ouroboros-3 autophage test 2 and 3 mean performance data.

			Pressure, bar				Mass Flow Rate, g/s			
Test no.	t_b, s	F_T, N	P_c	P_{ox}	P_{fuel}	MR[3]	$\dot{m}_{ox}$	$\dot{m}_{fuel}$	$\dot{m}_{fp}$	$\dot{m}_{ft}$
Test 2 cold start										
Target	30.0	50.84	3.00	3.60	3.60	1.00	22.76	22.76	22.76	-
2	23.6	31.98	2.18	2.51	2.61	0.35	10.69	32.40	30.20	2.2
CEA	-	27.13	2.18	-	-	0.35	10.69	32.40	30.20	2.2
Test 3 following a 28 second dwell time										
3	23.6	34.35	2.43	2.67	2.82	0.35	12.28	35.11	30.51	4.6
CEA	-	32.77	2.43	-	-	0.35	12.28	35.11	30.51	4.6

As with the previous tests, the oxidiser mass flow rate and mixture ratio were determined through a chemical equilibrium analysis model using the known combustion chamber pressure and fuel mass flow rates. In both tests, the HDPE fuel mass flow rate, $\dot{m}_{ft}$, was calculated by recording the average linear displacement rate and using the dimensions and density of the fuel tube.

[3]See footnote 1 from Table 6.3.

However, the fuel mass flow rate calculation of test 3 also needed to consider the additional fuel that was melted into the combustion chamber during the dwell time. A total fuselage displacement of 8 cm was observed corresponding to 70 g of additional fuel that had melted into the combustion chamber. Considering that the HDPE fuselage feed rate immediately resumed at test 3 engine startup (at a flow rate corresponding to 3.2 g/s) the combined calculated $\dot{m}_{ft}$ equaled 4.6 g/s with a total $\dot{m}_{fuel}$ of 35.11 g/s. Corrected data is shown in red.

Using the calculated value for $\dot{m}_{fuel}$ as well as the combustion chamber pressure of test 3 resulted in a slightly higher engine thrust than test 2. Compared to the Ouroboros-2 long dwell time test in Section 6.3 the results are quite similar (Table 7.7) with the autophage engine having a slightly higher relative thrust increase.

Table 7.7 Comparison of bi-propellant and autophage engine performance increase after a long dwell time.

	Initial			Restart		
Engine	F_T, N	P_c	Dwell time, s	F_T, N	P_c	Percent Increase, %
Ouroboros-2	92.25	4.66	43.5	94.94	4.73	2.9
Ouroboros-3	31.98	2.18	28.0	34.35	2.43	7.4

As previously discussed, a slight performance increase after the dwell time is expected due to thermal soakback which will increase the overall engine temperature and enthalpy of the propellants in the combustion chamber. However, the autophage engine may have benefited more from the thermal soakback as it could have allowed the HDPE to absorb much of that heat, phase transition to a liquid, and coat the inside of the combustion chamber. Then, as the engine restarted and in addition to the bi-propellant inlet conditions, the melted HDPE fuel could have began to depolymerise into ethylene gas when directly exposed to the high temperature combustion thereby increasing the combustion chamber pressure, which was reflected in the data. Additionally, the ratio of HDPE to propane fuel changed during test 3 of the Ouroboros-3 engine which would have introduced a slightly higher carbon content and influenced the engine thrust. Overall, more tests would need to be run in order to verify this relationship between dwell time and autophage performance.

7.3.2 Post Hot-Fire Inspection and Analysis

At the conclusion of tests 1, 2 and 3; the Ouroboros-3 engine was disassembled and inspected. Surprisingly, it was found that even with the long burn durations and total cumulative life on the engine, both the combustion chamber and injector remained fully intact, undamaged, and with minimal wear (Fig. 7.5 and Fig. 7.6). This was in stark contrast to the bi-propellant Ouroboros-2 tests which resulted in the combustion chamber being melted to failure. The longevity of this engine can be attributed to the fuel-rich and low-throttle inlet conditions which operated the engine at relatively low temperatures with the combustion chamber wall temperature never exceeding 600°C; well below the melting point of stainless steel.

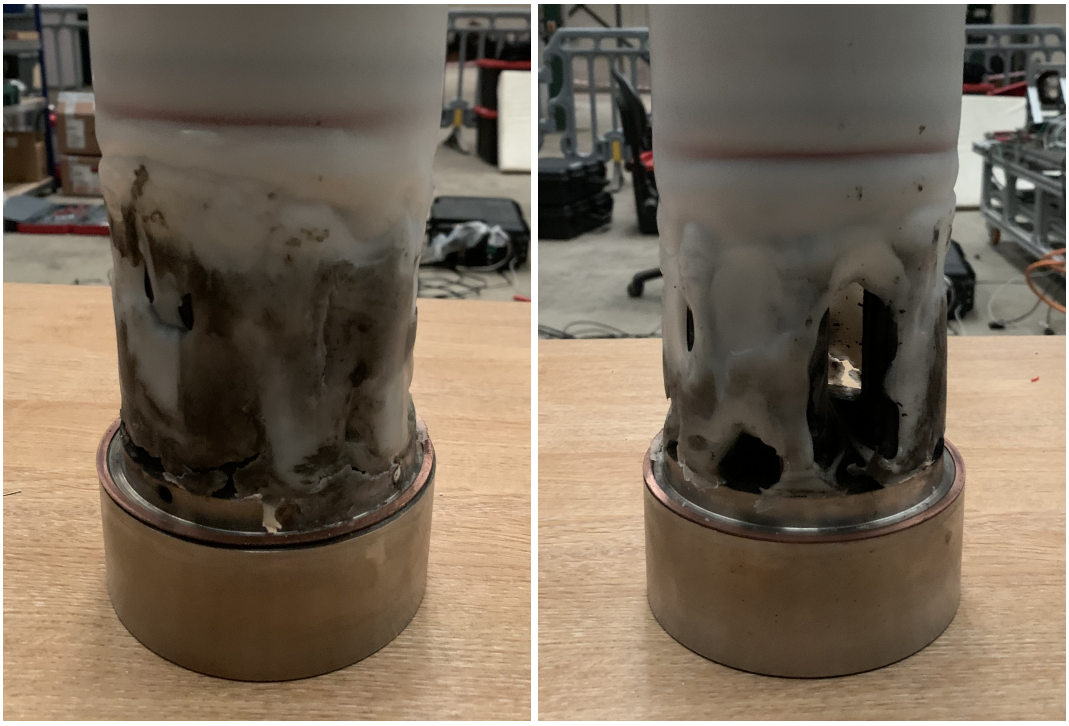

Fig. 7.5 Exterior view of the Ouroboros-3 combustion chamber after test 3.

Additionally, both the implementation of film cooling at the injector and the HDPE contribution to film cooling the downstream section of the combustion chamber likely also played a role in extending the life of the engine. In both images, the HDPE can be seen flowing around the inner chamber supports. This flow would have coated the inside of the chamber walls creating a boundary layer of film that would restrict wall temperature to a maximum corresponding to the boiling point of the fuel (further detail on film cooling is found in Section 3.3.1).

The modified injector design with the blocked oxidiser annulus also proved to be an effective contributor to film cooling the combustion chamber supports. Referencing Fig. 7.6, soot deposits were seen on the injector face which corresponded to the unblocked sections of the oxidiser annulus. This suggests that the combustion process was occurring along those streamlines. Meanwhile, with the exception of the bottom left of the injector face, the sections where the oxidiser was blocked show minimal soot deposits indicating that combustion was not occurring along those streamlines and the propane fuel was successfully being applied as film coolant to the chamber supports. The structural integrity of the chamber supports after the test further supports that the engine was sufficiently cooled during the test.

Fig. 7.6 Interior view of the Ouroboros-3 combustion chamber and injector after test 3.

7.4 Test 4: Throttled Inlet Conditions at High Mixture Ratio

Following the initial success of the Ouroboros-3 engine autophage tests, a second test campaign was conducted in July, 2023. For these tests, a vortex flowmeter was procured and installed to measure oxidiser mass flow rate. Thus, the following performance data does not utilise a chemical equilibrium analysis to approximate oxidiser mass flow rate as was done for previous tests. However, potential two-phase flow may have skewed the fuel mass flow rate data and therefore a chemical equilibrium analysis was still used for analysis and to provide a corrected propane fuel mass flow rate.

Building on the success of the first three low-throttle and fuel-rich tests, test 4 used a new combustion chamber and injector. The test was intended to target a 75% throttle setting with a standard mixture ratio of 2.00. Unfortunately, the target mixture ratio was significantly exceeded but nonetheless provided valuable data and expanded the operating box of Ouroboros-3. This test would also operate the engine at steady state conditions before switching to pulsed operating modes. The intent was to evaluate how the throttle setting would influence the fuselage feed rate into the engine and compare the results to the earlier low-throttle setting tests as well as test 5 which would operate at 100% throttle settings and standard inlet conditions. The results of test 4 steady state operation are shown in Fig. 7.7 and pulsed operation in Fig. 7.8.

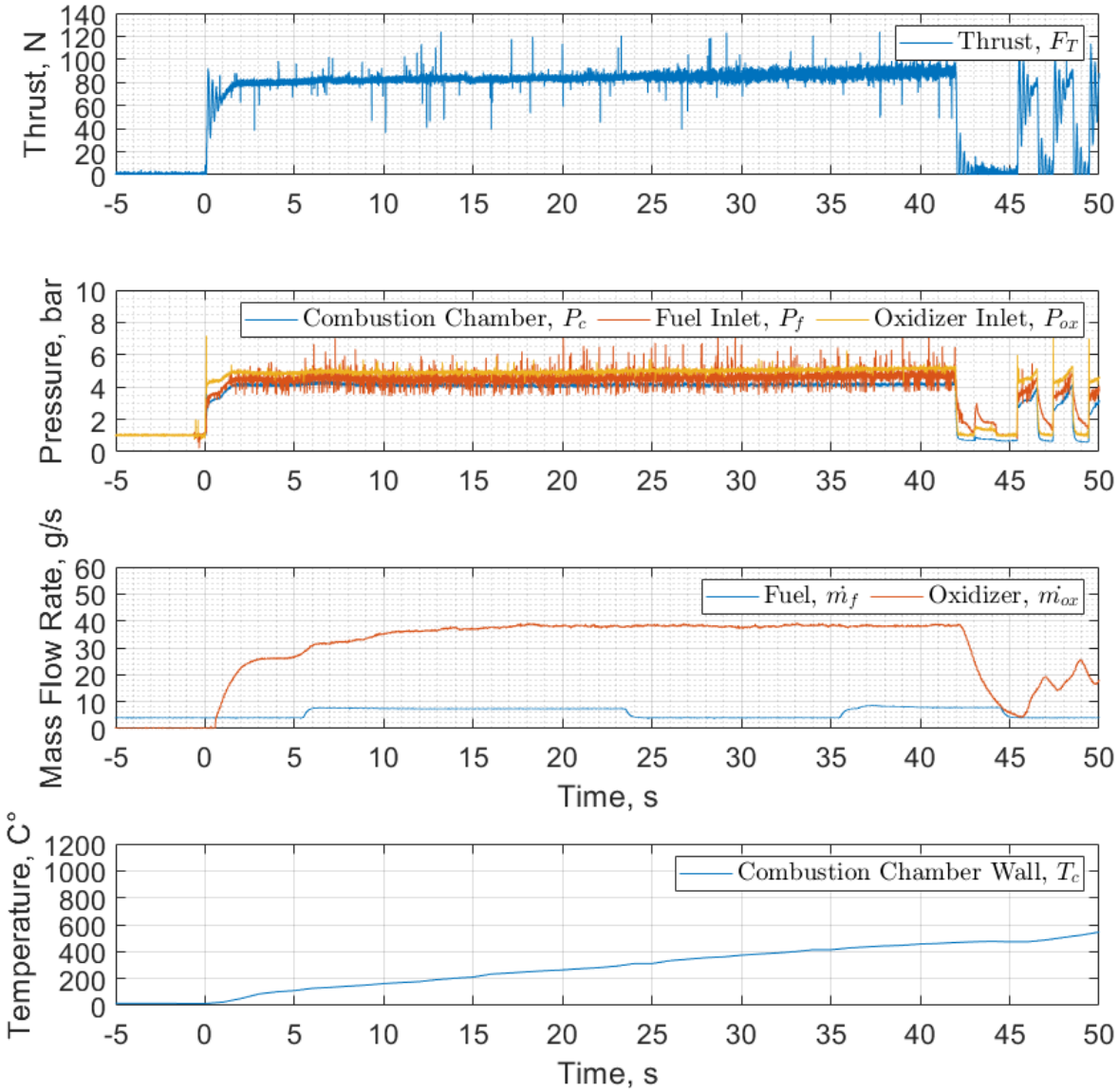

Fig. 7.7 Ouroboros-3 autophage test 4 steady state performance results at throttled, high mixture ratio inlet conditions.

The pulsed data was observed to a high amplitude, low-frequency oscillation in the thrust at the start of each pulse which coincided with a visual oscillation of the test platform for each engine start. This was determined to be a frequency of the test stand since the oscillation does not align with any pressure oscillation in the combustion chamber. Therefore, an infinite impulse response (IIR) filter was applied from 3-10 Hz in order to remove this frequency from the data. The unfiltered thrust data can be found in Appendix A.

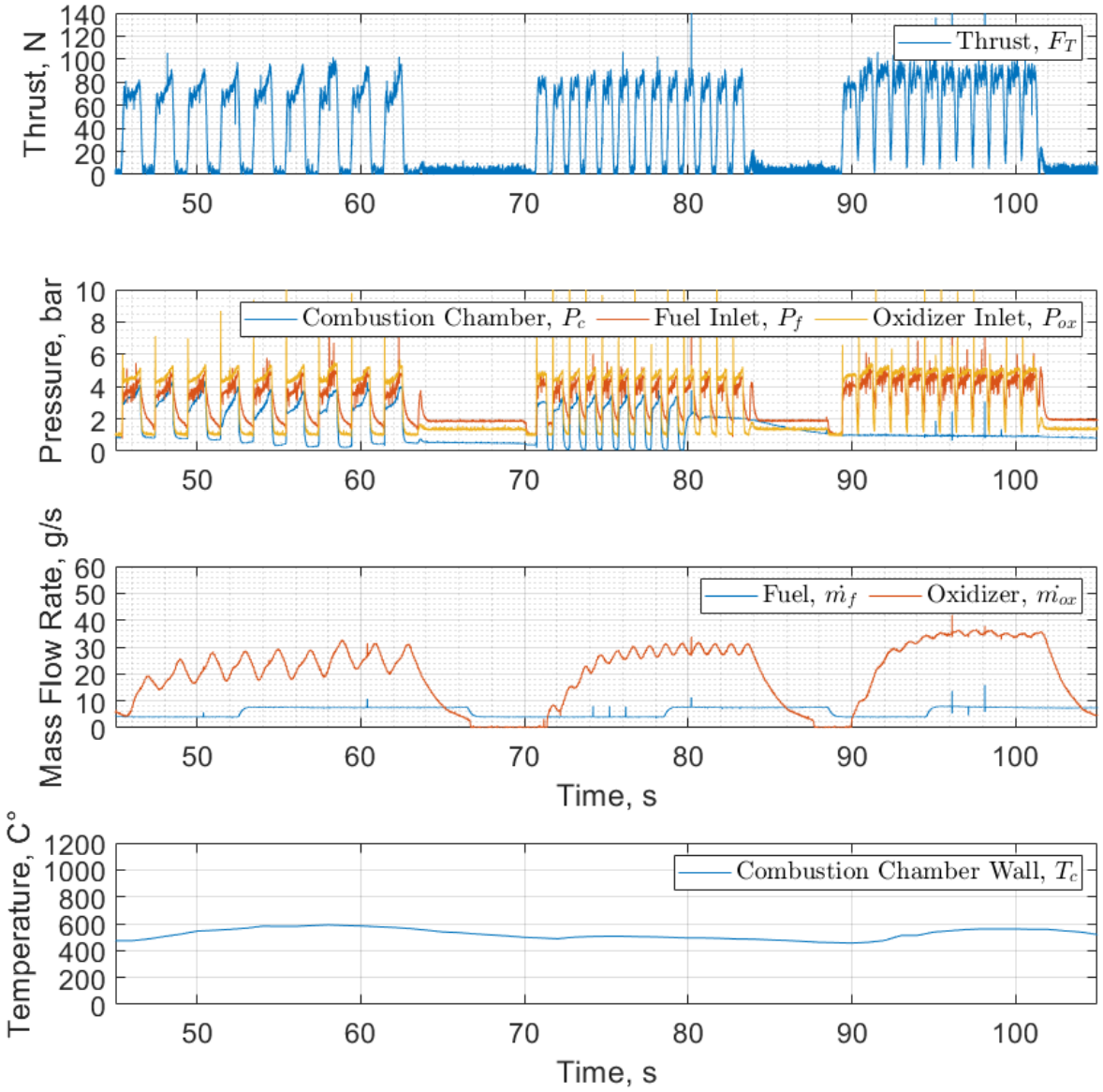

Fig. 7.8 Ouroboros-3 autophage test 4 pulsed mode performance results at throttled, high mixture ratio inlet conditions. Thrust data has been filtered to removed test platform oscillation from results.

Test Timeline

T - 05.0 s Engine countdown begins.

T + 00.0 s Control valves open, oxidizer reaches nominal pressure, engine ignition.

T + 00.4 s Combustion chamber pressure reaches a steady state threshold of approximately 3.50 bar. The plume is recorded to appear pale blue, an indicator that only propane fuel is burning.

T + 00.8 s Combustion chamber pressure begins increasing again.

T + 01.2 s Combustion chamber pressure reaches 90% of full scale output. The plume is recorded as appearing orange/yellow, an indicator that HDPE is contributing to the total fuel mass flow rate.

T + 05.5 s Propane fuel mass flow rate begins to increase.

T + 06.0 s Propane fuel mass flow rate reaches steady state.

T + 15.0 s Oxidiser mass flow rate reaches steady state.

T + 21.0 s The HDPE fuselage is observed to begin moving into the engine.

T + 23.5 s Propane fuel mass flow rate drops off.

T + 25.0 s Thrust roughness significantly increases.

T + 36.0 s Propane fuel mass flow rate increases back to steady state.

T + 40.0 s Steady state fuselage feed rate is measured at 5.7 mm/s.

T + 42.0 s Control valves are closed and a purge valves are opened for a 1 second purge before pulsed operation begins.

T + 45.5 s Pulsed operating mode begins at 0.5 Hz and 50% duty cycle.

T + 62.5 s The engine is shut down and purged for 5 seconds.

T + 73.5 s The engine is reignited and pulsed operating mode begins again at 1.0 Hz and 50% duty cycle.

T + 83.0 s The engine is shut down and purged for 5 seconds.

T + 89.5 s The engine is reignited and pulsed operating mode begins at 1.0 Hz and 75% duty cycle.

T + 101.5 s The engine is fully shut down and purged, cumulative on-time of the engine is calculated at 61.25 s.

7.4.1 Experimental Results

While test 4 used the most instrumentation out of all previous tests, there was a minor issue with the propane fuel flowmeter. As can be seen from the data, the fuel mass flow rate not only has a very long hysteresis before even moving, but it also drops off part way through the test. Because of this behavior, there is a likelihood that there was either two phase flow through the flowmeter or a bubble which could have caused the measurement to drop out. However, since variable area flowmeters have a minimum flow that they can detect and this flowmeter was designed for liquid measurement, a high velocity gas flow could theoretically still provide the same mass flow rate to the engine by condensing downstream of the flowmeter.

Under this assumption, the steady state fuel mass flow rate measurement was used to evaluate engine performance and assumed to be constant throughout the test in order to provide an upper bound on the data. Additionally, the averaged fuel mass flow rate was calculated according to the procedure in Section 6.3.2 in order to provide a lower bound to the data. The resulting performance data is shown in Table 7.8.

Table 7.8 Ouroboros-3 steady state hot-fire test mean performance results compared to fixed mass flow rate chemical equilibrium analysis.

		Pressure, bar				Mass Flow Rate, g/s				
Type	F_t, N	P_c	P_{ox}	P_f	MR	$\dot{m}_{ox}$	$\dot{m}_{fuel}$	$\dot{m}_{fp}$	$\dot{m}_{ft}$	FR, mm/s
Upper bounded performance data										
Target	75.89	4.00	4.80	4.80	2.00	30.23	15.11	-	-	-
Data	84.34	4.29	4.98	4.58	3.10	37.91	12.21	7.41	4.8	5.7
CEA	76.91	4.10	-	-	3.10	37.89	12.22	7.29	4.7	5.6
Lower bounded performance data										
Data	84.34	4.29	4.98	4.58	3.30	37.91	11.43	6.63	4.8	5.7
CEA	72.97	3.95	-	-	3.30	37.63	11.40	6.60	4.8	5.7

Considering both the upper and lower bounded performance data results, both performed better than the theoretical chemical equilibrium analysis with the lower bounded performance (according to the time-averaged fuel mass flow rate) over-performing by 15.6% while the upper bounded performance only over-performed by 9.7%. Thus, we can deduce that the fuel mass flow meter was likely skewed and under-reporting the actual fuel mass flow rate.

Furthermore, if combustion chamber pressure and mixture ratio are set constant another chemical equilibrium analysis can be calculated (shown in Table 7.9). This analysis instead solved for the required propellant mass flow rates to meet the measured combustion chamber pressure and mixture ratio. In this case, the analysis yielded the lowest variance between the thrust data and the theoretical thrust at only +3.2%, which was within the margin of error of the previous bi-propellant tests. Additionally, the analysis showed that both the oxidiser and fuel mass flow rate measurements were slightly skewed with oxidiser mass flow rate error at -4.8% and total fuel mass flow rate error at -5.0%.

Table 7.9 Ouroboros-3 steady state hot-fire test mean performance results compared to a fixed chamber pressure chemical equilibrium analysis.

		Pressure, bar				Mass Flow Rate, g/s				
Type	F_t, N	P_c	P_{ox}	P_f	MR	$\dot{m}_{ox}$	$\dot{m}_f$	$\dot{m}_{fp}$	$\dot{m}_{ft}$	FR, mm/s
Target	75.89	4.00	4.80	4.80	2.00	30.23	15.11	-	-	-
Data	84.34	4.29	4.98	4.58	3.10	37.91	12.21	7.41	4.8	5.7
CEA	81.76	4.29	-	-	3.10	39.83	12.85	8.05	4.8	5.7

Overall, the chemical equilibrium analysis yielded the lowest error compared to the sensor data when the combustion chamber pressure was the anchored variable. Thus, this was determined to be the best model by which the engine data could be evaluated against. Anchoring the model using combustion chamber pressure is also consistent with all previous experimental results which also used the combustion chamber pressure as the anchor variable in the corresponding chemical equilibrium analyses.

7.4.2 Post Hot-Fire Inspection and Analysis

Following a long nitrogen purge to cool the system, the engine was disassembled and inspected. Since the engine operated nominally throughout the test with no signs of a failure, combustion

chamber wall temperature did not exceed 600°C, and only had a cumulative life of 61.25 s of operation, it was expected that there would be minimal or no signs of damage as with the previous engine. And while this was true for the injector, there were some indications of impending failure of the combustion chamber supports.

The interior of the engine is shown in Fig. 7.9. There, we can see a faint pintle spray pattern on the injector face which matches the designed propane film cooling of the chamber supports. We can also see pooling of the HDPE at the bottom of the engine after shutdown; along the top of the engine though, the chamber supports appear to have slightly melted. This shows the effect of gravity on engine cooling since only the top two supports showed signs of melting. As the HDPE fuselage was melted, the molten plastic would have been pulled along the sides of the engine to pool at the bottom. Thus, testing the engine in a horizontal configuration likely created a very effective boundary layer on the bottom of the engine but left the supports at the top exposed to the combustion gases.

However, the damage is very localised to only the top chamber supports indicating that both cooling mechanisms were very effective when this engine's cumulative life is compared to that of the bi-propellant Ouroboros-2 engine that used no cooling. An improvement to future designs would be to use materials with high thermal conductivity such as copper alloys. Unlike stainless steel, copper alloys would efficiently transfer the heat away from the hot spots and could significantly prolong the life of the engine.

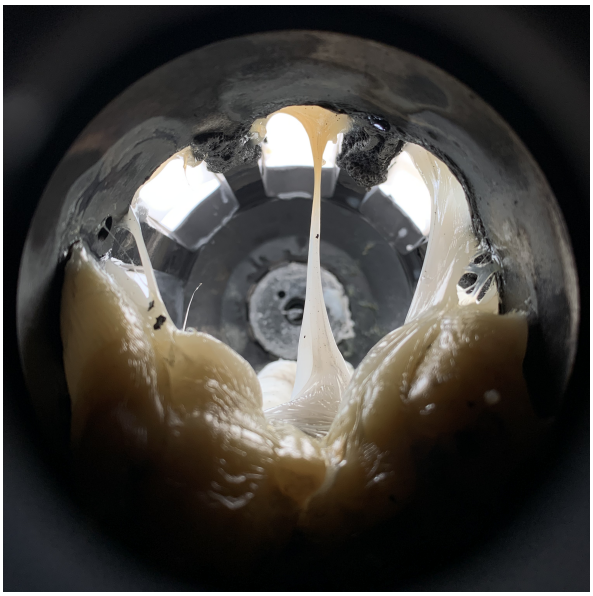

Fig. 7.9 Interior view of the Ouroboros-3 combustion chamber and injector after test 4.

A convenient bi-product of the melted chamber supports though is that the spray angle of the injector can be determined and compared to the unmodified pintle injector spray angle from Section 6.5.2. In this case, the chamber supports are melted at the nozzle end of the inner chamber. Using the CAD model of the engine, that angle was found to be 12.5°; approximately half of the previous Ouroboros-2 spray angle. This correlated with the modifications to the Ouroboros-3 injector that blocked sections of the annulus. The modifications would have increased oxidiser injection velocity and TMR as was discussed in Section 3.3.3.

While the experimental spray angles are approximately double the theoretical values according to the design, they do follow the same trend. This variation could also be explained by the HDPE influencing the size and shape of the recirculation zones which could change the shape of the streamline where the bulk of the combustion is occurring. However, in order to understand the impact of the HDPE on the flow within the combustion chamber, additional research would need to be conducted on the specifics of the relationship between pintle injector spray angle and autophage combustion.

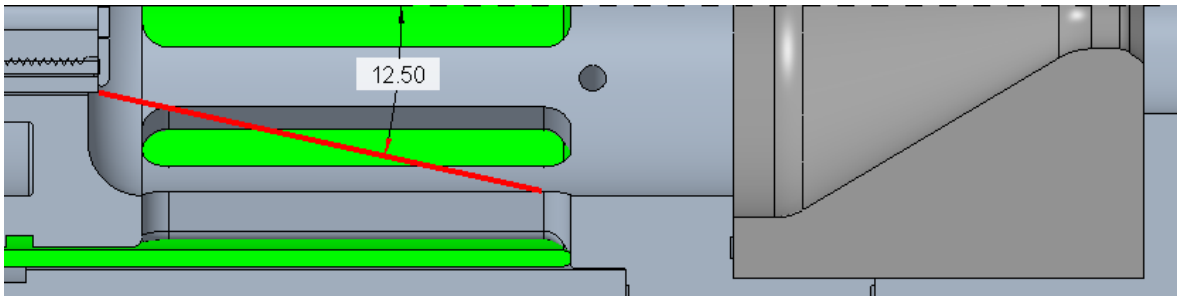

Fig. 7.10 Estimated angle of the Ouroboros-3 main combustion streamline based on post hot-fire testing analysis.

Nevertheless, the injector performed exceptionally well and showed no signs of damage. Some soot deposition was observed in both the annulus and pintle gap up with most deposits occurring up to a maximum of 5 mm from the outlet, but some outliers were up to 2 cm from the outlet. This soot deposition was most likely a result of the pulsed operating mode and was determined to be nominal since there was less overall soot than in the Ouroboros-2 injector.

Fig. 7.11 Exterior view of the Ouroboros-3, annulus-blocked injector after test 4.

7.5 Test 5: Standard Inlet Conditions in Steady State and Pulsed Mode

The final test campaign was the culmination of all previous tests and was designed to operate the engine at its designed standard inlet conditions, mixture ratio of 2.00, and a 100% throttle setting. Being the last test of the research, it would operate the Ouroboros-3 engine in both steady state and pulsed mode with the expectation of testing the engine past its operating limits and to failure. Steady state performance is shown in Fig. 7.12 and pulsed mode performance in Fig. 7.13. As done previously for test 4, a filter was applied to the pulsed mode data in order to eliminate the test platform low-frequency oscillation.

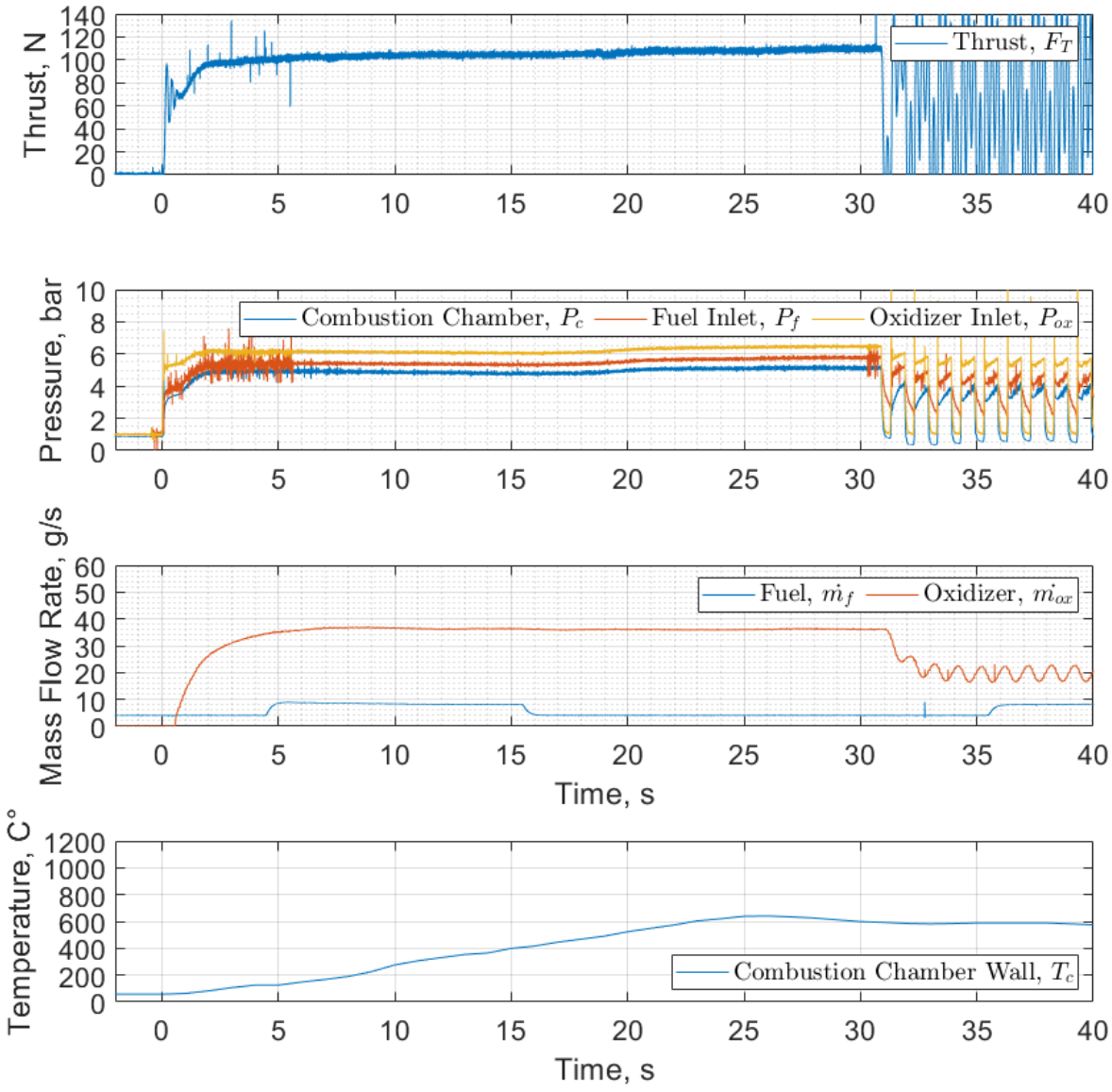

Fig. 7.12 Ouroboros-3 autophage test 5 performance results at standard inlet conditions.

The intent was to fully validate the autophage operation of the engine at its steady state design point which could be used to determine the effect of engine throttling and mixture ratio on the fuselage feed rate. The results could then be analysed to determine the percent contribution of the HDPE fuselage to both the fuel mas flow rate and total propellant mass

flow rate at the various inlet conditions. Additionally, the range of pulsed operating modes would serve to further verify the effect of off-time on fuselage mass flow rate contribution and overall autophage performance. As predicted, most of the pulsed modes were observed to permit the fuselage to be inserted during engine off-time.

The final pulsed modes were also designed to use an off-time of less than the theorised minimum off-time requirement (determined in Section 6.3.2) to validate the hypothesis. A new combustion chamber was used for this test;but, the first Ouroboros-3 injector was used once again which resulted in a cumulative test time of nearly 200 s with no signs of damage to the pintle injector.

Overall, the engine was successfully tested to failure which occurred immediately after the high frequency, high duty cycle pulsed mode at 2 Hz and 75% duty cycle. This corresponded to an off-time of only 125 ms which, as anticipated, was insufficient to allow the fuselage to be advanced into the engine. This eliminated the film cooling effect of the HDPE on the chamber walls and caused the chamber supports to melt due to the high temperature.

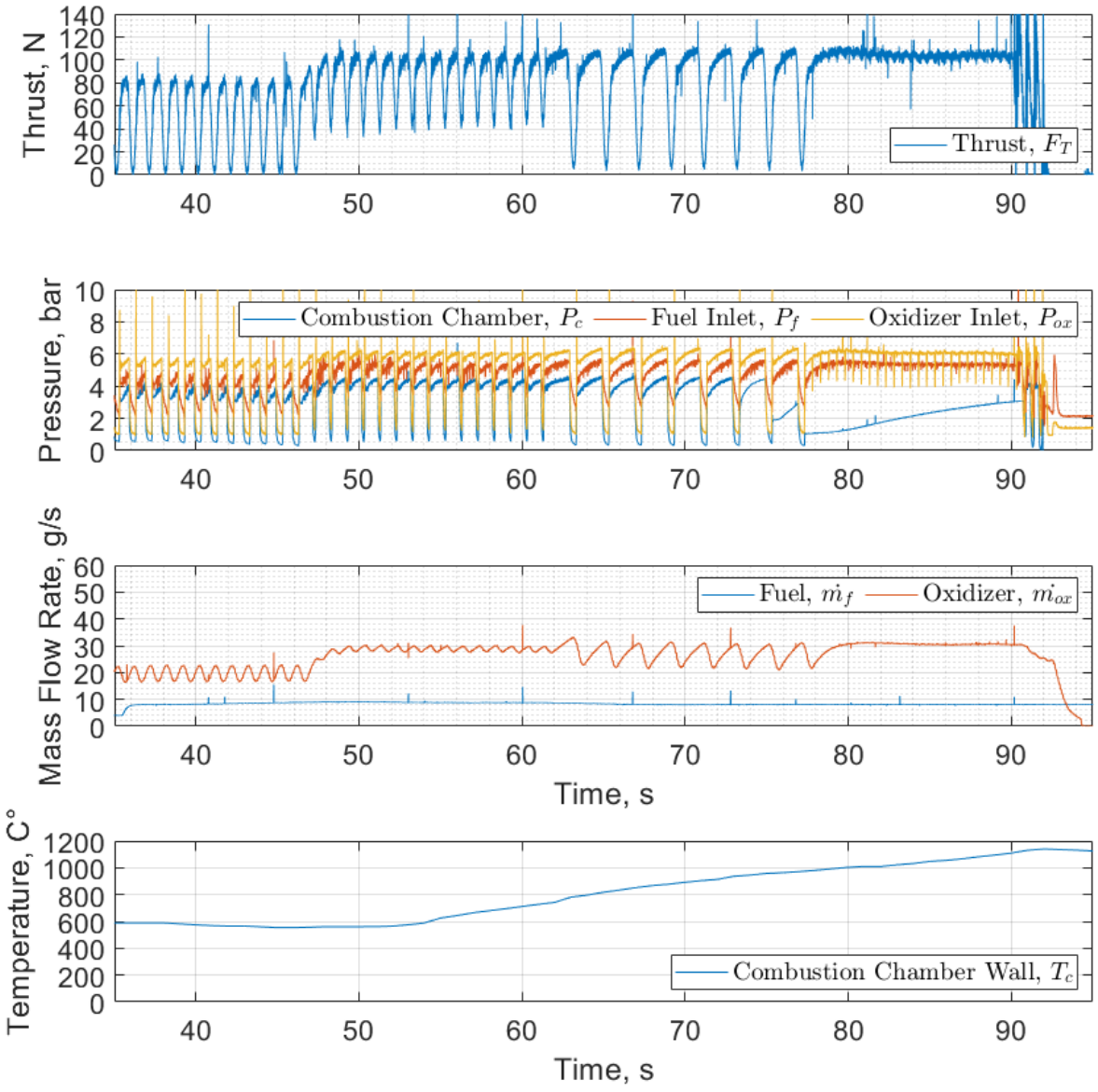

Fig. 7.13 Ouroboros-3 autophage test 5 performance results at standard inlet conditions.

Test Timeline

T - 05.0 s Engine countdown begins.

T + 00.0 s Control valves open, oxidizer reaches nominal pressure, engine ignition.

T + 00.4 s Combustion chamber pressure reaches a steady state threshold of approximately 3.50 bar. The plume is recorded to appear pale blue, an indicator that only propane fuel is burning.

T + 00.8 s Combustion chamber pressure begins increasing again.

T + 01.6 s Combustion chamber pressure reaches 90% of full scale output. The plume is recorded as appearing orange/yellow, an indicator that HDPE is contributing to the total fuel mass flow rate.

T + 05.0 s Oxidiser mass flow rate reaches steady state.

T + 05.5 s Propane fuel mass flow rate begins to increase.

T + 06.0 s Propane fuel mass flow rate reaches steady state.

T + 16.0 s Propane fuel mass flow rate drops off.

T + 17.0 s The HDPE fuselage is observed to begin moving into the engine. At the same time both inlet pressures, chamber pressure and thrust are observed to increase.

T + 25.0 s Steady state chamber wall temperature reaches a peak of 650°C.

T + 30.0 s Steady state fuselage feed rate is measured at 10.0 mm/s.

T + 31.0 s Steady state mode is turned off and pulsed mode is turned on. The pulsed mode is operated at 1 Hz and 50% duty cycle.

T + 46.0 s Pulsed operating mode is switched to 1.0 Hz and 75% duty cycle.

T + 54.0 s Combustion chamber wall temperature is observed to begin increasing.

T + 61.0 s Pulsed operating mode is switched to 0.5 Hz and 75% duty cycle.

T + 77.0 s Pulsed operating mode is switched to 2.0 Hz and 75% duty cycle. Peak combustion chamber wall temperature reaches 1140°C.

T + 90.0 s Pulsed operating mode is switched to 2.0 Hz and 50% duty cycle. The engine immediately experiences a failure with the injector being ejected up the fuselage.

T + 92.0 s The engine is fully shut down and purged, cumulative on-time of the engine is calculated at 72.25 s.

7.5.1 Experimental Results

Test 5 of the Ouroboros-3 engine was a successful demonstration of autophage operation at its design point and standard inlet conditions. It was able to operate the engine for a long duration both in steady state and across multiple different pulsed modes. Ultimately, it resulted in an intentional engine failure (Fig. 7.14) which also provided confirmation of the most likely failure mode of a direct fuselage insertion architecture.

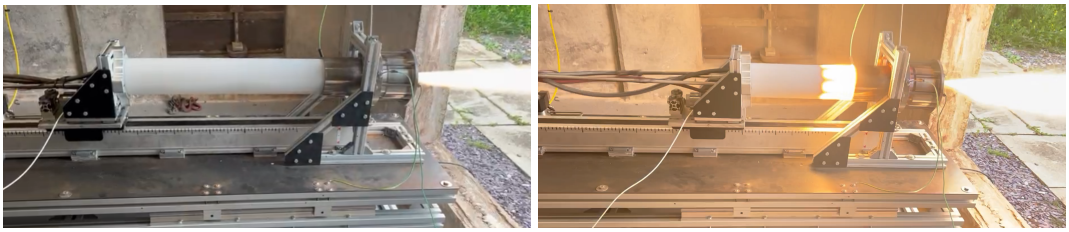

(a) (b)

Fig. 7.14 Ouroboros-3 engine test 5 operation at a) steady state and b) failure.

The resulting mean performance data for steady state operation is detailed in Fig. 7.10. As with previous tests, this data was compared to a combustion chamber pressure anchored chemical equilibrium analysis (CEA) model to provide the theoretical performance of the engine. In general, the engine performed within a small margin of error of the theoretical performance with just a +2.0% error in thrust measurement.

Table 7.10 Ouroboros-3 steady state hot-fire test mean performance results.

		Pressure, bar				Mass Flow Rate, g/s				
Type	F_t, N	P_c	P_{ox}	P_f	MR	$\dot{m}_{ox}$	$\dot{m}_f$	$\dot{m}_{fp}$	$\dot{m}_{ft}$	FR, mm/s
Target	101.7	5.00	6.00	6.00	2.00	37.73	18.87	-	-	-
Data	105.1	5.05	6.22	5.50	2.17	37.05	16.68	8.38	8.3	10.0
CEA	103.0	5.05	-	-	2.17	38.92	17.94	9.04	8.9	10.7

One unusual behavior was that of the fuel inlet pressure, P_f, which exhibited significantly more roughness at engine start. This was considered to be a start-up transient that dissipated as the engine transitioned from bi-propellant to autophage operation. Additionally, during the final pulsed mode operation, the combustion chamber pressure was observed to drift; likely due to fuel-oxidiser reaction products (FORP) causing a blockage in the sensor tube from the aggressive pulsing. Nevertheless, test 5 exhibited the least amount of roughness across all sensors indicating smooth and steady combustion characteristics which was to be expected since the engine was oeprating at its design point.

7.5.2 Post Hot-Fire Inspection and Analysis

After the engine failure, the engine was inspected and photographed. It was then disassembled and each of the subsequent components was inspected to determine any other failure modes. Different viewpoints of the effects of the failure are shown in Appendix B and a view of the final engine assembly is shown below in Fig. 7.15.

One of the key things seen during the failure was the outline of the injector face and the chamber supports as the injector was ejected into the HDPE fuselage. Looking closely, the chamber supports themselves were different lengths with the shortest ones located at the top of the engine. This correlates with the previous hypothesis of gravity acting on the melted HDPE fuel causing it to pool at the bottom of the combustion chamber due to the horizontal hot firing. During the test, the top supports were significantly more melted indicating a longer exposure to the hot gases than the bottom supports; this is clearly seen in Fig. 7.16.

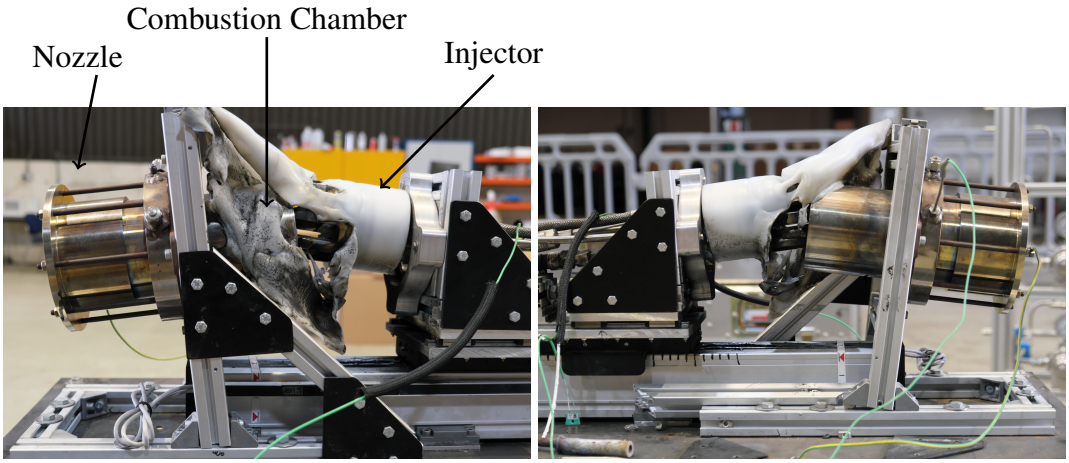

Fig. 7.15 Ouroboros-3 engine photos after the conclusion of testing.

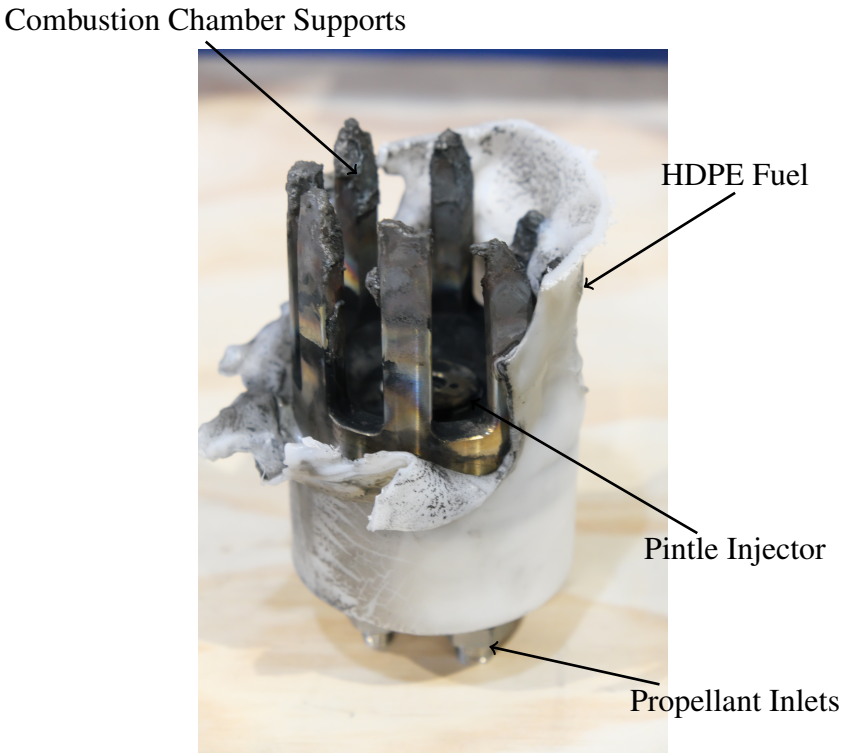

Fig. 7.16 Ouroboros-3 combustion chamber after test 5.

The length of the melted combustion chamber supports also correlates with the previous analysis in Section 7.4.2 which estimated the injector spray angle at approximately 12.5°.

Considering the pintle injector itself in Fig. 7.17, no damage was noted even though this particular injector had a cumulative life of nearly 200 seconds of on-time. Furthermore there was a significant amount of soot deposition on the injector face so the effects of film cooling were not visible; this deposition was due to the HDPE burning around the combustion chamber after the failure.

Overall though, the injector was very successful and did not succumb to overheating which is a common failure mode of pintle injectors [118]. In addition to operating in autophage, these tests demonstrated that a pintle injector which uses an annular blockage could be a viable design and could benefit from future research.

Fig. 7.17 Ouroboros-3 injector after test 5 and 198.9 s of cumulative on-time.

While the nozzle bulkhead and graphite nozzle showed no visible damage, as they were removed from the engine assembly, a thin sheet of steel was recorded as having molded to the shape of the nozzle. This is shown in Fig. 7.18.

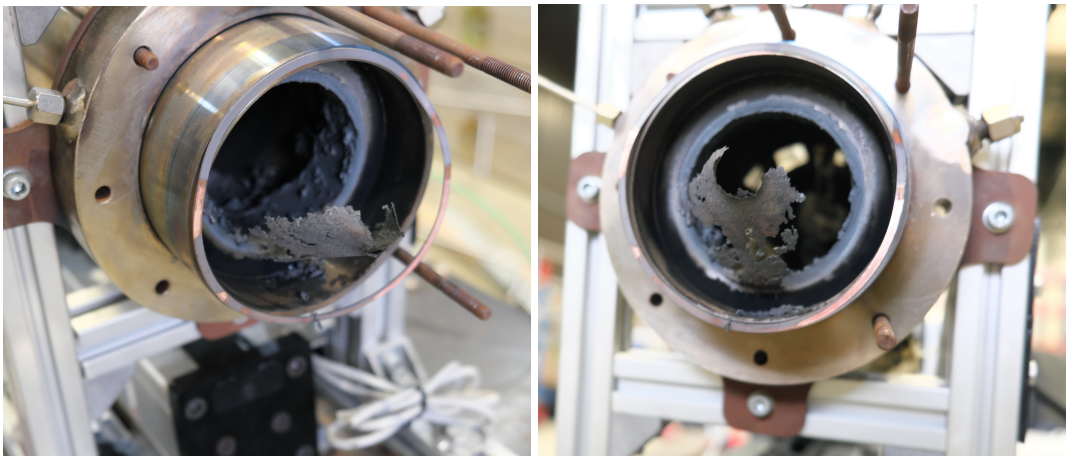

(a) (b)

Fig. 7.18 Molten steel molded to the nozzle shape during hot-fire testing.

Overall, the root cause behind this engine failure was due to thermal runaway during pulsed mode operation. During all steady state tests, the engine showed no difficulty in maintaining chamber wall temperature below 600°C which correlates with the depolymerisation temperature and boiling point of HDPE [20]. However, the final pulsed modes of test 5 did not allow for the HDPE to be advanced and melted in the engine which was likely the root cause of the failure. Moreover, pulsed operating modes are known to cause engines to operate at higher temperatures [145] and while some pulsed modes proved advantageous to yield a faster HDPE feed rate the high frequency, high duty cycle modes ultimately led to the engine failure and complete meltdown of the inner combustion chamber, the remains of which can be seen inside the chamber shell in Fig. 7.19.

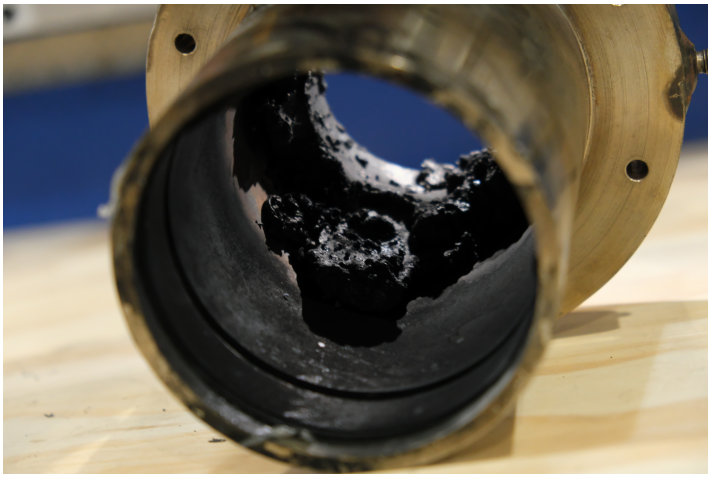

Fig. 7.19 Melted remnants of the Ouroboros-3 combustion chamber inside the chamber shell.

7.6 Autophage Steady State Performance Analysis and Operating Box

The initial three steady state tests of the Ouroboros-3 autophage engine successful validated the operation of an autophage engine concept using a direct fuselage insertion architecture. The tests demonstrated nominal engine operation at fuel-rich inlet conditions, engine throttling, as well as engine cut-off and a commanded engine restart after a long dwell time. Overall, the high-density polyethylene fuel tube was successfully inserted and used as fuel in conjunction with its bi-propellants. This resulted in performance data that showed nominal predicted thrust, combustion chamber pressures, and I_{sp}.

The subsequent tests 4 and 5 were able to operate the engine at steady state using a higher throttle setting and higher mixture ratios to further expand the operating box. Experimental results again showed nominal engine performance across the full range of tests when compared to theoretical values. The full range of tests provided sufficient results in order to evaluate the effect of throttle setting, mixture ratio, and chamber temperature on autophage feed rate. The results of this analysis forms the foundation of future autophage research into both scaling the concept and optimising the designs which could eventually lead to use on flight hardware.

7.6.1 Comparison of Experimental vs. Theoretical Performance

Table 7.11 details the performance results of each autophage hot-fire test compared to the theoretical performance according to a chemical equilibrium analysis model. The models were anchored using the measured combustion chamber pressures and mixture ratios in order to calculate the expected engine performance and can be referenced in the previous sections. The autophage performance was then compared the previous bi-propellant tests in order to identify any potential variation between the two configurations.

Table 7.11 Comparison of steady state autophage performance to bi-propellant performance.

			Actual Performance		CEA Performance		Percent Error	
Test	P_c, bar	MR	F_t, N	I_{sp}, s	F_t, N	I_{sp}, s	F_t	I_{sp}
Autophage Results								
1	5.04	1.10	96.54	125	100.6	132	-4.0%	-5.3%
2	2.18	0.35	31.98	38	27.04	64	+18.3%	-40.8%
3	2.43	0.35	34.35	42	32.77	69	+4.8%	-39.7%
4	4.29	3.10	84.34	165	81.76	158	+3.2%	+4.4%
5	5.05	2.17	105.1	189	103.0	185	+2.0%	+2.2%
Bi-Propellant Results								
1a	4.65	1.07	95.54	135	90.97	130	+5.0%	+3.8%
1b	4.49	1.01	96.58	132	90.97	130	+6.2%	+1.5%
2a	2.43	1.05	92.25	130	93.03	127	-0.8%	+2.4%
2b	4.29	1.07	94.94	130	93.03	127	+2.1%	+2.4%
5	6.76	1.33	143.5	156	147.3	160	-2.6%	-2.5%

The variance between the autophage and bi-propellant tests was very minimal for mixture ratios above 1.00; however, the low mixture ratio autophage tests showed significant variance in the I_{sp}. However, a lower I_{sp} should be expected when operating as an autophage system since HDPE has a higher molecular weight than propane fuel[4]. This should result in lower specific impulse and was indeed shown in the data of autophage tests 2 and 3. The inherent cooling provided by the HDPE, which is beneficial at higher mixture ratios, would have also have a negative effect on the I_{sp} due to the melting and vaporisation process necessary for it to be used as a combustion reactant. This would lower the overall enthalpy of the combustion gases resulting in low I_{sp}. While the low mixture ratio tests showed effective throttling of the engine, future autophage operation should focus on operating at higher mixture ratios which can leverage the film cooling provided by the HDPE for improved performance such as demonstrated by autophage test 4.

[4]The high density polyethylene molecule consists of $(C_2H_4)_n$ while the chemical formula for propane is C_3H_8. The slightly higher amount of carbon in HDPE as well as the thermal energy required to depolymerise it should correlate with a reduction in engine I_{sp} when compared to a bi-propellant engine which only operates on propane.

7.6.2 Evaluation of the Autophage Contribution to Total Fuel Mass Flow Rate and Total Propellant Mass Flow Rate

Using the performance data and measured HDPE mass flow rate, the contribution of the autophage fuselage to the overall performance of the engine was able to be calculated. Table 7.12 shows the HDPE feed rate which was calculated as a time-averaged linear displacement of the fuselage during steady state operation for all the tests with the exception of test 1 (due to the short test duration and not reaching a steady state feed rate this test was excluded from analysis). The feed rate was then converted to HDPE mass flow rate, $\dot{m}_{ft}$, according to the dimensions and density of the fuselage; the test 3 mass flow rate was corrected to account for the mass of the fuselage that was inserted during the long dwell time. The resulting $\dot{m}_{ft}$ was then compared to the total fuel mass flow rate and total propellant mass flow rate of each test to determine to percent contribution of autophage operation to the performance.

Table 7.12 Ouroboros-3 steady state hot-fire test mean performance results.

				Mass Flow Rate, g/s				FR,	$\frac{\dot{m}_{ft}}{\dot{m}_{fuel}}$	$\frac{\dot{m}_{ft}}{\dot{m}_{ox}+\dot{m}_{fuel}}$
Test	F_t, N	P_c, bar	MR	$\dot{m}_{ox}$	$\dot{m}_{fuel}$	$\dot{m}_{fp}$	$\dot{m}_{ft}$	mm/s		
1	96.54	5.04	1.10	39.99	37.39	37.39	-	-	-	-
2	31.98	2.18	0.35	10.69	32.40	30.20	2.2	2.6	6.8%	5.1%
3	34.35	2.43	0.35	12.28	35.11	30.51	4.6	3.2	13.1%	9.7%
4	84.34	4.29	3.10	37.91	12.21	7.41	4.8	5.7	39.3%	9.6%
5	105.1	5.05	2.17	36.22	16.68	8.38	8.3	10.0	49.8%	15.7%

Based on the results for steady state operation, the throttle setting (chamber pressure) of the engine had the greatest effect on the feed rate and the total propellant mass flow rate contribution. A clear positive correlation was seen between tests 2-5 that as throttle setting increased so did both the total propellant mass contribution and fuel mass contribution. This was an expected result since higher throttle settings result in higher engine temperatures which should more readily melt the HDPE fuselage inside the chamber.

Mixture ratio was also observed to have a slight positive correlation with both the total propellant mass contribution and total fuel mass contribution but the relationship had a weaker correlation than the throttle setting. Figures 7.20 and 7.21 show general trends of the data; however, it is important to note that since both chamber pressure and mixture ratio were varied across the tests, the charts only demonstrate a general trend rather than a true independent to dependant variable relationship.

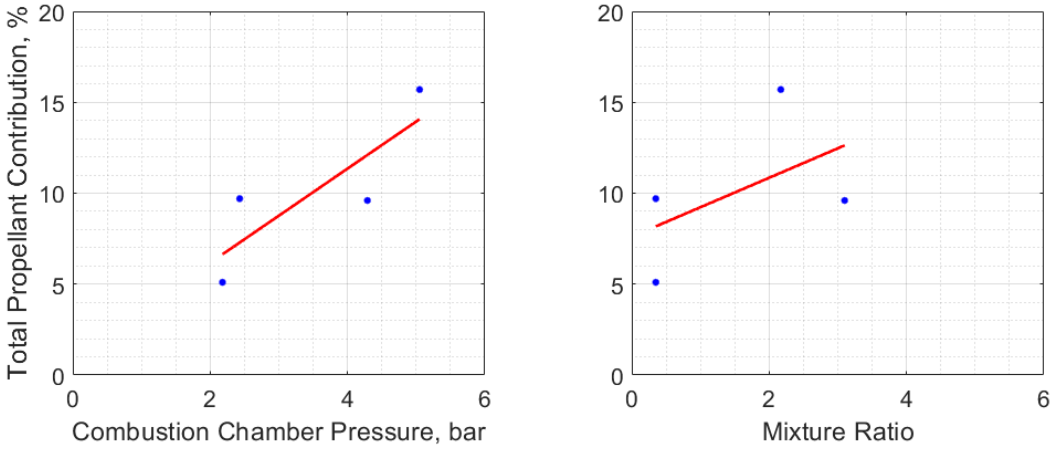

Fig. 7.20 Ouroboros-3 autophage combustion chamber pressure vs. total propellant mass flow rate contribution.

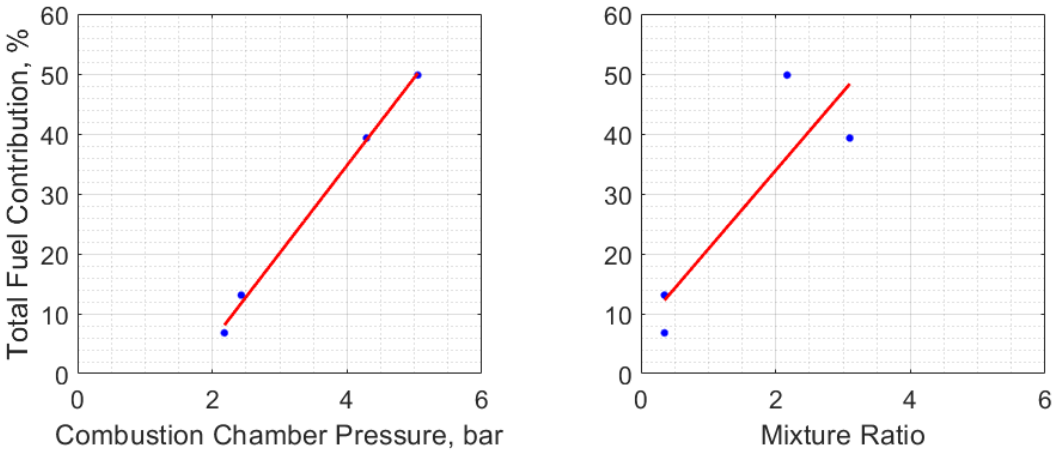

Fig. 7.21 Ouroboros-3 autophage combustion chamber pressure vs. total fuel mass flow rate contribution.

When the temperature data is considered over the full run, we can better see the effects of mixture ratio on engine performance. Figure 7.22 shows the resulting thermal data across the burn time for all autophage tests but the ones of interest are test 1 and test 5. Both of those tests had similar initial engine performance however test 1 had a much lower mixture ratio. The thermal data shows test 5 engine temperature increased at a much faster rate than test 1 which resulted in the engine transitioning to a steady state autophage feed rate quicker (autophage transition is indicated by the markers). Therefore, we can conclude that mixture ratio does indeed have an indirect effect on autophage performance by raising combustion chamber wall temperature, but throttle setting has a more significant effect.

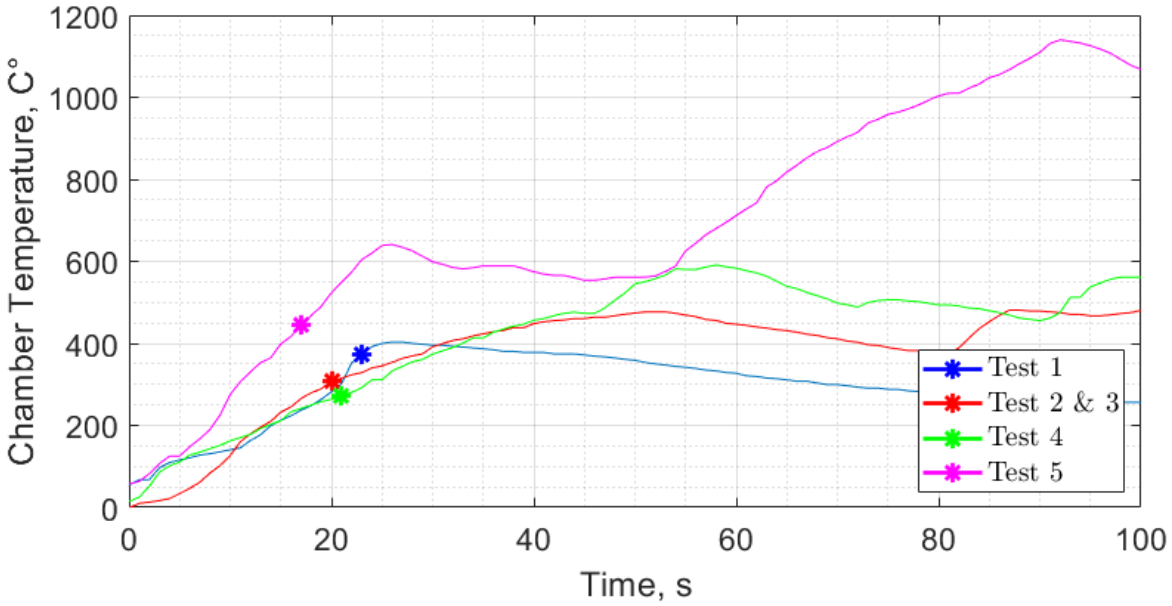

Fig. 7.22 Comparison of chamber wall temperatures over full run duration.

More tests would be needed to be conducted to independently isolate both the effect of chamber pressure and mixture ratio. Nevertheless, these tests do validate that these two parameters have an effect on autophage engine performance and that engine inlet conditions can be used as a method for controlling the feed rate of an autophage launch vehicle in order to optimise the thrust profile and flight trajectory. Additionally, across all of the tests, the autophage total propellant mass contribution aligned with the range of typical structural efficiencies of conventional launch vehicles [146]. Therefore, a full-scale autophage engine could feasibly operate within that range with the fuselage accounting for a reasonable portion of the total propellant mass.

7.6.3 Effects of the Transition to Autophage Operation

Engine Ignition

An interesting result of the Ouroboros-3 autophage tests was the transition from engine start to autophage start. This was identified as a period of steady state operation whereby the engine was only burning propane fuel before transitioning to a mixture of propane and HDPE. Videos taken during the tests show this transition as an over-expanded pale blue plume that quickly changes to nominal expansion with a yellow/orange plume as shown in Fig. 7.23.

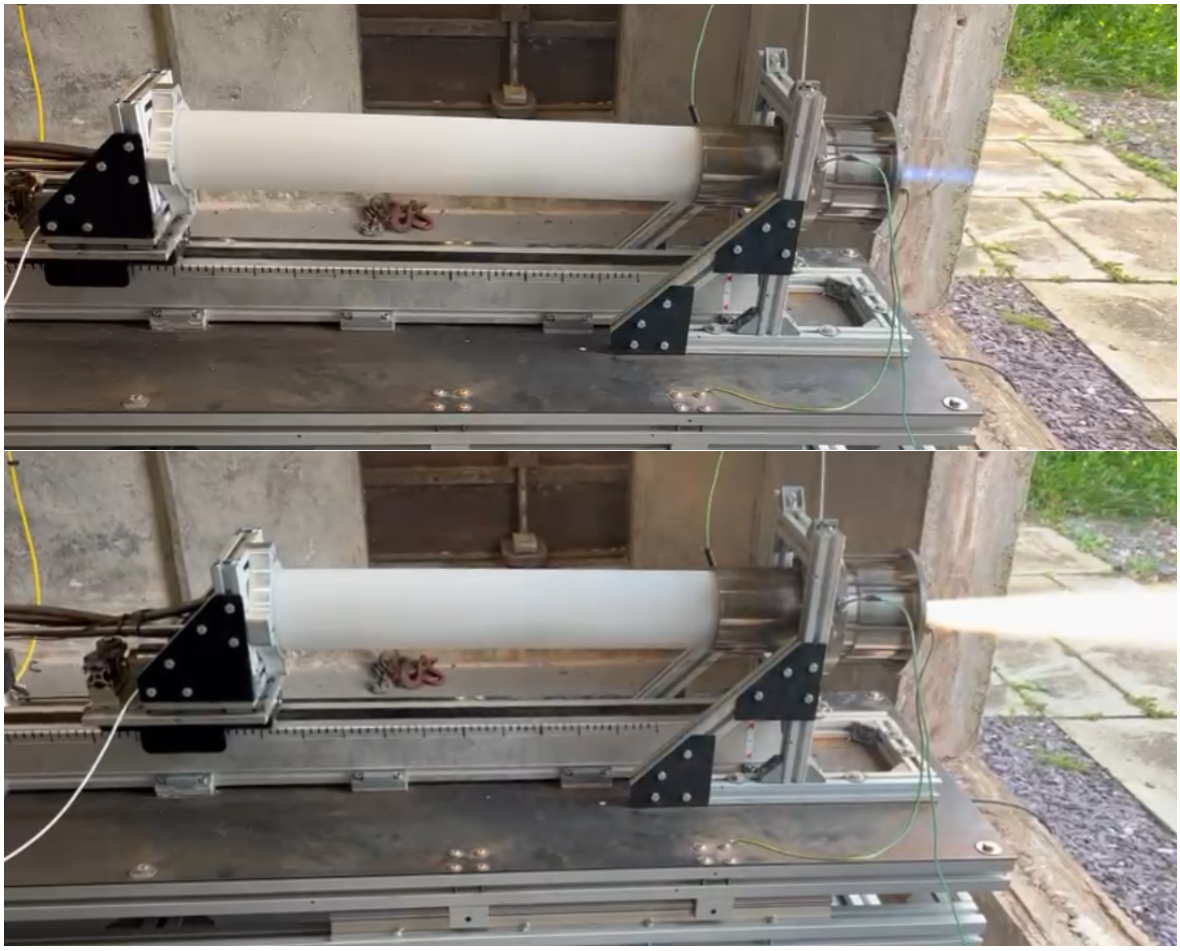

Fig. 7.23 Transition from bi-propellant to autophage operation.

Evaluating the combustion chamber pressure rise time during the autophage engine ignition showed a range of results detailed in Table 7.13 (all rise and decay time charts can be found in A). First, test 1 had a similar rise time profile to the bi-propellant tests which was expected since the mixture ratio and throttle settings were similar. However, tests 2 and 3 were conducted when the engine was warm and showed extremely fast rise times as well as caused the chamber pressure to overshoot steady state. The autophage HDPE could have caused this fast rise time by off-gassing within the chamber and causing rapid ignition when the control valves were opened and oxidiser entered the chamber.

Table 7.13 Ouroboros-2 tests 2a & 2b chamber pressure rise and decay times.

Test no.	F_t, N	P_c	MR	t_r, ms	t_d, ms
1	96.54	5.04	1.10	300	100
2	31.98	2.18	0.35	50	100
3	34.35	2.43	0.35	50	300
4	84.34	4.29	3.10	1100	100
5	105.1	5.05	2.17	1600	100

The final two tests, 4 and 5, showed a different behavior though. Both of these tests demonstrated the aforementioned transition from bi-propellant ignition to autophage ignition. The rise time of test 5, Fig. 7.24, best demonstrates this transition. Here we can see a very fast

initial increase in chamber pressure which then steadied at approximately 0.4 seconds until 0.8 seconds where it again began to rise, now with an increased chamber pressure roughness. This correlated exactly with the plume color change seen in the test video and in Fig. 7.23 and is certainly indicative of the transition from bi-propellant to autophage. The thrust decay time though was mostly nominal with similar values to the bi-propellant tests.

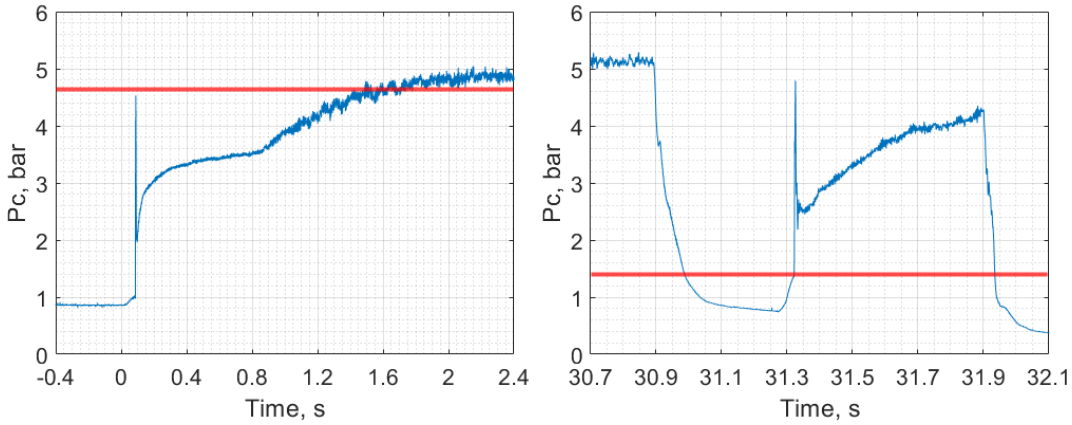

(a) Test 5 rise time

(b) Test 5 decay time

Fig. 7.24 Comparison of the Ouroboros-3 combustion chamber pressure rise and decay times.

Autophage Feed

Besides the engine ignition transient, the second transition to autophage operation was the start of fuselage feed into the engine. This was hypothesised to be correlated with combustion chamber wall temperature since a high heat flux should result in theory result in more melting of the HDPE and a quicker transition to a steady state feed rate. Figure 7.25 shows the burn time versus combustion chamber wall temperature data for all cold start tests (test 1, 2, 4 and 5) with markers indicating the point at which fuselage movement was observed.

All the low-throttle setting tests resulted in approximately the same temperature slope and autophage start time. Test 5 on the other hand (which was operated at the highest throttle setting), showed a steeper slope and began the transition to autophage feed sooner. The combustion chamber wall temperature recorded at that point was 445°C; much higher than the melting point of HDPE.

Once the transition to steady state feed rate began, test 4 showed an increase in thrust roughness while test 5 showed a slight increase in both inlet conditions and performance. Both the thrust roughness and performance increase could be a result of the vaporisation of HDPE causing a shift in the combustion chamber recirculation zones or the flow streamlines. However, if the results of test 5 can be replicated or modeled it could be an indicator that autophage operation could actually increase engine performance in addition to being a secondary fuel source. This could be considered a topic for future research in order to determine why test 5 saw a performance increase during the autophage transition.

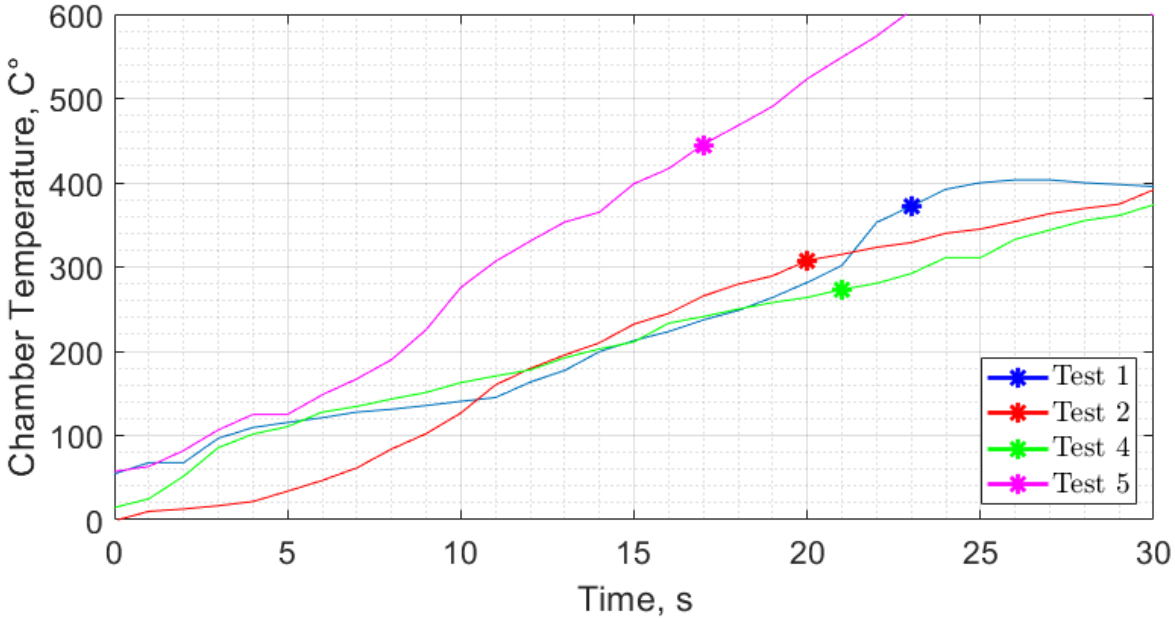

Fig. 7.25 Effect of combustion chamber wall temperature on transition to autophage feed.

7.6.4 Frequency Analysis

The collection of spectrograms and persistence diagrams across all of the Ouroboros-3 tests can located in Appendix B. Two sets of spectrograms were created, one to consider low-frequency instabilities from 0-500 Hz and the other for high frequency instabilities from 0-5 kHz.

Evaluating the frequency showed a few key items. First, across all tests except for test 3, the low-frequency chug instability that was observed during the Ouroboros-2 bi-propellant tests at 200 Hz was present even with the modified injector. However, the pressure drop across both P_{ox} and P_{fuel} were noted to still be low than expected for all the tests which could have caused the instability to persist. Another consideration is that the instability could be a result of the combustion chamber design rather than the injector. To validate this would required both the injector and combustion chamber to be further tested. However, we can conclude that autophage operation did not cause this particular instability to become worse.

Another frequency that was noted was in the thrust data at approximately 1.1 kHz for all tests. This frequency was not observed on any other sensors which suggests that it could be a natural frequency of the test platform itself. Additionally, there was some unsteadiness to that frequency which could be explained by the movement of the actuator. The movement of the actuator would shift the center of gravity of the test platform such that it might slightly adjust the natural frequency of the platform throughout the test. In either case, this frequency did not occur in the combustion chamber pressure sensor which confirms it is not a combustion instability.

There were however, two high frequencies that where detected by P_c data for tests 4 and 5 at 2.3 kHz and 3.3 kHz. These frequencies were not detected during test 1-3 though which could indicate the beginnings of a high frequency combustion instability that could manifest at higher throttle settings. However, the power spectrum of both those points was quite low

according to the persistence diagrams. Since both engines operated for over 30 second steady state durations without issues we concluded that the observed frequencies did not manifest into catastrophic high frequency instabilities which could have led to engine failure.

7.7 Autophage Pulsed Mode Performance Analysis and Operating Box

In addition to being operated in steady state mode, the Ouroboros-3 engine was also operated in multiple pulsed modes during tests 4 and 5. Pulsed mode was chosen to evaluate the effect of the variable on-off-time on both the feed rate and feed force of the HDPE fuel tube. By pulsing the engine, it was theorised that the fuel tube could be fed at a lower feed force at certain operating frequencies and duty cycles since it was directly inserted into the combustion chamber.

The tested frequencies and duty cycles are listed in Table 4.4 and were operated sequentially during tests 4 and 5. The selected frequencies and duty cycles were a result of the analysis conducted on the Ouroboros-2 rise and decay times which presumed that the engine required a minimum on-time of 750 ms to reach steady state and a minimum off-time of 250 ms to drive the fuselage into the engine.

The pulsed mode performance results for test 5.b are shown in Fig. 7.26 with the remainder of the pulsed mode data located in Appendix A.4. The data showed that there was in fact a reduction in required feed force for most of the frequencies and duty cycles during engine off-time. Review of the test videos also showed that the fuselage was inserted during the off-time and feed rate stopped during the on-time as was theorised. However, as expected the engine was unable to utilise the short off-time window during test 5.d to insert the fuselage and so feed rate stopped during that test.

Table 7.14 contains both the maximum and minimum feed force for both the on-time and off-time of each test. The only test that did not see a decrease in engine feed force was test 5.d which was as previously mention, no feed rate was observed. The results showed that this was an insufficient amount of time for the inlet conditions to decay and the engine performance data showed near steady state behavior. Test 5.e did not have data gathered due the engine failure at the start of the test.

Based on the feed force data, engine off-time correlated with a reduction in F_F which is best see in tests 4.a-c. However, F_F was also observed to actually increase over the steady state F_F during engine on-time. This was a bi-product of the linear actuator programming which was set to operate the linear actuator at a constant current. In steady state operation this correlated with a constant feed force. However, this could have caused the feed force load cell to measure a higher load than expected during each engine pulse due to the sudden increase in chamber pressure acting on the fuselage cross-sectional area at engine ignition.

In addition to the effect on feed force, the frequency and duty cycle were also observed to have a significant correlation on the autophage contribution to both the total fuel mass and total propellant mass flow rates. The HDPE mass flow rate was derived from the average linear displacement of the fuselage during each 15 second pulsed mode duration and calculated for

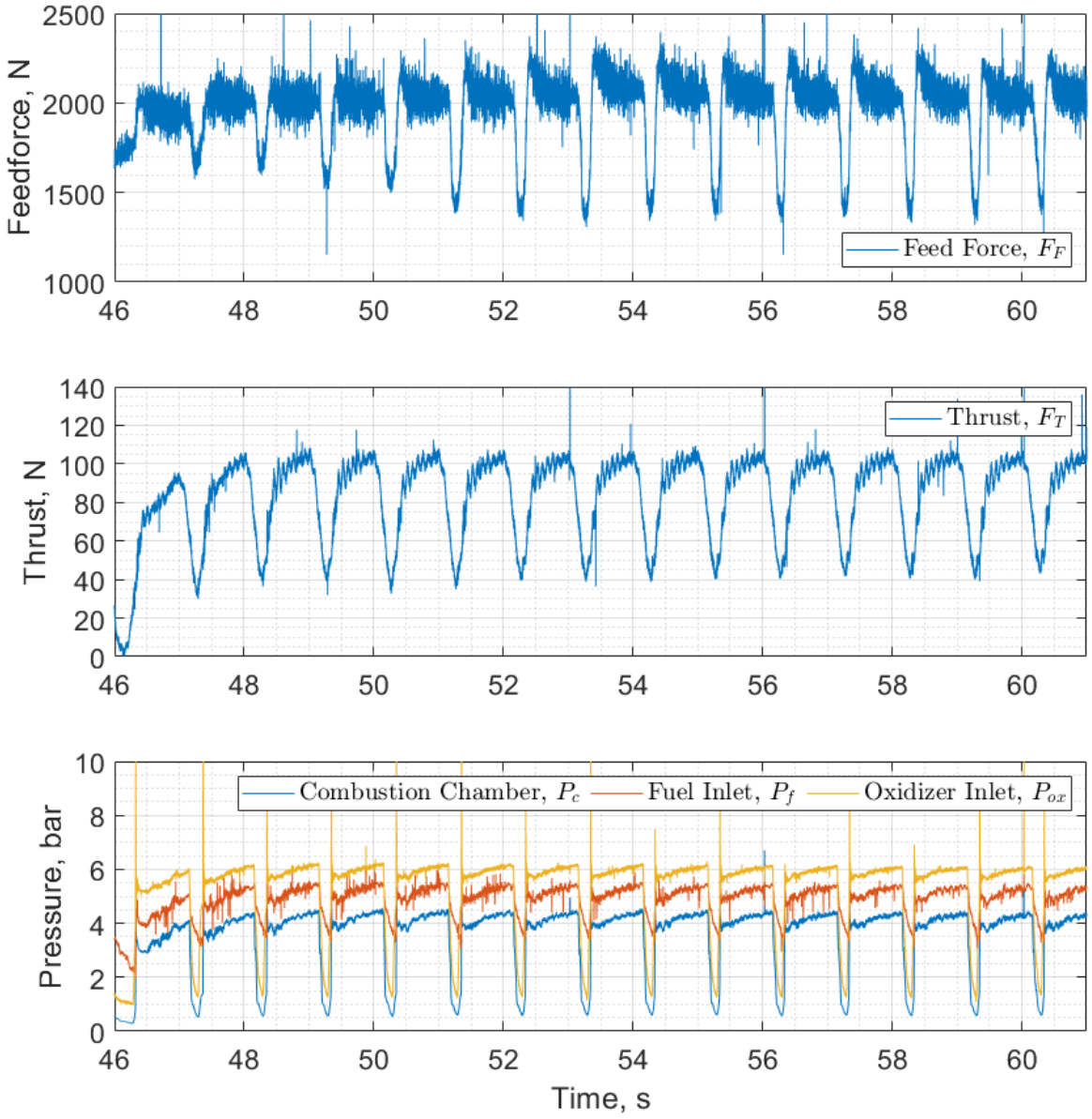

Fig. 7.26 Ouroboros-3 autophage test 5.b pulsed mode performance results at 1.0 Hz and 75% duty cycle.

both g/s and g/pulse. Then, assuming the same $\dot{m}_{fp}$ and $\dot{m}_{ox}$ (from the corresponding steady state tests), but adjusted for the on-time, the mass flow rate data was used to determine the autophage contribution to both the total fuel and total propellant mass flow rates. This was then compared to the steady state data given by tests 4.ss and 5.ss.

When compared to the previous steady state values, pulsed mode was able to both increase and decrease the autophage contribution to the total fuel and propellant mass flow rates depending on both the frequency and duty cycle.

The first finding is best shown in tests 4.a-c which demonstrated a clear trend between an increase in off-time having a positive correlation with an increase in autophage contribution. It was also noted that test 4.c had a lower autophage contribution when compared to steady state operation. Considering the results of tests 5.a-5.c, we can also see the effect of duty cycle on the autophage contribution. Even though test 5.c had an off-time of 500 ms which should have been plenty of time for fuselage insertion, the autophage contribution was actually less than

Table 7.14 Ouroboros-3 pulsed mode resulting feed force and feed rate

Test	f, Hz	DC, %	Off-t, ms	F_F, N		$\dot{m}_{ft}$		$\frac{\dot{m}_{ft}}{\dot{m}_{fuel}}$	$\frac{\dot{m}_{ft}}{\dot{m}_{ox}+\dot{m}_{fuel}}$
				Max	Min	g/s	g/pulse		
4.ss	-	-	-	1836	1836	4.80	-	39.3%	9.6%
4.a	0.5	50	1000	2062	1730	4.42	8.84	54.4%	16.3%
4.b	1.0	50	500	2106	1674	3.77	3.77	50.4%	14.3%
4.c	1.0	75	250	2273	1296	2.26	2.26	28.9%	6.2%
5.ss	-	-	-	1828	1828	8.30	-	49.8%	15.7%
5.a	1.0	50	500	2040	1618	5.10	5.10	54.9%	18.6%
5.b	1.0	75	250	2206	1363	2.96	2.96	32.0%	8.1%
5.c	0.5	75	500	1995	1707	4.47	8.94	41.6%	11.8%
5.d	2.0	75	125	1940	1862	0	0	0	0
5.e	2.0	50	250	-	-	-	-	-	-

the steady state baseline (5.ss). In fact, all the tests that operated at a 75% baseline showed a reduction in autophage contribution to both the total fuel and propellant mass flow rates whereas each test conducted at 50% duty cycle showed an increase. Directly comparing tests 5.a and 5.c demonstrates this best since the off-time was the same but the lower duty cycle had a higher autophage contribution. Thus we can conclude that both off-time and duty cycle have a direct affect on the HDPE mass flow rate and can effectively control the autophage contribution.

An added benefit of the longer off-time tests was that the fuel tube was melted while the engine was off which allowed the HDPE to coat the combustion chamber walls promoting the previously discussed film cooling. Referencing the temperature data in Fig. 7.22, the engine was able to maintain a steady T_c for tests 4.a and 4.b between 400-600°C which were operated at 50% duty cycle; T_c was also noted to begin increasing during test 4.c when the engine switched to a 75% duty cycle.

Additionally, for test 5.a, pulsed mode also had this effect on chamber wall temperature; this was best shown when T_c decreased when the engine changed from steady state operation to 1.0 Hz 50% duty cycle and again started to increase once the engine began operating at 75% duty cycles. In general, both the frequency and pulse duty cycles are known to have an effect on engine operating temperatures [145] which are typically higher when engines are pulsed. However, the results of these tests showed that in the case of a direct fuselage insertion autophage engine, combustion chamber wall temperature can be both increased or decreased depending on the duty cycle. In conclusion, pulsed mode offers both a method of controlling the autophage contribution but also combustion chamber wall temperatures; this offers another set of variables which could be used to optimise the autophage engine design for a flight trajectory.

Furthermore, the rise in chamber wall temperature from pulsed mode operation actually resulted in the chamber supports of the inner combustion chamber melting through (discussed in Section 7.5.2) which led to the engine failure shown in Fig. 7.27. The specific pulsed mode for test 5.d was identified as the most likely root cause of the failure since that particular frequency and duty cycle significantly increased wall temperature by preventing the HDPE

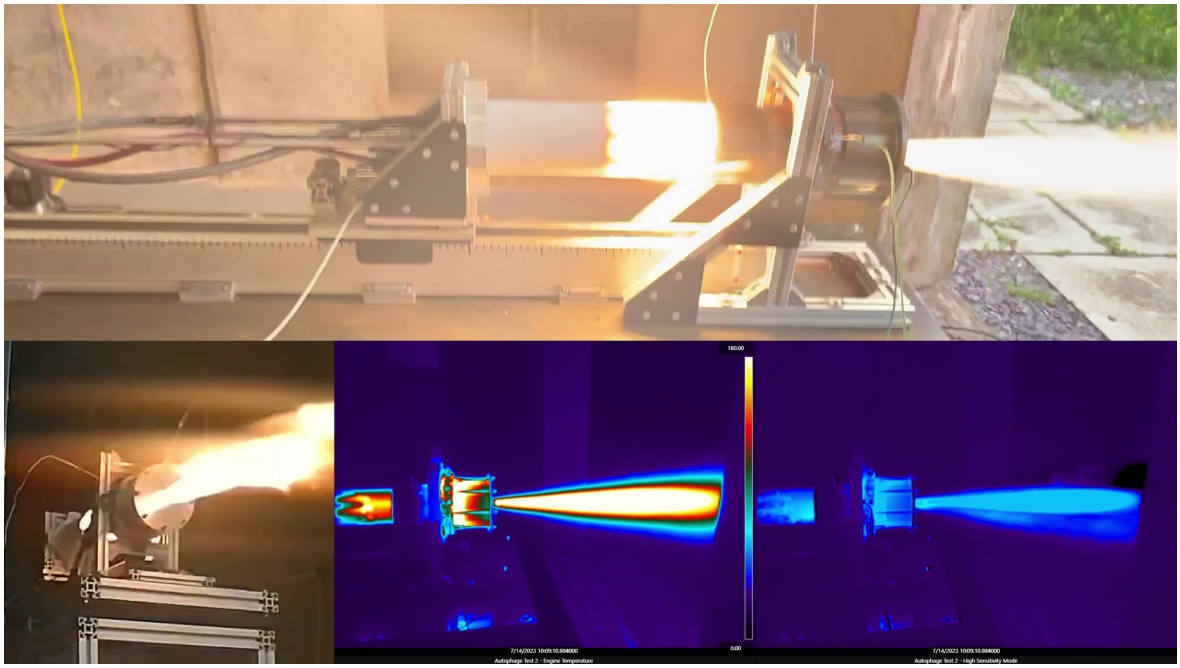

Fig. 7.27 Ouroboros-3 engine failure during test 5.e. The inner combustion chamber structure failed due to elevated wall temperatures causing the injector assembly to be ejected into the HDPE fuselage.

from being inserted into the engine thereby eliminating the necessary HDPE film cooling of the chamber supports.

In conclusion, pulsed mode offers both a method of controlling the autophage contribution but also combustion chamber wall temperatures. Operating at a 50% duty cycle yielded an increase in autophage contribution to the total fuel and propellant mass flow rates when compared to steady state at the same inlet conditions. Additionally, the pulsed operating modes were able to influence T_c: at 50% duty cycles this resulted in cooling the engine and reducing T_c while at 75% duty cycles T_c increased and eventually resulted in the engine failure. Overall, the results of these tests present another set of variables which could be used to optimise the autophage engine design for a flight trajectory.

Chapter 8

Conclusions

8.1 Conclusions

This study was undertaken with two key objectives: to develop a feasible architecture for an autophage propulsion system and to investigate the key parameters and operating box of that architecture. As a whole, this research met both objectives. First, it evaluated two different engine architectures for autophage operation: the depolymerisation chamber architecture and the direct fuselage insertion architecture. Both of these architectures considered the autophage element to be a supplementary fuel source to a main bi-propellant combustion process. This would allow the autophage component of a full-scale launch vehicle to theoretically consist of a fuselage that could be burned throughout the course of the launch vehicle's trajectory; resulting in an infinitely-staged vehicle.

The results of the depolymerisation chamber architecture test (Ouroboros-1) showed that this architecture is not currently feasible on small thrust class engines. This was due to the difficulty in effectively transferring combustion chamber temperature to the high-density polyethylene (HDPE) fuselage without resulting in a compressive hoop-stress engine failure. However, larger thrust class engines could still benefit from this architecture by using both topology optimised cooling channels and turbomachinery. Thus, a larger engine could benefit from the optimised heat transfer from the cooling channels and a lower depolymerisation chamber pressure that could significantly reduce the required fuselage feed force and prevent the compressive hoop-stress failure mode.

Building on the lessons learned from Ouroboros-1, the direct fuselage insertion architecture showed far more promising results and ultimately resulted in actual autophage operations. The initial bi-propellant tests conducted on Ouroboros-2 demonstrated a performance baseline that would later be used as a control to which the autophage tests could be compared. They also evaluated the chamber pressure rise and decay times in order to determine the baseline pulsed modes for autophage operation. The overall success of that architecture as a bi-propellant engine led to using it in the autophage configuration (Ouroboros-3) over a total of 5 tests.

Overall, the demonstration of the Ouroboros-3 engine marked the completion of the second objective of this study. The extensive testing demonstrated that at steady state conditions, the

autophage fuel can account for between 6.8-49.8% of the total fuel mass and 5.1-15.7% of the total propellant mass. Considering that the structural mass of conventional launch vehicles is typically between 5-12%, we can conclude that an autophage engine could in fact burn a launch vehicles structure at a rate that could result in an infinitely staged vehicle.

Moreover, the Ouroboros-3 tests showed a positive correlation with both throttle setting and mixture ratio on the fuselage feed rate and resulting autophage contributions to total mass flow rates. Furthermore, when operated in pulsed modes, the total engine off-time and duty cycle was also found to have a strong correlation on the autophage contribution to total fuel and total propellant mass flow rates. For tests with at 50% duty cycle, the autophage contribution increased over steady state while for tests at 75% it decreased. Additionally pulsed modes with a longer off-time (while at the same duty cycle) also showed a significant increase in the autophage contribution.

In conclusion, these tests not only showed that autophage engines could successfully operate with a nominal contribution to the total propellant mass but also identified key parameters that can be used to control the feed rate and the percent contribution of autophage operation to the total propellant mass. The results of these tests, both as video and data and their analysis, will establish an anchor for models that can be used in the future development of hybrid autophage engines.

8.2 Future Work

The results of the Ouroboros-3 engine were widely successful in elevating the concept of autophage propulsion systems to a technology readiness level (TRL) of 4 and have demonstrated a functional design in a laboratory environment. To further advance the field of autophage propulsion a number of steps need to occur. First, research efforts should focus on increasing the scale of autophage engines to higher thrust classes. While this study demonstrated the feasibility of autophage at a small scale, in order to be feasible on a launch vehicle the scale and thrust must increase significantly which can introduce additional challenges.

Second, research should be done into topology optimisation of regenerative cooling channels. Used in conjunction with engine scaling and turbomachinery, this could increase the feasibility of the autophage depolymerisation chamber architecture which could significantly reduce the required feed force of the fuselage. Additionally, a study should be conducted on feed force and engine performance optimisation to determine an optimal thrust class of engine. The study should evaluate engine sizes that could generate sufficient thrust in order to exceed the minimum feed force of the fuselage without buckling or compressive failure; this would allow for feeding the engine through inertial loading. This work should also consider optimising the potential trade-off of using more autophage propellant to reduce structural mass and whether it would be worth the potential reduction in I_{sp} that would result from using a higher ratio of solid to liquid fuel.

Successfully achieving the aforementioned objectives should result in a high enough technology readiness level such that a sub-orbital flight demonstrator could be considered. This flight demonstrator would able to operate by feeding the fuselage into the engine through

inertial loading. Various polymers should also be considered for the fuselage material and could even include carbon fibre doped or graphite doped polymers that generally increase the strength of the fuselage structure. The flight dynamics and trajectory of a changing mass and geometry launcher should also be studied prior to a flight test. Further studies would need to consider propellant storage as well, either in collapsible tanks or autophage tanks. While there is still significant work to be done in the field of autophage propulsion, the research within this body of work has shown that it is feasible and worth considering.

References

[1] E. Kulu, "Nanosatellite launch forecasts 2022 - track record and latest prediction," 36th Annual Small Satellite Conference, Logan, Utah, United States of America, Aug. 2022.

[2] E. Kulu, "Small launchers - 2023 industry survey and market analysis," 74th International Astronautical Congress, Baku, Azerbaijan, Oct. 2023.

[3] H. W. Jones, "The recent large reduction in space launch cost," International Conference on Environmental Systems, Albuquerque, New Mexico, United States of America, Jul. 2018.

[4] G. Galilei, *Dialogues Concerning Two New Sciences*. Macmillan, 1638.

[5] V. N. Sokolsky, *K. E. Tsiolkovsky Selected Works, English Translation*. Moscow, USSR: MIR Publishers, 1968.

[6] T. Kibbery, "Small launch vehicle sizing analysis with solid rocket examples," Combustion Subcommittee, Dayton, Ohio, United States of America, Jun. 2019.

[7] B. Garfinkel, "A solution of the Goddard problem," *Army Ballistic Research Laboratories, Report No. 1194*, 1963.

[8] S. Gordon and B. J. McBride, "Theoretical performance of liquid hydrogen with liquid oxygen as a rocket propellant," *NASA Memorandum (NASA-MEMO-5-21-59E)*, 1959.

[9] J. R. Wertz, D. F. Everett, and J. J. Puschell, *Space Mission Engineering: The New SMAD*. Hawthorn, California, United States of America: Microcosm Press, 2011.

[10] F. S. Billig, "Design and development of single-stage-to-orbit vehicles," *Johns Hopkins Apl Technical Digest*, 1990. [Online]. Available: https://api.semanticscholar.org/CorpusID:118984450.

[11] J. M. Roche, D. N. Kosareo, and D. Palac, "Structural sizing of a 25,000-lb payload, air-breathing launch vehicle for single-stage-to-orbit," Joint Army Navy Nasa Air Force (JANNAF) Conference, Jan. 2000.

[12] Z. N. Martinovic and J. A. Cerro, "A procedure for structural weight estimation of single stage to orbit launch vehicles (interim user's manual)," *NASA Technical Memorandum (NASA/TM-2002-211931)*, 2002.

[13] G. P. Sutton and O. Biblarz, *Rocket Propulsion Elements*, 9th. Hoboken, New Jersey, United States of America: John Wiley & Sons, Inc., 2017.

[14] V. Yemets *et al.*, "The infinite staging rocket - first step to realization," *International Astronautical Federation, IAF*, vol. 11, pp. 8624–8634, Jan. 2013.

[15] B. Mead Jr. Franklin, "Advanced propulsion concepts - project outgrowth," *Air Force Rocket Propulsion Lab Technical Report (AFRPL-TR-72-31)*, 1972.

[16] L. Damblane, "Self-propelling projectile," *U.S. Patent No. 2,114,214*, Apr. 1938.

[17] Z. A. Typaldos, "Autophage rocket," *U.S. Patent No. 3,250,216*, Mar. 1966.

[18] V. V. Yemets, S. Prince, and R. Wilkinson, "Investigations of a combustible inertial launch vehicle design," *Journal of the British Interplanetary Society*, vol. 68, no. 7, 2015.

[19] M. Corbett and J. A. Belisle, "Single stage autophage rocket," *U.S. Patent No. 4,703,694*, Nov. 1987.

[20] B. Wunderlich, "Specific heat of polyethylene single crystals," *The Journal of Physical Chemistry*, vol. 69, no. 6, pp. 2078–2081, 1965. DOI: 10.1021/j100890a045.

[21] V. Yemets, P. Harkness, M. Dron, A. Pashkov, K. Worrall, and M. Middleton, "Autophage engines: Towards a throttleable solid motor," *Journal of Spacecraft and Rockets*, vol. 5, no. 4, 2018. DOI: 10.2514/1.A34153.

[22] K. Bzdyk and P. Harkness, "Autophage engines for cubesat-scale nanolaunchers," 7th Reinvienting Space Conference, Belfast, United Kingdom, 2019.

[23] K. Bzdyk, P. Harkness, P. Shaw, and J. Tufft, "Investigation of the operating parameters and performance of an autophage, hybrid rocket propulsion system," in *AIAA SCITECH 2024 Forum*, 2024, p. 1604. DOI: 10.2514/6.2024-1604.

[24] K. Bzdyk *et al.*, "Development and roadmap of the ouroboros programme hybrid autophage propulsion system for rapid low-earth orbit access," in *9th Annual Space Propulsion Conference*, 2024.

[25] J. Tufft, K. Bzdyk, and H. Patrick, "Introduction of topology optimisation in regenerative cooling channel design within liquid rocket engines," in *9th Annual Space Propulsion Conference*, 2024.

[26] "Payload user's guide," *Rocket Lab USA, Inc.*, 2022.

[27] J. Holt and T. Monk, "Propellant mass fraction calculation methodology for launch vehicles and application to ares vehicles," in *AIAA SPACE 2009 Conference*. DOI: 10.2514/6.2009-6655.

[28] M. Pallone, M. Pontani, P. Teofilatto, and A. Minotti, "Design methodology and performance evaluation of new generation sounding rockets," *International Journal of Aerospace Engineering*, vol. 2018, no. 1, p. 1 678 709, 2018.

[29] T. Bui, D. Lux, M. Stenger, M. Munson, and G. Teate, "New air-launched small missile (alsm) flight testbed for hypersonic systems," in *44th AIAA Aerospace Sciences Meeting and Exhibit*. DOI: 10.2514/6.2006-221. eprint: https://arc.aiaa.org/doi/pdf/10.2514/6.2006-221. [Online]. Available: https://arc.aiaa.org/doi/abs/10.2514/6.2006-221.

[30] [REDACTED], "An outsider's view of the phoenix/awg-9 weapon system," Naval Intelligence Support Center, Tech. Rep. NPS-53WG77033, 1977.

[31] T. A. SMITH, "Hazard classification of u.s. military explosives and munitions," U.S. ARMY DEFENSE AMMUNITION CENTER, Tech. Rep., 2021.

[32] T. Moore and T. Moore, "Solid propulsion enabling technologies and milestones for navy air-launched tactical missiles," in *AIAA Centennial of Naval Aviation Forum "100 Years of Achievement and Progress"*. DOI: 10.2514/6.2011-6941.

[33] J. B. Nowell, "Missile total and subsection weight and size estimation equations," Naval Postgraduate School, Tech. Rep., 1992.

[34] W. J. Ketchum, "Orbital transfer vehicle concept definition and system analysis study," General Dynamics Corp, Tech. Rep. GDSS-SP-86-011, 1986.

[35] "Spacecraft mass estimation relationships and engine data," Eagle Engineering, Tech. Rep. 87-171, 1988.

[36] N. Sarigul-Klijn, C. Noel, and M. Sarigul-Klijn, "Air-launching earth to orbit: Effects of launch conditions and vehicle aerodynamics," *Journal of Spacecraft and Rockets*, vol. 42, pp. 569–575, May 2005. DOI: 10.2514/1.8634.

[37] L. Arrington, B. Reed, and J. Angel Rivera, "A performance comparison of two small rocket nozzles," in *32nd Joint Propulsion Conference and Exhibit*. DOI: 10.2514/6.1996-2582.

[38] I. Ivanov and I. Kryukov, "Numerical study of ways to prevent side loads in an over–expanded rocket nozzles during the launch stage," *Acta Astronautica*, vol. 163, pp. 196–201, 2019, Space Flight Safety-2018, ISSN: 0094-5765. DOI: 10.1016/j.actaastro.2019.02.032.

[39] G. Dettleff, "Plume flow and plume impingement in space technology," *Progress in Aerospace Sciences*, vol. 28, no. 1, pp. 1–71, 1991, ISSN: 0376-0421. DOI: 10.1016/0376-0421(91)90008-R.

[40] C. Génin, A. Gernoth, and R. Stark, "Experimental and numerical study of heat flux in dual bell nozzles," *Journal of Propulsion and Power*, vol. 29, no. 1, pp. 21–26, 2013. DOI: 10.2514/1.B34479.

[41] R. Lagier, "Ariane 5 user's manual," Arianespace, Tech. Rep. Issue 5, Revision 2, 2016.

[42] G. Hagemann, H. Immich, T. Nguyen, and G. Dumnov, "Advanced rocket nozzles," *Journal of Propulsion and Power*, vol. 14, pp. 620–633, Sep. 1998. DOI: 10.2514/2.5354.

[43] S. Khare and U. Saha, "Rocket nozzles: 75 years of research and development," *Sādhanā*, vol. 46, Jun. 2021. DOI: 10.1007/s12046-021-01584-6.

[44] C. Génin, D. Schneider, and R. Stark, "Dual-bell nozzle design," in *Future Space-Transport-System Components under High Thermal and Mechanical Loads: Results from the DFG Collaborative Research Center TRR40*, N. A. Adams *et al.*, Eds. Springer International Publishing, 2021, pp. 395–406, ISBN: 978-3-030-53847-7. DOI: 10.1007/978-3-030-53847-7_25.

[45] H. Kbab, M. Sellam, T. Hamitouche, S. Bergheul, and L. Lagab, "Design and performance evaluation of a dual bell nozzle," *Acta Astronautica*, vol. 130, pp. 52–59, 2017, ISSN: 0094-5765. DOI: 10.1016/j.actaastro.2016.10.015.

[46] M. Verma, N. Arya, and A. De, "Investigation of flow characteristics inside a dual bell nozzle with and without film cooling," *Aerospace Science and Technology*, vol. 99, p. 105 741, 2020, ISSN: 1270-9638. DOI: 10.1016/j.ast.2020.105741.

[47] G. V. R. Rao, "Analysis of a new concept rocket nozzle," in *Liquid Rockets And Propellants*. Rocketdyne, 1960, pp. 669–682. DOI: 10.2514/5.9781600864759.0669.0682.

[48] A. Goetz, G. Hagemann, J. Kretschmer, and R. Schwane, "Advanced upper stage propulsion concept - the expansion-deflection upper stage," in *41st AIAA/ASME/SAE/ASEE Joint Propulsion Conference and Exhibit*. 2012. DOI: 10.2514/6.2005-3752.

[49] J. Lee, J. Choi, and H. Huh, "Performance analysis of expansion–deflection nozzles with reduced lengths of nozzle extension at a high-altitude environment," *Journal of Mechanical Science and Technology*, vol. 37, pp. 1–12, Dec. 2023. DOI: 10.1007/s12206-023-1126-x.

[50] N. Taylor *et al.*, "Experimental investigation of the evacuation effect in expansion deflection nozzles," *Acta Astronautica*, vol. 66, pp. 550–562, Feb. 2010. DOI: 10.1016/j.actaastro.2009.07.016.

[51] R. A. Wasko, "Performance of annular plug and expansion–deflection nozzles including external flow effects at transonic mach numbers," NASA Glenn Research Center, Tech. Rep. NASA-TN-D-4462, 1968.

[52] T. Moon, S. Park, J. Choi, and H. Huh, "Research trends of an e-d nozzle for altitude compensation," *Journal of The Korean Society for Aeronautical & Space Sciences*, vol. 45, pp. 844–854, 2017. DOI: 10.5139/JKSAS.2017.45.10.844.

[53] N. Taylor *et al.*, "Experimental investigation of the evacuation effect in expansion deflection nozzles," *Acta Astronautica*, vol. 66, pp. 550–562, Feb. 2010. DOI: 10.1016/j.actaastro.2009.07.016.

[54] D. Ghosh and H. Gunasekaran, "Large eddy simulation (les) of aerospike nozzle assisted supersonic retro-propulsion (srp)," in *AIAA Aviation 2021 Forum*, Aug. 2021. DOI: 10.2514/6.2021-2489.

[55] H. Tian, Z. Guo, Z. Hao, L. Hedong, and C. Li, "Numerical and experimental investigation of throttleable hybrid rocket motor with aerospike nozzle," *Aerospace Science and Technology*, vol. 106, pp. 105–983, 2020, ISSN: 1270-9638. DOI: 10.1016/j.ast.2020.105983.

[56] C.-H. Wang, Y. Liu, and L.-Z. Qin, "Aerospike nozzle contour design and its performance validation," *Acta Astronautica*, vol. 64, no. 11, pp. 1264–1275, 2009, ISSN: 0094-5765. DOI: 10.1016/j.actaastro.2008.01.045.

[57] S. Eilers, M. Wilson, S. Whitmore, and Z. Peterson, "Side-force amplification on an aerodynamically thrust-vectored aerospike nozzle," *Journal of Propulsion and Power*, vol. 28, Jul. 2012. DOI: 10.2514/1.B34381.

[58] P. V. Deshpande, G. N. Nagaharish, A. Buradi, and A. Madhusudhan, "Influence of truncation on the performance of aerospike nozzles using numerical technique," in *Recent Trends in Thermal and Fluid Sciences*, D. P. Mishra, A. K. Dewangan, and A. Singh, Eds., Singapore: Springer Nature Singapore, 2023, pp. 229–244, ISBN: 978-981-19-3498-8.

[59] V. Anand and E. Gutmark, "Rotating detonation combustors and their similarities to rocket instabilities," *Progress in Energy and Combustion Science*, vol. 73, pp. 182–234, 2019. DOI: 10.1016/j.pecs.2019.04.001.

[60] M. Fotia, T. Kaemming, J. Hoke, and F. Schauer, "Study of the experimental performance of a rotating detonation engine with nozzled exhaust flow," *Journal of Propulsion and Power*, vol. 32, Jan. 2015. DOI: 10.2514/6.2015-0631.

[61] T. Mundt, C. Knowlen, and M. Kurosaka, "Scale effects on rotating detonation rocket engine operation," *Applications in Energy and Combustion Science*, vol. 19, 2024. DOI: 10.1016/j.jaecs.2024.100282.

[62] I. Shaw *et al.*, "A theoretical review of rotating detonation engines," in *Detonation - New Era for Engines*. Intechopen, Dec. 2019, ISBN: 978-1-83880-558-6. DOI: 10.5772/intechopen.90470.

[63] S. Frolov, V. Aksenov, V. Ivanov, and I. Shamshin, "Large-scale hydrogen–air continuous detonation combustor," *International Journal of Hydrogen Energy*, vol. 40, no. 3, pp. 1616–1623, 2015, ISSN: 0360-3199. DOI: 10.1016/j.ijhydene.2014.11.112.

[64] W. Wu, Y. Wang, W. Han, G. Wang, M. Zhang, and J. Wang, "Experimental research on solid fuel pre-combustion rotating detonation engine," *Acta Astronautica*, vol. 205, pp. 258–266, 2023. DOI: 10.1016/j.actaastro.2023.02.007.

[65] X.-Y. Liu, M. Cheng, Y.-Z. Zhang, and J.-P. Wang, "Design and optimization of aerospike nozzle for rotating detonation engine," *Aerospace Science and Technology*, vol. 120, 2022, ISSN: 1270-9638. DOI: 10.1016/j.ast.2021.107300.

[66] M. B. Padwal, B. Natan, and D. Mishra, "Gel propellants," *Progress in Energy and Combustion Science*, vol. 83, p. 100 885, 2021, ISSN: 0360-1285. DOI: 10.1016/j.pecs.2020.100885.

[67] M. L. Pinns, W. T. Olson, H. C. Barnett, and R. Breitwieser, "Naca research on slurry fuels," NACA, Tech. Rep., 1958.

[68] I. A. Goodman and V. O. Fenn, *Preparation and Properties of Concentrated Boron-hydrocarbon Slurry Fuels*. National Advisory Committee for Aeronautics, 1954.

[69] L. K. Tower and J. R. Branstetter, "Combustion performance evaluation of magnesium-hydrocarbon slurry blends in a simulated tail-pipe burner," NACA, Tech. Rep., 1951.

[70] B. Natan and S. Rahimi, "The status of gel propellants in year 2000," *International journal of energetic materials and chemical propulsion*, vol. 5, no. 1-6, 2002.

[71] A. Haddad, B. Natan, and R. Arieli, "The performance of a boron-loaded gel-fuel ramjet," *Progress in propulsion physics*, vol. 2, pp. 499–518, 2011.

[72] D. RAPP and R. ZURAWSKI, "Characterization of aluminum/rp-1 gel propellant properties," in *24th joint propulsion conference*, 1988, p. 2821.

[73] P. C. Pinto, N. Hopfe, J. Ramsel, W. Naumann, A. Thumann, and G. Kurth, "Scalability of gelled propellant rocket motors," in *7th European conference for aeronautics and space sciences (EUCASS), Milan, Italy*, 2017.

[74] K. Hodge, T. Crofoot, and S. Nelson, "Gelled propellants for tactical missile applications," in *35th Joint Propulsion Conference and Exhibit*, 1999, p. 2976.

[75] A. S. Gohardani *et al.*, "Green space propulsion: Opportunities and prospects," *Progress in Aerospace Sciences*, vol. 71, pp. 128–149, 2014, ISSN: 0376-0421. DOI: 10.1016/j.paerosci.2014.08.001.

[76] R. K. Masse, B. A. Glassy, R. A. Spores, A. T. Vuong, Z. Zhu, and T. L. Pourpoint, "Hydrazine-based green monopropellant blends," in *AIAA SCITECH 2024 Forum*, 2024. DOI: 10.2514/6.2024-1619.

[77] R. A. Spores, "Gpim af-m315e propulsion system," in *51st AIAA/SAE/ASEE Joint Propulsion Conference*, 2015, p. 3753.

[78] R. Masse, M. Allen, R. Spores, and E. A. Driscoll, "Af-m315e propulsion system advances and improvements," in *52nd AIAA/SAE/ASEE Joint Propulsion Conference*, 2016, p. 4577.

[79] M. Mosier, G. Harris, B. Richards, D. Rovner, and B. Carroll, "Pegasus first mission-flight results," in *Annual AIAA/Utah State University Conference on Small Satellites*, 1990.

[80] M. N. Rhode, W. C. Engelund, and M. R. Mendenhall, "Experimental aerodynamic characteristics of the pegasus air-launched booster and comparisons with predicted and flight results," American Inst. of Aeronautics and Astronautics, Tech. Rep., 1995.

[81] E. Waters, D. M. Creech, and A. Philips, "Air launch: Examining performance potential of various configurations and growth options," in *AIAA SPACE 2013 Conference and Exposition*. AIAA, 2013. DOI: 10.2514/6.2013-5422.

[82] N. Sarigul-Klijn, C. Noel, and M. Sarigul-Klijn, "Air-launching earth to orbit: Effects of launch conditions and vehicle aerodynamics," *Journal of Spacecraft and Rockets - J SPACECRAFT ROCKET*, vol. 42, pp. 569–575, May 2005. DOI: 10.2514/1.8634.

[83] A. Ponomarenko, "RPA: Design tool for liquid rocket engine analysis," Jan. 2009.

[84] S. Gordon and B. J. McBride, "Computer program for calculation of complex chemical equilibrium compositions and applications," *NASA Reference Publication 1311*, 1994.

[85] D. K. Huzel and D. H. Huang, "Modern engineering for design of liquid-propellant rocket engines (Revised and enlarged edition)," *Progress in Astronautics and Aeronautics*, vol. 147, Jan. 1992.

[86] H. W. Douglass, H. W. Schmidt, N. E. Van Huff, and D. A. Fairchild, "Liquid rocket engine fluid-cooled combustion chambers," *NASA Special Publication (NASA-SP-8087)*, 1972.

[87] T. Kanda, G. Masuya, Y. Wakamatsu, A. Kanmuri, N. Chinzei, and M. Niino, "Effect of regenerative cooling on rocket engine specific impulse," *Journal of Propulsion and Power*, vol. 10, no. 2, pp. 286–288, 1994. DOI: 10.2514/3.23741.

[88] M. E. Boysan, "Analysis of regenerative cooling in liquid propellant rocket engines," M. Sc. Thesis, Middle East Technical University, Ankara, Turkey, 2008.

[89] V. Yemets, M. Dron, and A. Pashkov, "Autophage engines: Method to preset gravity load of solid rockets," *Journal of Spacecraft and Rockets*, vol. 57, no. 2, 2020. DOI: 10.2514/1.A34597.

[90] M. M. de Oliveira, A. A. Couto, G. F. C. Almeida, D. A. P. Reis, N. B. de Lima, and R. Baldan, "Mechanical behavior of inconel 625 at elevated temperatures," *Metals*, vol. 9, no. 3, 2019, ISSN: 2075-4701. DOI: 10.3390/met9030301.

[91] D. Bartz, "Turbulent boundary-layer heat transfer from rapidly accelerating flow of rocket combustion gases and of heated air," in *Advances in Heat Transfer*, vol. 2, Elsevier, 1965, pp. 1–108.

[92] E. Sichler, J. D. Montes, and F. O. Chandler, "One dimensional thermal steady state analysis and procedure for a low-pressure liquid oxygen and liquid methane rocket engine," in *2018 Joint Propulsion Conference*, 2018, p. 4602.

[93] C. Kirchberger *et al.*, "Prediction and analysis of heat transfer in small rocket chambers," in *46th AIAA Aerospace Sciences Meeting and Exhibit*, 2008, p. 1260.

[94] T. K. Bose, "Comparison of rocket nozzle heat transfer calculation methods," *Journal of Spacecraft and Rockets*, vol. 15, no. 4, pp. 253–255, 1978.

[95] E. Mayer, "Analysis of convective heat transfer in rocket nozzles," *ARS Journal*, vol. 31, no. 7, pp. 911–917, 1961.

[96] W. M. Grisson, "Liquid film cooling in rocket engines (aedc-tr-91-1)," *Arnold Engineering Development Center, Arnold Air Force Base, Tennessee, Air Force Systems Command, United States Air Force. Available in Defense Technical Information Center (DTIC)*, 1991.

[97] T. Palacz and J. Cieślik, "Experimental study on the mass flow rate of the self-pressurizing propellants in the rocket injector," *Aerospace*, vol. 8, no. 11, 2021, ISSN: 2226-4310. DOI: 10.3390/aerospace8110317.

[98] E. V. Niño and M. R. H. Razavi, "Design of two-phase injectors using analytical and numerical methods with application to hybrid rockets," AIAA Propulsion and Energy 2019 Forum. DOI: 10.2514/6.2019-4154.

[99] R. Payri, F. Salvador, J. Gimeno, and J. De la Morena, "Analysis of diesel spray atomization by means of a near-nozzle field visualization technique," *Atomization and Sprays*, vol. 21, pp. 753–774, Jan. 2011. DOI: 10.1615/AtomizSpr.2012004051.

[100] B. Waxman, B. Cantwell, G. Zilliac, and J. Zimmerman, "Mass flow rate and isolation characteristics of injectors for use with self-pressurizing oxidizers in hybrid rockets," 49th AIAA/ASME/SAE/ASEE Joint Propulsion Conference, Jul. 2013, ISBN: 978-1-62410-222-6. DOI: 10.2514/6.2013-3636.

[101] H. Ciezki, T. Tiedt, J. Kampen, and N. Bartels, "Atomization behavior of newtonian fluids with an impinging jet injector in dependence upon reynolds and weber numbers," 41st AIAA Joint Propulsion Conference, Jul. 2005. DOI: 10.2514/6.2005-4477.

[102] S. Karic *et al.*, "Fine grain, high-density graphite for rocket motor nozzles," 6th International Scientific Conference on Defensive Technologies, Oct. 2014.

[103] G. R. Kinnery and W. G. Lidman, "Investigation of ceramic, graphite, and chrome-plated graphite nozzles on rocket engine," *NACA Research Memorandum (NACA-RM-E8L16)*, 1949.

[104] M. A. Burnett and M. S. Wooldridge, "An experimental investigation of flame and autoignition behavior of propane," *Combustion and Flame*, vol. 224, pp. 24–32, 2021, A dedication to Professor Ronald K. Hanson, ISSN: 0010-2180. DOI: 10.1016/j.combustflame.2020.12.001.

[105] C. Campbell-Knight and J. Dyer, "Hybrid rocket motor overview," *Space Safety Magazine*, 2014. [Online]. Available: https://www.spacesafetymagazine.com/aerospace-engineering/rocketry/hybrid-rockets-overview/.

[106] L. Gardner, A. Insausti, K. Ng, and M. Ashraf, "Elevated temperature material properties of stainless steel alloys," *Journal of Constructional Steel Research*, vol. 66, no. 5, pp. 634–647, 2010, ISSN: 0143-974X. DOI: 10.1016/j.jcsr.2009.12.016.

[107] M. Son, K. Radhakrishnan, J. Koo, O. C. Kwon, and H. D. Kim, "Design procedure of a movable pintle injector for liquid rocket engines," *Journal of Propulsion and Power*, vol. 33, no. 4, pp. 858–869, 2017. DOI: 10.2514/1.B36301.

[108] R. Rezende, V. Perez, and A. Pimenta, "Experiments with pintle injector design and development," 51st AIAA/SAE/ASEE Joint Propulsion Conference, Jul. 2015. DOI: 10.2514/6.2015-3810.

[109] D. Cieśliński, Z. Gut, and A. Parzybut, "Development of throttling capabilities of liquid rocket engines utilizing high-test peroxide as oxidizer," 8th Edition of the Space Propulsion Conference, Estoril, Portugal, May 2022.

[110] H. W. Douglass, H. Schmidt, M. Murray Bailey, G. S. Gill, W. H. Nurick, and R. B. Keller Jr., "Liquid rocket injectors," in *NASA Space Vehicle Design Criteria (Chemical Propulsion), NASA-SP-8089*.

[111] S. Lee, D. Kim, J. Koo, and Y. Yoon, "Spray characteristics of a pintle injector based on annular orifice area," *Acta Astronautica*, vol. 167, pp. 201–211, 2020, ISSN: 0094-5765. DOI: 10.1016/j.actaastro.2019.11.008.

[112] P. Kowalczuk and J. Drzymala, "Physical meaning of the sauter mean diameter of spherical particulate matter," *Particulate Science and Technology*, vol. 34, pp. 645–647, Oct. 2015. DOI: 10.1080/02726351.2015.1099582.

[113] P. Cheng, Q. Li, S. Xu, and Z. Kang, "On the prediction of spray angle of liquid-liquid pintle injectors," *Acta Astronautica*, vol. 138, pp. 145–151, 2017, The Fifth International Conference on Tethers in Space, ISSN: 0094-5765. DOI: 10.1016/j.actaastro.2017.05.037.

[114] P. Boettcher, I. G. Mikellides, D. A. Vaughan, J. E. Shephard, and J. Damazo, "Visualization of transverse annular jets," in *APS Division of Fluid Dynamics Meeting Abstracts*, ser. APS Meeting Abstracts, vol. 62, Nov. 2009.

[115] S. D. Heister, "Handbook of atomization and sprays," in Springer New York, NY, 2011, ch. Pintle Injectors, pp. 647–656. DOI: 10.1007/978-1-4419-7264-4.

[116] G. Dressler and J. Bauer, "Trw pintle engine heritage and performance characteristics," 36th AIAA/ASME/SAE/ASEE Joint Propulsion Conference and Exhibit. DOI: 10.2514/6.2000-3871.

[117] M. Son, K. Radhakrishnan, Y. Yoon, and J. Koo, "Numerical study on the combustion characteristics of a fuel-centered pintle injector for methane rocket engines," *Acta Astronautica*, vol. 135, pp. 139–149, 2017, ISSN: 0094-5765. DOI: 10.1016/j.actaastro.2017.02.005.

[118] D. Kang, S. Han, R. C., and Y. Ko, "Design of pintle injector using kerosene-lox as propellant and solving the problem of pintle tip thermal damage in hot firing test," *Acta Astronautica*, vol. 201, pp. 48–58, 2022, ISSN: 0094-5765. DOI: 10.1016/j.actaastro.2022.08.029.

[119] G. Zhang, G. Li, L. Li, and G. Tang, "Thermal performance of mmh/nto rocket thrust chamber based on pintle injector by using liquid film cooling," *Applied Thermal Engineering*, vol. 223, p. 120 035, 2023, ISSN: 1359-4311. DOI: 10.1016/j.applthermaleng.2023.120035.

[120] J. Tufft, "The development of a low-cost, universal rocket engine test stand," *University of Glasgow, Masters of Mechanical Engineering Final Year Project*, 2022.

[121] M. U. Ltd. "Pg45 data sheet." (), [Online]. Available: https://www.store.matara.com/wp-content/uploads/PG45-datasheet.pdf. [Accessed: 05.12.2021].

[122] C. Elliott, V. Vijayakumar, W. Zink, and R. Hansen, "National instruments labview: A programming environment for laboratory automation and measurement," *JALA: Journal of the Association for Laboratory Automation*, vol. 12, no. 1, pp. 17–24, 2007. DOI: 10.1016/j.jala.2006.07.012.

[123] *AKD User Guide*, Revision M. Kollmorgen Corporation, May 2014.

[124] R. S. Okojie, R. D. Meredith, C. T. Chang, and E. Savrun, "High temperature dynamic pressure measurements using silicon carbide pressure sensors," *Additional Papers and Presentations*, vol. 2014, no. HITEC, pp. 000 047–000 052, 2014.

[125] M. Leonardi, F. Di Matteo, J. Steelant, F. Nasuti, and M. Onofri, "Non-linear analysis of low-frequency combustion instabilities in liquid rocket engines," 6th European Conference for Aeronautics and Space Sciences, Jun. 2015. DOI: 10.1051/eucass/201911295.

[126] A. Blackman, "Studies of screeching combustion and pressure-wave, flamefront interaction," *Combustion and Flame*, vol. 5, pp. 175–190, 1961, ISSN: 0010-2180. DOI: 10.1016/0010-2180(61)90093-1.

[127] R. Baidya, A. Pesyridis, and M. Cooper, "Ramjet nozzle analysis for transport aircraft configuration for sustained hypersonic flight," *Applied Sciences*, vol. 8, p. 574, Apr. 2018. DOI: 10.3390/app8040574.

[128] D. Cuppoletti, E. Gutmark, H. Hafsteinsson, and L.-E. Eriksson, "The role of nozzle contour on supersonic jet thrust and acoustics," *AIAA Journal*, vol. 52, no. 11, pp. 2594–2614, 2014. DOI: 10.2514/1.J052974.

[129] V. ZAPRYAGAEV, V. Pickalov, N. Kiselev, and A. Nepomnyashchiy, "Combination interaction of taylor–goertler vortices in a curved shear layer of a supersonic jet," *Theoretical and Computational Fluid Dynamics*, vol. 18, pp. 301–308, Nov. 2004. DOI: 10.1007/s00162-004-0141-5.

[130] H. Ziebland and R. C. Parkinson, *Heat Transfer in Rocket Engines*. Technical Editing and Reproduction Ltd., 1971.

[131] J. Beér and K. Lee, "The effect of the residence time distribution on the performance and efficiency of combustors," *Symposium (International) on Combustion*, vol. 10, no. 1, pp. 1187–1202, 1965, Tenth Symposium (International) on Combustion, ISSN: 0082-0784. DOI: 10.1016/S0082-0784(65)80255-7.

[132] J. Bennewitz and R. Frederick, "Overview of combustion instabilities in liquid rocket engines - coupling mechanisms and control techniques," Jul. 2013, ISBN: 978-1-62410-222-6. DOI: 10.2514/6.2013-4106.

[133] R. Pecha and B. Gompf, "Microimplosions: Cavitation collapse and shock wave emission on a nanosecond time scale," *Physical review letters*, vol. 84, no. 6, p. 1328, 2000.

[134] D. Peregrine, "The acoustic bubble. by tg leighton. academic press, 1994. 613 pp.£ 95. isbn 0-12-441920-8.," *Journal of Fluid Mechanics*, vol. 272, pp. 407–408, 1994.

[135] Y. Liu *et al.*, "Cavitation erosion on different metallic materials under high hydrostatic pressure evaluated with the spatially confined sonoluminescence," *Ultrasonics Sonochemistry*, vol. 107, p. 106 920, 2024.

[136] M. Casiano, J. Hulka, and V. Yang, "Liquid-propellant rocket engine throttling: A comprehensive review," *Journal of Propulsion and Power*, vol. 26, Aug. 2009. DOI: 10.2514/6.2009-5135.

[137] J. Martin, W. Armbruster, J. S. Hardi, D. Suslov, and M. Oschwald, "Experimental investigation of self-excited combustion instabilities in a lox/lng rocket combustor," *Journal of Propulsion and Power*, vol. 37, no. 6, pp. 944–951, 2021. DOI: 10.2514/1.B38289.

[138] W. Marshall, S. Pal, and R. Santoro, "Combustion instability studies in a rectangular rocket chamber," in *44th AIAA/ASME/SAE/ASEE Joint Propulsion Conference & Exhibit*. DOI: 10.2514/6.2008-4656.

[139] F. J. Stoddard, "Inherent stability of central element coaxial liquid-liquid injectors," *TRW Applied Technology Division (N94-25043)*, Nov. 1993. [Online]. Available: https://ntrs.nasa.gov/citations/19940018570.

[140] K. Sakaki *et al.*, "Longitudinal combustion instability of a pintle injector for a liquid rocket engine combustor," *Combustion and Flame*, vol. 194, Jun. 2018. DOI: 10.1016/j.combustflame.2018.04.017.

[141] J. Cha, E. Andersson, and A. Bohlin, "A numerical approach to optimize the design of a pintle injector for lox/gch4 liquid-propellant rocket engine," *Aerospace*, vol. 10, no. 7, 2023, ISSN: 2226-4310. DOI: 10.3390/aerospace10070582.

[142] J. Kang, J. Ran, J. Niu, J. Shi, J. He, and Z. Yang, "Experimental and theoretical study on propane pyrolysis to produce gas and soot," *International Journal of Hydrogen Energy*, vol. 44, no. 41, pp. 22 904–22 918, 2019, ISSN: 0360-3199. DOI: 10.1016/j.ijhydene.2019.06.214.

[143] P. Bauer, J. Haines, and T. Hellwig, "Soak-back heating response of thruster components for steady and pulsed firing," in *15th Thermophysics Conference*. DOI: 10.2514/6.1980-1515.

[144] D. B. Makel and S. D. Rosenberg, "Carbon deposition model for oxygen-hydrocarbon combustion. task 6: Data analysis and formulation of an empirical model," *Contractor Report (NASA-CR-183986)*, 1990. [Online]. Available: https://ntrs.nasa.gov/citations/19900016779.

[145] A. Gennadievich, S. Sergeevna, L. ZHANG, and E. Nikolaevich, "Thermal state calculation of chamber in small thrust liquid rocket engine for steady state pulsed mode," *Chinese Journal of Aeronautics*, vol. 32, no. 2, pp. 253–262, 2019, ISSN: 1000-9361. DOI: 10.1016/j.cja.2018.12.022.

[146] J. A. Bonometti, J. W. Dankanich, and K. L. Frame, "Reusable propulsion architecture for sustainable low-cost access to space," Joint Army Navy Nasa Air Force (JANNAF) Conference, Monterey, CA, United States, 2005.

Appendix A

Ouroboros-3 Additional Data Charts

A.1 Specific Impulse

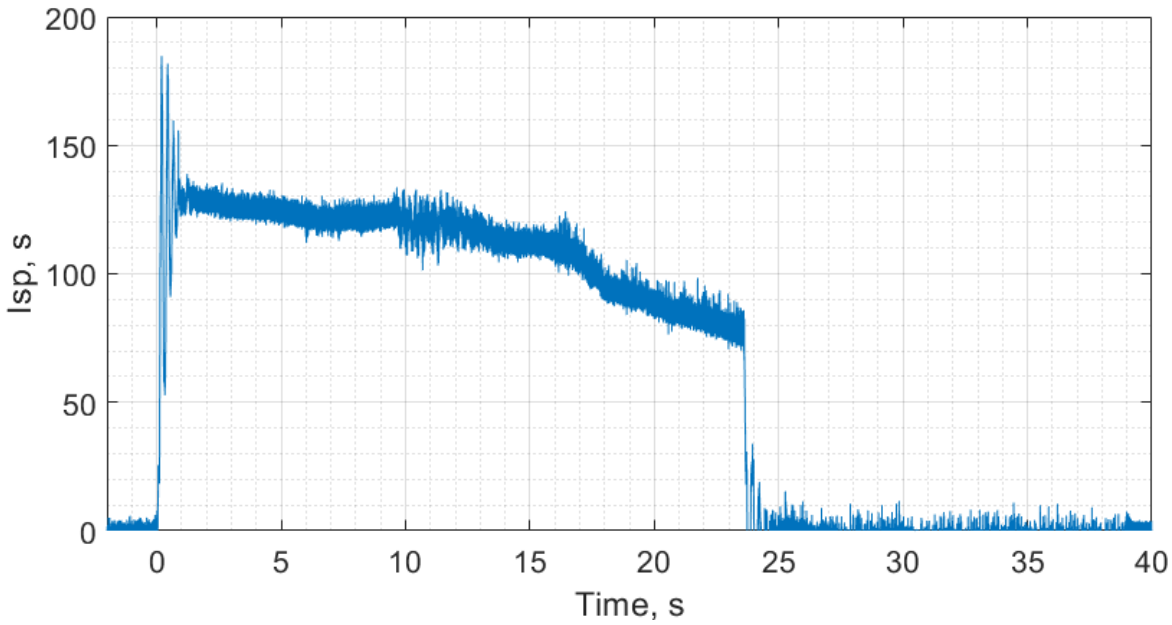

Fig. A.1 Ouroboros-3 specific impulse from test 1 performance data.

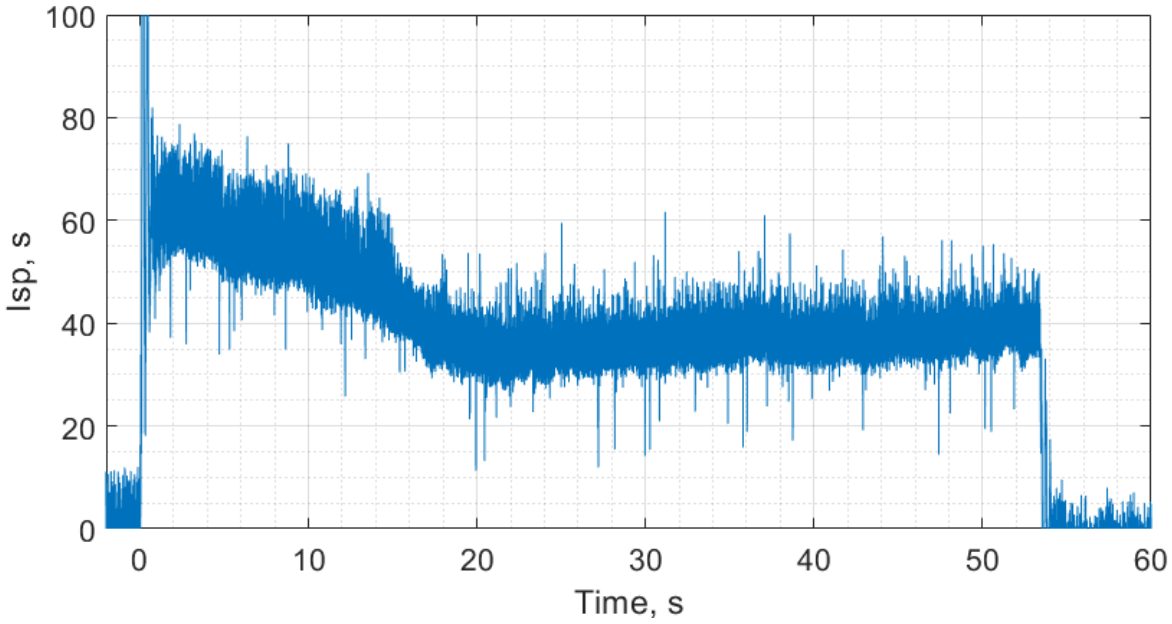

Fig. A.2 Ouroboros-3 specific impulse from test 2 performance data.

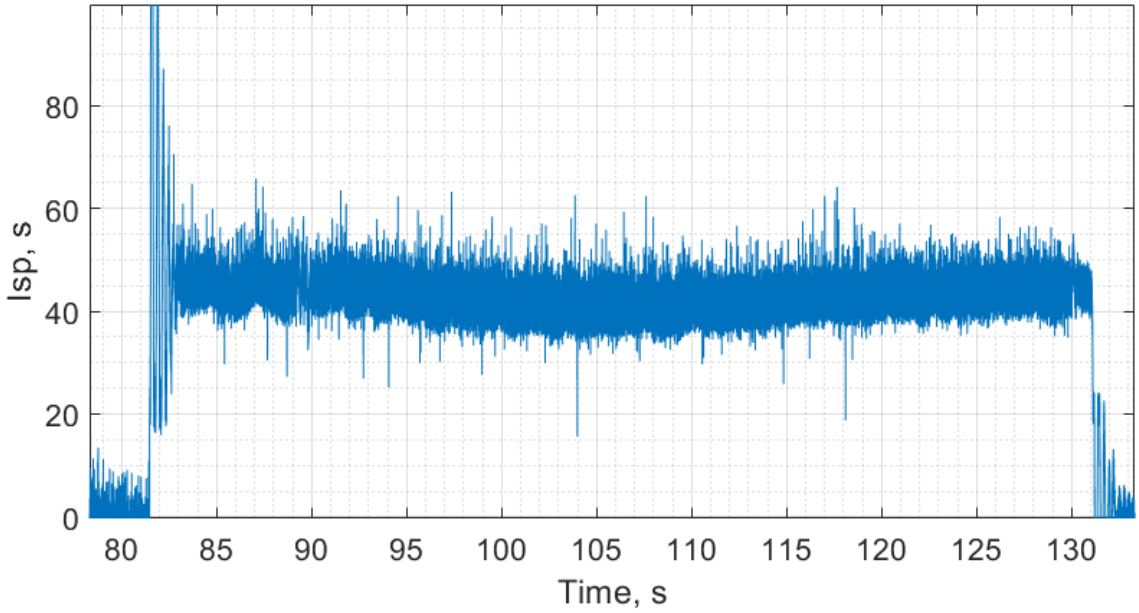

Fig. A.3 Ouroboros-3 specific impulse from test 3 performance data.

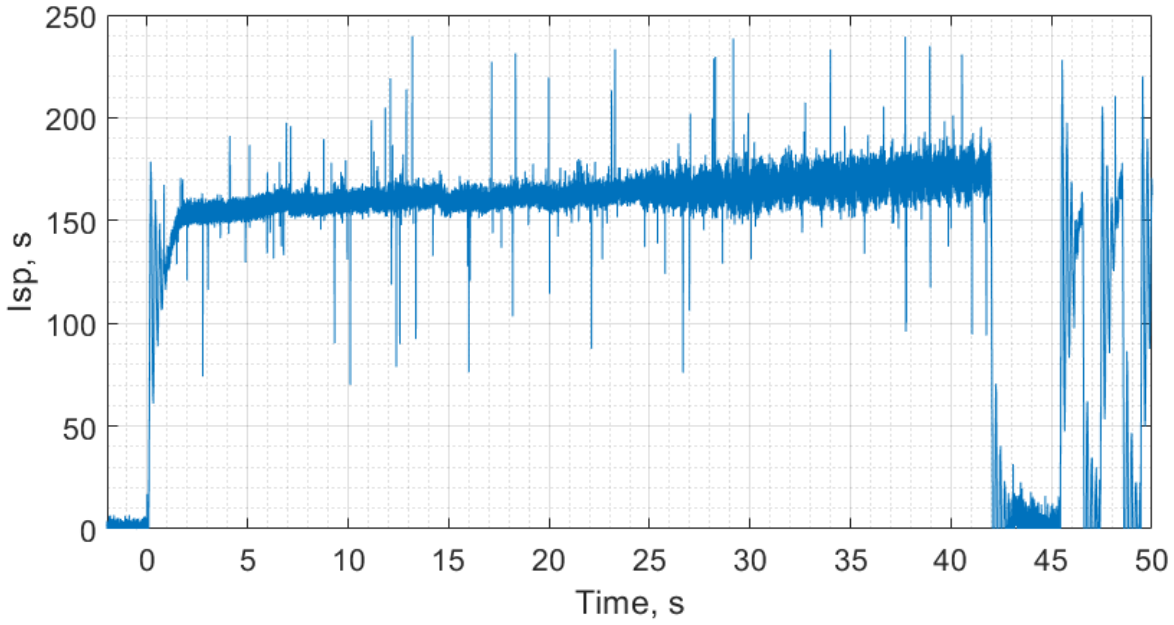

Fig. A.4 Ouroboros-3 specific impulse from test 4 performance data.

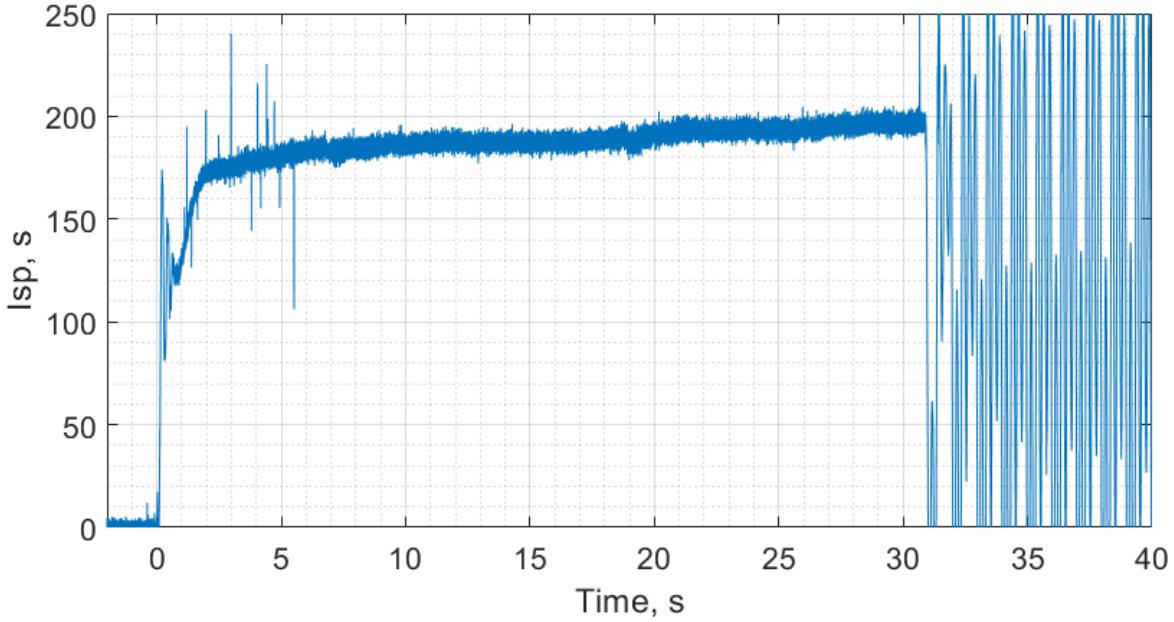

Fig. A.5 Ouroboros-3 specific impulse from test 5 performance data.

A.2 Combustion Chamber Pressure Rise and Decay

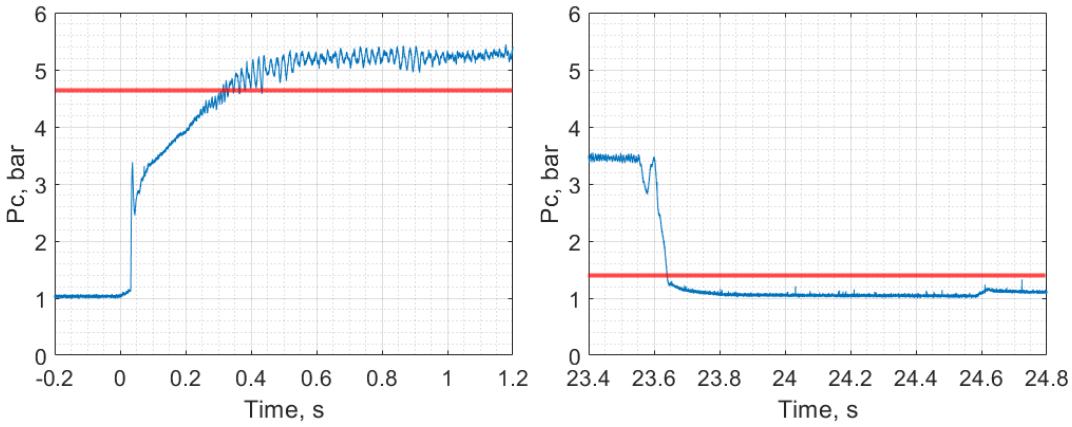

(a) Test 1 rise time (b) Test 1 decay time

Fig. A.6 Ouroboros-3 test 1 combustion chamber pressure rise and decay time.

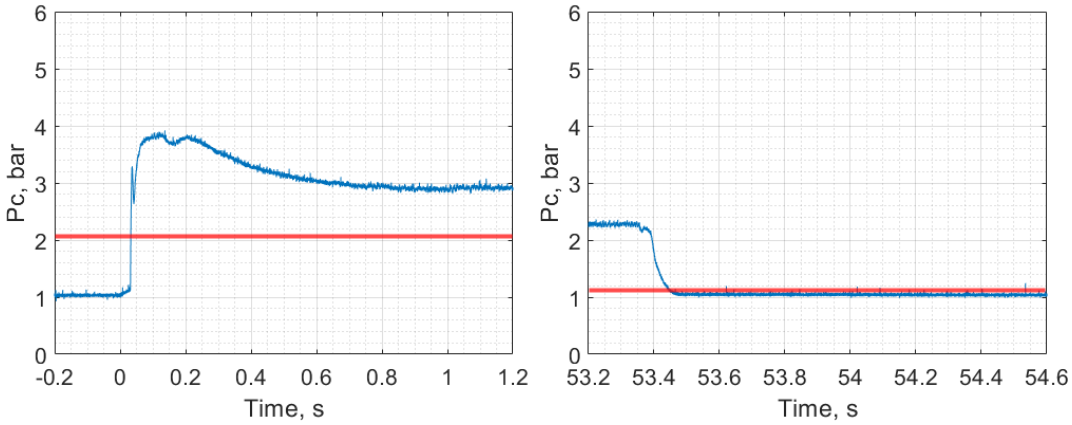

(a) Test 2 rise time (b) Test 2 decay time

Fig. A.7 Ouroboros-3 test 2 combustion chamber pressure rise and decay time.

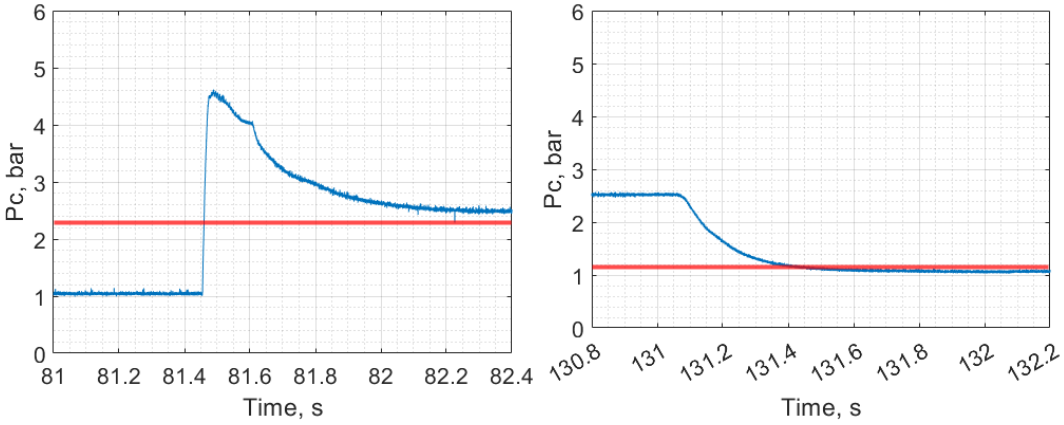

(a) Test 3 rise time (b) Test 3 decay time

Fig. A.8 Ouroboros-3 test 3 combustion chamber pressure rise and decay time.

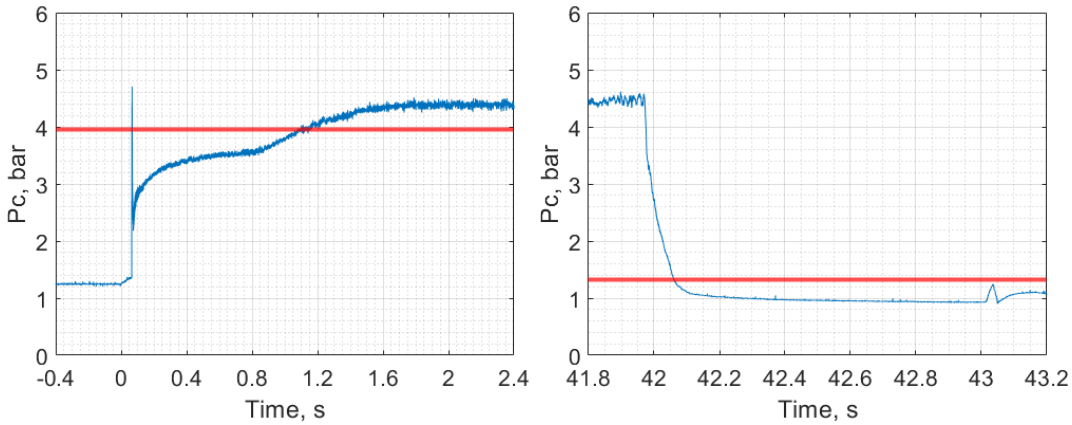

(a) Test 4 rise time (b) Test 4 decay time

Fig. A.9 Ouroboros-3 test 4 combustion chamber pressure rise and decay time.

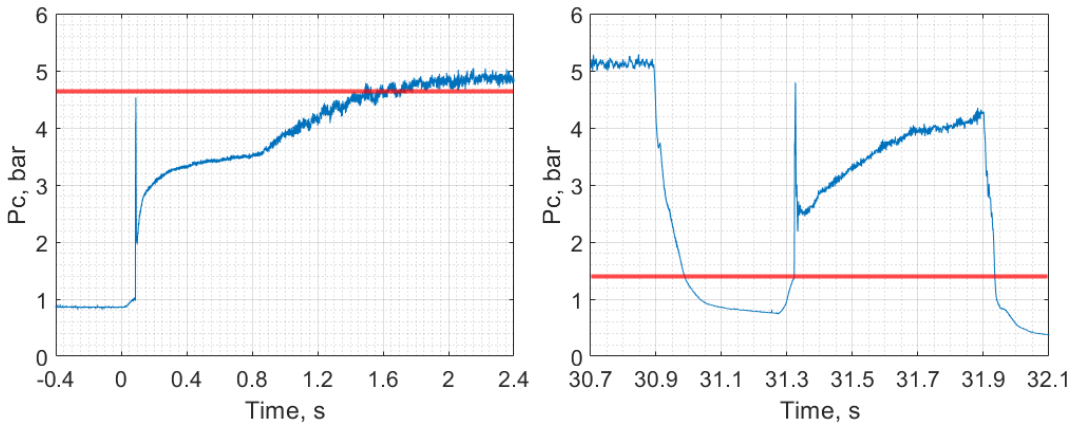

(a) Test 5 rise time (b) Test 5 decay time

Fig. A.10 Ouroboros-3 test 5 combustion chamber pressure rise and decay time.

A.3 Pulsed Mode with Unfiltered Thrust

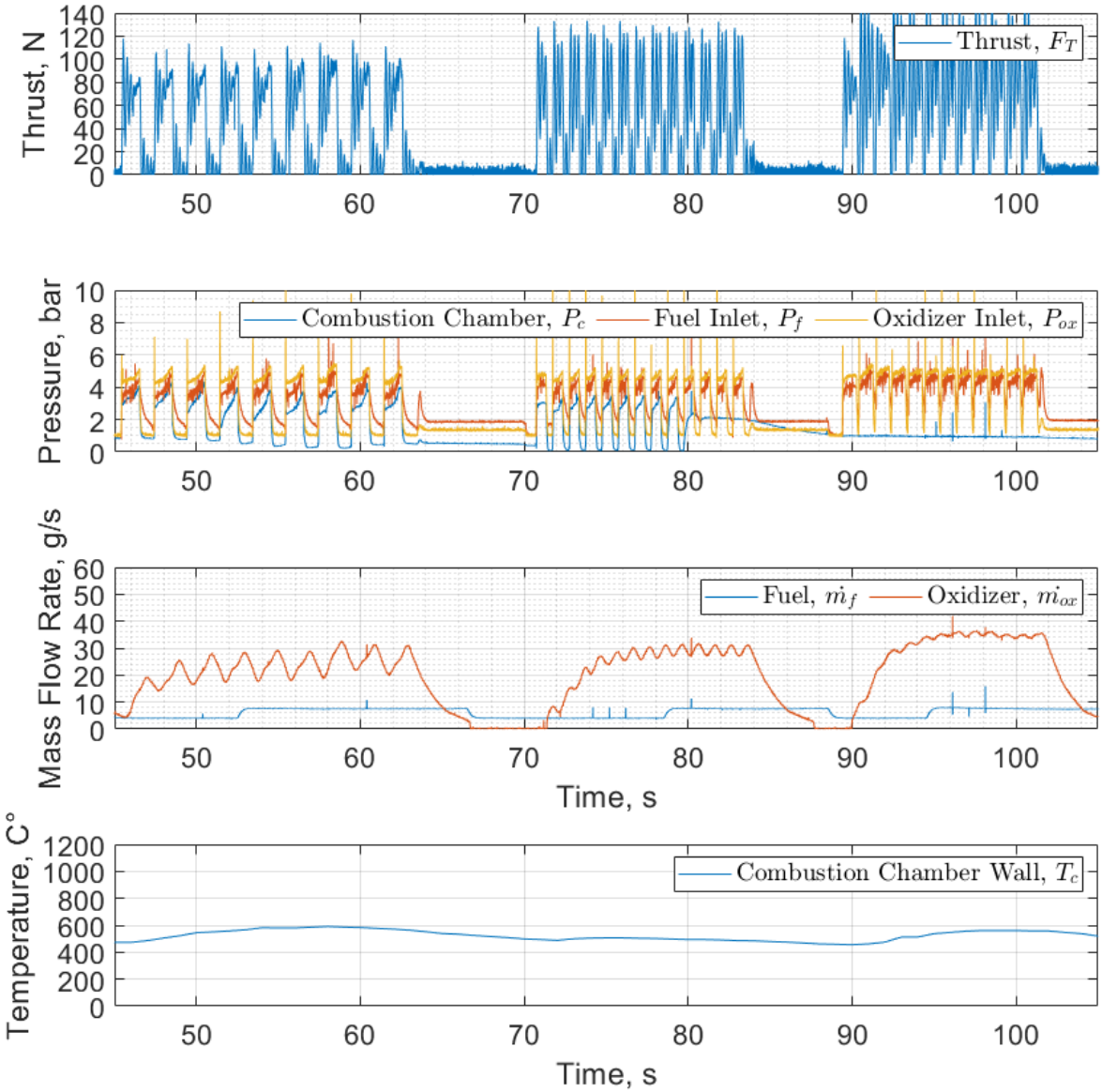

Fig. A.11 Ouroboros-3 autophage test 4 pulsed mode performance results at throttled, high mixture ratio inlet conditions.

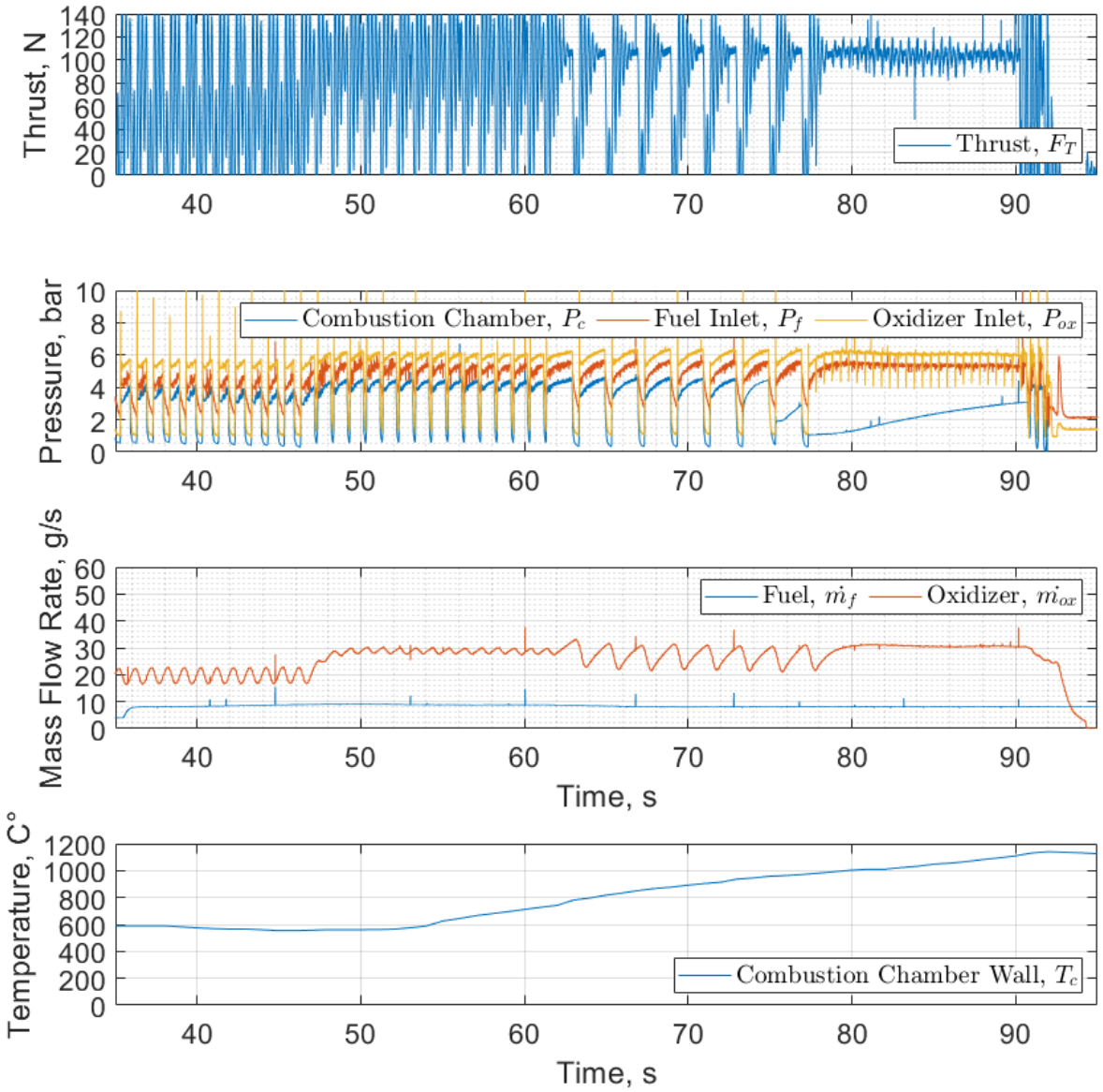

Fig. A.12 Ouroboros-3 autophage test 5 pulsed mode performance results at standard inlet conditions.

A.4 Pulsed Mode With Feed Force

A.4.1 Autophage Test 4 Pulsed Modes

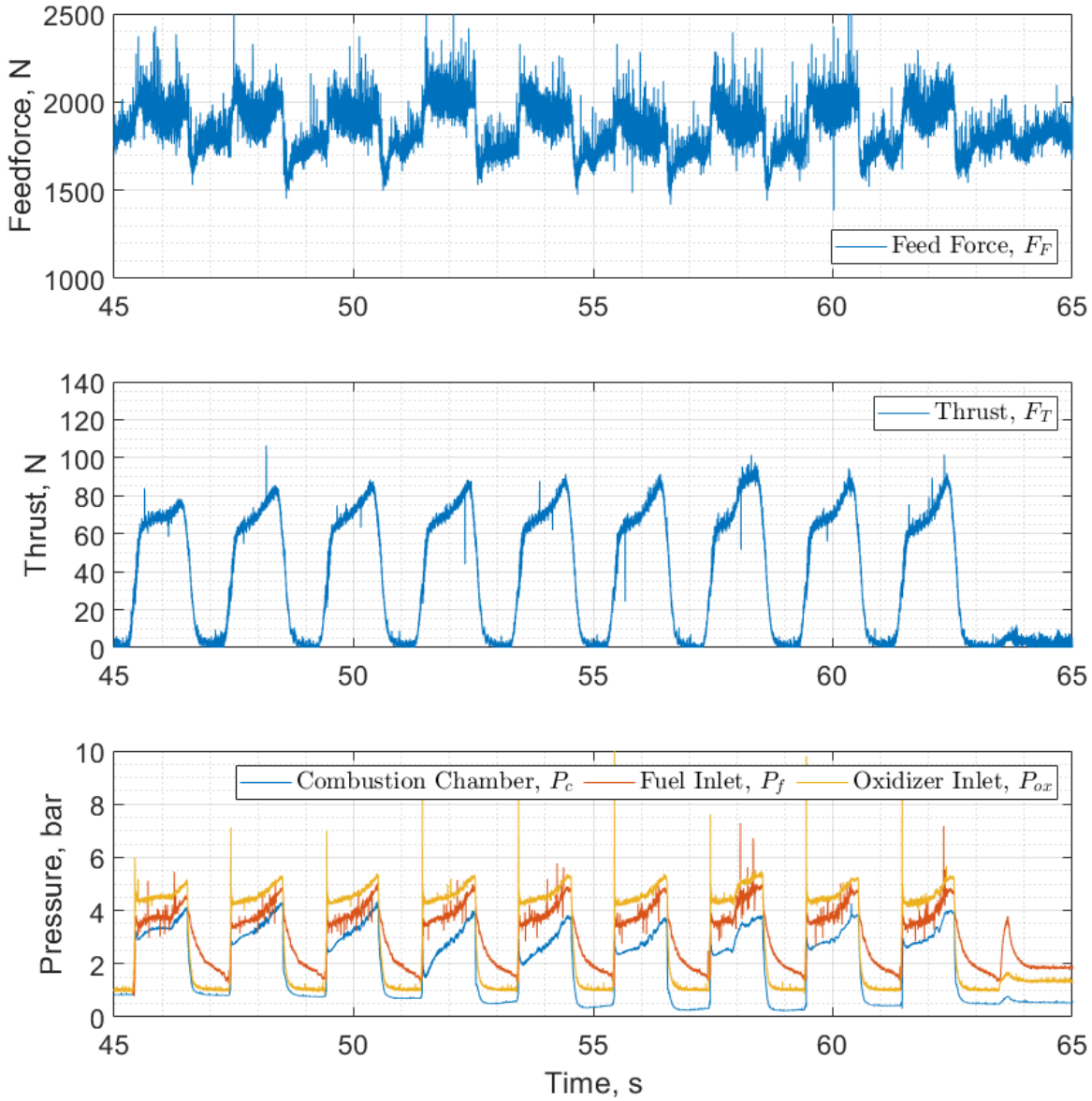

Fig. A.13 Ouroboros-3 autophage test 4.a pulsed mode performance results at 0.5 Hz and 50% duty cycle.

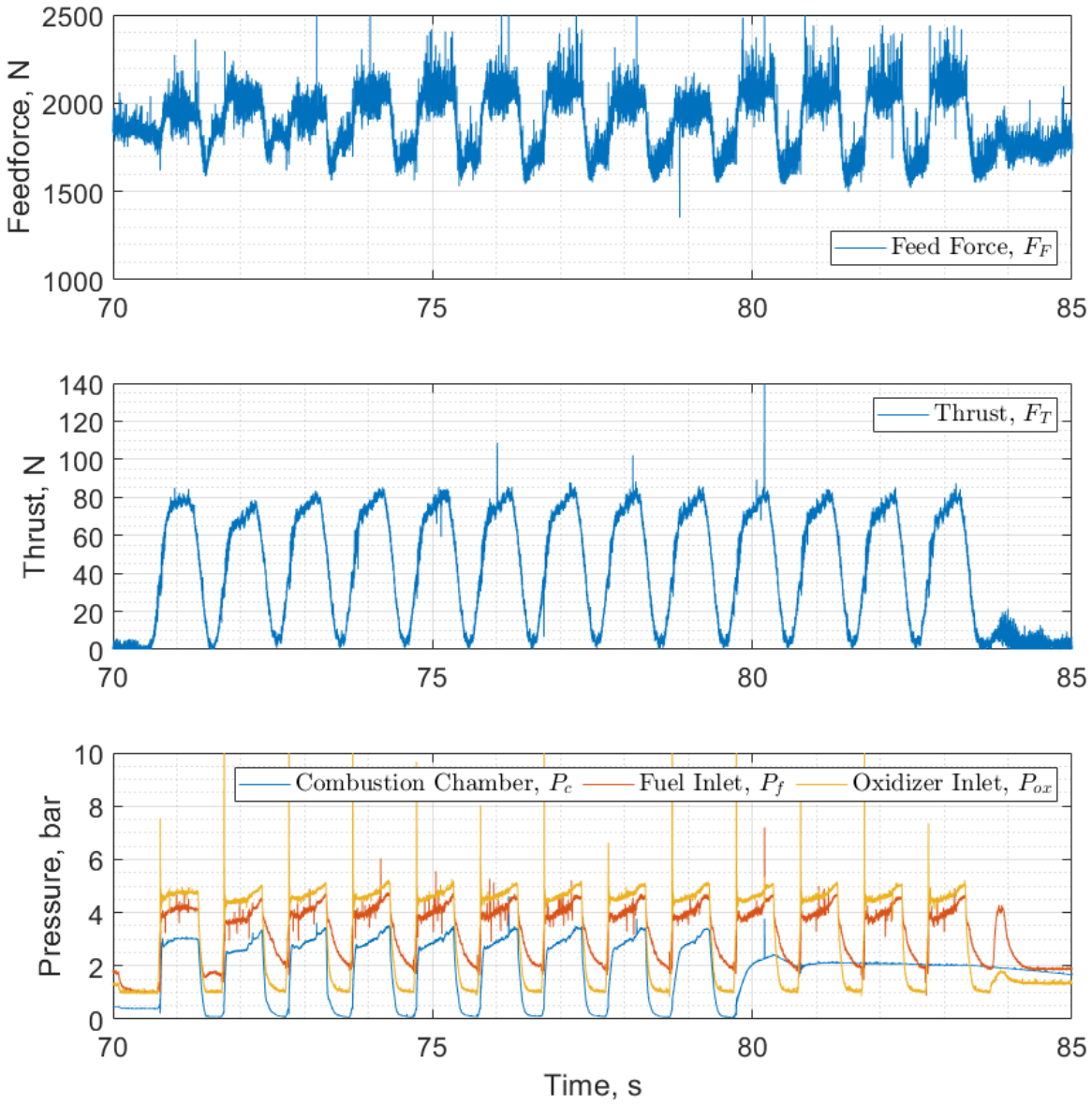

Fig. A.14 Ouroboros-3 autophage test 4.b pulsed mode performance results at 1.0 Hz and 50% duty cycle.

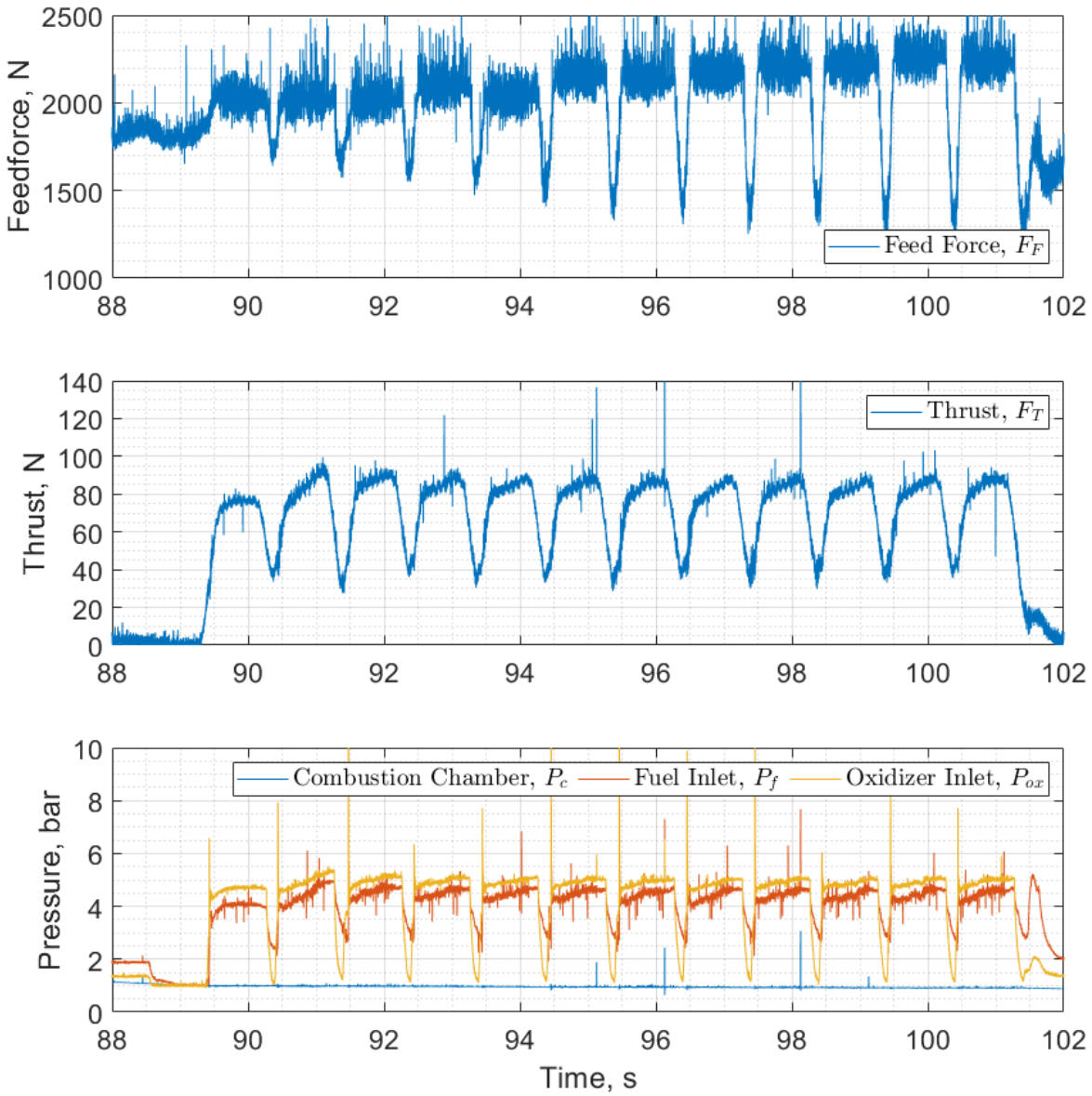

Fig. A.15 Ouroboros-3 autophage test 4.c pulsed mode performance results at 1.0 Hz and 75% duty cycle.

A.4.2 Autophage Test 5 Pulsed Modes

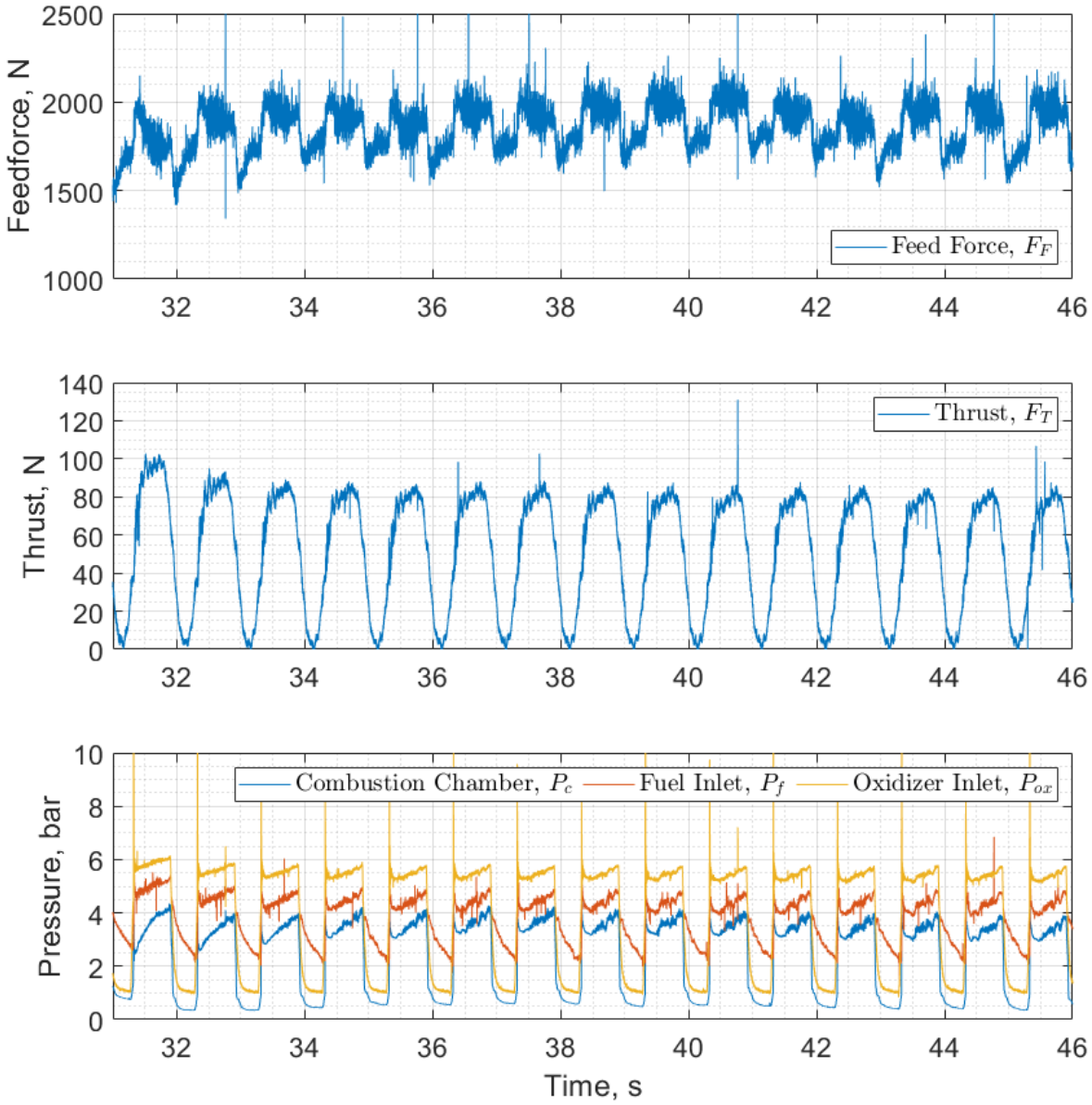

Fig. A.16 Ouroboros-3 autophage test 5.a pulsed mode performance results at 1.0 Hz and 50% duty cycle.

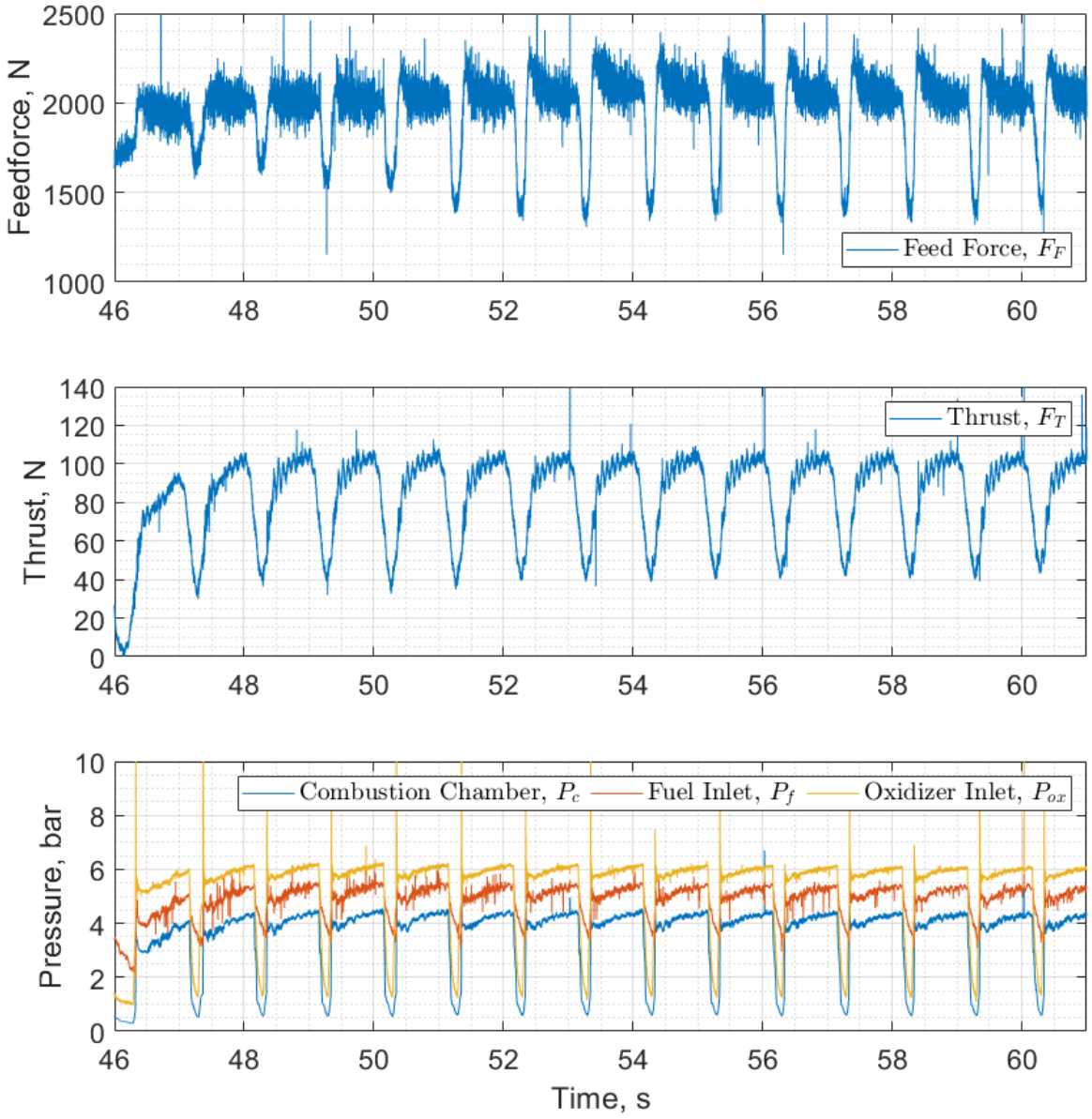

Fig. A.17 Ouroboros-3 autophage test 5.b pulsed mode performance results at 1.0 Hz and 75% duty cycle.

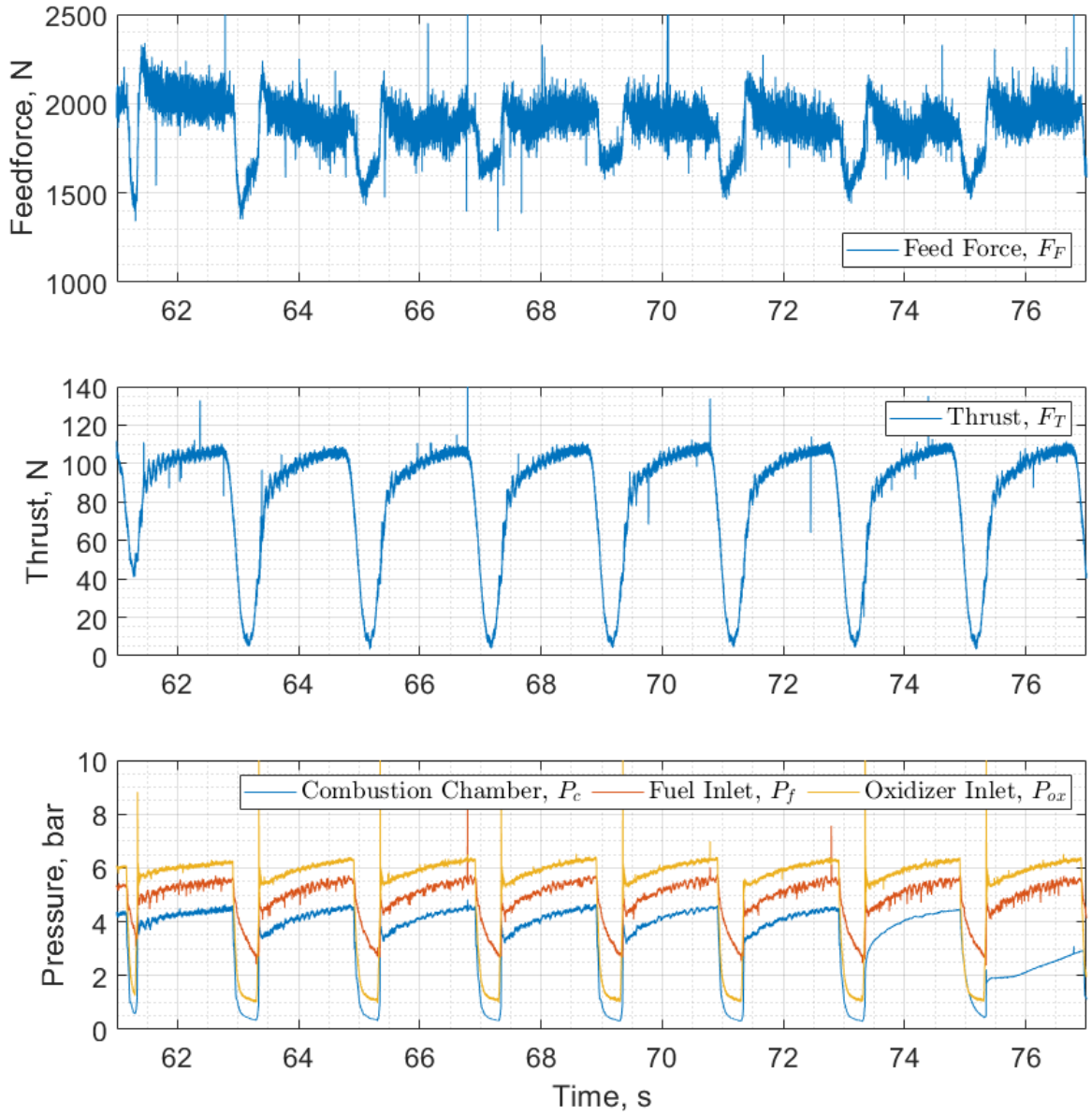

Fig. A.18 Ouroboros-3 autophage test 5.c pulsed mode performance results at 0.5 Hz and 75% duty cycle.

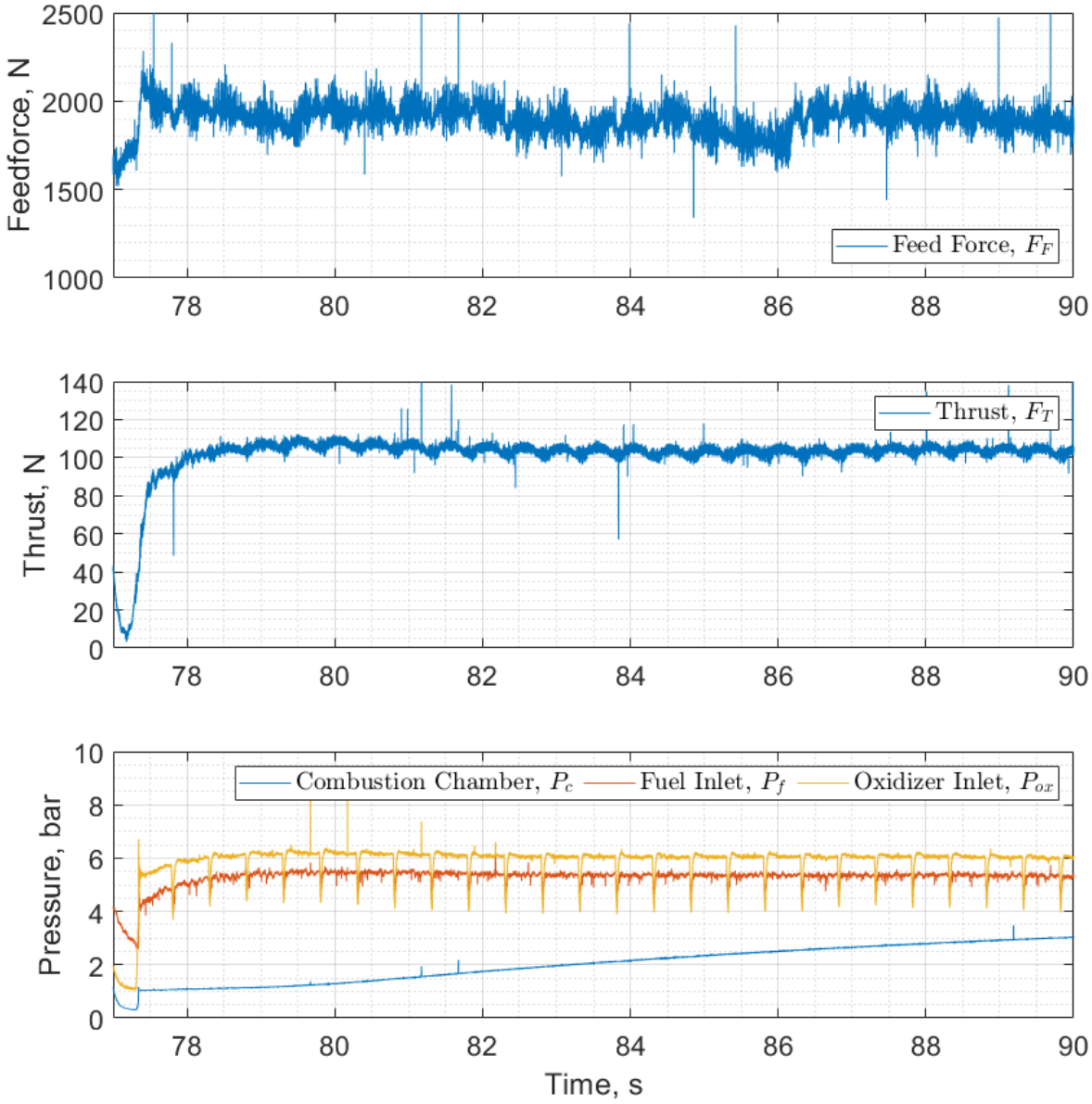

Fig. A.19 Ouroboros-3 autophage test 5.d pulsed mode performance results at 2.0 Hz and 75% duty cycle.

Appendix B

Ouroboros-3 Frequency Analysis Charts

B.1 Spectrograms

B.1.1 0-500 Hz Frequency Charts

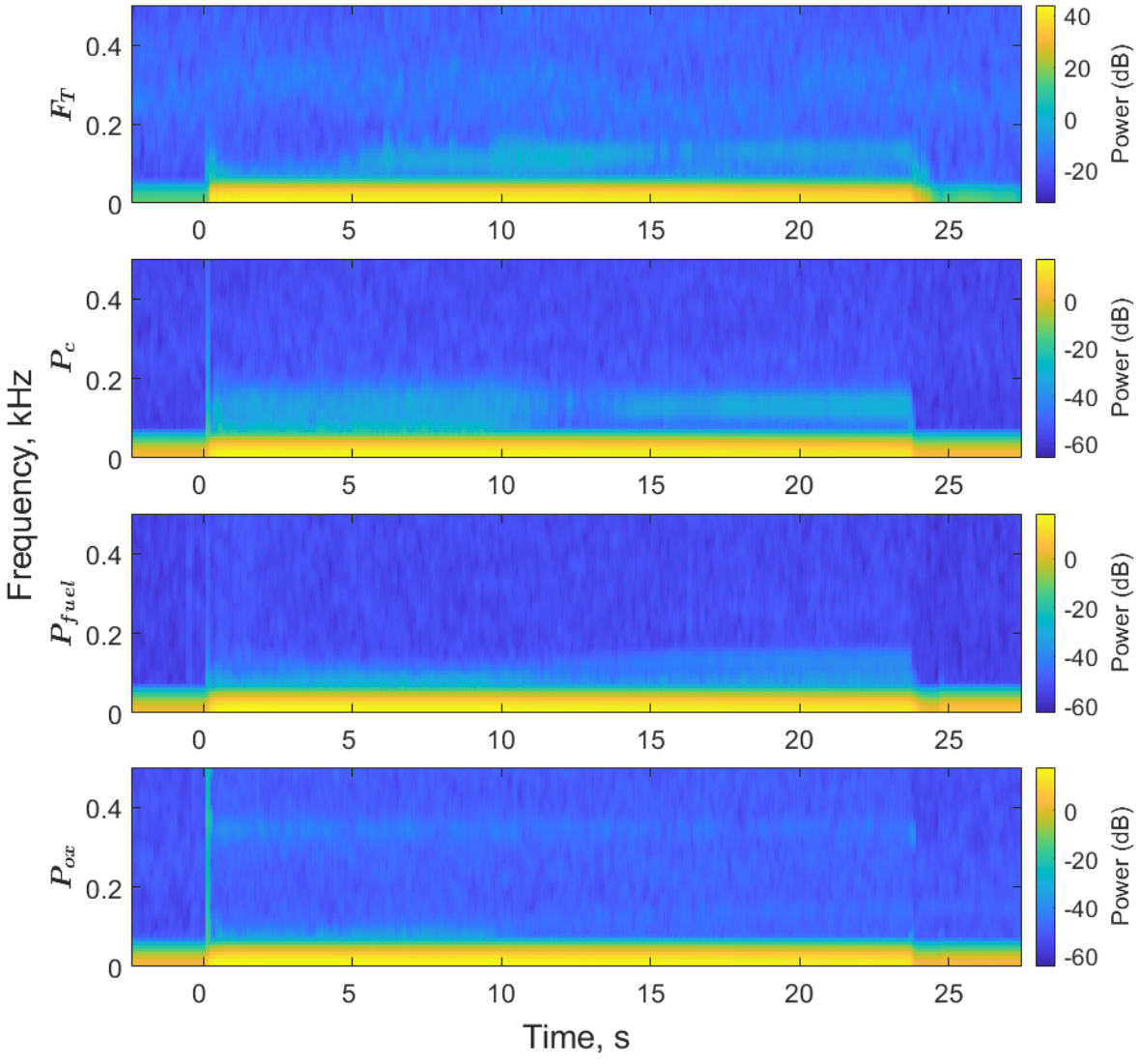

Fig. B.1 Ouroboros-3 autophage test 1 steady state low frequency spectrogram.

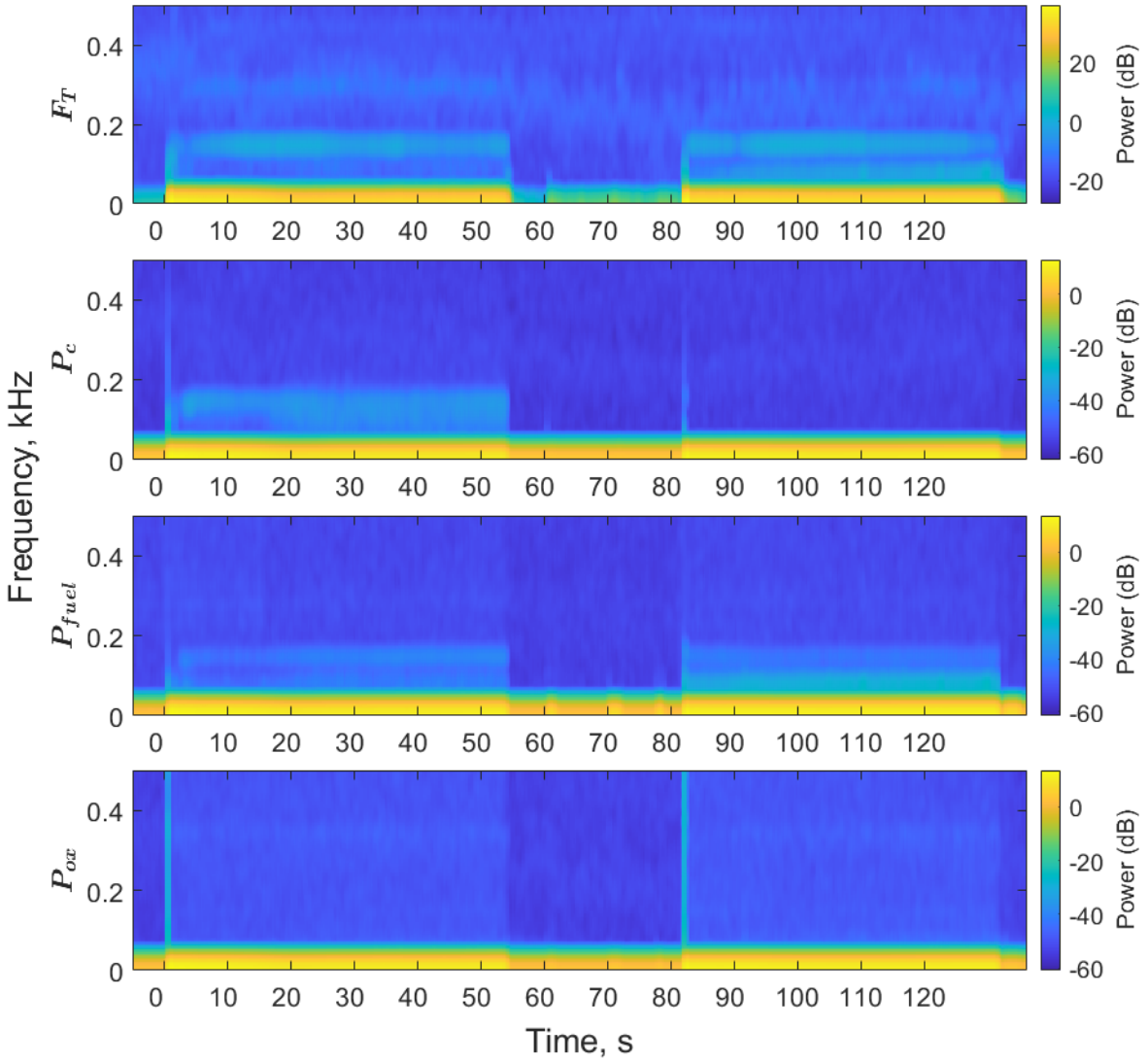

Fig. B.2 Ouroboros-3 autophage tests 2 and 3 steady state low frequency spectrogram.

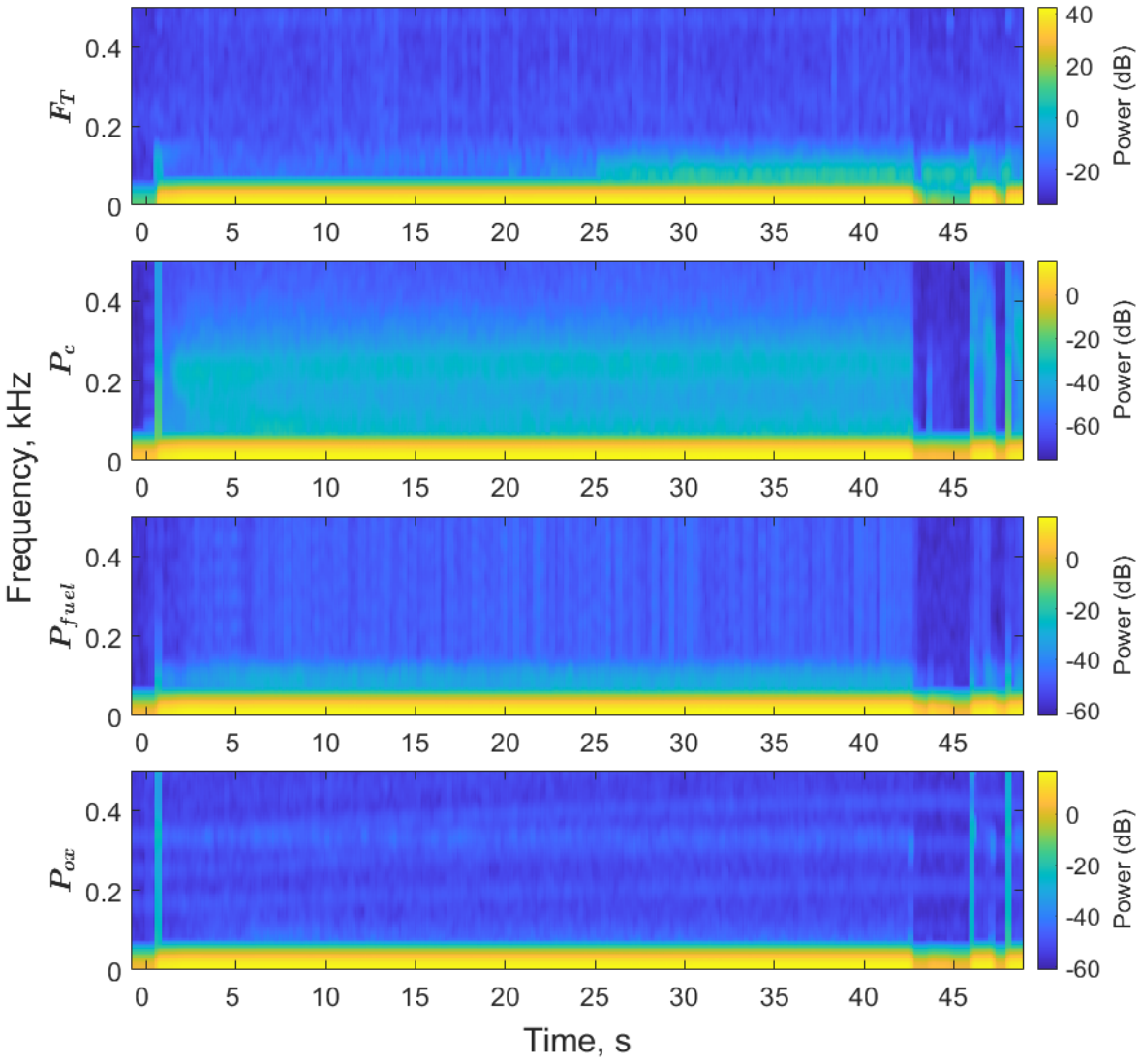

Fig. B.3 Ouroboros-3 autophage test 4 steady state low frequency spectrogram.

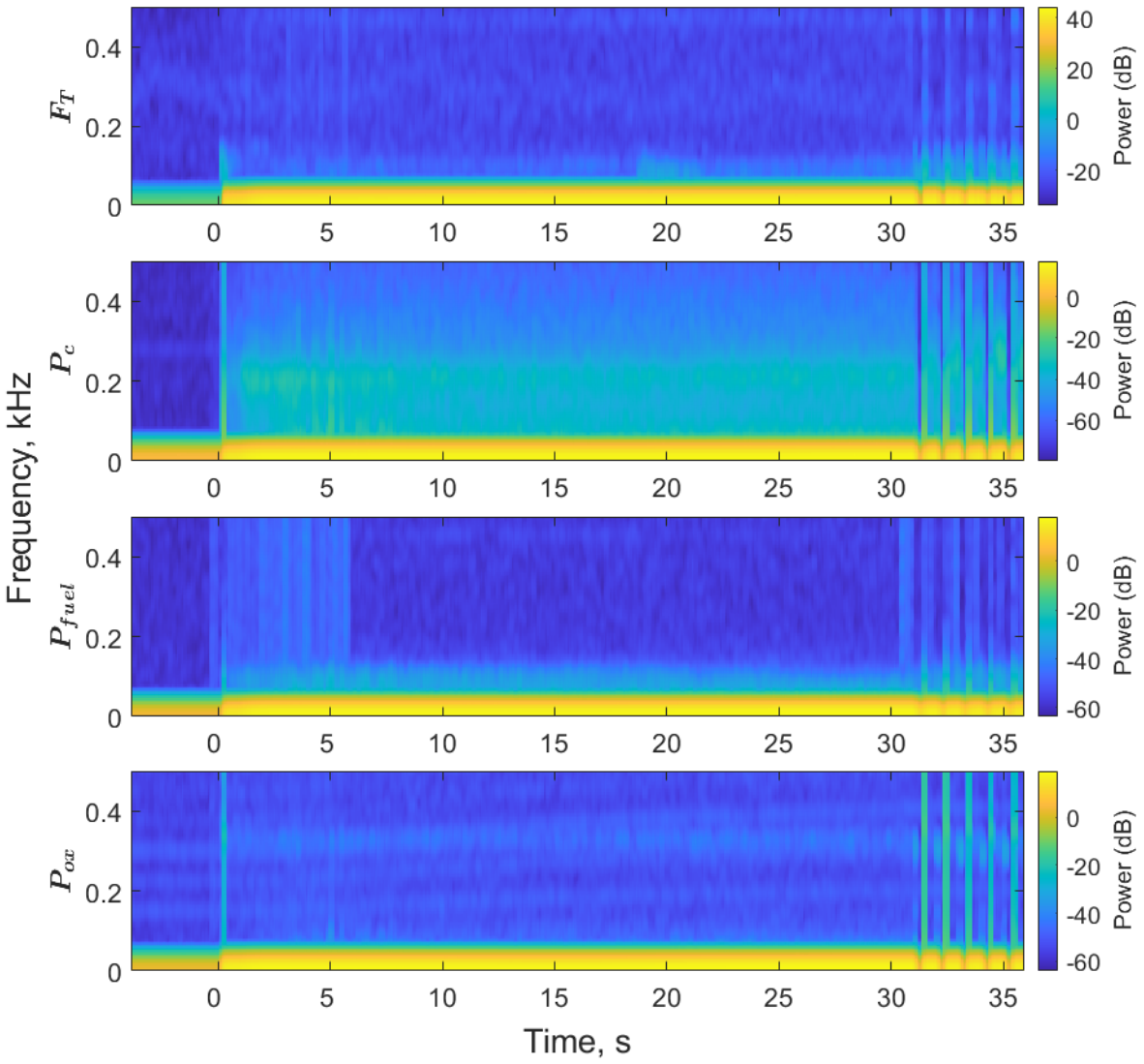

Fig. B.4 Ouroboros-3 autophage test 5 steady state low frequency spectrogram.

B.1.2 0-5 kHz Frequency Charts

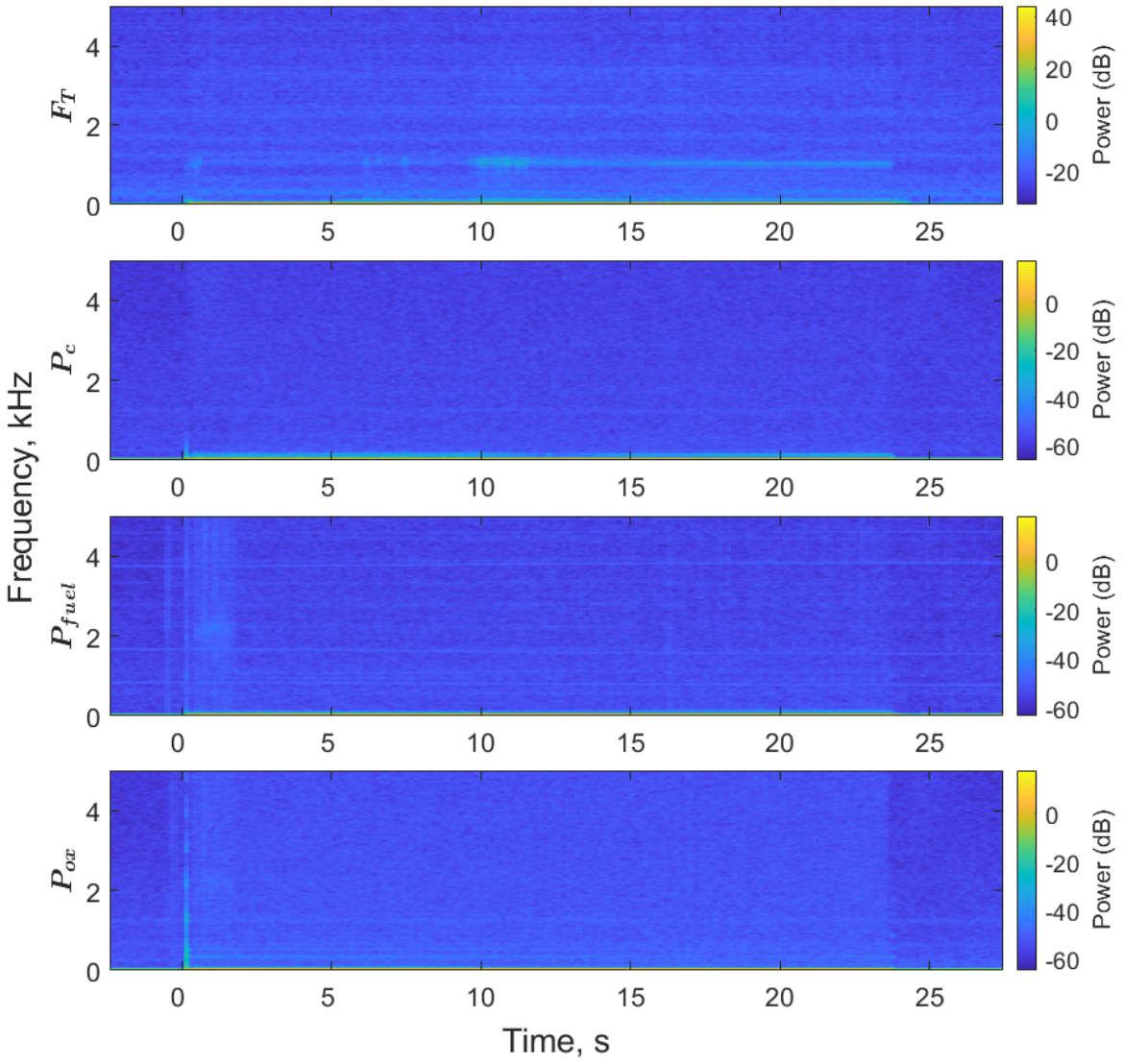

Fig. B.5 Ouroboros-3 autophage test 1 steady state high frequency spectrogram.

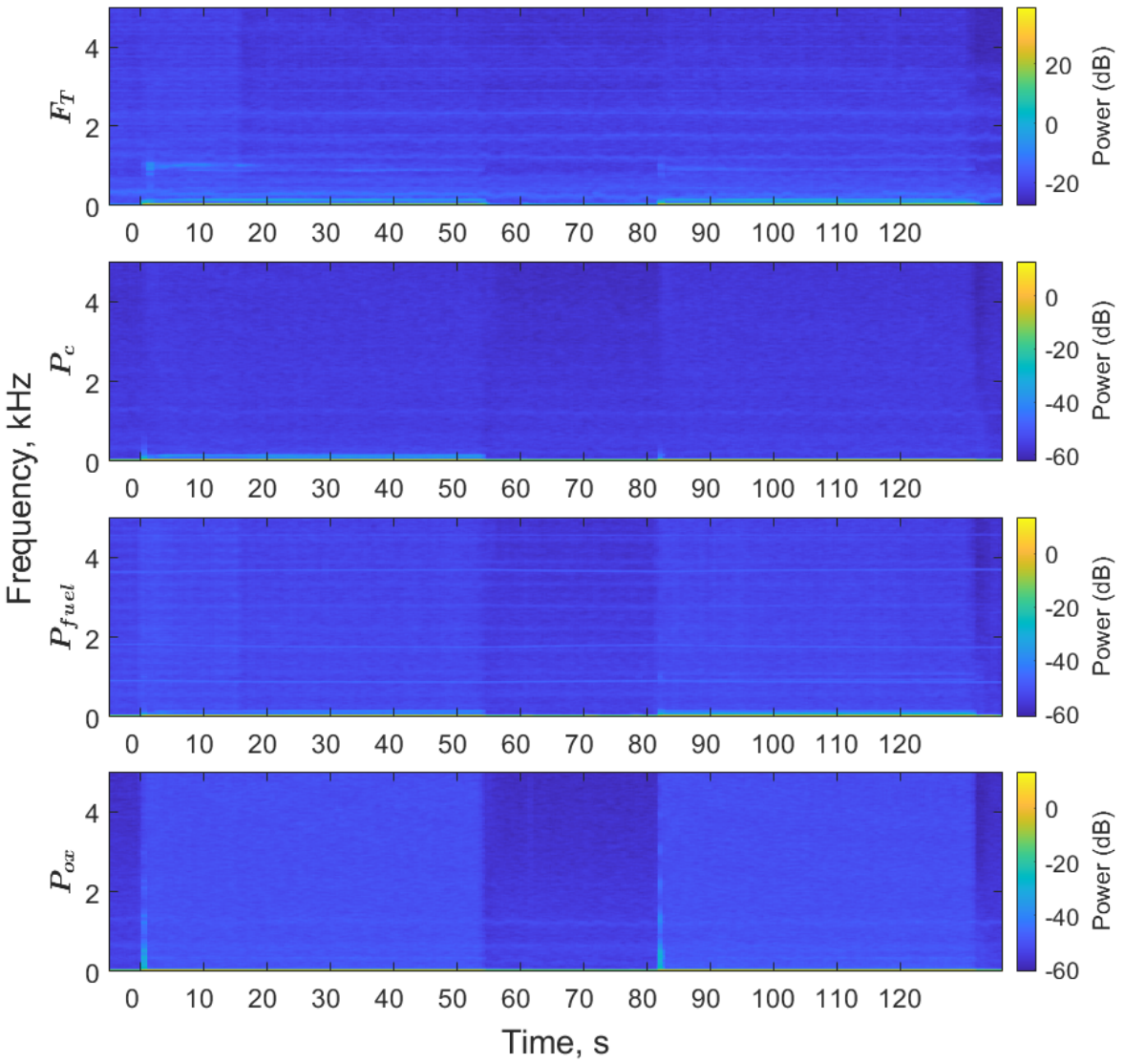

Fig. B.6 Ouroboros-3 autophage tests 2 and 3 steady state high frequency spectrogram.

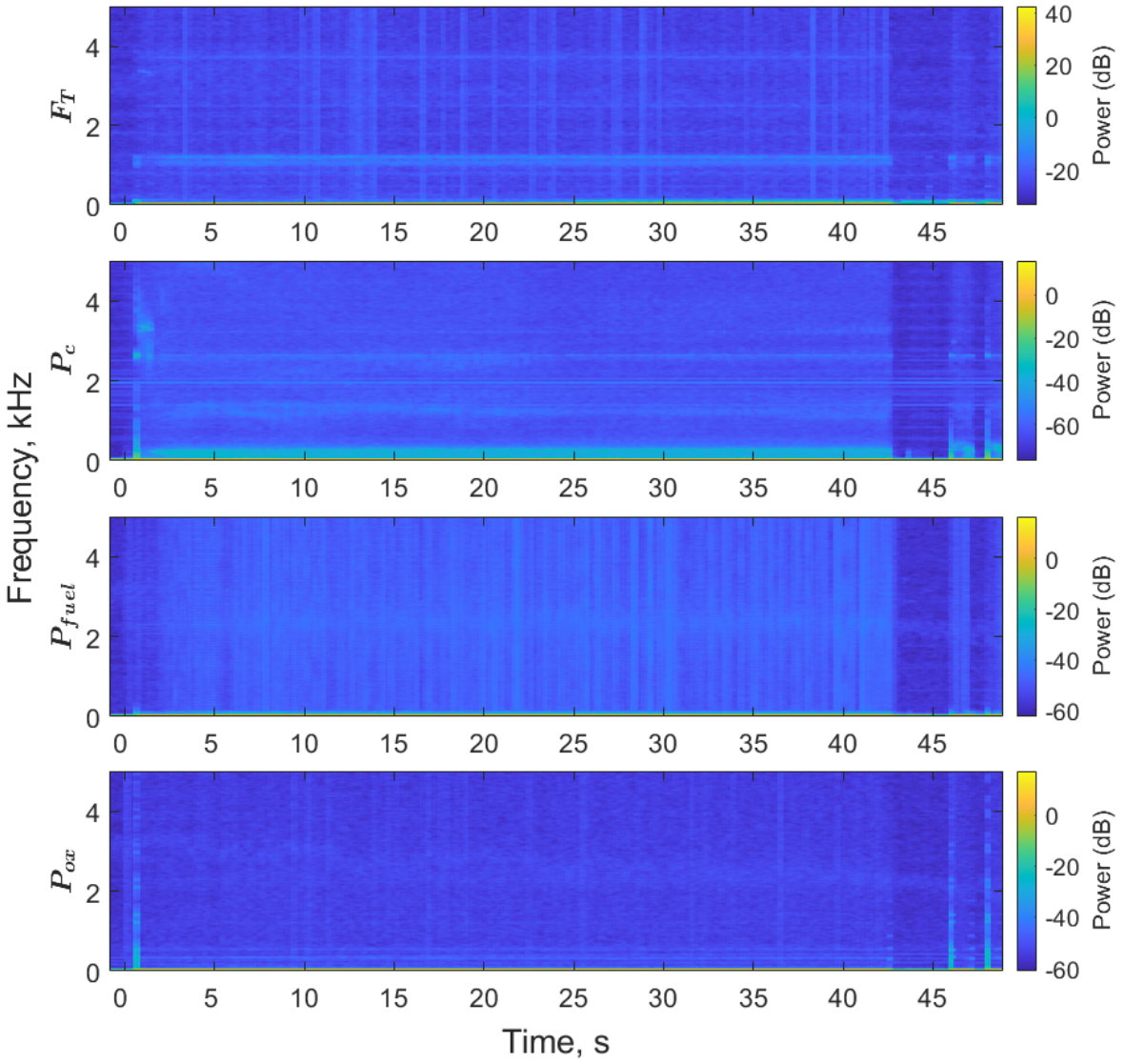

Fig. B.7 Ouroboros-3 autophage test 4 steady state high frequency spectrogram.

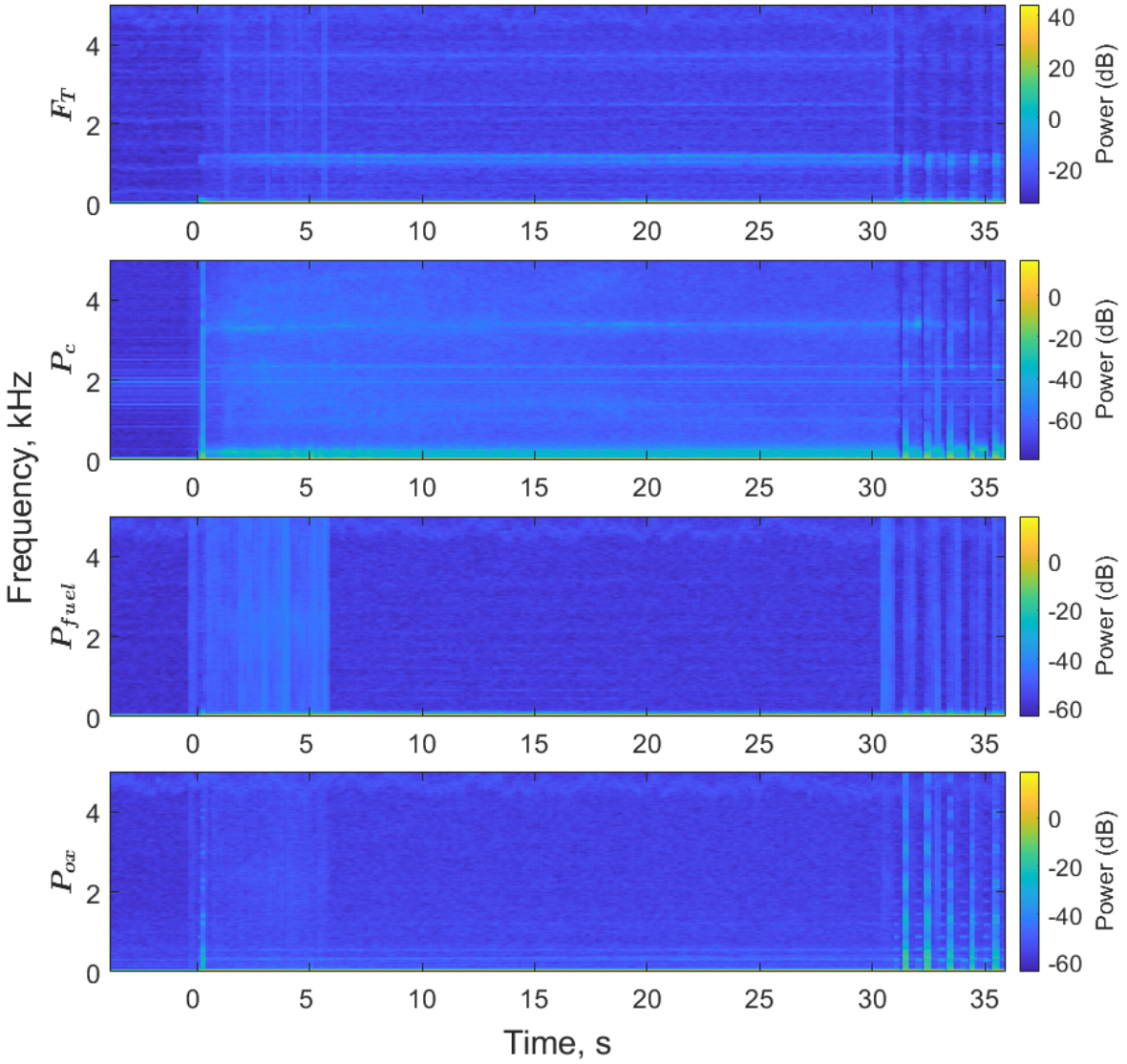

Fig. B.8 Ouroboros-3 autophage test 5 steady state high frequency spectrogram.

B.2 Persistence Diagrams

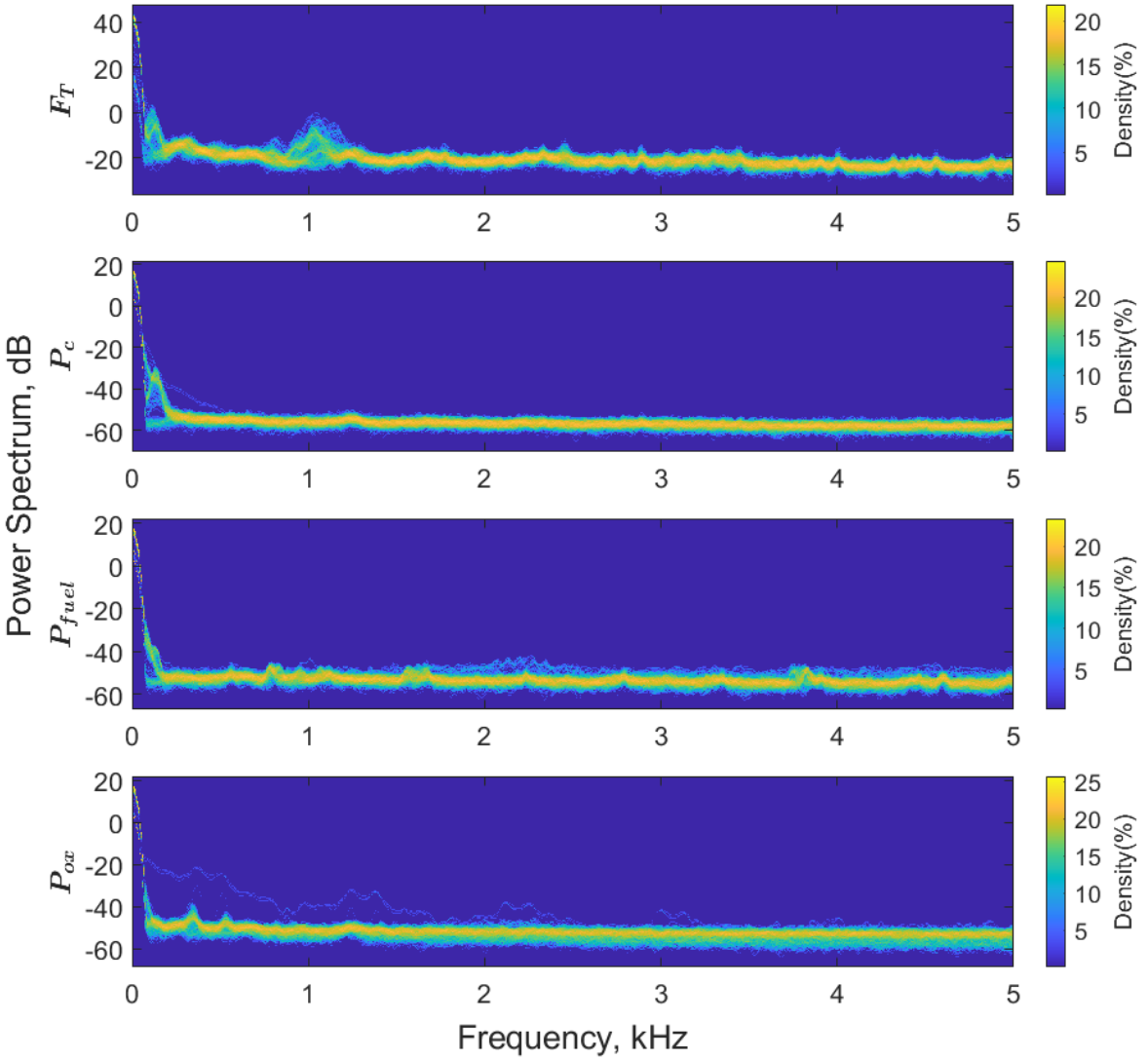

Fig. B.9 Ouroboros-3 autophage test 1 steady state persistence diagram.

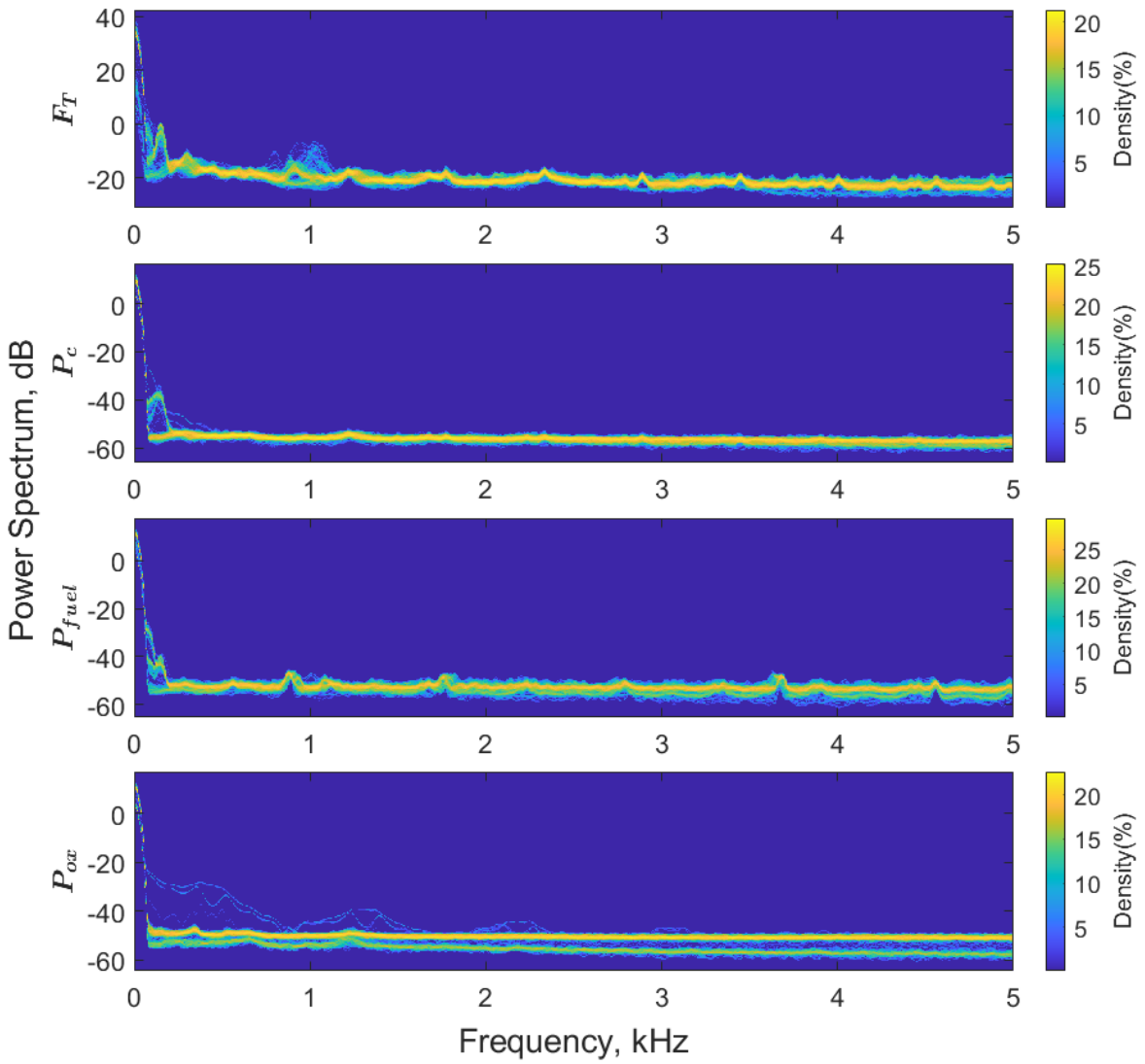

Fig. B.10 Ouroboros-3 autophage tests 2 and 3 steady state persistence diagram.

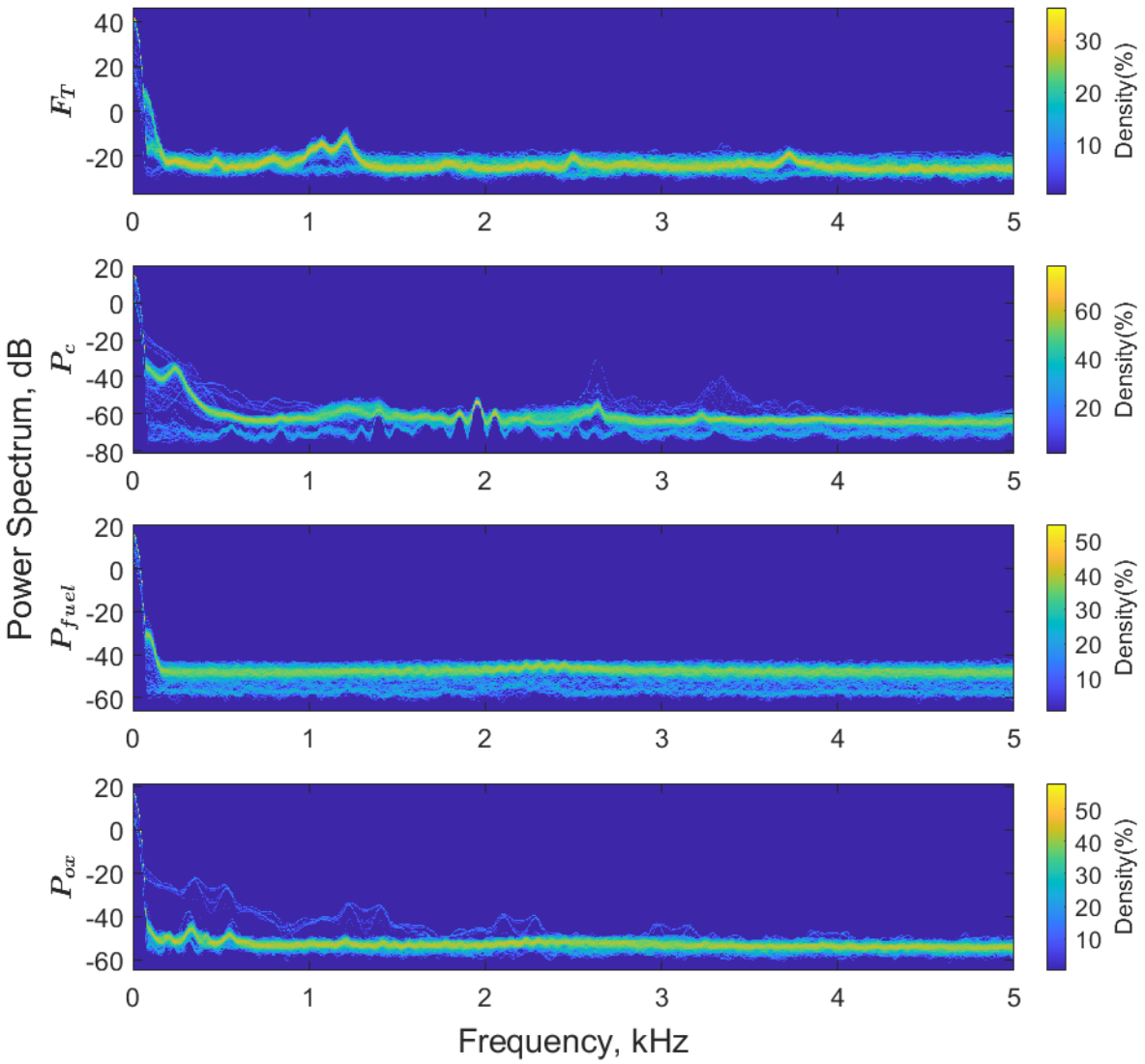

Fig. B.11 Ouroboros-3 autophage test 4 steady state persistence diagram.

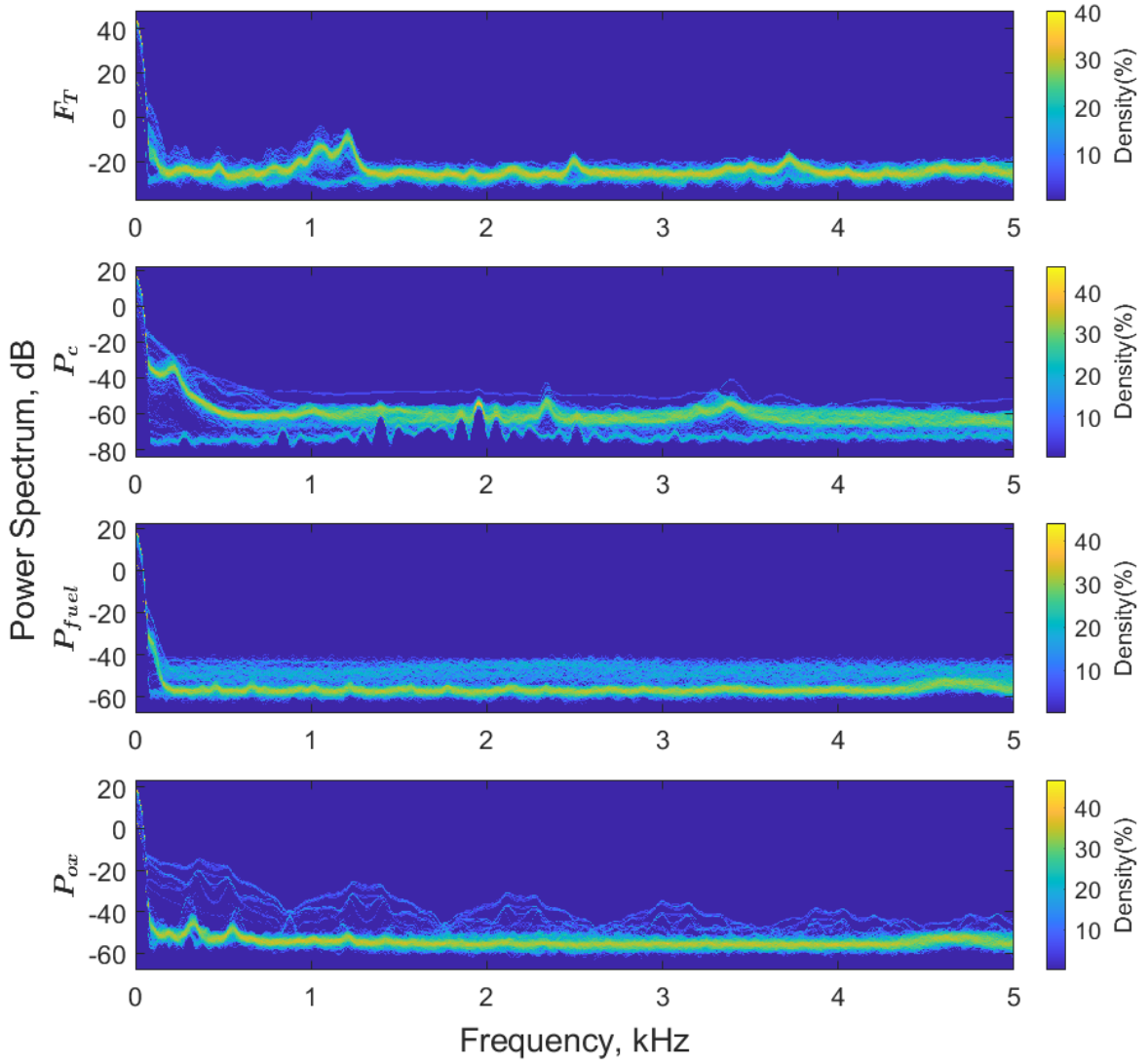

Fig. B.12 Ouroboros-3 autophage test 5 steady state persistence diagram.